Multiscale Modeling of the Mantle Rheology

Patrick Cordier, Alexandra Goryaeva

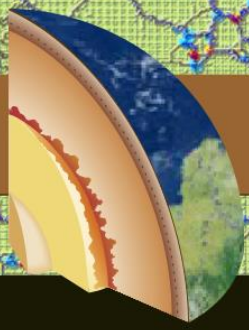

Multiscale Modeling of the Mantle Rheology

The RheoMan Project

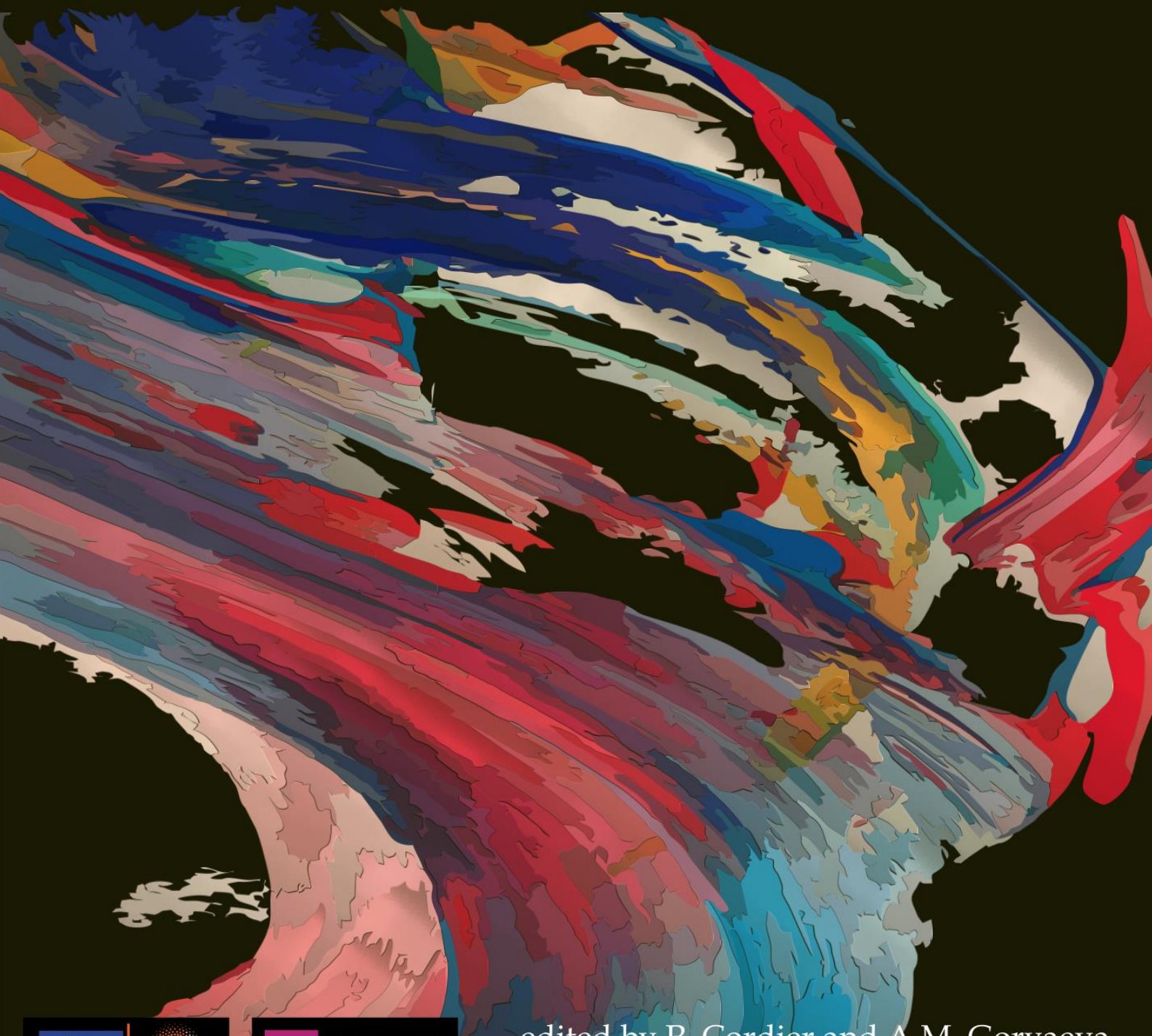

edited by P. Cordier and A.M. Goryaeva

erc European Research Council Established by the European Commission

Université de Lille

Contributors to the scientific content of the book (alphabetic order): Francesca Boioli, Philippe Carrez, Patrick Cordier, Alexandra M. Goryaeva, Karine Gouriet, Pierre Hirel, Antoine Kraych, Srinivasan Mahendran, Alexandre Mussi, Billy Nzogang, Riccardo Reali, Sebastian Ritterbex and Xiao-Yu Sun

Coordination, formatting and copy editing: Alexandra M. Goryaeva

Production editor: Patrick Cordier

May 25th, 2018

Printed in France by «Print Forum», 59290 Wasquehal

ISBN 978-2-9564368-0-5
e-ISBN 978-2-9564368-1-2

Cover picture : « *The Rheology of Colours* » by Alexandra M. Goryaeva

Picture of polycrystal : « *Disclinations decorating grain boundaries in olivine aggregate* ». Courtesy of S. Demouchy and B. Beausir

Université de Lille

Multiscale Modeling of the Mantle Rheology

The RheoMan Project

Edited by Patrick Cordier and Alexandra M. Goryaeva

Table of contents

Foreword

Rheology is the study of material flow. It plays a crucial role in our understanding of the solid Earth, because much of what we seek to learn about dynamic processes in the Earth involves stresses while much of what we do observe involves deformations. The two are linked through the rheological properties of rocks. Unfortunately, rocks have a complicated deformation behaviour that owes to their complex internal structure. Studies concerned with the rheological properties of rocks thus bring earth and material scientists together, while bridging spatial scales that range from atomic distances to the dimensions of our planet.

It is particularly challenging to understand the deformation behaviour of rocks when we look into the deep Earth, that is the sublithospheric mantle which extends from beneath the tectonic plates to the Core Mantle Boundary. Here the enormous pressures, temperatures and very low strain rates conspire to yield exotic conditions that are hard to duplicate in the laboratory. This means that laboratory deformation experiments provide us with a mere approximate guidance to the rheological properties that should prevail in the Earth's interior.

An earth scientist may approach this challenge by looking at deformation experiments performed for us by nature, such as the well-known glacial rebound problem. Interpretations of this classic natural experiment combine estimates of the original glacial load with observations of the resulting deformation (relaxation) history upon the loads removal. Glacial rebound studies have allowed geodynamicists to set an empirical constraint on the bulk viscosity of the sublithospheric mantle down to about 1400 km depth that we now call the *Haskell* value (10^{21} Pa·s), albeit with limited spatial or radial resolution. In their quest to constrain deep Earth rheology further, geodynamicists have also applied sophisticated global dynamic Earth models. The latter exploit more subtle information on convectively maintained internal loads of the Earth's mantle, namely in the form of mantle plumes and subducted slabs, and the dynamic topography at the Earth's surface and the Core Mantle Boundary that these loads induce. Together with geodetic information on the Earth's Geoid, such models require that the viscosity of the Earth's mantle increases substantially with depth, albeit again with considerable uncertainty.

Natural experiments are insightful. But they are hampered by observational limitations. More relevantly, they are limited in that they provide us with empirical relations on the deformation behaviour of rocks with no recourse to the underlying physical mechanisms that permit material flow. A powerful and complementary approach comes from material sciences, because the rheological properties of rocks can be investigated on fundamental grounds from theoretical studies at the atomic level, and that is where **RheoMan** comes in. For this six year ERC funded (Advanced Grant) project, Patrick Cordier has assembled an extraordinary team of scientists and young investigators to query the rheology of the Earth's mantle from a novel multiscale modelling approach. The approach links our understanding of elementary mechanisms at the microscopic scale, such as dislocation core and mobility modeling, with the deformation behaviour observed at the macroscopic scale, such as flow laws.

RheoMan has yielded surprising results. For instance, geodynamicists might not have suspected the existence of a so-called athermal regime, where viscosity is independent of temperature. RheoMan also showed that in silicates lattice friction increases very much with pressure. This means that pure climb creep should be more efficient than diffusion creep at the high-pressure conditions of the deep Earth. That important result, which

implies high lower mantle strength, broadly agrees with geodynamic mantle viscosity inferences derived from the sinking rates of subducted slabs or models of the Geoid. For the deepest mantle near the Core Mantle Boundary, where a transition from Bridgmanite to Post Perovskite (ppv) occurs, RheoMan suggests a substantial viscosity reduction that should go along with a weak D" layer in regions dominated by the ppv phase. The latter result also aligns with geodynamic expectations.

RheoMan thus confirms some geodynamic inferences on deep Earth rheology and challenges others. But the fundamental advance of this project stems from the fact that it delivers an understanding of the underlying physical deformation mechanisms of the rheological properties that one should assume for dynamic Earth models. Such Earth models will inform work on an increasing range of Earth processes from sublithospheric stresses to estimates of future sea level changes. The physics based constraints derived from RheoMan on the rheology of the Earth's mantle presented in this book therefore are vital and most welcome.

Hans-Peter Bunge
Professor of Geophysics
Ludwig-Maximilians-Universitaet Muenchen

Introduction

Introduction

The research project *Multiscale modelling of the **rheo**logy of **man**tle minerals* (acronym RheoMan) was submitted to the 2011 Advanced Grant call of the European Research Council. Its aim was to provide a new approach of the rheology of the mantle from the mineral physics point of view which would take advantage of the most recent developments of computational materials science.

From the geodynamical perspective, understanding mantle convection is essential to model the thermal and chemical evolution of the Earth and to constrain the forces driving plate tectonics. The rheological properties of the mantle are traditionally inverted from surface geophysical data. Several radial profiles of the viscosity of the mantle have been thus proposed but a lot of uncertainties remain.
A more detailed model of mantle rheology could potentially be obtained from the knowledge of the constitutive flow laws of mantle phases. A lot of progresses had been achieved to extend the *P-T* range accessible to rheological studies. However, constitutive flow laws were only available at the time of the submission of the project for minerals from the uppermost upper mantle. Significant progresses have been done while our project went on. However, extrapolation of phenomenological flow laws to Earth's conditions over several orders of magnitude remains highly questionable.

Recently, a new field has emerged in materials science called multiscale modelling. It allows to link our understanding of a few elementary mechanisms (usually at the microscopic scale) with the behaviours observed at the macroscopic scale. This offers a unique opportunity to set a microphysics-based model of the rheology of mantle phases. To correctly describe the physics of plastic flow in mantle conditions, one needs a basis which includes an accurate description of the electronic structure of minerals since pressure in the range of the Earth's mantle strongly affect interatomic bonding. The so-called *ab initio* techniques provide approximate solutions of the Schrödinger equation which describes the behaviour of electrons responsible for the interatomic bonding. These calculations do not require adjustable empirical parameters. They are however very computer demanding and cannot describe defects which involve a large number of atoms and results from *ab initio* calculations must be transferred to alternative techniques like the Peierls-Nabarro model or atomistic calculations based on empirical potentials validated by the density functional theory (DFT) calculations. These calculations give an access to an unprecedented understanding of the core structure of these defects. This knowledge is extremely important in constraining the motility of dislocations. The first approach is to infer the resistance that the lattice opposes to dislocation glide: the Peierls stress. More importantly, in high-pressure minerals usually characterized by high lattice friction, one needs to model how thermal activation assists dislocation mobility. The major difficulty encountered here is that thermally activated glide involves elementary processes which operates at timescales much larger than those accessible by standard atomic scale calculations. We must then rely on transient state theory approaches provided that we have model to describe the intermediate configurations explored during glide. These models allow to calculate one of the most important parameter: the velocity of dislocations as a function of temperature, pressure and stress. Plastic deformation is however the result of the complex, collective behaviour of a large collection of dislocations. This field also has benefited from the increase of performance of computers and these calculations are now able to simulate plastic strains of a few 0.1% in volumes of about ~1 μm^3.

Prior to the RheoMan project, this set of techniques has been applied, as a proof of concept, to MgO which usually plays the role of the drosophila for ceramics and minerals.

In the following pages, one can see how this approach has been applied to the most important phases of the Earth's mantle. Before that, a brief presentation of theses phases is provided as well as more information of the numerical techniques and models used during the project. Beyond the original proposition, we have also tried to build a link between the theoretical approach and experimental validations. In particular, we have developed more quantitative techniques in transmission electron microscopy which are also presented. Finally, we present some results on grain boundaries and disclinations which were not planned originally but for which new results have been produced during the project.

Last but not least, a research project is also a human adventure which gathered experienced and young researchers from seven countries all together and lead to the defence of six PhD thesis. We believe that this sets the ground for bright new avenues in the future in the field of mantle rheology.

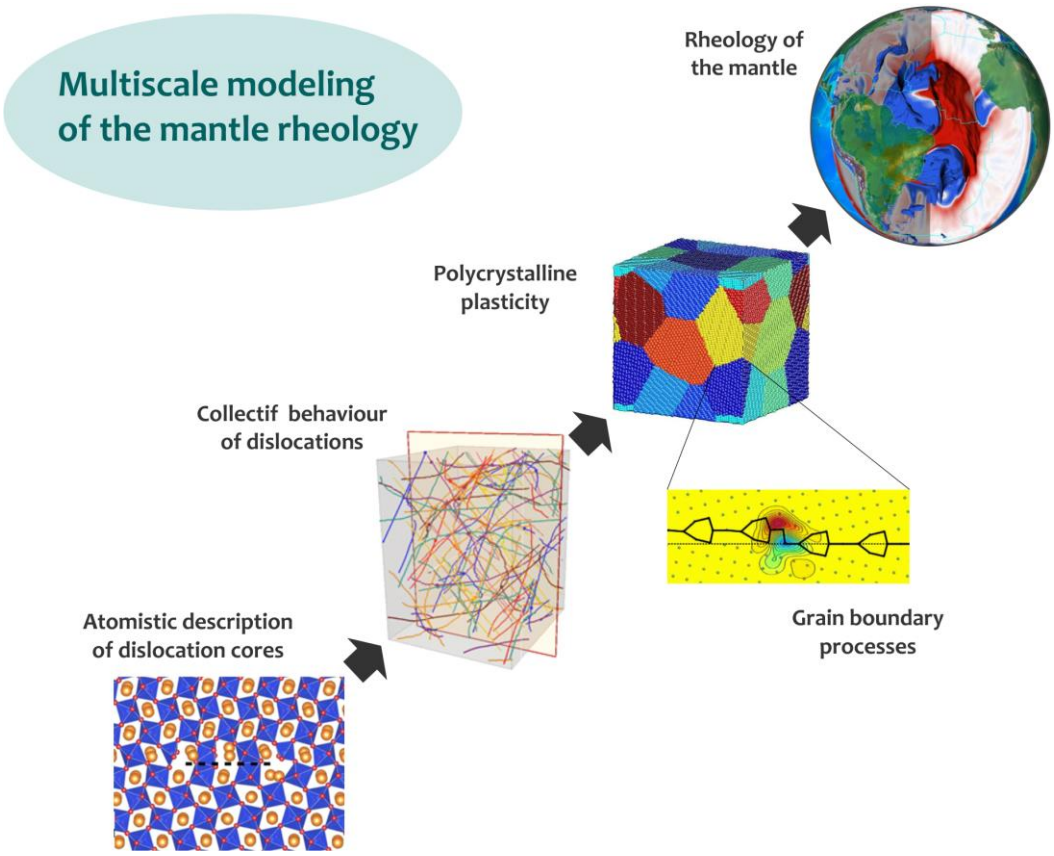

Chapter 1

Defects and Plastic Deformation in Crystalline Solids

1.1. Crystal defects: the zoo

The perfect crystal is, in most cases, a theoretical concept which provides a good description for the variety of ordered atomic arrangements in solids. This structural description of a material is able to account for some intrinsic physical properties like elasticity. However, plastic flow or brittle failure cannot be accurately described from the properties of perfect crystals and it is necessary to introduce the notion of defects.

1.1.1. Point defects

The simplest defect can be found at the atomic scale, for instance when an atom is missing on a site where it is expected to be: this defect is called a *vacancy* (Fig. 1.1.1a). Despite its name «defect», a vacancy is in fact an element which has to be present in a crystal at thermodynamic equilibrium with an intrinsic concentration:

$$c_0 = \exp\left(-\frac{\Delta G_f}{kT}\right) \tag{1.1.1}$$

One can also find an atom occupying a site which is not normally occupied (Fig. 1.1.1b): this is an *interstitial* atom.

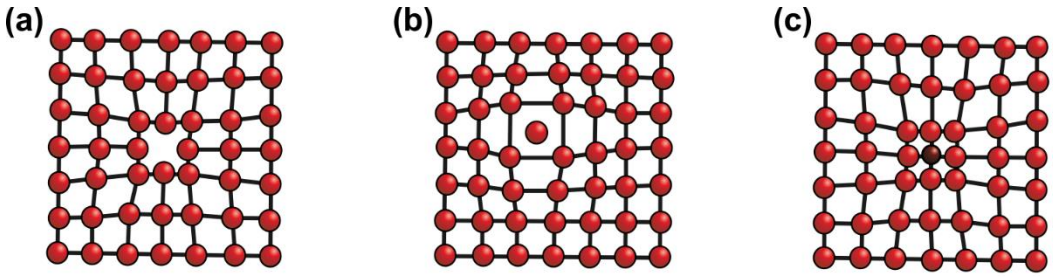

Figure 1.1.1. Point defects in a crystal: **(a)** vacancy; **(b)** interstitial and **(c)** substitutional atoms

This simple description is sufficient to describe defects in monoatomic metals. Minerals are usually solids with an ionic character and are constituted of charged species: anions and cations. In this case, a point defect (vacancy or interstitial) cannot exist alone since it would unbalance charges. Because of these coupling effects needed to maintain charge equilibrium, the point defect chemistry can be affected by the introduction of *substitutional impurity* cations/anions (Fig. 1.1.1c) with a valence different from the host atom, or when a substitutional atom has several accessible valence states (*e.g.* Fe^{2+}, Fe^{3+}). The vacancy concentration is then extrinsic, *i.e.* controlled by the impurity content and not only by temperature as in the intrinsic case.

1.1.2. Line defects

In 1907, Volterra introduced six types of distortions involving lines defects (Fig. 1.1.2) in a continuous medium in order to account for internal stresses in solids.

Three of them are translational defects (Fig. 1.1.2 a-c), meaning that across a (non-unique) surface terminating on the line, the discontinuity of the elastic displacement field $\mathbf{u_e}$ is a constant vector **b**. These defects have been called *dislocations*. Because of this discontinuity, the elastic distortion field $\mathbf{U_e}$ is point-wise irrotational and its non-vanishing curl defines a smooth dislocation density tensor field called the Nye tensor field:

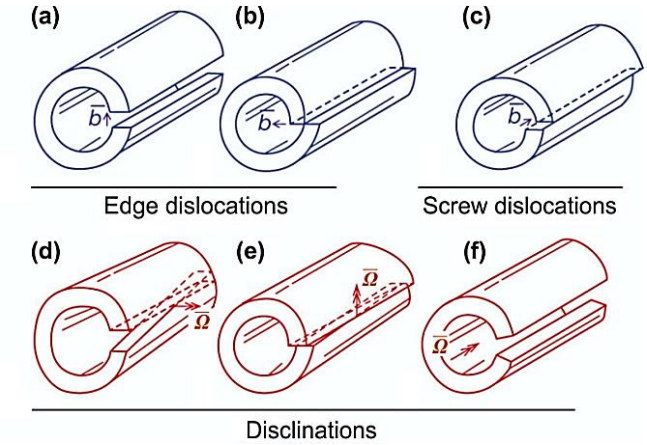

Figure 1.1.2. The six types of line defects introduced by Volterra (1907). The blue cylinders **(a-c)** illustrate translational defects, called dislocations, that are characterized by a Burgers vector **b**; the red cylinders **(d-f)** correspond to disclinations, that are characterized by a Frank vector **Ω** and incorporate a rotational component. The figure is adopted from Cordier *et al.* (2014)

$$\boldsymbol{\alpha} = \mathbf{curl}\,\mathbf{U_e} \tag{1.1.2}$$

The Burgers vector **b** can be retrieved from this description by the integration of the density tensor field along an appropriate surface S of unit normal **n**:

$$\mathbf{b} = \int_S \boldsymbol{\alpha} \cdot \mathbf{n}\, dS \tag{1.1.3}$$

The other three defects (Fig. 1.1.2 d-f) are called *disclinations*. They result in a similar way from a discontinuity $\boldsymbol{\omega_e}$ in the rotation field across a surface bound by the defect line. Similarly to the dislocations, the strength of the disclinations can be described by a vector, called the Frank vector **Ω**. In presence of disclinations, the elastic curvature field is irrotational and the disclination density tensor is defined by the non vanishing curl of this field:

$$\boldsymbol{\theta} = \mathbf{curl}\,\boldsymbol{\kappa_e} \tag{1.1.4}$$

The Frank vector is then obtained by integration of the disclination density field:

$$\boldsymbol{\Omega} = \int_S \boldsymbol{\theta} \cdot \mathbf{n}\, dS \tag{1.1.5}$$

The dislocation-based theory of crystal slip was set in 1934 by the simultaneous publication of the three renowned papers from Orowan, Taylor and Polanyi. These papers defined the concept of *edge dislocations*. The so-called *screw dislocations* were described later by Burgers.

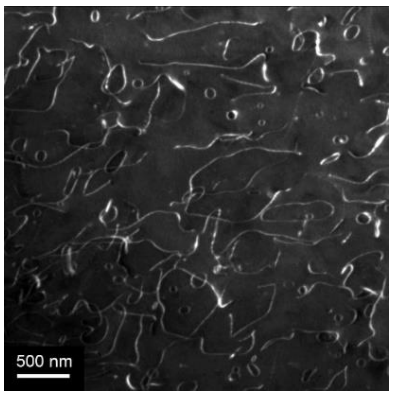

Figure 1.1.3. TEM micrograph of dislocations in olivine

A dislocation is a linear defect that cannot end in a crystal. It must terminate on another defect, *e.g.*, on a grain boundary or on a surface, or on itself forming a loop (Fig. 1.1.4). Locally, it is characterized by a line vector **L** and by the Burgers vector **b** which magnitude is constant along the line. An edge dislocation (Figs. 1.1.2a-b, 1.1.4) corresponds to the case where $\mathbf{L} \perp \mathbf{b}$, whereas a screw dislocation (Figs. 1.1.2c, 1.1.4) corresponds to the case where $\mathbf{L} \parallel \mathbf{b}$. In most cases, the actual orientation of these two vectors is in between the edge and screw configurations, which corresponds to the so-called mixed character. Schematically, the edge dislocations is commonly described as the insertion of

an extra-half plane, whereas the screw dislocation is a pole about which the atomic planes are spiralling.

The presence of a dislocation in a crystal is responsible for a surrounding elastic displacement field **u**, which in turn gives rise to a strain and a stress field (described by second rank tensors **ε** and **σ**). An important property of dislocations is that these strain and stress fields are long-ranged with schematically (in cylindrical coordinates centered on the dislocation line supposed to be straight):

$$\sigma \propto \frac{\mu b}{2\pi r} f(\theta) \tag{1.1.6}$$

where μ is the shear modulus and $f(\theta)$ describes the complex shape of the fields around the line. It can be seen that stress (this is also the case for strain) becomes infinite as r approaches zero. Linear elasticity used to derive this relation breaks down in the region near the dislocation line which is called the *core*. In this region, crystal lattice is highly distorted and involves specific distorted configurations with large displacements. Accurate description of this region at the atomic scale is crucial for deriving intrinsic properties of dislocations. In the following chapters, we will see how the atomic arrangement in the vicinity of the dislocation controls the dislocation mobility in a given plane or its ability to change from one primary glide plane to another (cross-slip mechanism).

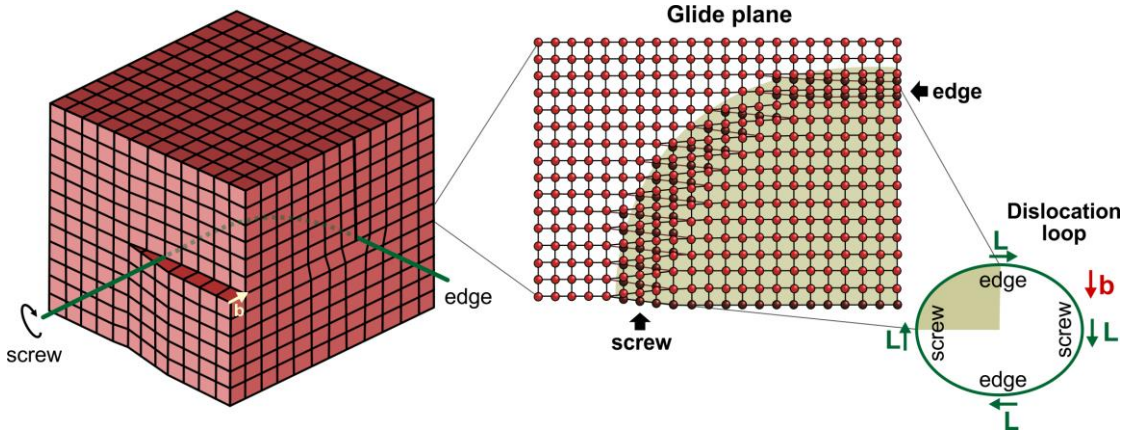

Figure 1.1.4. Dislocation loop in a crystal

1.1.3. Grain boundaries

In a rock which represents an aggregate or a polycrystal, individual crystals (grains) terminate on a grain or on a phase boundary. A *grain boundary* is a two-dimensional defect which introduces a misorientation between two crystals. This kind of defects creates no long-range stress field.

The so-called low-angle grain boundaries (or subgrain boundaries) represent a special case because they can be well-described by a distribution of dislocations. One usually distinguishes *tilt boundaries* made of edge dislocations and *twist boundaries* constituted by two families (or more) of screw dislocations.

The description of high-angle grain boundaries (traditionally, the limit is placed at *ca.* 15° misorientation) is more difficult because their structure must be described at the atomic scale. Although in some cases a melt layer can be present at the interface, crystalline order has been shown to persist up to a very narrow defective layer which can be usually described by specific structural units.

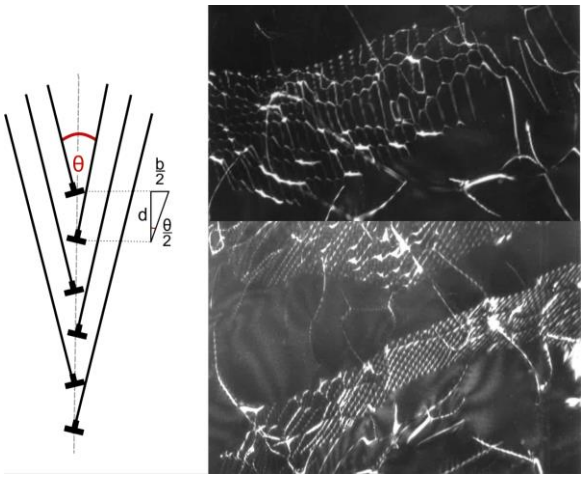

Figure 1.1.5. Left: schematic illustration of the Read & Shockley model; right: TEM micrograph of subgrain boundaries in garnets

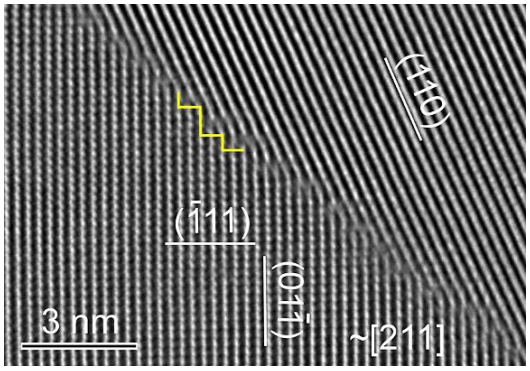

Figure 1.1.6. High-resolution TEM micrograph of an edge-on grain boundary in $SrTiO_3$ (Sternlicht *et al.* 2015)

1.2. Motion of defects and its role in plastic deformation

Plastic flow is a transport phenomenon which results from the motion of defects in response to stress. Hence, the mobility of defects is of primary importance for modeling plastic deformation.

1.2.1. Point defect mobility

The presence of vacancies in a crystal allows activating atomic mobility at high temperature. Under thermal vibrations, a neighbouring atom can jump into a vacancy position.

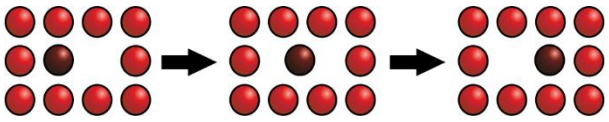

Figure 1.1.7. Vacancy exchange in a crystal

This is formally equivalent to the opposite jump of the vacancy allowing to define the diffusion coefficient of vacancies:

$$D_v = D_{0v}\, exp\left(-\frac{\Delta H_m}{kT}\right) \tag{1.1.7}$$

where $\Delta \boldsymbol{H_m}$ is the activation enthalpy for the migration of vacancies and $\boldsymbol{D_{0v}}$ is the prefactor which contains entropic terms. Atomic mobility is thus possible if a vacancy is present as a first neighbour of a given atom. The self-diffusion coefficient of a given species is thus a function of the relevant vacancy concentration:

$$D_{sd} = D_v c_0 = D_0\, exp\left(-\frac{\Delta H_f + \Delta H_m}{kT}\right) \tag{1.1.8}$$

1.2.2. Dislocation mobility

Dislocation glide. Under an applied stress, the dislocation may move in the plane containing both the dislocation line **L** and the Burgers vector **b**. This conservative motion is called *glide*. For any dislocation having an edge component, this motion is restricted to the glide plane (Fig. 1.1.8). A screw dislocation can, in principle, glide in any plane containing the Burgers vector.

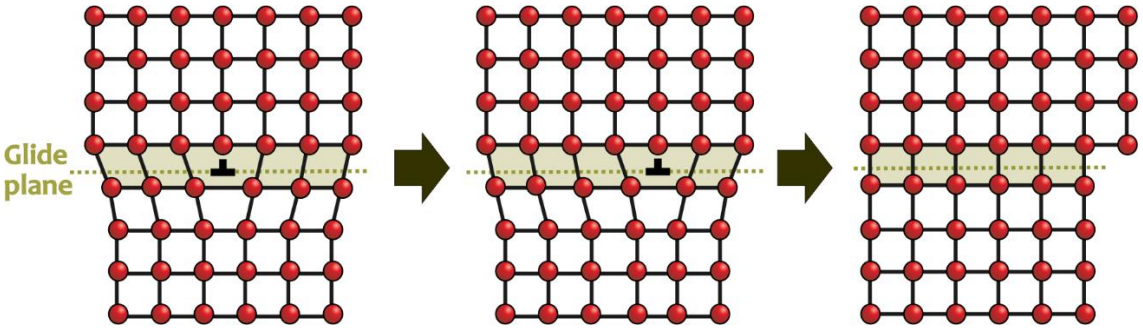

Figure 1.1.8. Schematic illustration of an edge dislocation glide

In between two neighbouring stable positions (Fig. 1.1.8), the dislocation must explore unstable configurations with higher energies, described by the so-called Peierls potential (for more details see section 3.1.4). The crystal lattice thus opposes a friction force, called *lattice friction*, to the dislocation motion. This force is maximum for a straight rigid dislocation moving without the assistance of thermal activation (*i.e.* at 0 K). In this case the lattice friction is commonly described through the *Peierls stress* σ_p (Fig. 1.1.9). At finite temperature, dislocations glide at stresses lower than the Peierls stress due specific thermally activated mechanisms. In section 3.1.4, we describe one of them, called the *kink-pair mechanism*.

Above a given temperature T_a (Fig. 1.1.9), thermal activation overcomes the lattice friction and dislocation glide becomes athermal. In this regime, the dislocation velocity is proportional to the applied resolved shear stress and the flow stress is only controlled by dislocations-dislocations interactions.

At higher temperatures, atomic diffusion becomes active and new mechanisms like dislocation climb can operate and high-temperature thermally activated regime may be observed before the melting temperature T_m.

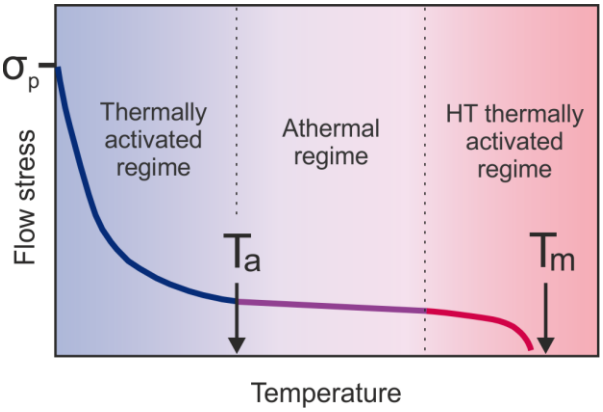

Figure 1.1.9. Evolution of the flow stress with increasing temperature

Dislocation climb. At high-temperatures, dislocations can act as sources or sinks for vacancies. Figure (1.1.10) illustrates a case where a vacancy diffuses toward an edge dislocation. Being absorbed at the dislocation core, it enhances a step motion perpendicular to the glide plane. This type of dislocation motion is called *climb*. It is controlled by the flux

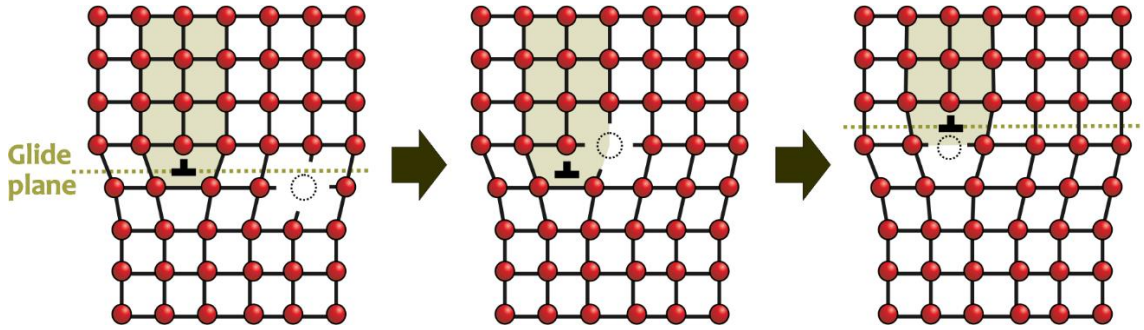

Figure 1.1.10. Schematic illustration of edge dislocation climb due to vacancy absorption

of vacancy which diffuses toward (or from) the dislocation core. In this case, the climb velocity of dislocations is given by:

$$v_c = \eta \frac{D_{sd}}{b}\left[exp\left(\frac{\tau^c \Omega}{RT}\right) - \frac{c_\infty}{c_0}\right] \tag{1.1.9}$$

Where $\boldsymbol{D_{sd}}$ is the vacancy self-diffusion coefficient, Ω is the vacancy formation volume, η is a geometrical factor that depends on the geometry of the flux field, and $\boldsymbol{c_\infty}$ and $\boldsymbol{c_0}$ are the vacancy concentration far from the dislocation and the equilibrium vacancy concentration in the bulk volume, respectively. At high temperature and low stress, assuming that far away from dislocation cores the vacancy concentration is constant and equal to the equilibrium concentration in the bulk volume ($\boldsymbol{c_\infty} = \boldsymbol{c_0}$), one finds:

$$v_c \approx \frac{D_{sd}\Omega\tau^c}{bRT} \tag{1.1.10}$$

1.2.3. Grain boundary mobility

At low temperature, grain boundaries usually act as obstacles to the transfer of plastic strain from one grain to another. At high temperature, the situation is completely different. Grain boundary mobility can be enhanced and these defects may contribute to plastic strain. As illustrated in Figure 1.1.11, grain boundary can move in their plane (sliding), perpendicular to it (migration) or by a combination of sliding and migration (shear-coupled grain boundary migration).

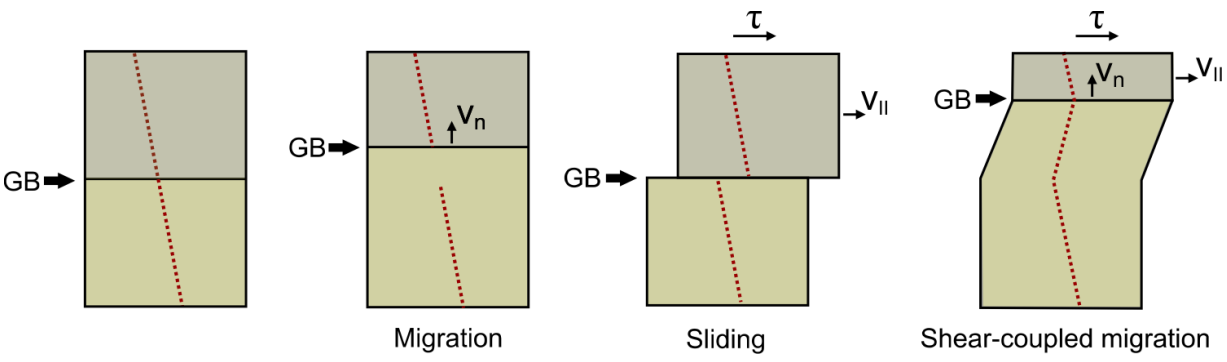

Figure 1.1.11. Different types of grain boundary motion

Commonly, it is assumed that the velocity of grain boundaries is proportional to the driving force F:

$$v_{gb} = MF \tag{1.1.11}$$

where M is the mobility. This parameter is likely to be thermally activated and dependent on the grain boundary structure, misorientation, impurity content, *etc*.

1.3. From crystal defects to creep

1.3.1. Flow resulting from the transport of matter

One of the most important challenges in studying rheology is to scale up microscopic processes to describe macroscopic flow. Thanks to the presence of point defects, matter can be transferred in a solid at high temperature providing a possible contribution to plastic strain. The case where plastic deformation results exclusively from atomic diffusion is usually called *diffusion creep*.

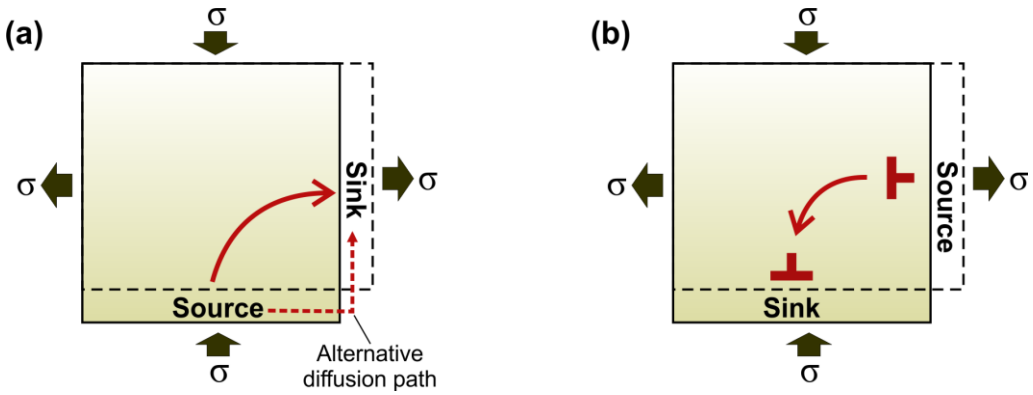

Figure 1.1.12. Schematic illustration of diffusion creep **(a)** and pure climb (Nabarro) creep **(b)**

An elegant model of this creep process has been proposed by Nabarro (1948) and Herring (1950) and it was further named *Nabarro-Herring creep*. The basic ingredient of this model is, as first suggested by Nabarro, that non-hydrostatic stress fields on surfaces of grain boundaries can give rise locally to different vacancy concentrations. Grain boundaries where a normal compressive stress applies act as sinks whereas boundaries under normal tensile loading act as sources. Hence, a steady flow of matter can establish between boundaries within grains of polycrystalline solid (Fig. 1.1.12a).

The rigorous treatment of this model leads to a physics-based constitutive equation:

$$\dot{\varepsilon}_{NH} = A_{NH} \frac{D_{sd} \Omega \sigma}{d^2 kT} \tag{1.1.12}$$

where Ω is the atomic volume and d is the grain size. This creep mechanism has several important properties. It is linear viscous (Newtonian): $\dot{\varepsilon} \propto \sigma$. The creep rate is also strongly grain size dependent ($\dot{\varepsilon} \propto d^{-2}$). This creep mechanism is usually considered to be active in small-grained materials at high-temperature and low stress without producing strong lattice preferred orientations.

Alternatively, diffusion could occur preferentially along grain boundaries. This mechanism, called *Coble creep*, is characterized by a slightly different rheological law which is still Newtonian viscous and grain-size dependent:

$$\dot{\varepsilon}_C = A_C \frac{D_{gb}\delta\Omega\sigma}{d^3 kT} \tag{1.1.13}$$

where δ is a phenomenological parameter characterizing the «thickness» of the grain boundaries with respect to the diffusion process.

Nabarro-Herring and Coble creep mechanisms will dominate if grain boundaries are the effective sources and sinks for diffusing species. The crystals (grains) may however contain defects playing the same role. Nabarro (1967) has suggested that dislocations could serve as sources and sinks for diffusing species (Fig. 1.1.12b). These dislocations must have different Burgers vectors for sources and sinks and will move by climb. In the treatment proposed by Nabarro (1967), this creep process follows a law of the type:

$$\dot{\varepsilon}_N = A_N \left(\frac{D\mu b}{kT}\right)\left(\frac{\sigma}{\mu}\right)^3 \tag{1.1.14}$$

1.3.2. Flow resulting from the transport of shear

Here we describe a creep mechanism where plastic flow results mostly from the transport of shear by dislocation glide also called *dislocation creep*. The essential transport equation that describes the plastic strain resulting from dislocation motion is the Orowan equation:

$$\dot{\varepsilon} = \rho b v \tag{1.1.15}$$

where b is the amplitude of the Burgers vector (the elementary amount plastic strain carried by one dislocation), ρ is the dislocation density (describing the number of mobile dislocations that contribute to strain) and v is the «average» dislocation velocity. Except for some very simple cases, for instance, where only one mechanism like dislocation glide is operating, it is difficult to access to these parameters. Usually, in high-temperature creep, it is considered that several mechanisms (glide and climb) are operating simultaneously and thus, contrary to diffusional creep, there exist no simple model which completely (and quantitatively) describes dislocation creep. A well-described by Poirier (1985), constitutive equations for dislocation creep result from a phenomenological analysis of quasi-steady state creep. The thermal activation of the creep rate and its strong stress sensitivity have led to the definition of high-temperature creep-rate based on the empirical equation proposed by Dorn (1955):

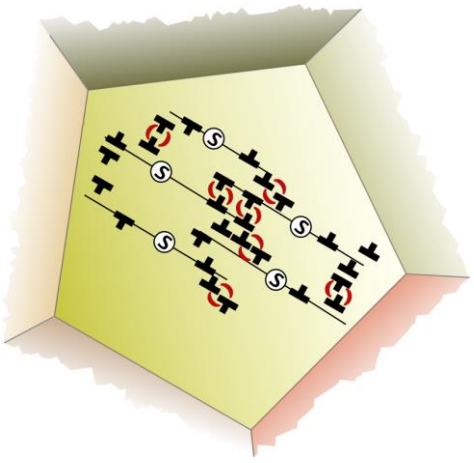

Figure 1.1.13. Dislocation-dislocation interactions in a crystal

$$\dot{\varepsilon}_{PL} = \dot{\varepsilon}_0 \sigma^n \, exp\left(-\frac{Q}{RT}\right) \tag{1.1.16}$$

This power-law equation can be found under several variations in the literature. Experimentalists have tried to develop the pre-exponential term to incorporate the influence of several parameters like the oxygen fugacity, water fugacity, chemistry, *etc*. On the other hand, the fact that the apparent activation energy for creep Q is usually close to the activation energy for self-diffusion has led to propose models for diffusion- or recovery-controlled power law creep. Among them one can cite the early model of Weertman (1968) in which dislocations produced by sources and moving by glide are trapped by dislocation-dislocation interactions (Fig. 1.1.13) which are released by diffusion-controlled recovery processes (usually dislocation climb).

These models give semi-quantitative interpretation of the stress exponent factor n which is typically in the range of 3-5. It also should be noted that the power-law equation can be found under different forms, including:

$$\dot{\varepsilon}_{PL} = A_{PL}\left(\frac{D\mu b}{kT}\right)\left(\frac{\sigma}{\mu}\right)^n \tag{1.1.17}$$

1.3.3. Flow resulting from the motion of grain boundaries

There is currently no well-defined model to describe the creep behaviour of solids which results from the mobility of grain (and sub-grain) boundaries. Most recent contributions refer to this process as «grain-boundary sliding» and describe its contribution by introducing a grain size sensitivity to a power-law equation:

$$\dot{\varepsilon}_{GBS} = A_{GBS}\frac{\sigma^n}{d^p} exp\left(-\frac{Q}{RT}\right) \tag{1.1.18}$$

References

J.M. Burgers (1939) Proc. Kon. Ned. Akad. Wetenschap.42: 293, 378
P. Cordier *et al.* (2014) Nature 507: 51
J.E. Dorn (1955) J. Mech. Phys. Solids 3: 85
C. Herring (1950) J. Appl. Phys. 21: 437
F.R.N. Nabarro (1948) Report Conf. on Strength of Solids. The Physical Society, London. p. 75
F.R.N. Nabarro (1967) Philos. Mag A 16: 231
E. Orowan (1934) Z. Phys. 89:605, 614, and 634
M. Paterson (2013) Materials science for structural geology. Springer, pp. 246
J.P. Poirier (1985) Creep of crystals. Cambridge university press, pp. 260
M. Polanyi (1934) Z. Phys. 89: 660
H. Sternlicht *et al.* (2015) J. Mater. Sci. 51: 467
G.I. Taylor (1934) Proc. Roy. Soc. London A 145: 362.
V. Volterra (1907) Ann. Ecole Norm. Super. Paris 24: 400
J. Weertman (1968) Phil. Mag. 18: 959
J. Weertman & J.R. Weertman (1992) Elementary dislocation theory. Oxford university press, pp. 213

Chapter 2

Deep Earth Interior

2.1. Structure of the Earth and dynamic processes in the mantle

An important source of information about the inner structure and composition of the planet comes from geophysical observations and from seismic waves that propagate through the Earth or along its subsurface. The travel time of seismic waves represents the first observable. Seismic wave velocities depend on the elastic properties and on the density of the matter through which the waves travel. This allowed distinguishing the major divisions of the Earth's interior (Fig. 2.1.1) into a silicate mantle which extends to a depth of ~2900 km, and an iron rich metallic core with a radius of ~3400 km, subdivided into a liquid outer core (characterized by absence of V_S) and a solid inner core.

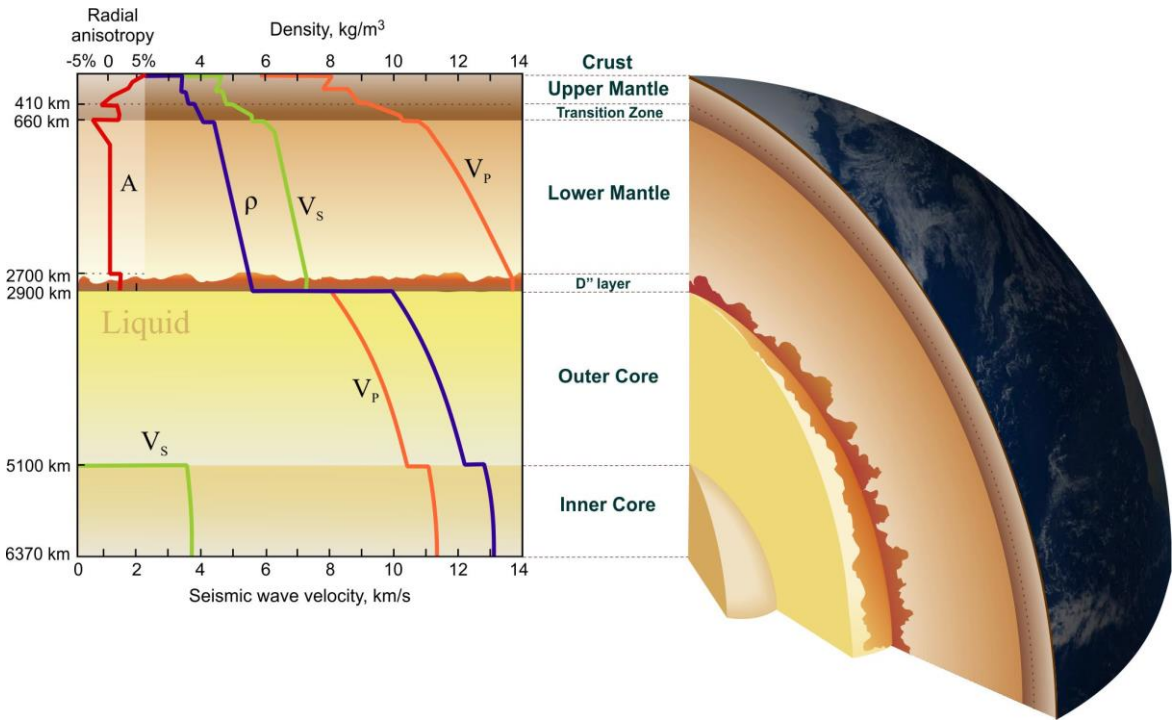

Figure 2.1.1. Simple representation of the Earth's inner structure, subdivided into a silicate mantle and a metallic core. The seismic wave velocities (V_p and V_s) and the density profile (ρ) correspond to the PREM model by Dziewonski & Anderson (1981), radial seismic anisotropy (A) is taken from Mainprice *et al.* (2000)

The Earth's mantle is not homogeneous with depth: abrupt variations in seismic body wave velocities indicate changes in structure or/and composition of the Earth's interior with depth. Based on such observations, the Earth's mantle is further divided into two major parts: the upper mantle that extends to a depth of about 410 km and mostly consists of $(Mg,Fe)Si_2O_4$ olivine (60%), $(Mg,Fe,Ca)_2Si_2O_3$ pyroxenes and $(Mg,Fe,Ca)_3Al_2Si_3O_{12}$ garnets; and the lower mantle between 660 km and 2700 km, mostly made up of $(Mg,Fe,Al)(Si,Fe,Al)O_3$ bridgmanite, and (Mg,Fe)O ferropericlase (see the diagram on Figure 2.1.2). Besides these two major regions, there are two highly anisotropic boundary layers of ~200 km thickness (Fig.2.1.1): the transition zone (TZ) which separates the lower and the upper mantle, and the D" layer located right above the core-mantle boundary (CMB). Sharp seismic discontinuities in the transition zone are known to be associated with subsequent phase transitions of $(Mg,Fe)Si_2O_4$ olivine into wadsleyite at ~410 km depth and ringwoodite at ~520 km depth (Fig. 2.1.2), while the nature of the profound D" layer, lying almost halfway to the Earth's centre, is still a matter of ongoing debates. Being located at the interface between the outer core and the lowermost mantle, where liquid iron alloy meets solid silicates, this region represents one of the most complex

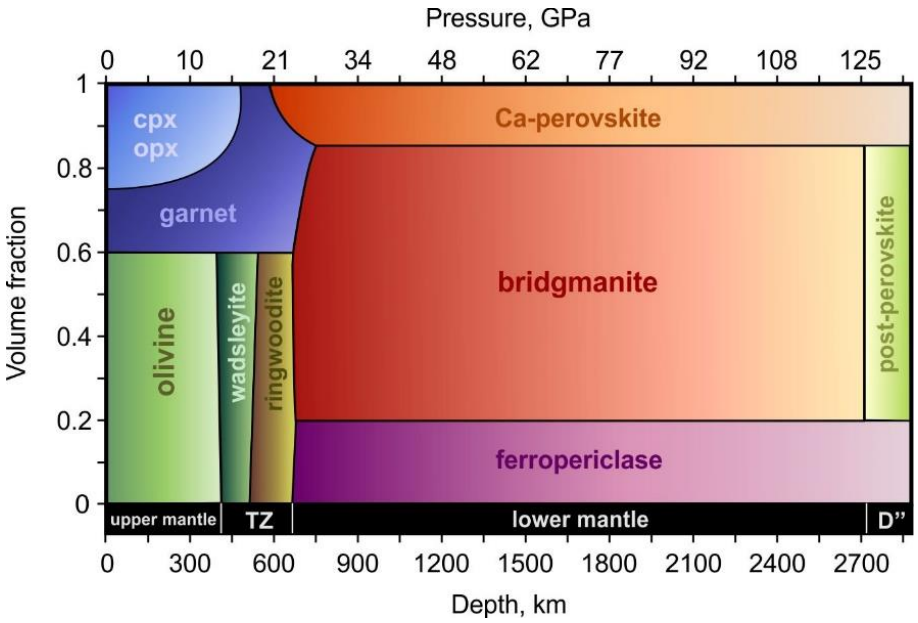

Figure 2.1.2. Mineralogy of the pyrolytic mantle as a function of depth, based on the geotherm by Brown & Shankland (1981)

boundary layers of the Earth, where, for instance, the density contrast exceeds the one between the crust and the atmosphere (Fig. 2.1.1).

Numerous seismological observations (*e.g.* Thomas *et al.* 2004; Lay 2008; Hutko *et al.* 2009; Long 2009; Cobden and Thomas 2013 *etc.*) indicate that the D″ region is much more complex and heterogeneous than the rest of the lower mantle, where no major discontinuities are detected.

In the D'' region, global structures are topographically detected in the deep mantle beneath Africa and South-Central Pacific (Fig. 2.1.3). These zones are characterized by shear wave velocity anomalies of -2 to -5%, and therefore, defined as *large low shear-wave velocity provinces* (LLSVPs). It is generally accepted that these provinces, covering ~20% of the CMB, are hotter than the rest of the mantle and represent the main source of mantle plumes (see Davies *et al.* 2015 for a review). Location of LLSVPs is strongly correlated with location of the hot spots and the reconstructed eruption sites on the Earth's surface (Fig. 2.1.3). However, seismic observations in LLSVPs cannot be explained by thermal anomalies alone. The exact nature of LLSVPs is still not clear and understanding compositional anomalies (*e.g.* enrichment in iron) is needed to better explain them.

Other low velocity anomalies at the bottom of the mantle are characterized by significant drop of V_P and V_S velocities by ~10% (Garnero & Helmberger 1995) and, therefore, commonly referred as *ultralow velocity zones* (ULVZ). In contrast to LLSVPs, ULVZs form compact local structures of 5-40 km. These zones are generally observed at the edges of LLSVPs (Fig. 2.1.4).

Locally, regional seismic data also indicates the presence of abrupt vertical changes in speed of both *P* and *S* waves at the top of D″ region. Such structures are detected between ~100 km and 450 km above the CMB in different parts of the globe (Cobden *et al.* 2015) and commonly referred as D″ discontinuity. Mapping these regions (Fig. 2.1.3) clearly demonstrates that the D″ discontinuity forms a kind of lenses locally disposed in colder regions out of LLSVPs, *i.e.* these structures are likely associated with subducted slabs (Fig. 2.1.4), where the post-perovskite phase is expected to be stable.

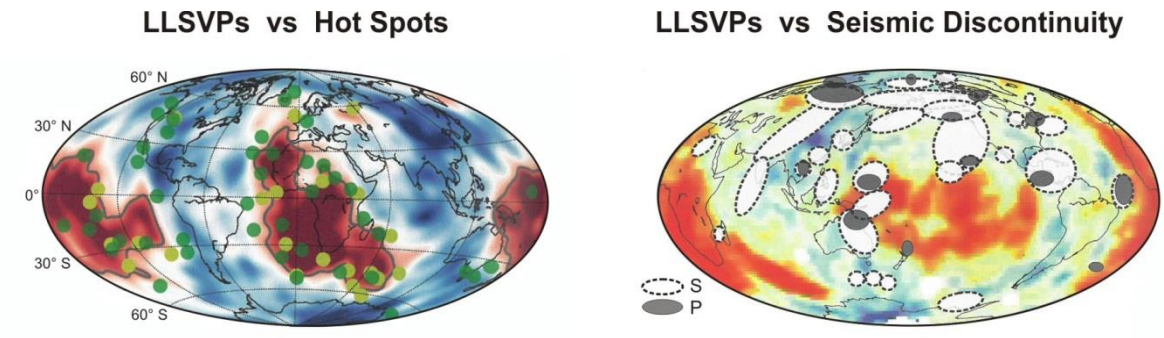

Figure 2.1.3. Superposing the shear wave tomography at the CMB (2800 km depth) with location of surface hotspots (dark green dots on the left panel), reconstructed eruption sites (light green dots on the left panel) and with S- and P-waves seismic discontinuities (right panel). On both plots, LLSVPs correspond to the red arrears. The pictures are taken from (Davies *et al.* 2015) and (Cobden *et al.* 2015), respectively

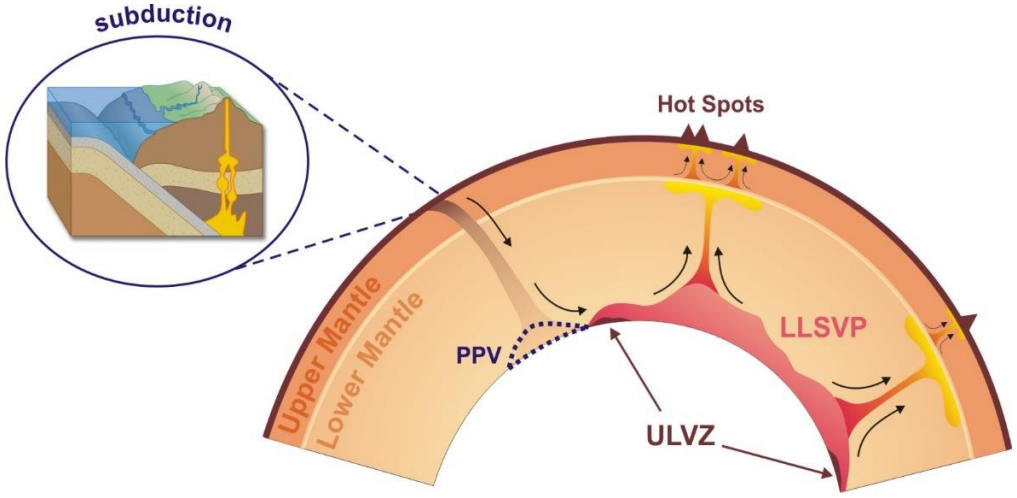

Figure 2.1.4. Schematic illustration of the distinct large scale structures at the bottom of the mantle and their role in mantle convection. LLSVP corresponds to the large low shear wave velocity provinces. Mantle plumes are generated at their top and entrain some fractions of the matter from the deep interior towards the surface. ULVZ stands for the ultralow velocity zones. The PPV zone corresponds to the lenses of post-perovskite, thought to be stable in relatively cold regions beneath the subducting slabs. The picture is modified from Deschamps *et al.* (2015)

Although being solid, the mantle undergoes slow convection due to the temperature and density gradient between its different regions (Fig. 2.1.5). At the surface, downwelling zones are associated with cold and dense subducting slabs (the portion of a tectonic plate) sinking into the mantle, while the upwelling regions mainly correspond to the hot mantle plumes, rising from sources which may be as deep as the CMB (Fig. 2.1.4). Mantle convection is one of the most important features for the dynamics of the Earth since it drives most large-scale geological processes at the surface of our planet. It is however extremely difficult to study mantle convection since it occurs on timescales much longer than the human timescale. From the physics point of view, convection can be modeled if the constitutive equations which relate stress (built up by density variations) and strain-rate are known. A first approximation is to describe this behaviour by a single parameter: viscosity. More sophisticated descriptions may consider the existence of a yield stress or a non-linear stress dependence of viscosity on stress. From the observational point of view the first constraint on the rheology of the mantle has been placed by Haskell (1935)

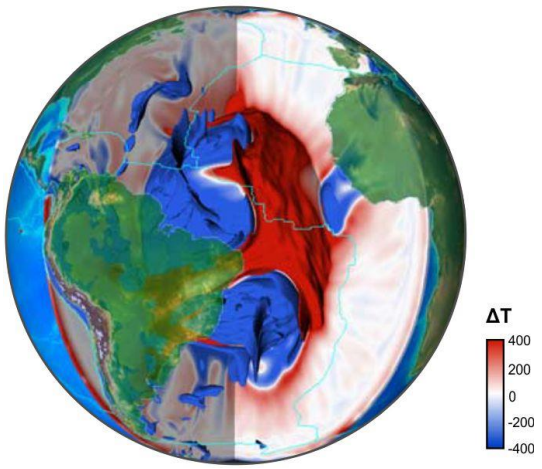

Figure 2.1.5. 3D representation of lateral temperature variations (ΔT on the scale) in the Earth's mantle, based on the high-resolution mantle circulation models with pyrolite composition by Schuberth *et al.* (2009)

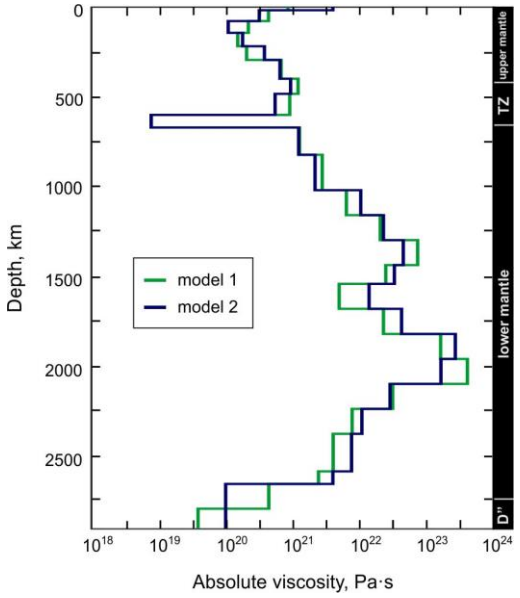

Figure 2.1.6. Viscosity profiles (Mitrovica & Forte 2004) from the inversions of glacial isostatic adjustment and convection data sets. For more details about the models, see the original paper by Mitrovica & Forte (2004)

who, from the analysis of post-glacial uplift, proposed the viscosity of the upper mantle to be of the order of 10^{21}-10^{22} Pa·s. This estimation has been proved to be very robust over the years, especially for the upper mantle. However, further studies based on modeling of convection (Bunge *et al.* 1996), geoid (Hager & Richards 1989; King 1995; Bunge & Richards 1996), plate velocity (Ricard *et al.* 1993; Butterworth *et al.* 2014), true polar wander (Philips *et al.* 2009) and length of day variations (Sabadini & Yuen 1989) have consistently pointed out a significant increase of viscosity (originally placed at the 660 km discontinuity) in the range of 10-100 between the transition zone and the lower mantle (Fig. 2.1.6). Most proposed profiles consist in a more or less broad viscosity hill in the middle of the mantle, at a depth roughly between 1200 km and 2000 km (Ricard & Wuming 1991; Mitrovica & Forte 2004; Morra *et al.* 2010). Some recent studies however rather suggest a rheology contrast located around 1000 km depth (Ballmer *et al.* 2015; Rudolph *et al.* 2015).

Another very strong constraint on mantle convection is provided by seismic anisotropy. Except the bulk of the lower mantle, seismic anisotropy is observed at most places (Montagner & Kenneth 1996; Mainprice *et al.* 2000). Seismic anisotropy is likely to provide indications on active deformation mechanisms. Unlike diffusion creep, dislocation creep is very efficient in producing crystal preferred orientations which can be related to seismic anisotropy to provide a snapshot of past flow in the mantle.

References

M. Ballmer *et al.* (2015) Science Advances, 1: e1500815
J. Brown and T. Shankland (1981) Geophys. J. Int. 66: 579
H.-P. Bunge *et al.* (1996) Nature 379: 436
H.-P. Bunge & Richards (1996) Geophys. Res. Lett. 23: 2987
N. Butterworth *et al.* (2014) J. Geodynam. 73: 1
L. Cobden & C. Thomas (2013) Geophys. J. Int. 194: 1091

L. Cobden *et al.* (2015) in "The Earth heterogeneous mantle", eds. A. Khan, F. Deschamps, Springer, pp. 391-440
D. Davies *et al.* (2015) in "The Earth heterogeneous mantle", eds. A. Khan, F. Deschamps, Springer, pp. 441-477
F. Deschamps *et al.* (2015) in "The Earth heterogeneous mantle", eds. A. Khan, F. Deschamps, Springer, pp. 479-515
A. Dziewonski & D. Anderson (1981) Phys. Earth Planet. Inter. 25: 297
E. Garnero & D. Helmberger (1995) Earth Planet. Sci. Lett. 91: 161
B. Hager & M. Richards (1989) Phil. Trans. Roy. Soc. A, 328: 309A
N. Haskell (1935) Physics 6: 265
A. Hutko *et al.* (2009) Phys. Earth Planet. Inter. 173: 60
S. King (1995) Geophys. J. Int. 122: 725
T. Lay (2008) Geophys. Res. Lett. 35: L03304
M. Long (2009) Earth Planet. Sci. Lett. 283: 181
D. Mainprice *et al.* (2000) Geophys. Monogr. Ser., AGU, vol. 117, ed. S.-I. Karato *et al.*, pp. 237-264
J. Mitrovica & A. Forte (2004) Earth Planet. Sci. Lett. 225: 177
J. Montagner & B. Kenneth (1996) Geophys. J. Int. 125: 229
G. Morra *et al.* (2010) Phys. Earth Planet. Inter. 180: 271
B. Philips *et al.* (2009) Gondwana Research 15: 288
Y. Ricard *et al.* (1993) J. Geophys. Res. 98: 21895
Y. Ricard & B. Wuming (1991) Geophys. J. Int. 105: 561
M. Rudolph *et al.* (2015) Science 350: 1349
R. Sabadini & D. Yuen (1989) Nature 339: 373
B. Schuberth *et al.* (2009) Geochem. Geophys. Geosyst. 10: Q01W01
C. Thomas *et al.* (2004) J. Geophys. Res. 109: B08307

2.2. Essential minerals of the mantle

2.2.1. Olivine

The majority of the upper mantle consists of $(Mg,Fe)_2SiO_4$ olivine, named for its characteristic olive-green colour (Fig. 2.2.1a). Mantle olivine is a solid solution in between Mg_2SiO_4 forsterite and Fe_2SiO_4 fayalite. Mantle olivine (with contains roughly 10% iron) is stable up to 14 GPa and 2000 K (Fei *et al.* 1990) equivalent to the *P-T* conditions of *ca.* 400 km depth. Olivine builds up to 60% of the upper mantle (Fig. 2.1.2).

The structure of olivine was first determined by Bragg and Brown in 1926. This mineral has an orthorhombic symmetry (space group *Pbnm*, $z = 4$) with the unit cell parameters $a = 4.753$ Å, $b = 10.190$ Å, $c = 5.978$ Å for $(Mg,Fe)_2SiO_4$ at ambient conditions (Fujino *et al.* 1981). The crystal structure of olivine is commonly described as a distorted hcp framework of O atoms, with ½ octahedral sites occupied by Mg/Fe atoms, and ⅛ tetrahedral sites occupied by Si atoms. The Si-tetrahedra do not interconnect with each other (Fig. 2.2.1b), hence the olivine structure belongs to the class of orthosilicates (nesosilicates). Structurally, divalent cations with octahedral coordination occupy two different sites: M1 with the Wykoff position *4a* (on inversion centres) and M2 with the Wykoff position *4c* (on mirror planes).

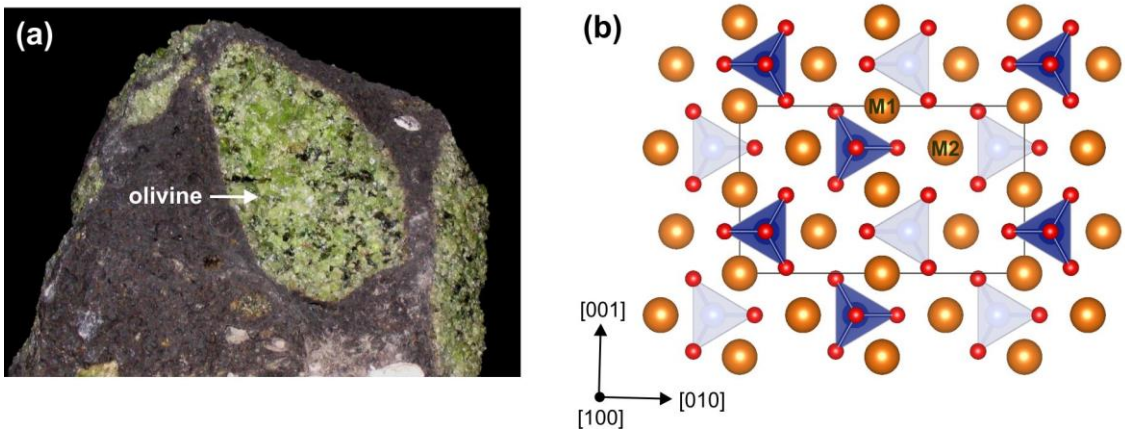

Figure 2.2.1. **(a)** Olivine crystals in a mantle xenolith from Massif Central (France). **(b)** Crystal structure of olivine. Si-tetrahedra are shown in blue, Mg atoms – in orange, and O atoms - in red

Being a major constituent of the upper mantle, olivine has a dominant influence upon the rheology in that region. Thus, deformation of olivine has been the subject of numerous experimental studies (for a review, see Kohlstedt *et al.* 1995; Hirth & Kohlstedt 2003). In this literature, the prevailing deformation mechanisms include the transport of matter by diffusion and of shear by motion of dislocations. However, the dislocation-based crystal plasticity of olivine is challenged by a lack of slip systems. For plastic flow to occur homogeneously by dislocation glide alone, at least five independent slip systems must operate, according to the Von Mises criterion (Von Mises 1928). In orthorhombic olivine (throughout this book we refer to *Pbnm* notation), plastic slip is restricted to [100] and [001] directions with no possibility of shear along [010]. The lack of slip systems in olivine can be offset by a more general analysis of plastic deformation in solids. Indeed, plastic deformation does not result only from the motion of dislocations, but, as we show further, from grain boundary mobility (sliding or migration) which can be related to defects called *disclinations* (see the chapters 1 and 6 for more details).

References

W. Bragg & G. Brown (1926) Z. Kristallogr. 63: 538
Y. Fei *et al.* (1990) J. Geophys. Res. 95: 6915
K. Fujino *et al.* (1981) Acta Cryst. B 37: 513
G. Hirth & D. Kohlstedt (2003) in "Inside the Subduction Factory", ed. J. Eiler. AGU, pp. 83–105
D. Kohlstedt *et al.* (1995) J. Geophys. Res. 100: 17587
R. Von Mises (1928) Z. Angew. Math. Mech. 8: 161

2.2.2. Wadsleyite

With increasing pressure, $(Mg,Fe)_2SiO_4$ olivine undergoes a phase transition to wadsleyite, named in honour of Australian solid-state chemist Arthur D. Wadsley (1918-1969). In nature, wadsleyite was first found in shock veins from the Peace River meteorite (Price *et at.* 1983). Wadsleyite is known to be stable in the upper transition zone (410-520 km depth) with the *P-T* conditions of 13-18 GPa and 1600-1800 K (Fei *et al.* 1990). This high-pressure phase is about 8% denser than olivine.

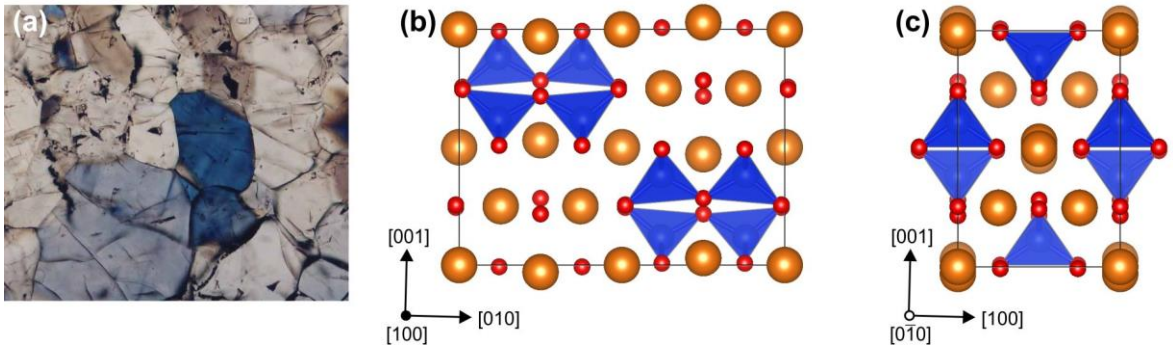

Figure 2.2.2. (a) Synthetic wadsleyite polycrystal in polarized light. **(b, c)** Unit cell of wadsleyite. Si-tetrahedra are shown in blue, Mg atoms – in orange, and O atoms - in red

The crystal structure of wadsleyite maintains orthorhombic features, however increase in pressure (and density) induces higher symmetry of the structure (space group *Imma*, $z = 8$) with respect to olivine as well as clusterization of isolated Si-tetrahedra to double tetrahedra groups Si_2O_7. Thus, wadsleyite belongs to the class of sorosilicates (diorthosilicates). Mg/Fe atoms have octahedral coordination of O atoms. The unit cell parameters at 18.5 GPa are $a = 5.70$ Å, $b = 11.44$ Å, and $c = 8.26$ Å (Horiuchi & Sawamoto 1981).

Deformation experiments on synthetic wadsleyite samples (Thurel & Cordier 2003; Thurel *et al.* 2003) and theoretical PNG-modeling (Metsue *et al.* 2010) suggest ½⟨111⟩{101} and [100](010) to be the easiest slip systems in this phase.

References

Y. Fei *et al.* (1990) J. Geophys. Res. 95: 6915
H. Horiuchi & H. Sawamoto (1981) Amer. Miner. 66: 568
A. Metsue *et al.* (2010) Acta Mater. 58: 1467
G. Price *et al.* (1983) Canad. Mineral. 21: 29
E. Thurel & P. Cordier (2003) Phys. Chem. Miner. 30: 256
E. Thurel *et al.* (2003) Phys. Chem. Miner. 30: 271

2.2.3. Ringwoodite

Ringwoodite is the second high-pressure polymorph of $(Mg,Fe)_2SiO_4$ olivine. The mineral was named after Australian geochemist Alfred Edward «Ted» Ringwood (1930–1993), who studied polymorphic phase transitions in olivine and pyroxene. This phase was first identified in the Tenham meteorite in 1969 (Binns *et al.* 1969) and further it was inferred to be the major constituent of the lower transition zone (525 - 660 km depth) with *P-T* conditions in the range of 18 - 25 GPa and 1700 – 1900 K.

Ringwoodite exhibits a cubic spinel-type crystal structure (space group $Fd\bar{3}m$, $z = 8$) where a close-packed structure is built by O atoms, ½ octahedral sites are occupied by Mg, and ⅛ tetrahedral sites – by Si atoms. The unit cell parameter of Mg_2SO_4 ringwoodite at ambient pressure is $a = 8.071$ Å (Ringwood & Major 1970). Similarly to olivine, ringwoodite belongs to the class of orthosilicates with isolated SiO_4 tetrahedral units.

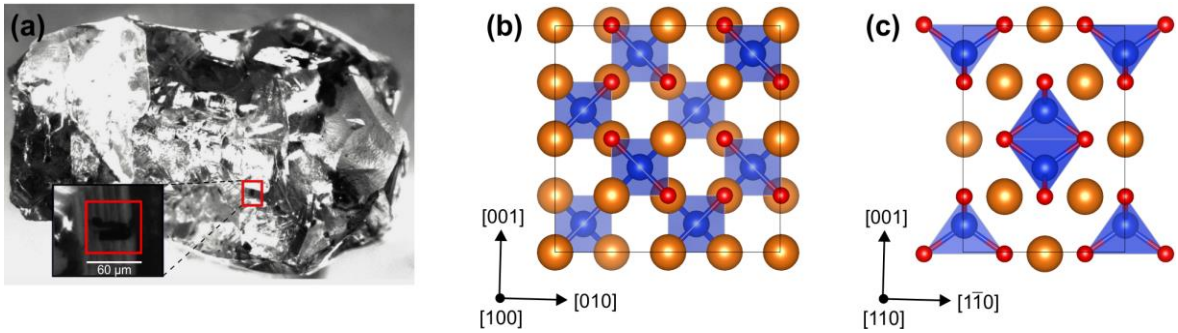

Figure 2.2.3. (a) Ringwoodite inclusion in a diamond from the Juina area of Mato Grosso, Brazil (Pearson *et al.* 2014). **(b, c)** Crystal structure of ringwoodite. Si-tetrahedra are shown in blue, Mg atoms – in orange, and O atoms - in red

The slip directions in $(Mg,Fe)_2SiO_4$ ringwoodite are of the ½⟨110⟩ type, corresponding to the shortest lattice repeats in this structure. TEM analysis of recovered ringwoodite samples deformed in D-DIA, (Karato *et al.* 1998; Wenk *et al.* 2005), RDA (Hustoft *et al.* 2013; Miyagi *et al.* 2014) and DAC (Meade & Jeanloz 1990, Wenk *et al.* 2004) systematically indicate that ½⟨110⟩ dislocation glide mainly in the {111}, {110} and {001} planes.

References

R. Binns *et al.* (1969) Nature 221: 943
J. Hustoft *et al.* (2013) Earth Planet. Sci. Lett. 361: 7
S.-I. Karato *et al.* (1998) Nature 395: 266
C. Meade & Jeanloz (1990) Nature 348: 533
L. Miyagi *et al.* (2014) Phys. Earth Planet. Inter. 228: 244
D. Pearson *et al.* (2014) Nature 507: 221
A. Ringwood & Major (1970) Phys. Earth Planet. Inter. 3: 89
H.-R. Wenk *et al.* (2004) Earth Planet. Sci. Lett. 226: 507
H.-R. Wenk *et al.* (2005) Phys. Earth Planet. Inter. 152: 191

2.2.4. Bridgmanite

Bridgmanite (Mg,Fe,Al)(Si, Fe, Al)O_3, originally called magnesium silicate perovskite, is expected to compose up to 93% of the lower mantle (Murakami *et al.* 2012) and therefore it is likely the most abundant mineral in the Earth making up 38% of its volume. Bridgmanite has a wide range stability field from 24 GPa to *c.a.* 125 GPa and 1800 K - 3000 K, corresponding to 670 – 2900 km depth (Fig. 2.1.2). Originally synthesized in the laboratory in 1974 by Lin-Gun Liu, this phase was first discovered in nature in a heavily shocked Tenham meteorite (Tomioka & Fujino 1997). In 2014, the mineral was named «bridgmanite» (Tschauner *et al.* 2014) in honour of Percy Bridgman (1882 – 1961), the 1946 Nobel laureate in Physics, for his fundamental contributions to high-pressure research.

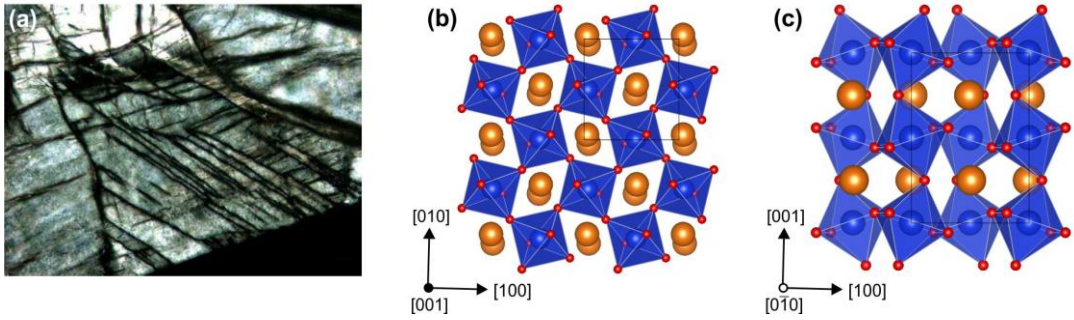

Figure 2.2.4. **(a)** Bridgmanite polycrystal synthesized in multianvil at 23 GPa; 2000K - polarized light. **(b, c)** Bridgmanite crystal structure. Si-tetrahedra are shown in blue, Mg atoms – in orange, and O atoms - in red

Bridgmanite has orthorhombically distorted perovskite-type crystal structure (space group *Pbnm*, $z = 4$) with the unit cell parameters $a = 4.65$ Å, $b = 4.80$ Å and $c = 6.70$ Å at 30 GPa (Fiquet *et al.* 1998). With increasing pressure, Si atoms change their typical tetrahedral coordination to octahedral configuration and coordination number of Mg increases to eight. Orthorhombic distortion of bridgmanite (with respect to the cubic perovskite structure) results from rotation and tilting of the SiO_6 octahedra and the offset in the position of Mg atoms (Figs. 2.2.4 b, c). These structural distortions increase with pressure (Fiquet *et al.* 2000).

High pressure deformation of bridgmanite is challenging to perform. Some recent experiments suggest indications of slip after transformation from San Carlos olivine in DAC (Wenk *et al.* 2004) and from multianvil deformation experiments (Cordier *et al.* 2004; Miyajima *et al.* 2009). Recently, the first shear deformation experiments at lower mantle conditions of bridgmanite and magnesiowüstite aggregates were reported by Girard *et al.* (2016). However, no information on deformation mechanisms or texture development was obtained from this study.

References

P. Cordier *et al.* (2004) Nature 19: 837
G. Fiquet *et al.* (1998) Phys. Earth Planet. Inter. 105: 21
G. Fiquet *et al.* (2000) Geophys. Res. Lett. 27: 21
J. Girard *et al.* (2016) Science 351: 144
L. Liu (1974) Geophys. Res. Lett. 1: 277
N. Miyajima *et al.* (2009) Phys. Earth Planet. Inter. 174: 153
M. Murakami *et al.* (2012) Nature 485: 90
O. Tschauner *et al.* (2014) Science 346: 1100
N. Tomioka & K. Fujino (1997) Science. 277: 1084
H.-R. Wenk *et al.* (2004) Earth Planet. Sci. Lett. 226: 507

2.2.5. Post-perovskite

The first experimental evidence of (Mg,Fe)SiO_3 perovskite → post-perovskite phase transition was detected in 2004 in a laser-heated diamond anvil cell (LHDAC) at *P-T* conditions in excess of 125 GPa and 2500 K (Murakami *et al.* 2004), *i.e.* close to that at the CMB. The existence of this high-pressure phase was also confirmed by *ab initio* calculations (Oganov & Ono 2004).

The post-perovskite (ppv) phase exhibits orthorhombic $CaIrO_3$-type crystal structure (space group *Cmcm*, *z*=4) with anisotropic unit cell parameters $a = 2.456$ Å, $b = 8.042$ Å and $c = 6.093$ Å at 121 GPa (Murakami *et al.* 2004). The occupied Wyckoff positions are *4c* for Mg, *4a* for Si, and *4c* and *8f* for O. After the phase transformation, the rigid 3-D network of Si-octahedra of bridgmanite is broken in one direction and the 2D Si-layers parallel to (010) are formed (Fig. 2.2.5b). As such, ppv structure can be considered as a phyllosilicate. Along the [100] direction, Si-octahedra share edges forming rutile-like chains (Fig. 2.2.5a) which are interconnected by apical oxygen atoms along the [001] direction (Fig. 2.2.5b), building up (010) Si-layers.

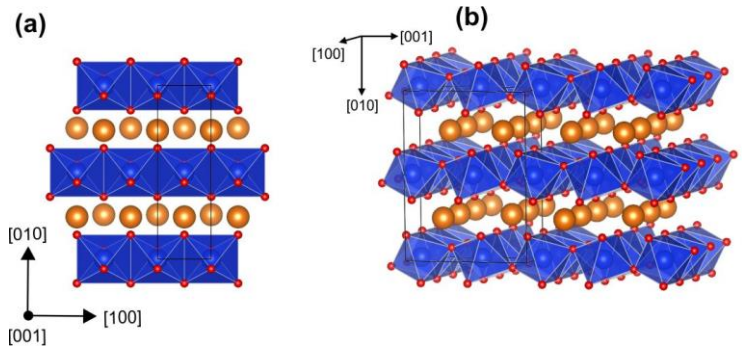

Figure 2.2.5. Crystal structure of $MgSiO_3$ post-perovskite. Si-octahedra are shown in blue, Mg atoms – in orange, and O atoms - in red

For the high-pressure ppv, information about easy slip systems, dislocations and their behaviour under stress is still scarce. Silicate ppv is only stable at very high *P-T* conditions and cannot be quenched to ambient pressure, therefore, deformation experiments on this phase are limited to *in situ* XRD measurements of textures, which one can tentatively relate to easy slip systems. So far, there are only three LHDAC experiments on (Mg,Fe)SiO_3. These experiments suggest a slip in (110)/(100) planes (Merkel *et al.* 2007) or in (001) plane (Miyagi *et al.* 2010). Alternatively to the silicate composition, low-pressure $CaIrO_3$ ppv analogue, stable at ambient pressure, allows direct TEM analysis of recovered samples. In contrast to the high-pressure $MgSiO_3$, experimental studies of $CaIrO_3$ consistently report the presence of [100] and [001] dislocations gliding in (010) plane parallel to the structural layering (Miyajima *et al.* 2010; Hunt *et al.* 2016). It is interesting to note, that {110} twin domains are systematically observed in the $CaIrO_3$ samples deformed in DAC (Miyajima *et al.* 2010; Niwa *et al.* 2012). However, one should keep in mind that there is still no plausible definition of a good isostructural analogue for $MgSiO_3$ ppv, accounting for bond strength contrast between the layers that controls the plastic anisotropy in this material.

References

S. Hunt *et al.* (2016) Phys. Earth Plan. Inter. 257: 91
S. Merkel *et al.* (2007) Science 316: 1729
L. Miyagi *et al.* (2010) Science 329: 1639
N. Miyajima *et al.* (2010) J. Phys. Conf. Ser. 215: 012097
M. Murakami *et al.* (2004) Science 304: 855
K. Niwa *et al.* (2012) Phys. Earth Planet. Inter. 194-195: 10
A. Oganov & S. Ono (2004) Nature 430: 445

2.2.6. Ferropericlase

Ferropericlase (Mg,Fe)O is the second most important phase of the lower mantle after (Mg,Fe)SiO_3 bridgmanite (Fig. 2.1.2). The Mg-rich end-member of the solid solution is called periclase, from the Greek *περικλάω*, to break around, in allusion to the cleavage. The mineral is stable at ambient conditions has been shown to remain stable at pressures up to 360 GPa (McWilliams *et al.* 2012).

Periclase MgO exhibits a cubic rock salt structure (space group $Fm\bar{3}m$, z=4). In this structure, Mg and O atoms form identical sublattices (Fig. 2.2.6b) that represent a cubic (three-layer) stacking of close-packed planes parallel to {111}.

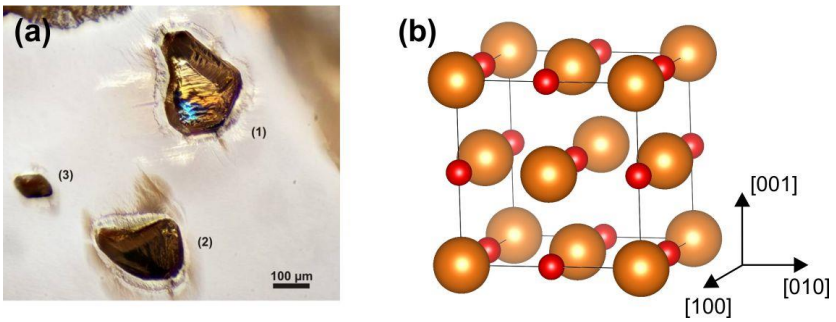

Figure 2.2.6. **(a)** Ferropericlase inclusions in a diamond from Juina deposit, Mato Grosso, Brazil (Master thesis of R. Reali, Univ. Padova). **(b)** Crystal structure of MgO: Mg atoms are shown in orange, O - in red

At ambient conditions, the easiest slip system in MgO is ½⟨110⟩{110}, followed by ½⟨110⟩{100} (Haasen *et al.* 1985; Foitzik *et al.* 1989). Experimental studies indicate that in absence of confining pressure, CRSS for slip in {110} is one order of magnitude lower than that in {100} (Foitzik *et al.* 1989). Under high-pressure conditions, only few experiments have been performed (Li *et al.* 2004; Yamazaki & Karato 2002; Heidelbach *et al.* 2003). Pressures of the lower mantle were only achieved by Merkel *et al.* (2002) and Marquardt & Miyagi (2015) using a DAC at ambient temperature. The results of these studies show some discrepancies. While Merkel *et al.* (2002) concludes that {110} are the only active planes, Yamazaki & Karato (2002), Heidelbach *et al.* (2003) as well as Li *et al.* (2004) suggest that glide in {100} as well as in {111}, may contribute significantly to the total deformation. The Marquardt & Miyagi (2015) study finds that the strength of ferropericlase increases by a factor of three at pressures from 20 to 65 GPa in excellent agreement with the theoretical prediction of Amodeo *et al.* (2012). In overall, from these experiments, it is difficult to conclude about the effect of temperature, pressure and strain rates on the deformation mechanisms of MgO under the lower mantle conditions.

References

J. Amodeo *et al.* (2012) Philos. Mag. 92: 1523
A. Foitzik *et al.* (1989) Mater. Sci. Eng. A113: 399
P. Haasen *et al.* (1985) In "Dislocations in solids", University of Tokyo Press, pp. 455–462
F. Heidelbach *et al.* (2003) J. Geophys. Res. 108: 2154
L. Li *et al.* (2004) J. Appl. Phys. 95: 8357
H. Marquardt & L. Miyagi (2015) Nature Geosci. 8: 311
S. Merkel *et al.* (2002) J. Geophys. Res. 107: 2271
R. McWilliams *et al.* (2012) Science 338: 1330
D. Yamazaki and S.-I. Karato (2002) Phys. Earth Planet. Inter. 131: 251

Chapter 3

Techniques

Modeling defects and their mobility at the atomic scale

3.1.1. Generalized Stacking Faults

The concept of a generalized stacking fault (GSF), also called γ-surface, was introduced in the 1960's by V. Vitek for bcc metals (Vitek 1968). It is a theoretical concept which probes the ability of a crystal structure to undergo a shear localized in a given plane. At this stage, crystal defects are not considered. A simulation cell is built with the target slip plane put horizontal in the middle, as illustrated on Figure 3.1.1a. The energy cost resulting from a rigid-body shear in the slip plane is then calculated by displacing the upper part of the simulation cell over the lower part by the displacement vector $\vec{f} = \vec{e}_1 a_1 + \vec{e}_2 a_2$ in this plane. For instance, applying the displacement increment $e_i = 0.05 a_i$ provides an energy landscape with a resolution of 400 points. After shearing the upper part, atomic relaxations are allowed along the direction perpendicular to the glide plane only, *i.e.*, along z, exclusively in order to avoid spurious recovery of the perfect crystal geometry during energy minimization. The excess energy γ is commonly considered per unit surface area.

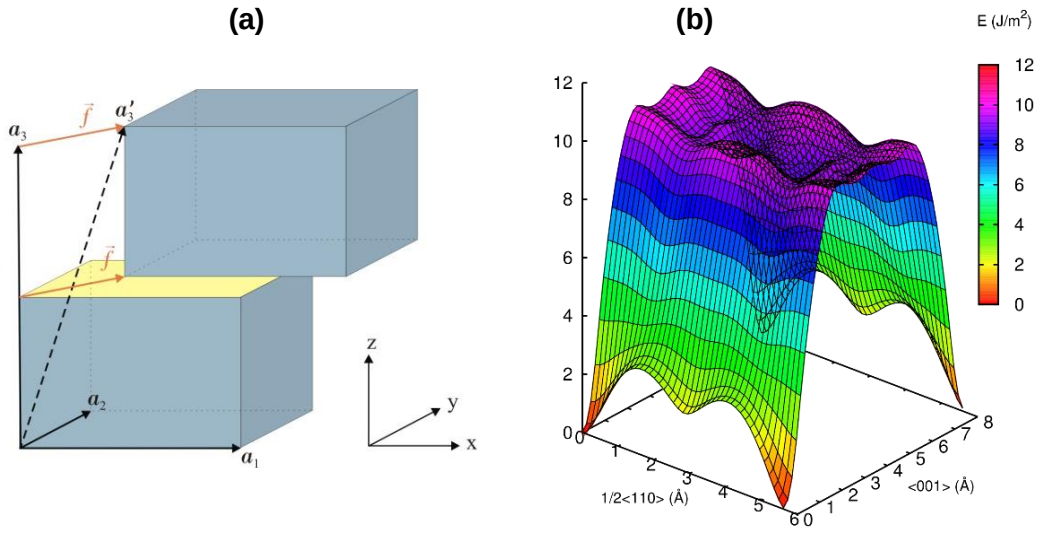

Figure 3.1.1. **(a)** Schematic illustration of GSF calculations procedure; **(b)** γ-surface calculated in ringwoodite in the (110) plane at 20 GPa

For instance, in ringwoodite, calculations of γ-surfaces (Fig. 3.1.1b) indicate that $\frac{1}{2}\langle 1\bar{1}0\rangle$ is an easy shear direction within the (110) plane. Moreover, the presence of a local minimum energy at half way along that shear direction suggests an existence of a stable stacking fault and dissociation of $\frac{1}{2}\langle 1\bar{1}0\rangle$ Burgers vector into two collinear partials.

GSF calculations represent a very useful numerical tool to find the easy shear paths (including planes and directions within these planes) in a crystal structure. Further, the easiest slip systems will be searched among the easy shear paths defined from the γ-surfaces.

References

V. Vitek (1968) Philos. Mag. 18: 773

3.1.2. Modelling dislocations with the Peierls-Nabarro model

Rudolf Peierls was a solid-state physicist who had only marginal interest in dislocations mostly motivated from his discussions and interactions with Egon Orowan:

> *«All I did was formulate and solve the equations representing his [Orowan] model. I had wanted this to be a joint paper with Orowan, but he refused. The matter did not seem important at the time and I did not take more interest in the problem of dislocations (…) At the Batelle symposium, 1967, I discovered that this paper had become one of the classics in the field (...) Nabarro had extended my argument and had also corrected a major algebraic error in my paper.»*
>
> *From «Bird of passage» by Rudolf Peierls*

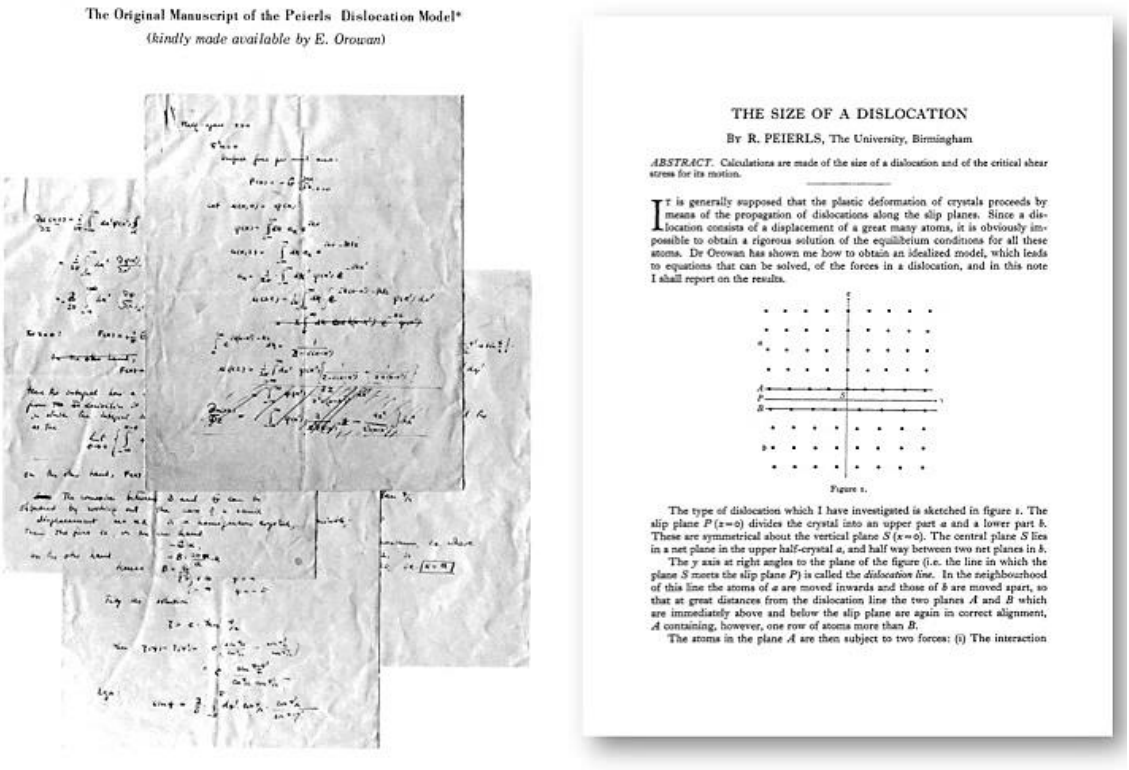

Figure 3.1.2. The original publication «The size of a dislocation» published in 1940 represents a classic. It has been followed by a paper of F.R.N. Nabarro published in 1947: «Dislocations in a simple cubic lattice». The model is now referred as to «the Peierls-Nabarro (PN) model»

Nevertheless, his name is attached to a model which represents a useful and efficient approach to calculate the core properties of dislocations.

The aim of the PN model is to describe the extension of the core of a dislocation within a continuum approach. It represents a regularization of the singularity that is associated with the Volterra dislocation. The PN model assumes that the misfit region of inelastic displacement is restricted to a single plane where the dislocation will glide and that linear elasticity applies far from it (Fig. 3.1.3a). The dislocation corresponds to a continuous distribution of shear S along the glide plane (Fig. 3.1.3b) and the function $S(x)$ describes the disregistry across the glide plane.

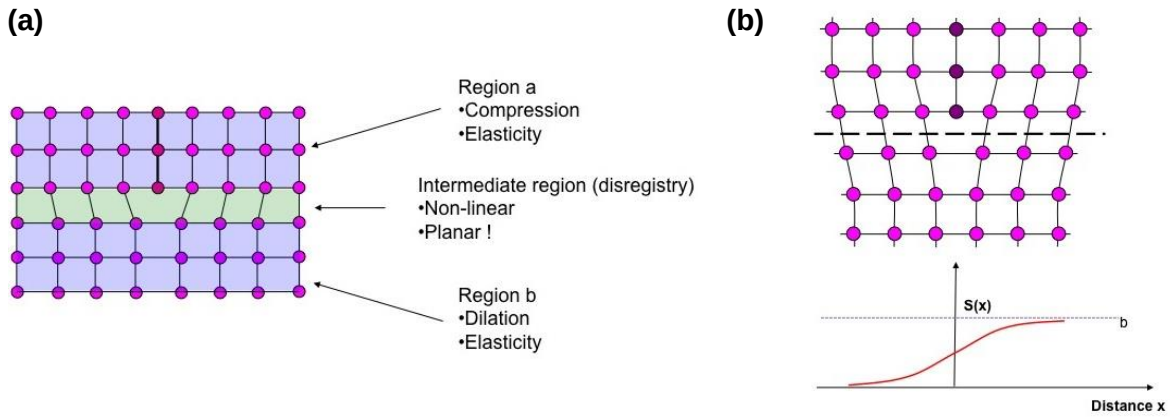

Figure 3.1.3. Schematic illustration of the PN-model principles

The stress generated by such a displacement can be represented by a continuous distribution of infinitesimal dislocations with density $\rho(x)$ for which the total summation is equal to the Burgers vector b. The restoring force F, acting between atoms on either sides of the interface, is balanced by the resultant stress of the distribution leading to the Peierls–Nabarro (PN) equation:

$$\frac{K}{2\pi}\int_{-\infty}^{+\infty}\frac{1}{x-x'}\left[\frac{dS(x')}{dx'}\right]dx' = \frac{K}{2\pi}\int_{-\infty}^{+\infty}\frac{\rho(x')}{x-x'}dx' = F\big(S(x)\big)\,, \tag{3.1.1}$$

where the energy coefficient K is a function of the dislocation character. This coefficient can be calculated within the framework of anisotropic elasticity. As originally proposed and further largely developed by Joos and Duesbery (1997), an analytical solution of the PN equation can be found by introducing a sinusoidal restoring force:

$$F\big(S(x)\big) = \tau^{max}\sin\left(\frac{2\pi S(x)}{b}\right), \tag{3.1.2}$$

where b is the magnitude of the dislocation Burgers vector and τ^{max} is the ideal shear strength (ISS) which is defined as the «maximum resolved shear stress that an ideal, perfect crystal can sustain without deforming plastically». Incorporating this expression in the PN equation leads to a classic solution for the disregistry function:

$$S(x) = \frac{b}{\pi}\tan^{-1}\frac{x}{\zeta} + \frac{b}{2} \tag{3.1.3}$$

where $\zeta = \frac{Kb}{4\pi\tau^{max}}$ represents the half-width of the dislocation density distribution $\rho(x)$.

In order to obtain the misfit energy corresponding to the Peierls dislocation and to determine the Peierls stress, the sum of the local misfit energy should be calculated at the position of atomic rows parallel to the dislocation line. Indeed, the PN equation holds for an elastic continuous medium whereas $S(x)$ can only be defined where an atomic plane is present. The misfit energy can be thus considered as the sum of misfit energies between pairs of atomic planes and can be written as:

$$W(u) = \sum_{m=-\infty}^{+\infty}\gamma\big(S(ma'-u)\big)\cdot a' \tag{3.1.4}$$

where a' is the periodicity of the energy landscape W, commonly taken as the shortest distance between two equivalent atomic rows in the direction of the dislocation's displacement. The Peierls stress is then given by:

$$\sigma_p = \max\left\{\frac{1}{b}\frac{dW(u)}{du}\right\} \tag{3.1.5}$$

The Peierls stress is often described as the critical resolved shear stress (CRSS) at 0 K which sometimes can lead a misunderstanding about the relevance of this theoretical concept. As described in sections 1.2.2 and 3.1.4, the motion of a dislocation is a stress-assisted thermally activated phenomenon. The evolution of the CRSS with temperature (Fig. 1.1.9) describes the interplay between the influence of stress and temperature with two extreme cases: (i) the Peierls stress at 0 K where lattice friction is overcome under the sole influence of stress (without temperature) and (ii) the athermal regime where thermal activation frees the dislocation from lattice friction. The Peierls stress can thus be viewed as a mechanical assessment of lattice friction.

In order to solve the misfit energy function analytically, Joos and Duesbery (1997) introduced a dimensionless parameter $\Gamma = \zeta/a'$. Then, some simple formulas can be derived for the extreme cases of very narrow ($\Gamma \ll 1$) and widely spread ($\Gamma \gg 1$) dislocations:

$$\sigma_p(\Gamma \ll 1) = \frac{3\sqrt{3}}{8}\tau^{max}\frac{a'}{\pi\zeta}; \quad \sigma_p(\Gamma \gg 1) = \frac{Kb}{a'}\exp\left(\frac{-2\pi\zeta}{a'}\right) \tag{3.1.6}$$

The analytical solution presented above can be applied in case of a sinusoidal restoring force and with the knowledge of the ISS value. As demonstrated by Vitek (1968), the restoring force introduced in the PN model is simply the gradient of the so-called γ-surface:

$$\vec{F}(S) = -\overrightarrow{\text{grad}}\,\gamma(S) \tag{3.1.7}$$

The introduction of GSF energies that can be accurately computed from first-principles has renewed interest in the PN model in allowing real dislocations structures to be predicted. The example below (Fig. 3.1.4) demonstrates an excellent agreement between the PN model and experimental HRTEM images for ⟨100⟩ edge dislocation cores in $SrTiO_3$.

Despite the high potential of the PN method, it could be difficult to infer in which plane a screw dislocation core would spread and glide since the PN model gives independent solutions for each plane. Several techniques have been proposed to extend the conceptual approach of the PN model to potentially more complex cases. The Peierls–Nabarro–Galerkin (PNG) method is one of them.

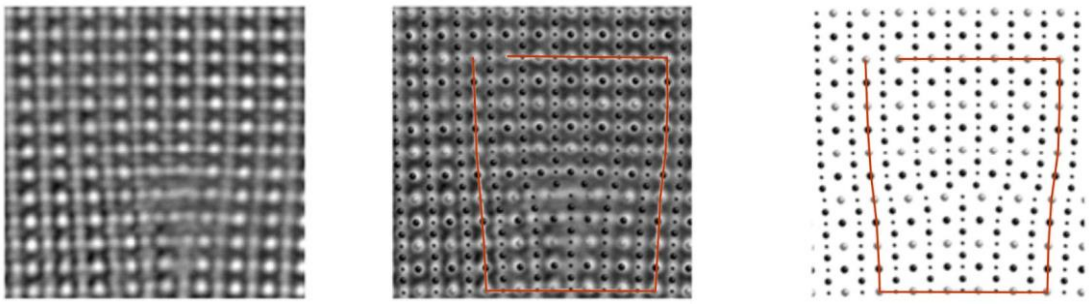

Figure 3.1.4. Comparison of the result from the PN model for a ⟨100⟩ edge dislocation core in $SrTiO_3$ (right) with the corresponding HRTEM micrograph (left) from Jia *et al.* (2005)

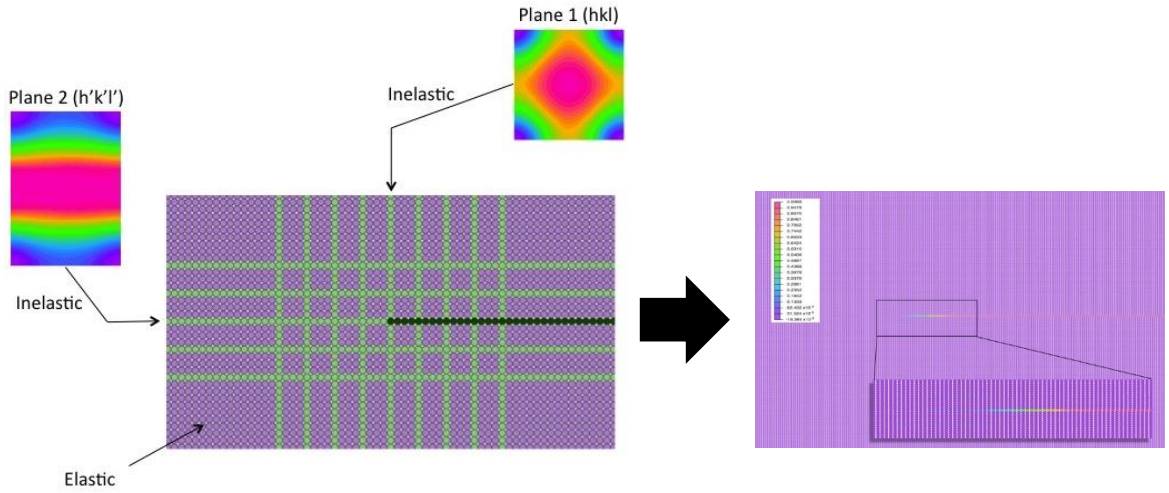

Figure 3.1.5. Schematics of the PNG method calculations

The PNG method developed by C. Denoual (CEA) is a generalization of the PN model which allows taking into account several glide planes simultaneously and to calculate complex (possibly non-collinear and even three-dimensional) cores. As in the initial PN model, the dislocation core structure emerges from the minimizing of an elastic energy (through an approximation of a continuous field representation) and an interplanar potential. The latter is a function of GSF energies from which the linear elastic part has been subtracted. In doing so, we strictly comply with the overall linear elastic behavior expected for small applied strains. In the PNG model two distinct fields are used: $u(r)$, a three-dimensional displacement field of the volume V, and a two-dimensional displacement discontinuity field $f(r)$, which is expressed in the normal basis of the S plane. Thus, $u(r)$ allows one to represent the continuous deformation around the dislocation core, whereas f represents the displacement jump when crossing S.

Potential glide planes (shown in green on Fig. 3.1.5) are introduced in the surrounding elastic medium (in purple) of the supercell with the same geometry as in the crystal. The dislocation is embedded in the middle of the supercell as a Volterra dislocation. After minimization, the relaxed system displays the shape of the dislocation core.

References

D. Ferré *et al.* (2008) Phys. Rev. B 77:014106
C. Jia *et al.* (2005) Phys. Rev. Lett. 95:225506
B. Joos & M. Duesbery (1997) Phys. Rev. Lett. 78:266
F. Nabarro (1947) Proc. Phys. Soc. 59:256
R. Peierls (1940) Proc. Phys. Soc. 52:34
V. Vitek (1968) Phil. Mag. 18:773

3.1.3. Modelling dislocation cores at the atomic scale

The PNG method extends the possibilities of the PN model. However, in some cases, the PN methods are still not sufficient and it is needed to fully model the dislocation core at the atomic scale. When simulating dislocations at the atomic scale there are still two major problems. The first one is due to the fact that all of the atoms in the crystal containing a dislocation are significantly displaced from their regular positions. Atoms far away from the core are always slightly displaced compared with atoms in a perfect reference

crystal. Indeed, the long-range displacement field is proportional to $1/r$. This means that the modelling approaches used to study point defects and surfaces, where the atomic structure away from the defect is identical to the structure of a perfect reference crystal, are not appropriate.

The second problem is a consequence of the previous one. The cell sizes that are required to obtain convergence of the calculations are such that they involve a number of atoms that often precludes first-principles calculations. The various approaches for modeling dislocation cores that side-step this issue in different ways are described below.

Simulation cell geometries

A dislocation produces a long-range elastic field. When introducing a dislocation in a simulation cell of finite size, the atomic planes at the boundaries are deformed. If we place two such boxes next to each other, the boundaries do not match and a region of void is found between two neighboring cells (Fig. 3.1.6). This is of course unphysical, and such a naive construction cannot yield proper results.

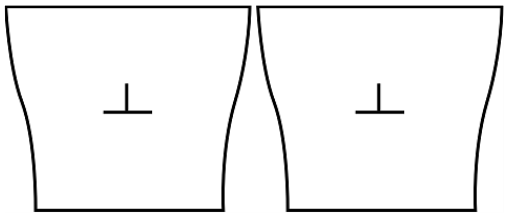

Figure 3.1.6. Placing together two simulation boxes containing edge dislocations

A first solution of this problem is to apply the so-called *cluster approach* and freeze the atoms at the boundaries of the simulation cell, as shown in Figure 3.1.7. By doing so, the long-range elastic field of the dislocation is maintained fixed and cannot evolve during the simulation, but the atoms inside the box can. Such a setup allows studying the core structure of an isolated dislocation.

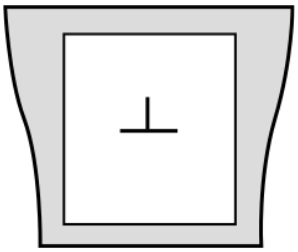

Figure 3.1.7. Cluster approach: a simulation cell with fixed boundaries

However this setup is not suitable for modeling dislocation motion. Indeed, if the dislocation moves it will get closer to a boundary. Since the boundaries are fixed the long-range elastic field of the dislocation will become wrong, and a spurious interaction between the fixed boundaries and the moving dislocation will make difficult the evaluation of a Peierls barrier. Furthermore, the dislocation will not be able to move across the fixed boundaries.

In order to study dislocation motion, one should make the simulation cell periodic along the direction of glide. Figure 3.1.8 shows how such a cell can be constructed for an edge dislocation: two systems are superimposed, the top one containing one more atomic plane than the bottom one. Then the top and bottom boundaries of the cell are fixed. After relaxation, an edge dislocation is formed, and the system is fully periodic both along the dislocation line and along the glide directions (see Bulatov & Cai 2006).

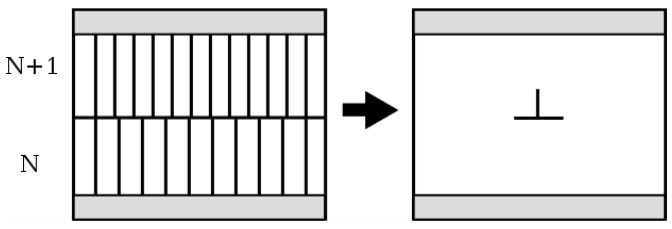

Figure 3.1.8. Building an edge dislocation: N+1 and N are the numbers of atomic planes in the upper and lower parts of the simulation cell, respectively. Grey zones represent the fixed atomic layers

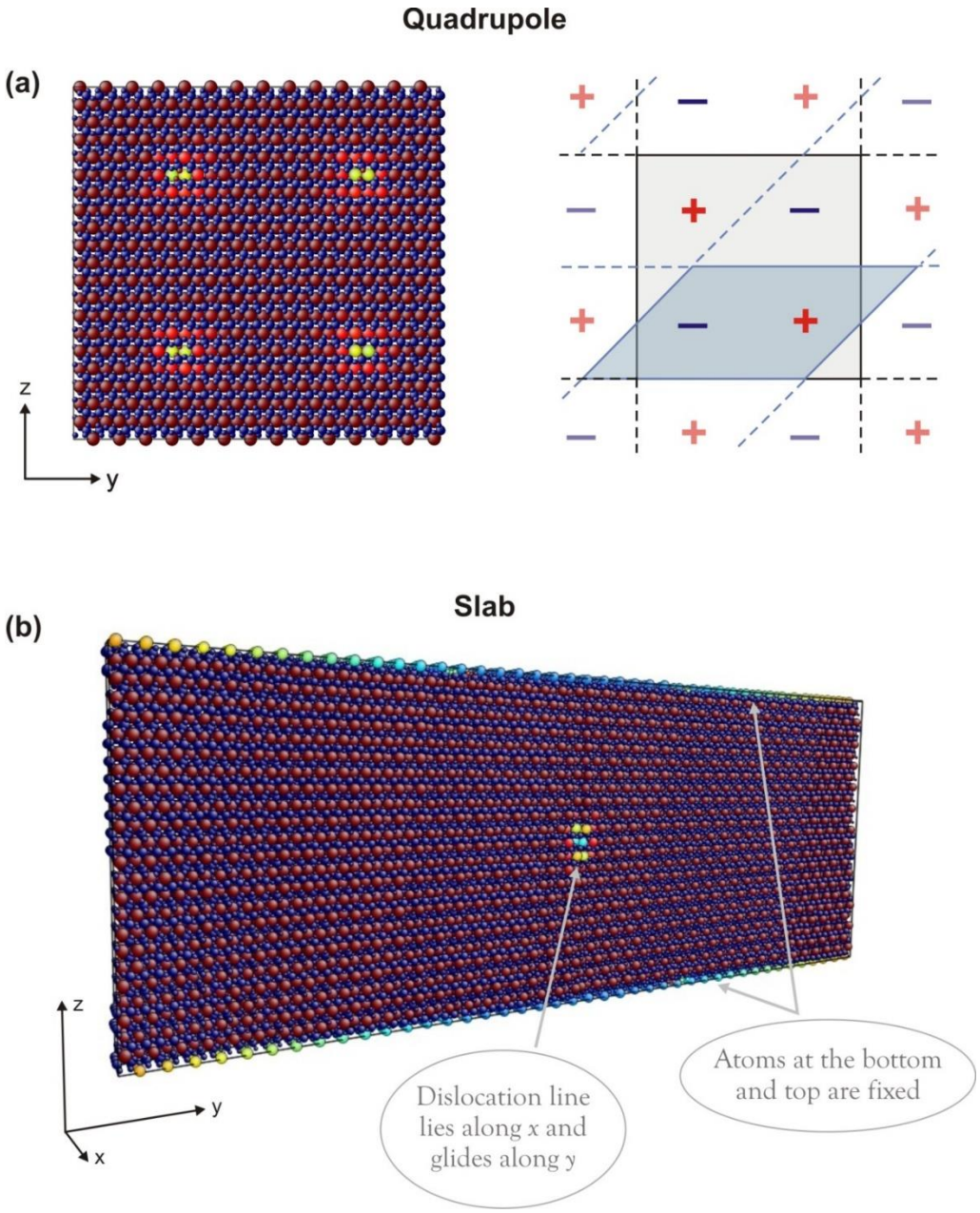

Figure 3.1.9. **(a)** Right panel: $MgSiO_3$ post-perovskite atomic array containing a quadrupole of [100] screw dislocations. Left panel: schematic illustration of a quadrupole and a dipole of screw dislocations in a fully periodic cell. **(b)** Slab simulation cell containing a single [100] screw dislocation in $MgSiO_3$ post-perovskite

In the case of ionic materials, the fixed free surfaces can be charged, which introduces an undesirable electric field inside the simulation cell. This can be solved by using a periodic cluster approach, *i.e.* by making the simulation cell periodic in the direction normal to the glide plane, so that positive and negative surfaces are close together and there is no net long-range electric field (Hirel *et al.* 2014). One must bear in mind that the atom positions in the frozen top regions (shaded areas in Fig. 3.1.8) do not correspond to the true long-range elastic field of the dislocation. This will result in spurious interactions if the dislocation moves far from its original position.

The undesirable effects of fixed boundaries can be removed when a *quadrupole* or a *dipole of dislocations* is embedded in the simulation cell (Fig. 3.1.9a). At long range the combined

elastic fields of the four (or two) dislocations vanish, and 3-D periodic boundary conditions can be used (Bigger *et al.* 1992; Cai 2005). No atoms should be frozen in this case.

Such a simulation setup allows studying dislocation motion, however it can require large simulation cells to minimize the interactions between neighboring dislocations. Indeed, dislocations of opposite signs attract each other, and if they are too close they may annihilate, leaving a supercell free of defects. For dislocations with very wide core structures, in particular dissociated dislocations, very large supercells are required.

In the RheoMan project we commonly use a periodic cluster approach, referred further as «slab» geometry (Figs. 3.1.8; 3.1.9b), to determine the geometry and the Peierls stress of edge and screw dislocations. Fully periodic atomic arrays containing a quadrupole or dipole of dislocations are employed to compute the activation energies for the migration of screw dislocations in Mg_2SiO_4 olivine and $MgSiO_3$ bridgmanite and $MgSiO_3$ post-perovskite, using the nudged elastic band (NEB) method, described further in the section 3.1.5.

References

J. Bigger *et al.* (1992) Phys. Rev. Lett. 69:2224

V. Bulatov & W. Cai (2006) Computer simulation of dislocations. Oxford University Press

W. Cai (2005) Modelling dislocations using a periodic cell. In: Handbook of materials modelling, ed. S. Yip. Springer, pp. 813–826

P. Hirel *et al.* (2014) Acta Mater. 79:117

3.1.4. Modelling dislocation glide: lattice friction and thermal activation

Glide is the conservative motion of a dislocation line in its glide plane. The latter is defined as the plane containing both the dislocation line **L** and the Burgers vector **b**. Thus, It is unambiguously determined for any dislocation with an edge character. Screw dislocations for which the dislocation line and the Burgers vector are parallel have potentially no specific glide plane. However, in practice, screw dislocations are found to glide in a small number of planes where they can glide easily. The easiness of glide depends on the lattice friction, *i.e.* on the force opposed by the crystal structure to dislocation motion. Moving from a low energy configuration to another one involves overcoming a potential barrier, also called the Peierls barrier V_p (Fig. 3.1.10). Lattice friction is an intrinsic property of a material which is commonly measured by the height of this barrier at 0 K (when no thermal activation assists the process) or, by the critical stress needed to overcome this barrier, also called Peierls stress σ_p. The V_p and σ_p values estimated for different glide planes describe anisotropic lattice friction in a material. Such a strategy represents a very efficient approach to identify the easiest slip systems in a material.

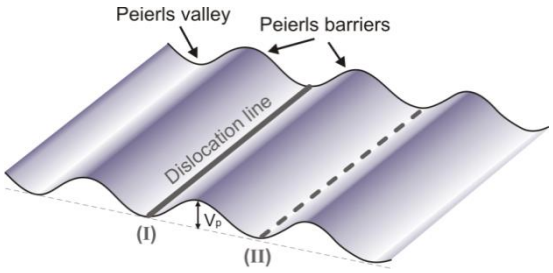

Figure 3.1.10. Lattice friction: schematic illustration of a straight dislocation line gliding over the Peierls potential from the valley (I) to the valley (II)

Computing lattice friction

The Peierls potential V_p can be calculated within the framework of the PN-model (see section 3.1.2) or using the NEB method (section 3.1.5) as the energy barrier that a straight dislocation line has to overcome in order to move from one stable position (in a Peierls valley) to the next one (Fig. 3.1.10). The corresponding Peierls stress σ_p can be computed from the maximum slope of the Peierls potential: $\max(dV_p/dx) = b\sigma_p$.

Alternatively, the critical stress σ_p, needed to trigger dislocation glide, can be found by applying a simple shear strain to the simulation cell in order to increase the shear stress in a glide plane. The force acting on the dislocation is then given by the Peach-Koehler equation:

$$\mathbf{F_L} = (\boldsymbol{\sigma} \cdot \mathbf{b}) \times \mathbf{L} \qquad (3.1.8)$$

Where $\mathbf{F_L}$ is a force acting on a unit length of a dislocation line **L**; **σ** is the applied stress tensor resulting from straining the cell; and **b** is the Burgers vector.

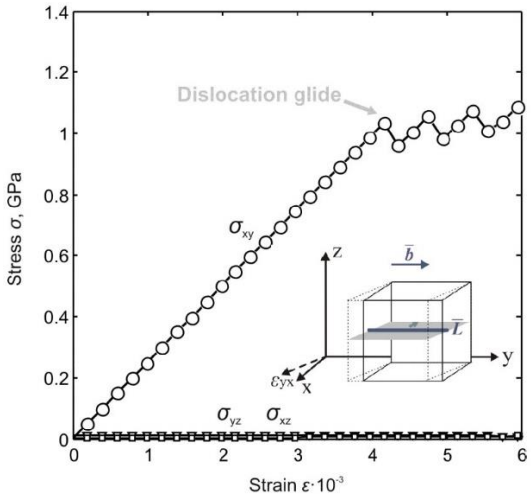

Figure 3.1.11. Evolution of the stress component σ_{xy} while applying a simple shear ε_{xy} to an orthorhombic simulation cell in order to trigger dislocation glide

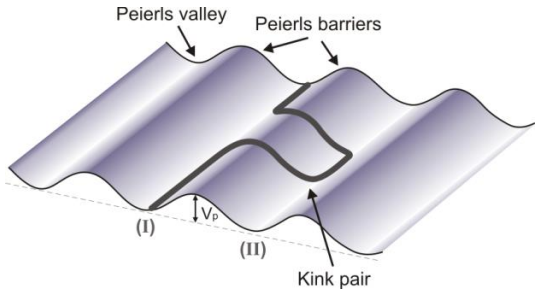

Figure 3.1.12. Thermal activation of dislocation glide: schematic illustration of the kink-pair mechanism which allows the dislocation line to pass from one Peierls valley to the next one at finite temperature

Dislocation glide at finite temperature

At finite temperature, the actual motion of a dislocation from one Peierls valley to the next one is assisted both by stress and thermal activation, which means that actual dislocation motion starts at stresses lower than the Peierls stress. A mechanism, proposed by Seeger to explain the occurrence of Bordoni peaks (anelasticity at low temperature in metals) involves nucleation of kink-pairs (Fig. 3.1.12) on a dislocation line followed by their propagation along the line. These kink-pairs can nucleate spontaneously under thermal fluctuations. Involving kinks of opposite signs, they are unstable and annihilate by mutual attraction. Under an applied shear stress, a critical configuration exists beyond which the two kinks spread, pulling the dislocation line into the next Peierls valley.

The kink-pair formation process can be described based on different models, *e.g.* the *kink-kink* (*KK*) *interaction model* (Seeger and Schiller 1962; Seeger 1984), the *elastic interaction (EI) model* (Koizumi *et al*. 1993, 1994) and the *line tension* (*LT*) *model* (Guyot & Dorn 1967). The first two models are rather suitable at the low stress regime, where the kink-pair shape is not much affected by the external stress. When the kinks are distant enough (*i.e.* the width w between kinks $\gg$ the height h of kinks), their elastic interaction does not depend on the exact shape of the slope and, therefore, can be assumed to a simple rectangular kink shape model, where dislocation line segments represent pure screw and pure

edge components. This approximation was first used for the KK interaction model, where the elastic interaction potential between such kinks is simply $-\mu h^2 b^2/8\pi w$ (Hirth & Lothe 1982; Seeger 1984). Further, this model was developed into the elastic interaction model (Koizumi *et al*. 1993; 1994), which allows distinguishing the rectangular and trapezoidal kink shapes, but it is only applicable at the low stress regime. In contrast to these two models, the LT model is also valid for the high stress regime and allows describing evolution of the kink-pair formation enthalpy with applied stress. This model is shown to be very effective for low lattice friction materials (like metals) where self-energy of a dislocation line is much higher than the Peierls barrier (Caillard & Martin 2003).

For all the models described above, the enthalpy ΔH of a kink pair can be generally defined as follows:

$$\Delta H = \Delta E_{el} + \Delta P - W_\sigma \tag{3.1.9}$$

where ΔE_{el} is the increase in elastic energy of the dislocation line; ΔP is the change in Peierls energy of the line portion which leaves the Peierls valley; W_σ is the negative contribution due to the work of the applied stress. The ΔH value decreases from $\Delta H(\sigma_a = 0) = H_{2k}$, the kink-pair formation enthalpy at zero applied stress, down to $\Delta H(\sigma_p) = 0$ at the Peierls stress. This expression is uniform for all the kink models described above, which only differ by the way the ΔE_{el} term, resulting from the increase of the length of the dislocation line, is defined. In contrast to the KK and the EI model, which provide the exact analytic expression for ΔE_{el} as a function of a kink-pair geometry (characterized by a given width w and height h), the LT model defines this term through the dislocation line stiffness that describes the line tension.

For our studies, we relied on the elastic interaction model to compute kink-pairs in $MgSiO_3$ bridgmanite and in Mg_2SiO_4 ringwoodite and wadsleyite; and on the LT model for $MgSiO_3$ post-perovskite. For more details about these models, we invite the reader to consult the corresponding sections of the Chapter 4.

References

D. Caillard & J. Martin (2003) Thermally activated mechanisms in crystal plasticity. Pergamon, pp. 452
J. Hirth & J. Lothe (1982) Theory of Dislocations. 857 p. Krieger Publishing Company
P. Guyot & J Dorn (1967) Canad. J. Phys. 45:983
H. Koizumi et al. (1993) Acta Metall. Mater. 41:3483
H. Koizumi & H. Kirchner (1994) Phil. Mag. 69:805
A. Seeger & P. Schiller (1962) Acta Metall. 10:348
A. Seeger (1984) In "Dislocation", ed. P. Veyssière, L. Kubin, J. Castaing, pp.141

3.1.5. Modelling transient states: the nudged elastic band

Some physical phenomena, such as migration of a vacancy (Fig. 1.1.7), motion of a dislocation line from a stable position to the next one (Figs. 1.1.8, 3.1.10), *etc.*, can be described simply as the overcoming of an energy barrier. As a rule, in this type of problems the initial and final states of the system are known, and one tries to determine the intermediate configurations between them and the energy barrier associated with the migration/transformation process. The Nudged Elastic Band (NEB) method is well suited to solve this kind of problem.

Construction of intermediate configurations

Since only the initial and final states of the system are known, one has to start with an initial guess of the intermediate states. The simplest solution is to use a linear interpolation: one assumes that along the path, atoms move from their initial position to final configuration following a straight linear path.

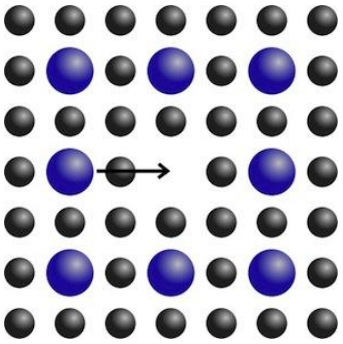

Figure 3.1.13. An example where linear interpolation is not suited: during the motion, the blue atom would occupy the same position a grey one

However, in some cases the linear interpolation may not be suitable (Fig. 3.1.13). For instance, if two atoms are located very close to each another in an intermediate configuration, or if part of the system is rotated. Also, when a straight dislocation moves from one stable position to the next one (Fig. 3.1.10), linear interpolation is completely unable to produce intermediate states where the dislocation contains kink pairs. In general, as soon as the path of atoms deviates significantly from a straight line, linear interpolation is poorly suited.

One practical way to construct intermediate configurations without making any assumption about the reaction path is to use molecular dynamics (MD). Starting from the initial step, one can perform MD simulations until the system ends up in a configuration close to the desired final state. The intermediate states produced during the MD run are naturally close to the minimum energy path. This approach is however difficult to apply if the process studied is a rare event. There are also other algorithms have been proposed to construct intermediate states (Smidstrup *et al.* 2014).

Optimization of the reaction path: NEB method

The initial path, built by linear interpolation (or another method) is often different from the minimum energy path (Fig. 3.1.16). Thus, the initial path has to be optimized. However the simple relaxation of intermediate configurations is inappropriate: these unstable configurations would end up in the closest stable state, *i.e.*, the initial or final state, which is not desired.

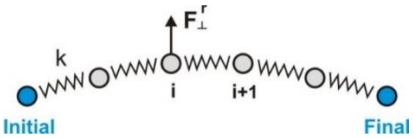

Figure 3.1.15. Intermediate images bonded together with springs. $F_\perp^r$ is the force component normal to the reaction path

In the Nudged Elastic Band (NEB) method (Jónsson *et al.* 1998), the intermediate configurations are bonded together with springs (Fig. 3.1.15), so that they are always constrained to remain between the configurations that precede and follow them. Then the band of configurations acts as an elastic chain. Among the true forces that applies to atoms, only the component normal to the reaction path is used ($F_\perp^r$). Along the reaction path it is the force due to the springs that applies to atoms ($F_\parallel^k$). The NEB calculation stops when the sum of these forces is zero (or drops below a given convergence criterion).

The saddle point configuration: the Climbing NEB

After optimization of the energy path,there is no guarantee that one of the intermediate configuration is exactly at the saddle point. The calculation can then be refined with the climbing NEB method (Henkelman *et al.* 2000). The configuration of highest energy is moved along the reaction path so as to maximize its energy. Its final configuration is the transition state (Fig. 3.1.16), or saddle-point configuration.

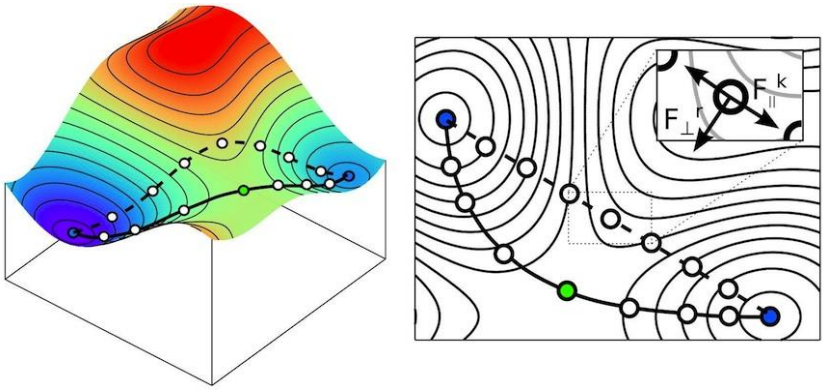

Figure 3.1.16. Principle of the NEB calculations. The dashed line shows the path corresponding to the initial guess for the intermediate state. After applying the NEB method, the configurations lie along the minimum energy path (solid line). The green dot on the energy landscape corresponds to the saddle point

References

G. Henkelman *et al.* (2000) J. Chem. Phys. 113:9901
H. Jónsson *et al.* (1998) in "Classical and Quantum Dynamics in Condensed Phase Simulations", ed. B. Berne, G. Ciccotti, & D. Coker. World Scientific, p. 385-404
S. Smidstrup *et al.* (2014) J. Chem. Phys. 140:214106

3.1.6. Deformation twinning

Dislocation glide and deformation twinning often represent complementary mechanisms contributing to plastic deformation of a material. Mechanical twinning is an important deformation mechanism in a wide range of structural (*e.g.* fcc, bcc, hcp metals and alloys) and geological materials (*e.g.* calcite, diopside, kyanite, plagioclases, quartz *etc.*). Regardless of the nature of a twinned material, morphology of a twin domain can be described as a lens or half lens characterized by thickness h and length l. Boundaries of a lenticular twin contain loops or half-loops of dislocations belonging to adjustment twinning planes separated from each other by Δh (Fig. 3.1.17a). Such a twin lens grows longer (along the twinning direction) by dislocation glide, while growing thicker (in the direction normal to the twinning plane) through successive nucleation of new dislocation loops.

Relying on the twin morphology described above, one can employ a dislocation-based mechanical model to address the corresponding twin formation energy. Commonly, to simplify the model, the distance between each i^{th} and the $(i+1)^{\text{th}}$ twinning dislocations (belonging to the neighboring adjustment planes) is assumed to be invariant and equal to d, as indicated on Fig. 3.1.17a. In general form, total energy E_{tot} of a lenticular twin (Fig. 3.1.17b) can be defined with the following equation:

$$E_{tot} = E_{GPFE} + E_{int} + E_{line} - W, \tag{3.1.10}$$

where E_{GPFE} is the twin boundary energy; E_{int} is the energy term resulting from elastic interaction of twinning partials; E_{line} is the twin dislocation line energy; and W stands for the work of applied stress. The first energy term E_{GPFE}, can be found relying on the

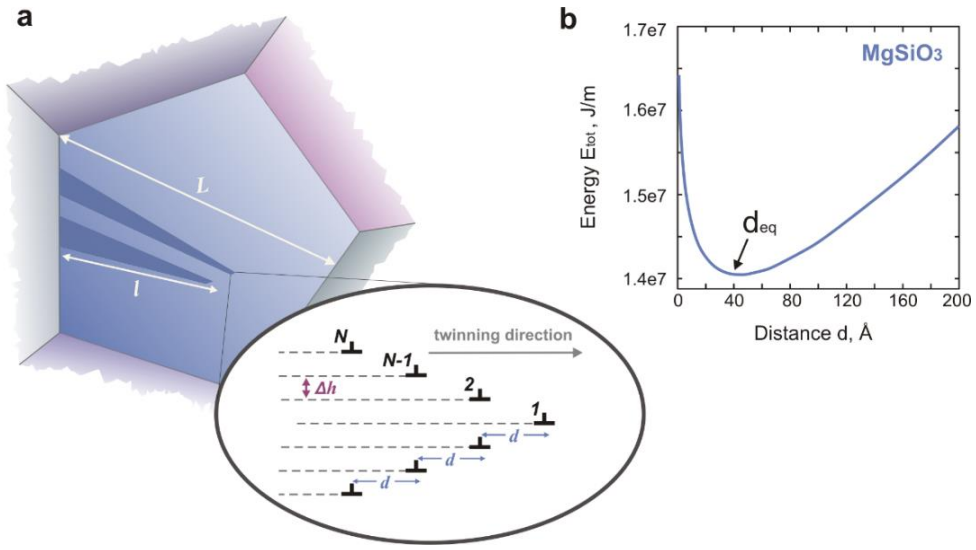

Figure 3.1.17. **(a)** Schematic illustration of a semi-lenticular twin morphology characterized by thickness h, length l and invariant spacing d between the neighboring twinning dislocations. **(b)** Evolution of the twin energy as a function of the spacing d between twinning dislocations in $MgSiO_3$ post-perovskite at 120 GPa

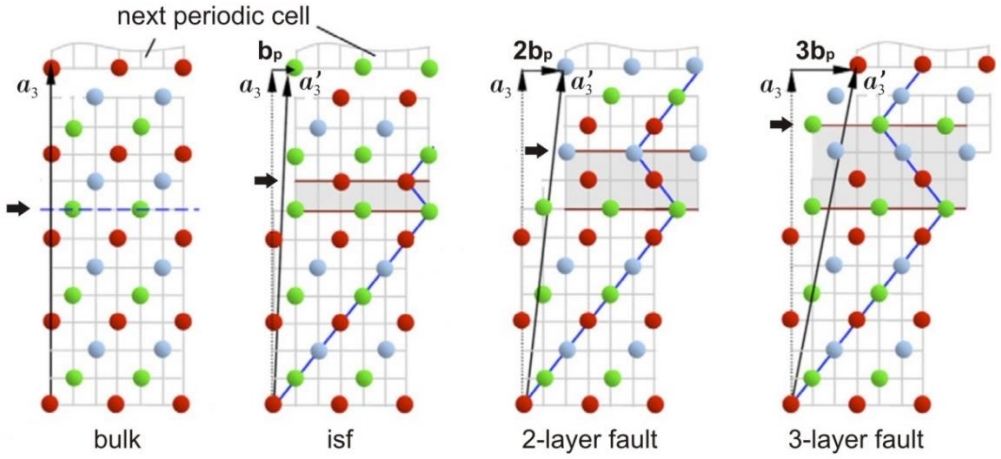

Figure 3.1.18. GPFE calculations at atomic scale. Location of a newly introduced shear level is indicated with a black arrow for each simulation cell. The picture is modified from the scheme provided by Kibey *et al.* (2007)

Generalized Planar Fault Energy (GPFE) landscape computed at the atomic scale. The other three terms contributing to E_{tot} are commonly defined from the elastic theory (Hirth & Lothe 1982). The critical twin nucleation stress τ^{crit} can be further computed while minimizing the total energy E_{tot} with respect to d: $\partial E_{tot}/\partial d = 0$. Among the four energy terms contributing to E_{tot} (Eq. 3.1.10), only the dislocation line energy E_{line} does not depend on the spacing d between the twinning dislocations and, therefore, does not have an effect on the critical twinning stress.

Computing the twinning energy landscape

At the atomic scale, deformation twinning is commonly modeled via twinning energy landscape, also called generalized planar fault energy (GPFE). This energy landscape results from the lattice shearing process due to the successive passage of twinning partials characterized by the displacement vector b_p (Fig. 3.1.18). In this process, the first

layer fault corresponds to the intrinsic stacking fault (*isf*) similar to that produced by GSF calculations, described in section 3.1.1. To compute the second layer fault energy, a new shear level (geometrically identical to the first one) should be introduced. Then, only the atoms above this level are rigidly shifted by the same displacement vector b_p, without affecting the existing first layer fault.

As such, the upper part of the simulation cell is displaced by $2b_p$ (Fig. 3.1.18). A similar procedure can be further repeated to create the third, fourth *etc.* layers. Once the energy calculations for N and N+1 layers yield the same GPFE, the twin nucleation event is reached and further increase in the defect thickness represents the twin growth. For instance, in GPFE calculations for fcc metals and alloys, formation of 3-layer twins is typically observed (Kibey *et al.* 2007; Wang & Sehitoglu 2013).

References:

J. Hirth & J. Lothe (1982) Theory of Dislocations. 857 p. Krieger Publishing
S. Kibey *et al.* (2007) Acta Mater. 55: 6843
J. Wang & H. Sehitoglu (2013) Acta Mater. 61: 6790

3.1.7. Grain boundaries

In this section we describe the procedure to investigate symmetric tilt grain boundaries (STGBs) at the atomic scale. Such grain boundaries can be constructed by tilting two perfect crystals by exactly the same, but of opposite signs, angles, cutting them horizontally, and stacking them together, as illustrated in Figure 3.1.19. Then, a minimization procedure (typically using conjugate-gradients) yields the optimum configuration of atoms.

One should bear in mind that the minimization procedure often converges to the closest local energy minimum, so there is no guaranty that it is the most stable configuration for

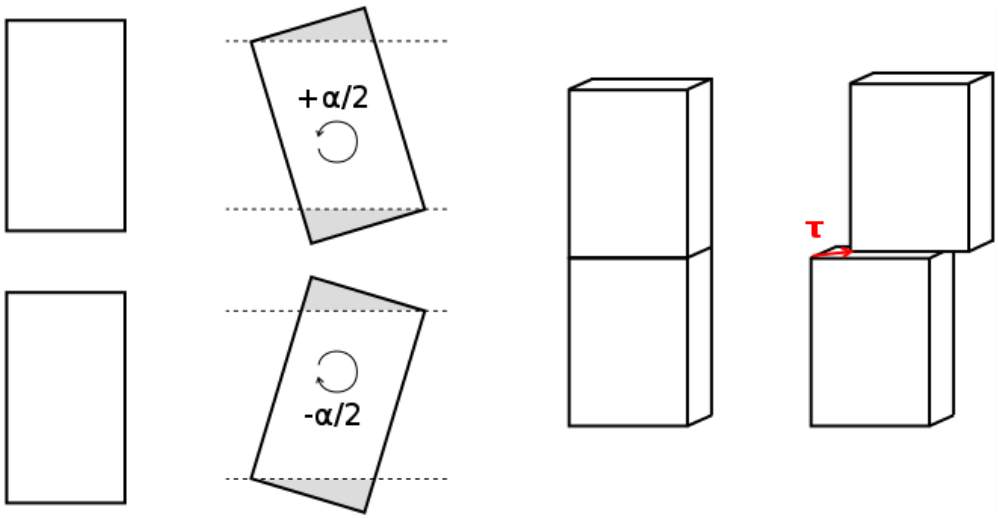

Figure 3.1.19. Method for the construction of symmetric tilt grain boundaries. Two single crystals are rotated by opposite angles, cut horizontally, and then stacked together. For a given misorientation α between the two crystals, several relative positions along the grain boundary plane are searched, as symbolized by the translation vector τ

a given misorientation angle α. Therefore, for each constructed grain boundary, several configurations should be built by shifting the top crystal along the grain boundary plane by a vector τ with respect to the bottom crystal (right panel of Fig. 3.1.19). Once the energy landscape of all these configurations, resembling a γ-surface (section 3.1.1), is computed, only the lowest energy configuration for each investigated angle α is conserved. The procedure can be automated for misorientations between the two grains ranging from $\alpha = 0$ to $\alpha = 90°$.

3.2. Modeling plasticity at the mesoscale

3.2.1. 2.5-Dimentional dislocation dynamics

Dislocation Dynamics (DD) is a simulation method developed to describe the collective motion of dislocations at the mesoscale and to address the intra-crystalline plastic behavior in different materials and under different external conditions.

DD simulations can capture the fundamental aspects of the evolution in time and space of an ensemble of dislocations, by using a continuum framework to describe the dislocations stress fields and by including atomistic features that govern dislocation motion and interactions as input parameters of the simulations (taken from experiments or atomistic simulations). In the classical formulation of 3D-DD, curved dislocation lines are discretized into small segments and their evolution is followed in their glide planes in a 3D simulation volume. An example of a 3D-DD simulation in copper is shown in Fig. 3.2.1, where an initial random distribution of dislocation loops evolves under the influence of an external loading. Periodic boundary conditions are applied along the x, y, and z directions, in order to define a simulation volume representative of bulk conditions. Dislocation loops expand in their glide planes and interact with each other under the influence of both the applied stress and the stress field induced by the dislocation microstructure. The loops also interact with each other through their elastic stress fields. The Peach-Kohler force is thus given by the following expression:

$$\mathbf{F_{PK}} = \mathbf{b} \cdot (\boldsymbol{\sigma}_{\mathbf{app}} + \boldsymbol{\sigma}_{\mathbf{int}}) \times \mathbf{L} \qquad (3.2.1)$$

where $\mathbf{b}$ and $\mathbf{L}$ are the dislocation Burgers vector and line, $\boldsymbol{\sigma}_{\mathbf{app}}$ is the applied stress due to external loading and $\boldsymbol{\sigma}_{\mathbf{int}}$ is the stress field induced by the dislocations microstructure.

In the so-called 2.5-Dimensional (2.5D) approach (Gomez-Garcia *et al*. 2006, Benzerga *et al*. 2004), the idea is to follow the motion of dislocation loops in a 2D reference plane that represents a cross section of a 3D volume (indicated as rectangular frames in Fig. 3.2.1). One advantage is to reduce the numerical cost of the simulation but also, as described in the following, to allow an easy introduction of dislocation climb events to model creep

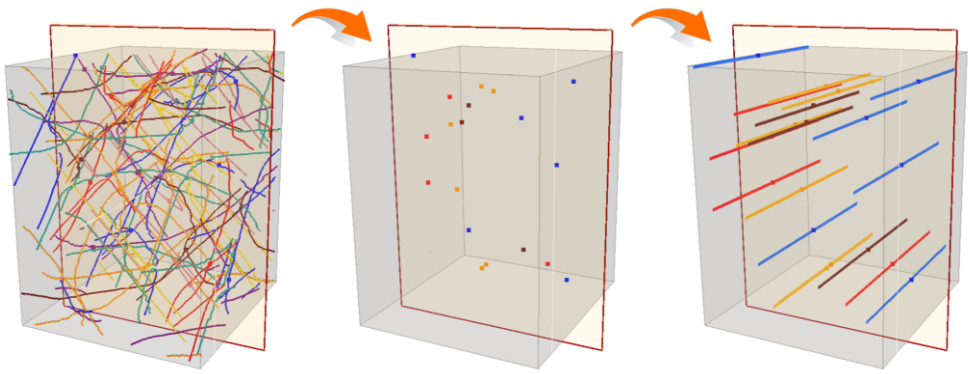

Figure 3.2.1. From 3D to 2.5D dislocation dynamics simulations. In a 3D volume dislocations appear as curved dislocation lines moving in their respective glide planes. Different colors are used to identify dislocations belonging to different glide planes. If we focus on a 2D reference plane, *i.e.*, a cross section of a 3D volume (red rectangle), dislocations cross such plane in discrete points. In the 2.5D-DD approach, we approximate dislocations in these discrete positions as parallel straight segments and then follow their motion in the 2D reference plane

behavior at high temperature. In the 2.5D-DD method, dislocations appear as points at the intersection between the reference plane and the dislocation lines, and are then assumed to be perfect straight segments perpendicular to the reference plane and parallel to each other, as shown in Figure 3.2.1. All the dislocations are assumed to be of edge character and such as their Burgers vector lies in the reference plane. In order to mimic realistic 3D mechanisms in the 2.5-D approach, additional local rules like dislocation multiplication, junction formation or emission of dislocation from sources, are implemented. Although the dislocation geometry is simplified this method has been demonstrated to be a useful tool to address several plasticity problems as dislocation patterning (Keralavarma *et al*. 2012) or high temperature creep (Boioli *et al*. 2015).

Schematically, after setting the initial conditions (dislocation initial configuration, applied load, *etc*...), the simulations consists mainly in the iteration of the following steps:

i. Calculation of the forces acting on each dislocation;
ii. Calculation of the dislocation velocity;
iii. Time integration and update of dislocation position;
iv. Calculation of the produced plastic strain;
v. Application of the local rules.

The forces acting on the dislocations are calculated by using the Peach-Koehler equation (Eq. 3.2.1). Once the forces are known, the velocities are calculated by using a mobility law which describes the dependence of the dislocation velocity on the effective stress. The latter depends on the physical mechanism controlling the dislocation motion and it may vary with the material and the temperature and pressure conditions. In order to capture the dynamics of dislocations, it is needed to characterize the evolution of the velocity of a single dislocation with stress. Typically, a mobility law can be extracted from experiments or from atomistic simulations. Once the expression for the velocity of individual dislocations is provided, dislocations are moved in the direction of forces by integrating the velocity over a time step. From the dislocation displacements, the plastic deformation produced during a time step is calculated. Finally, local rules that allow reproducing dislocation annihilation, multiplication and junction formation are applied (Gomez-Garcia *et al*. 2006, Benzerga *et al*. 2004).

In the classical formulation of the DD method, aimed to describe plasticity at low/moderate temperatures, dislocation motion is restricted to the dislocation glide planes. In this case the effective stress acting on dislocations is the shear stress resolved in the glide plane. At high temperature, diffusion processes become important. Thus, climb, *i.e.*, the motion of dislocation outside the glide plane (Fig. 1.1.10), which is promoted by the absorption or emission of point defects at the dislocation position, plays a key role in high temperature plasticity. Still, for a vast class of materials, dislocation glide is faster than climb, even at high temperature. Under this assumption, the competition between these two mechanisms during creep tests can be addresses in DD simulations by adopting the following procedure, which allows resolving both glide– and climb-related events (Keralavarma *et al*. 2012, Boioli *et al*. 2015):

i. The creep stress is applied and dislocations are moved by glide following the procedure described above and by adopting a small time step Δt_g.

ii. When dislocations reach a quasi-equilibrium configuration, *i.e.*, the dislocations are «jammed» and the plastic strain rate drastically decreases, dislocations are moved by climb, during a time step $\Delta t_c \gg \Delta t_g$.

iii. When a climb displacement of one Burgers vector is achieved by at least one dislocation, the time step is switched back to Δt_g and dislocations are moved again by glide only until a new «jammed» configuration is reached.

In these conditions the plastic strain is mainly produced by glide dislocation motion and climb is the controlling mechanism that allows dislocations to bypass obstacles during the deformation process. We say that plastic deformation is controlled by climb-assisted dislocation motion. This kind of behavior has been recently modelled in aluminum (Keralavarma *et al*. 2012) and during this project on olivine (Boioli *et al*. 2015).

Within the project, the 2.5D-DD simulations have been performed using the microMegas code developed at the LEM/CNRS-ONERA in Paris. For more details about DD simulations and the microMegas code we refer to Devincre *et al*. (2011).

References

A. Benzerga *et al*. (2004) MSMSE 12:159
F. Boioli *et al*. (2015) Phys. Rev. B. 92: 014115
B. Devincre *et al*. (2011) in "Mechanics of nano-objects". L'École des Mines de Paris, p. 85
D. Gomez-Garcia *et al*. (2006) Phys. Rev. Lett. 96:125503
S. Keralavarma *et al*. (2012) Phys. Rev. Lett. 109: 265504

3.2.2. Disclinations in grain boundaries: from atomistic to continuous

During the RheoMan project, we have worked in collaboration with C. Fressengeas and V. Taupin in Metz to develop an atomistic-to-continuum method to derive dislocation, generalized-disclination density fields and the associated elastic strain, rotation, curvature and second-distortion fields from the atomic structure of grain boundaries (Sun *et al.* 2016). Originally, the method was applied to a copper symmetrical tilt boundary as obtained from molecular dynamics simulations. The main aspects of this method are presented in Figures 3.2.2. and 3.2.3.

In continuum mechanics, calculation of the transformation gradient tensor requires information *both* on the reference and the final configurations. The reference configuration can be the initial unrelaxed configuration, then the final configuration will be the low-energy relaxed GB structure, but the opposite choice can be made either. If we use the vector **X** to denote the position of a point in a solid material with respect to a reference

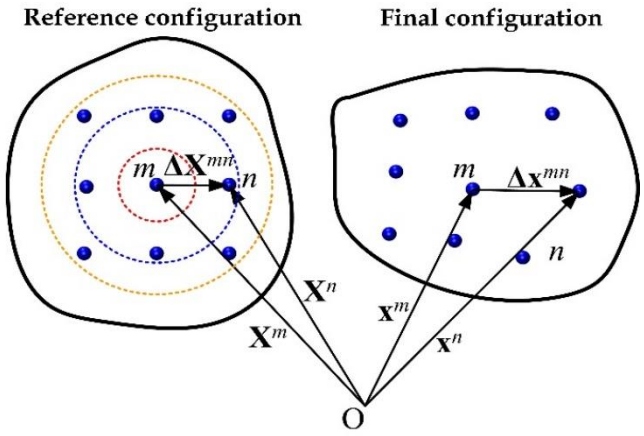

Figure 3.2.2. Illustration of the transformation gradient associated with the motion of material particles from the reference state to the final, relaxed state

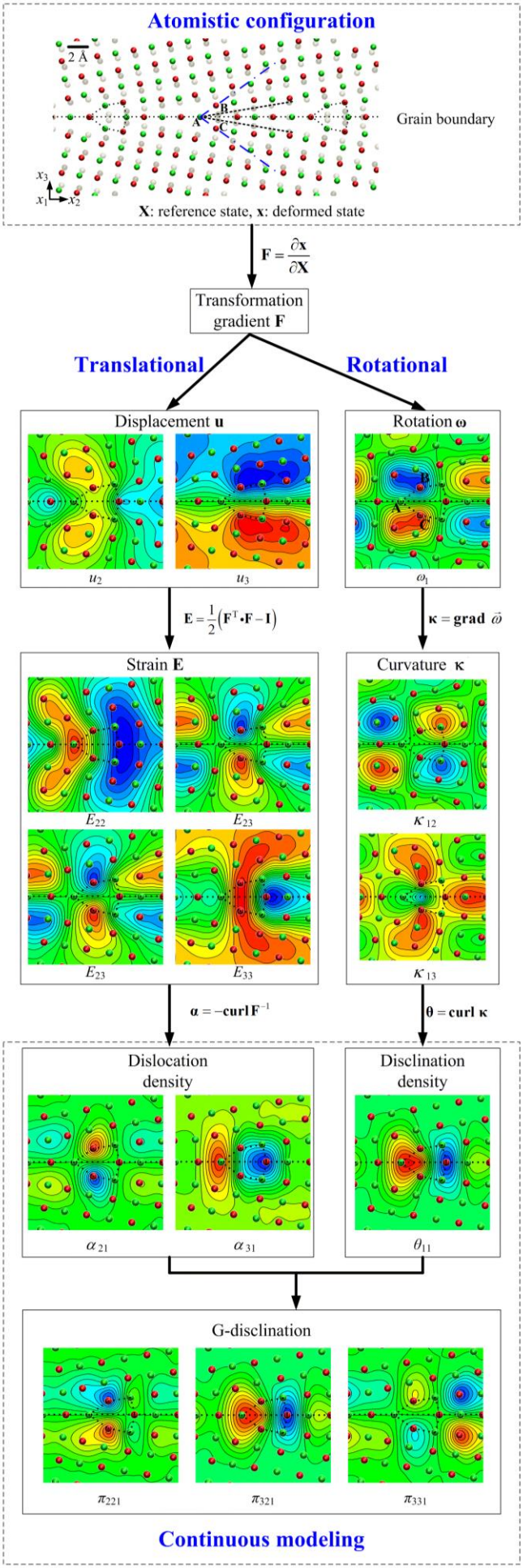

Figure 3.2.3. Schema of the atomistic-to-continuum method for modeling grain boundaries and the associated defects distributions

coordinate system and the vector $\mathbf{x}$ to represent the new position in the final configuration, the transformation gradient can be written as:

$$\mathbf{F} = \frac{\partial \mathbf{x}}{\partial \mathbf{X}}\,; \qquad \mathrm{F}_{ij} = \partial \mathrm{x}_i / \partial \mathrm{X}_j \tag{3.2.2}$$

The transformation gradient field associated with the current and reference atomic configurations is calculated by the following method. As shown in Figure 3.2.2, an atom *m* is located at a position $\mathbf{X^m}$ in the reference configuration. In the final configuration, this atom reaches its new position $\mathbf{x^m}$. Thus, for the reference and final configurations, the relative positions of a neighboring atom *n* with respect to atom *m* are

$$\mathbf{\Delta X^{mn}} = \mathbf{X^n} - \mathbf{X^m}\,; \qquad \mathbf{\Delta x^{mn}} = \mathbf{x^n} - \mathbf{x^m} \tag{3.2.3}$$

Then, the components of the transformation gradient at atom *m* induced by the variation of the relative position of atom *n* are approximated by

$$F_{ij}^{\mathrm{mn}} \approx \frac{\Delta \mathrm{x}_i^{\mathrm{mn}}}{\Delta \mathrm{X}_j^{\mathrm{mn}}} \tag{3.2.4}$$

Because there may be more than one neighboring atom near the atom *m*, the component of transformation gradient at the atom location is averaged over all neighboring atoms *n*:

$$F_{ij}^{m} = \frac{1}{N}\sum_{(r_{mn} \le r_{\mathrm{cutoff}})} F_{ij}^{mn}\,, \tag{3.2.5}$$

where r_{mn} is the distance between atoms *m* and *n* in the reference configuration, r_{cutoff} is a cut-off distance used to verify whether an atom *n* is in the neighborhood of atom *m*, and *N* is the total number of neighboring atoms identified within the cut-off distance.

The cut-off distance should not be too large (sketched by the yellow circle in Fig. 3.2.2) otherwise the local value of the transformation gradient would be overly smoothed. Conversely, it should not be too small or there would be no surrounding atom (sketched by the red circle in Figure 3.2.2). Thus, an appropriate cut-off distance should cover and only cover the nearest neighboring atoms (sketched by the blue circle in Figure 3.2.2). In the case of fcc, bcc and hcp lattices, the nearest neighbor distances are $\sqrt{2}a/2$, $\sqrt{3}a/2$ and a, respectively, where a is the lattice parameter.

Finally, all the atoms are projected onto the $(\mathbf{e_2}, \mathbf{e_3})$ plane, and two-dimensional interpolation is used to generate spatial field distributions in between atoms. It has been checked that the choice of a particular interpolation scheme does not interfere qualitatively with the results.

Once the transformation gradient tensor is calculated at each atomic position, the elastic strain, rotation, curvature, dislocation, disclination and generalized-disclination density fields are calculated in the boundary area by using the standard relationships of continuum mechanics (Fig. 3.2.3).

References

X.-Y. Sun *et al.* (2016) Int. J. Plasticity 77:75

3.3. Observations by Transmission Electron Microscopy

Theoretical modeling of plastic deformation requires information on the microstructures and their evolution with strain. One important aspect is the geometry of slip, *i.e.,* the glide, climb and cross-slip planes, amongst others. Electron tomography is a powerful tool which can provide the essential information about real 3D geometry of a dislocation microstructure.

In most cases, dislocation analyses by transmission electron microscopy (TEM) are limited to imaging. Quantification is usually restricted to Burgers vector identifications, and less often can provide advanced characterizations of actual slip systems (*i.e.* Burgers vector and glide planes) and dislocation reactions. Defining full characteristics of slip systems is rather difficult and time-consuming. The stereographic projection method gives the possibility to determine the dislocation glide planes but for one dislocation after the other and with a low accuracy. Given the tilt limitations of most TEM specimen holders, the configuration of interest might not be characterized. Electron tomography of dislocations represents a more advanced method allowing to fully characterize the dislocation 3D microstructure and slip systems. Contrary to the stereographic projection technique, the dislocation electron tomography method is very accurate and enables fast access to glide planes of a large number of dislocations.

However, as standard imaging, electron tomography is restricted to dislocation microstructures where individual dislocations can be observed, *i.e.,* when the dislocation density is not too large (below *ca.* 10^{15} m^{-2}). This limitation usually leads us to focus on early stages of deformation and prevent samples being deformed at large strains to be analyzed. In Scanning Electron Microscope (SEM) where dislocations are usually not imaged, Electron Backscattered Electron Diffraction (EBSD) has become a very powerful tool to characterize deformation samples. First deformed samples were characterized through the development of crystal preferred orientations. More recently, the fine structure of intragranular misorientations has been used to investigate deformation microstructures. Orientation mapping is now available at the scale of the TEM and we present some recent application of this tool to deformation of minerals.

It is worth noticing that TEM is not only an instrument for microstructure characterization. The development of micro-electronic and micro-electromechanical systems (MEMS) allows performing experiments such as tensile tests in the small space devoted to samples in TEM holders. We have taken advantage of such device to perform the first deformation experiment of olivine *in situ* in the TEM.

3.3.1. Electron Tomography

Reconstruction of a small size object (from several mm to several nm) is possible in 3D using TEM that gives projected images for different projected angles. These series of images are called *tilted series* (Fig. 3.3.1).

For usual sample-holders and TEM polar pieces gaps, the tilt angle range is lower than ±40°. This angular range could reach ±60° for high gaps TEM polar pieces and ±80° for sample-holders dedicated to tomography. The more the angular range increases, the more the omitted volume (missing wedge) decreases, and the more the reconstruction volume

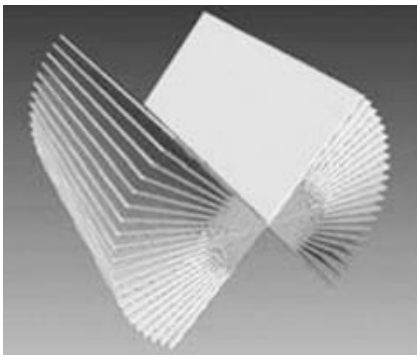

Figure 3.3.1. Tilted series (from Frank 2005)

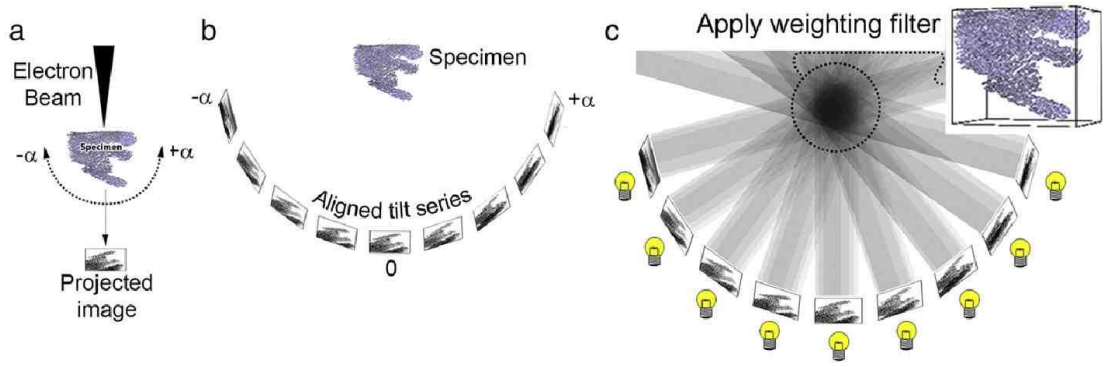

Figure 3.3.2. Weighted back projection (WBP) electron tomography technique. The illustration is from Liu *et al.* (2014)

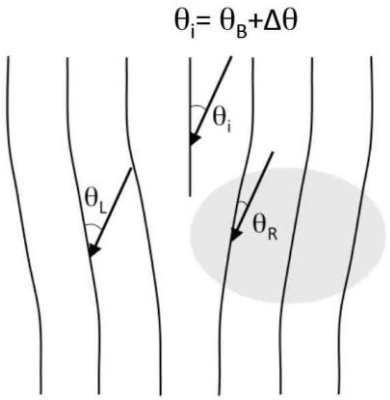

Figure 3.3.3. Schematic illustration depicting illumination of an edge dislocation core, slightly away from the perfect Bragg conditions. Perfect Bragg condition is only satisfied in the shaded area due to local plane bending

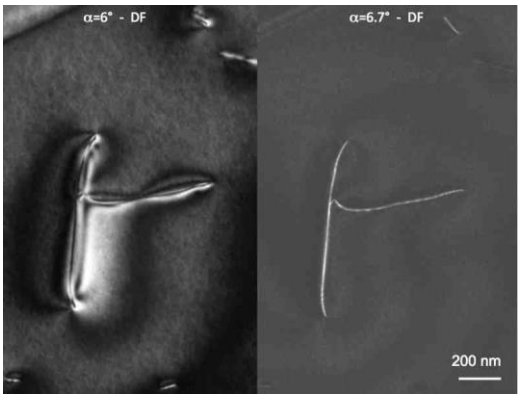

Figure 3.3.4. Change in dislocation contrast and image resolution due to a small (0.7°) angular deviation in dark-field imaging

quality rises. Several reconstruction algorithms exist. They are able to transform a tilted series to a stack. Figure 3.3.2 depicts the weighted back projection (WBP) technique.

The crystallographic plane distortions caused by dislocations are the source of dislocation contrasts observed on TEM micrographs. Figure 3.3.3 shows the example of an edge dislocation observed with the Bragg angle θ_B. On the right side of the dislocation core, some distorted planes are oriented in Bragg condition and give rise to localized diffraction. A small angle deviation $\Delta\theta$ gives the possibility to get a high-resolution dislocation image, close to the dislocation core. This imaging mode is called the *weak-beam dark-field* technique.

Due to the smallness of Bragg angles, dislocation contrasts are very sensitive to the crystal orientation (Fig. 3.3.4). This is an issue in tomography where large tilt ranges must be spanned. Consequently, the specimen needs to be perfectly oriented with the diffraction vector aligned along the tilt axis in order to avoid any Bragg angle variations during the tilted series acquisition (a precision of the order of a tenth of a degree is necessary). The HATA (high angular triple axis) sample holder is dedicated to dislocation analyses (Hata *et al.* 2011). Not only for its capability to reach an angular range of ± 80°, even for small polar piece gaps, but this sample holder makes it possible to rotate along two other axes perpendicular to the sample holder principal axis (± 7.5° along θ and ± 5° along Ω, see

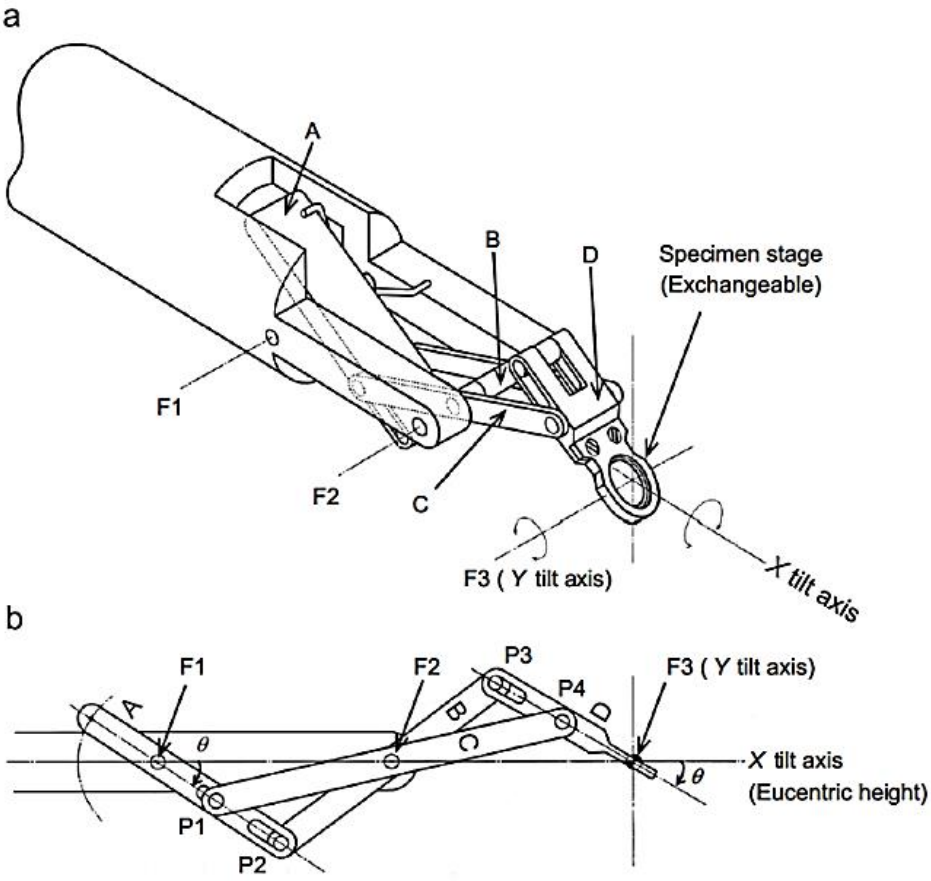

Figure 3.3.5. Double-tilt mechanism of the HATA specimen holder (Hata *et al.* 2011). Movable cantilevered frames **(a)** and side view of the θ tilt **(b)**

Fig. 3.3.5). The diffraction vector, which gives the best conditions to image dislocations, can be aligned to the nearest 0.1° from the sample holder principal axis, due to the two additional degrees of freedom.

Furthermore, the micrographs have to be homogeneous in contrast to get the best 3D reconstruction quality. For better image quality, the following two options can be employed: (i) using TEM with a field emission gun (FEG); (ii) using TEM with a LaB_6 filament associated with precession.

With the first option, the Scanning Transmission Electron Microscopy (STEM) technique allows obtaining a homogeneous contrast (Philips *et al.* 2011) while keeping a high signal over noise ratio. With the second option (Mussi *et al.* 2014), acquisitions performed with the TEM weak-beam dark-field technique gives a high signal over noise ratio. The association of a slight precession of the electron beam (Vincent & Midgley 1994) ensures homogeneous contrast (Fig. 3.3.6).

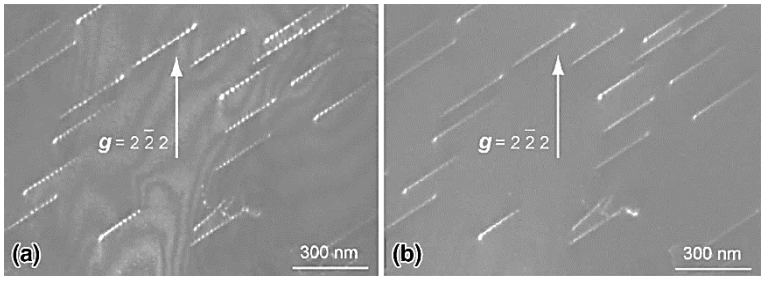

Figure 3.3.6. Contrast homogenization due to an electron beam precession (Rebled *et al.* 2011). The pictures are taken from Mussi *et al.* (2014)

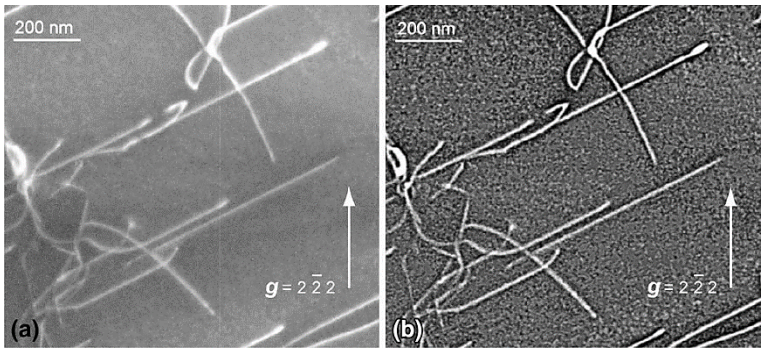

Figure 3.3.7. Dislocation contrast increase due to Kernel filtering and polynomial fit (Mussi *et al.* 2014)

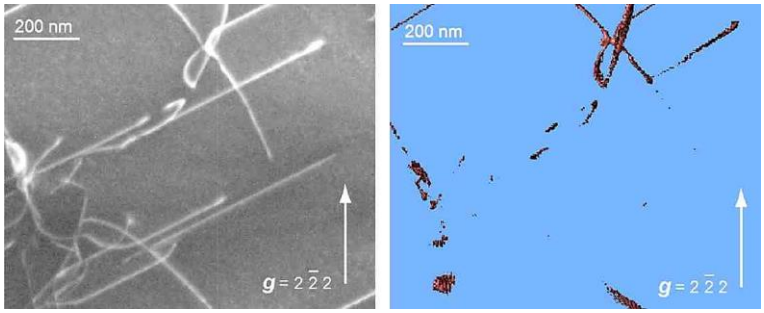

Figure 3.3.8. Unfiltered tilted series and the corresponding reconstructed volume (Mussi *et al.* 2014)

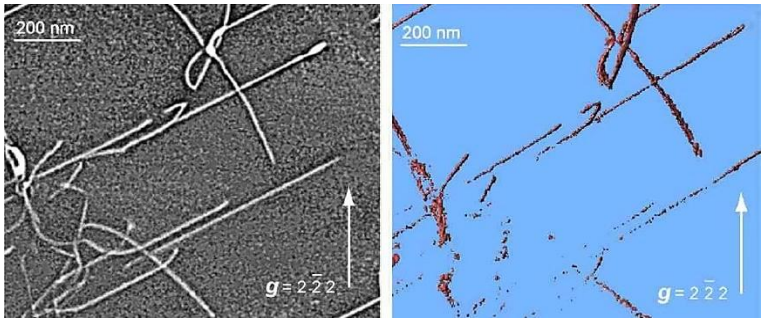

Figure 3.3.9. Filtered tilted series and the corresponding reconstructed volume (Mussi *et al.* 2014)

To increase the dislocation contrast, it is better to filter the tilted series images using, for example, Kernel filtering and polynomial fit (see Fig. 3.3.7). The filtering efficiently can be verified on the 3D reconstruction quality on Figures 3.3.8 and 3.3.9.

References

P. Buseck *et al.* (2001) PNAS 98:13490
O. Ersen *et al.* (2007) Solid State Sci. 9:1088
J. Frank (2005) Electron Tomography: Methods for three-dimensional visualization of structures in the cell. Springer
S. Hata *et al.* (2011) Ultramicrosco-py 111:1168
G. Liu *et al.* (2014) Mater. Charact. 87:1
A. Mussi *et al.* (2014) Phys. Chem. Miner. 41:537
P. Phillips *et al.* (2011) Ultramicroscopy 111:1483
J. Rebled *et al.* (2011) Ultramicroscopy 111:150
R. Vincent & P. Midgley (1994) Ultramicroscopy 53:271
M. Weyland *et al.* (2007) Nanocharacterization, RSC Publishing
D. Williams & C. Carter (2009) in "Transmission Electron Microscopy: A textbook for materials science". Plenum Press

3.3.2. Orientation Mapping

Microstructures that develop as a result of plastic deformation are constituted of patterns of dislocation features which are traditionally studied by TEM provided the dislocation density is not larger than *ca.* 10^{15} m^{-2}. Beyond that, individual dislocation contrasts overlap and cannot be resolved. Other parameters or proxies must then be found to follow the evolution of the plastic behavior. In 1993, Argon and Haasen have argued that a square root scaling law would describe the dependence of the mean misorientation angle on plastic strain due to random fluctuations in the long-range strain field of dislocations:

$$\theta_{avg} \propto \sqrt{\varepsilon} \tag{3.3.1}$$

Some studies on microstructural evolution in deformed fcc metals and alloys have confirmed this scaling behavior for misorientation (Hugues *et al.* 1997; 1998). Although, so far, these scaling laws have only been tested on metals, it is still interesting to note that they were found to be quite robust being independent of material properties like stacking fault energy, solute content *etc.*, and process parameters like temperature, strain, strain rate, strain paths *etc.*, suggesting a rather universal behavior. Scanning Electron Microscope (SEM) based Electron Backscattered Electron Diffraction (EBSD) provides a very efficient and largely automated technique to sample long range and short range information on misorientations within deformed samples. It is today possible to acquire orientation maps in the TEM with the ASTAR™ tool from NanoMEGAS (Rauch & Véron 2014). The TEM is set in micro-beam mode and the incident electron beam is scanned over the area thanks to a dedicated hardware control system of the TEM deflecting coils. The individual exposure time at each location is a few tens of milliseconds. The spot patterns are collected with an external CCD camera that points on the TEM phosphorous screen and stored in the computer memory for further indexation and post processing. Electron diffraction spot patterns are indexed (providing the local crystal orientations) by comparing individually obtained patterns via cross-correlation matching techniques with pre-calculated electron diffraction templates generated every 1° (orientation resolution).

The number of spots present in the diffraction patterns increases significantly when using precessed illumination and the intensity distribution gets closer to the kinematical diffracting conditions. We commonly used precession angles in the range 0.5-1° to improve the indexation rate.

From the orientation maps, virtual bright field (VBF) maps can be generated which represents the fluctuation of the central beam intensity of the diffraction patterns. This builds up a STEM-like bright field contrast directly related to the orientation maps. The quality of indexation from template matching is quantified by the image correlation index which is calculated for every template (Rauch & Dupuy 2005):

$$Q(i) = \frac{\sum_{j=1}^{m} P(x_j, y_j) T_i(x_j, y_j)}{\sqrt{\sum_{j=1}^{m} P^2(x_j, y_j)} \sqrt{\sum_{j=1}^{m} T_i^2(x_j, y_j)}} \tag{3.3.2}$$

In this expression, the diffraction pattern is represented by the intensity function $P(x, y)$ and every template i is described by the function $T_i(x, y)$. The highest Q value corresponds to the solution. The reliability of this solution can be quantified by the ratio of the matching indexes for the two best solutions Q_1 and Q_2:

$$R = 100\left(1 - \frac{Q_1}{Q_2}\right) \tag{3.3.3}$$

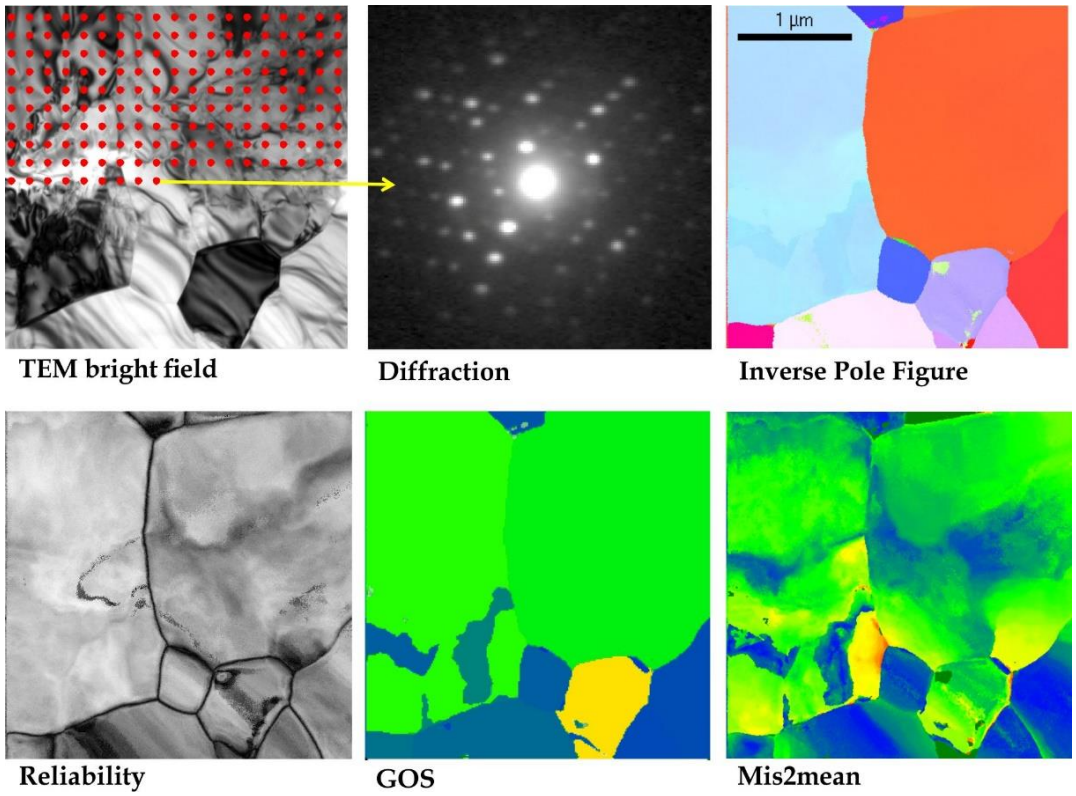

Figure 3.3.9. Illustration of the acquisition process of misorientation maps and further post-processing for polycrystalline olivine (the sample was kindly provided by M. Thieme and S. Demouchy, Montpellier)

In reliability maps, the brighter the pixel (*i.e.* the highest the reliability index) the more reliable is the indexation proposed. On the contrary, the darker the pixel, the least reliable is the solution. This is typically the case at grain boundaries where two solutions of co-existing grains overlap or when for some reasons, the quality of the diffraction patterns is less.

Although *Q*-maps have been proposed as a first approach to detect residual plastic strain, several parameters can affect this parameter. Alternatively, one can focus on the measurements of local misorientations as recently developed in the EBSD community (*e.g.* Wright *et al.* 2011). As commonly used in EBSD, several quantities are calculated from the orientation maps:

- **The Kernel Average Misorientation** (KAM) calculates the average misorientation between a pixel *i* and its neighbors, provided that the misorientation does not exceed a predefined threshold value, *e.g.* 5°, thus the incorporation of well-defined grain boundaries is avoided. If plastic deformation results from dislocation glide and crystal lattice rotation, this approach allows a quantitative evaluation of the local plastic strain gradients (Godfrey *et al.* 2006). A kernel is a set of points of prescribed size surrounding the scan point of interest. The size of the kernel is generally prescribed to the n^{th} nearest-neighbors. Hence this parameter is sensitive to the step size of the measurement grid.

- **The Grain Orientation Spread** (GOS) is the average deviation in orientation between each point in a grain and the average orientation of the grain. This approach leads to assigning the same value to every scan point contained within a grain.

- **The Grain Reference Orientation Deviation** (GROD) is based on the misorientation between a reference point of that grain and the other points. The reference point can be the mean misorientation of the grain (in that case the GROD is also called Mis2mean) or the point of the grain where the KAM is the lowest.

KAM, GROD and GOS approaches appear to be complementary. GROD maps show the orientation field referenced to a fixed point whereas KAM approach shows the magnitude of the gradient, which can be seen as the first derivative of the orientation field.

References

A. Argon & P. Haasen (1993) Acta Met. Mat., 41: 3289
A. Godfrey *et al.* (2006) Metall. Mater. Trans. A 36: 2371
D. Hughes *et al.* (1997) Acta Mater. 45: 105
D. Hughes *et al.* (1998) Phys. Rev. Lett. 81: 4664
E. Rauch & L. Dupuy (2005) Arch. Metall. Mater. 50: 87
E. Rauch & M. Véron (2014) Mater. Charact. 98: 1
S. Wright *et al.* (2011) Microsc. Microanal. 17: 316

3.3.3. *In situ* Nanomechanical Testing

Note: the work described in this section was performed in collaboration with D. Schryvers and H. Idrissi using picoindenter and electron microscopes from EMAT (Antwerpen, Belgium).

In situ nanomechanical testing in a transmission electron microscope offers a very promising pathway by which dislocation dynamics can be observed directly during deformation. This approach allows characterizing individual defect/mechanisms with the possibility to measure quantities which can be directly compared or introduced in simulations. Several types of equipment are now available that allow nanomechanical testing in the TEM to perform:

- **Nanoindentation:** where a nanoindentor applies localized stresses to electron transparent samples in order to observed local deformation mechanisms.

- **Bending:** using bend cantilevers or nanobeams, essentially in order to drive fracture while observing the extent of damage.

- **Compression:** where a flat-punch is used to compress microscale or nanoscale pillars and more recently particles under TEM observation.

- **Tensile loading** (that we describe below). We favored this approach since it allows a much better control of the stress and strain, more compatible with measurements.

We used a PI 95 TEM Picoindenter from Hysitron Inc (Now Bruker). It involves a conductive diamond flat punch indenter and a special Micro-Electro-Mechanical-System (MEMS) device called push-to-pull (PTP). Owing to four identical springs distributed symmetrically at the corners of this device, the compression (push) of the semi-circular end of the PTP device using the flat punch indenter is converted into an uniaxial tensile loading (pull) on the middle gap of the PTP device (Fig. 3.3.9). The springs are arranged such that the force acting on them is parallel to the force on the tensile specimen. Free-standing beams of the studied material (in our case olivine) are cut by FIB and transferred to the PTP device using an Omniprobe micromanipulator on a FEI dual beam FIB/SEM instrument. The beams are then attached to the PTP device using electron beam deposited platinum (Pt).

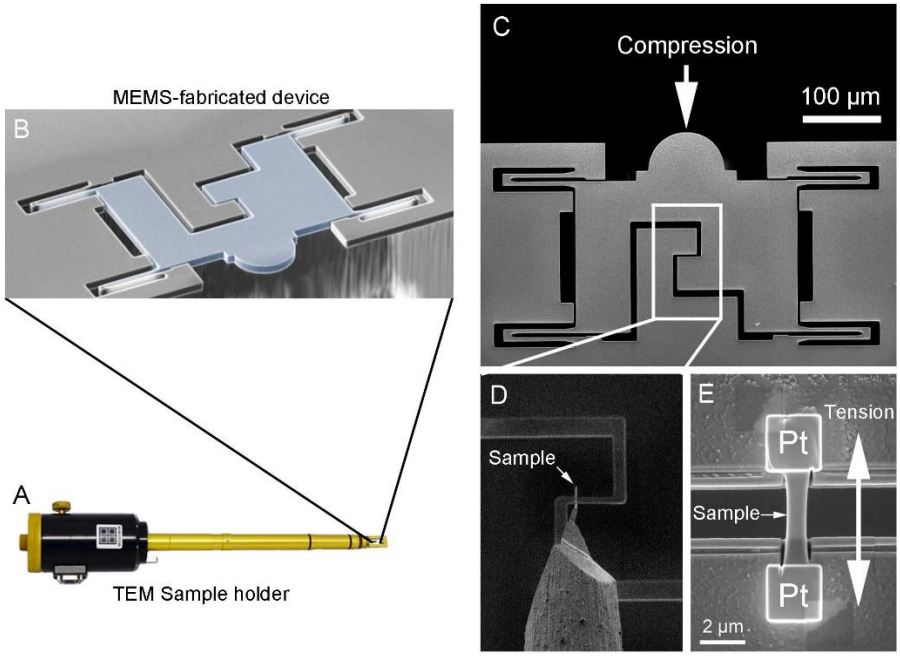

Figure 3.3.10. Push-to-Pull (PTP) device: **(a)** TEM Sample holder. **(b)** MEMS-fabricated PTP device. **(c)** Optical image of the PTP device used for in situ TEM tensile experiments. The compression of the semicircular end in **(c)** induces uniaxial tension in the middle gap shown in **(d)** and **(e)**. **(d, e)** SEM images showing the transfer of an FIB-prepared olivine sample onto the PTP device and the mounting of the sample in the middle gap using electron beam–deposited platinum (Pt), respectively

Chapter 4

Dislocation Glide in Minerals

4.1. Olivine

It is well accepted that the slip systems in olivine involve two different types of dislocations, with either [100] or [001] Burger vector, corresponding to the shortest lattice repeats of the *Pbnm* orthorhombic structure (see section 2.2.1). Depending on the temperature range, pressure or strain rate conditions set in experiments, different slip systems have been reported. Therefore, within the course of the RheoMan project, we decided to investigate the ground state properties of dislocations with [100] and [001] Burgers vectors in Mg_2SiO_4 forsterite. To provide unbiased constraints of the slip planes, we focus our atomic-scale calculations on the properties of the screw dislocation characters, keeping in mind that the spreading of a screw dislocation core may reflect the primary slip plane of a gliding dislocation loop. A particular attention has been given to the choice of the force field used to model forsterite. Indeed, in order to account for polarisation effects in Mg_2SiO_4, we have chosen to rely on the so-called THB1 potential (Price & Parker 1987) parameterised with the inclusion of a core–shell (C/S) assumption.

4.1.1. [001] dislocations in forsterite

According to our simulations, [001] screw dislocations are characterised by compact cores located between four SiO_4 tetrahedra with a dislocation line centred on a Mg cation site (Fig. 4.1.1). The structure of the [001] stable core does not show any particular evidence of spreading in any preferential plane. In (010), (100) or {110}, the core extension remains below few Ångströms which allows preserving the shape of the SiO_4 tetrahedra (*i.e.* the presence of the strong Si-O bonds intrinsically limits any spreading of the dislocation core).

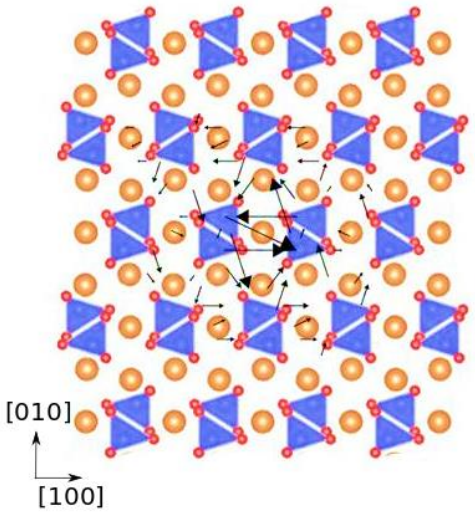

Figure 4.1.1. [001] screw dislocation core in forsterite. The atomic configuration is viewed along the dislocation line. The solid arrows display the differential displacement along the Burgers vector direction between the pairs of neighboured atoms

At ambient pressure, we further investigated the lattice friction opposed to the glide of this compact core in (010), (100) or {110}. Regardless of the glide plane, the Peierls stress of [001] dislocation is significantly high with values between 6 to 8 GPa. The glide in (100), (010), or {110} may be activated at comparable stress levels. However, more importantly, by analysing the glide of the dislocation submitted to a resolved stress comparable to its Peierls stress, we discovered the occurrence of several planar core configurations corresponding to high energy transient states of the dislocation core. Such an occurrence of transient states is important as it suggests that the dislocation motion should be achieved through a specific locking–unlocking mechanism (Couret & Caillard 1989).

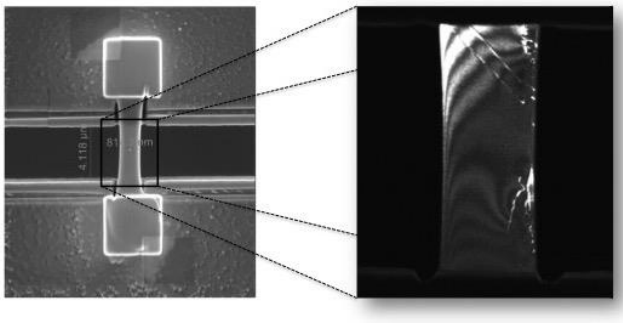

Figure 4.1.2. View of the experiment: a thin strip of olivine single crystal oriented for [001] slip in (011) is fixed in the push-to-pull with platinum. Right: the orientation of the foil has been chosen so as to allow good visualization of the dislocations by weak-beam dark field (see details in Idrissi *et al.* 2016)

Although, the investigation of the thermal activation of a locking-unlocking mechanism was out of the scope of the numerical dislocation modeling in forsterite, the use of micro-mechanical testing apparatus coupled with TEM that allows determining the velocity of this [001] dislocation experimentally. These experiments have been performed with the picoindenter equipped with a push-to-pull described in section 3.3.3.

This experiment takes an advantage of the small size of the samples (*ca.* 4×1×0.2 μm^3) which guarantees that the sample contains no defects larger than a few tens of nm. By application of Griffth's law, this raises the fracture stress to levels high enough that olivine remains in the ductile field, even at room temperature. In the experiment, we deliberately introduced sources from which dislocation loops could expand and cross the sample. Experiments were run at constant load, increased step by step so that the velocity of screw dislocations could be measured as a function of stress. The results are presented in Fig. 4.1.3.

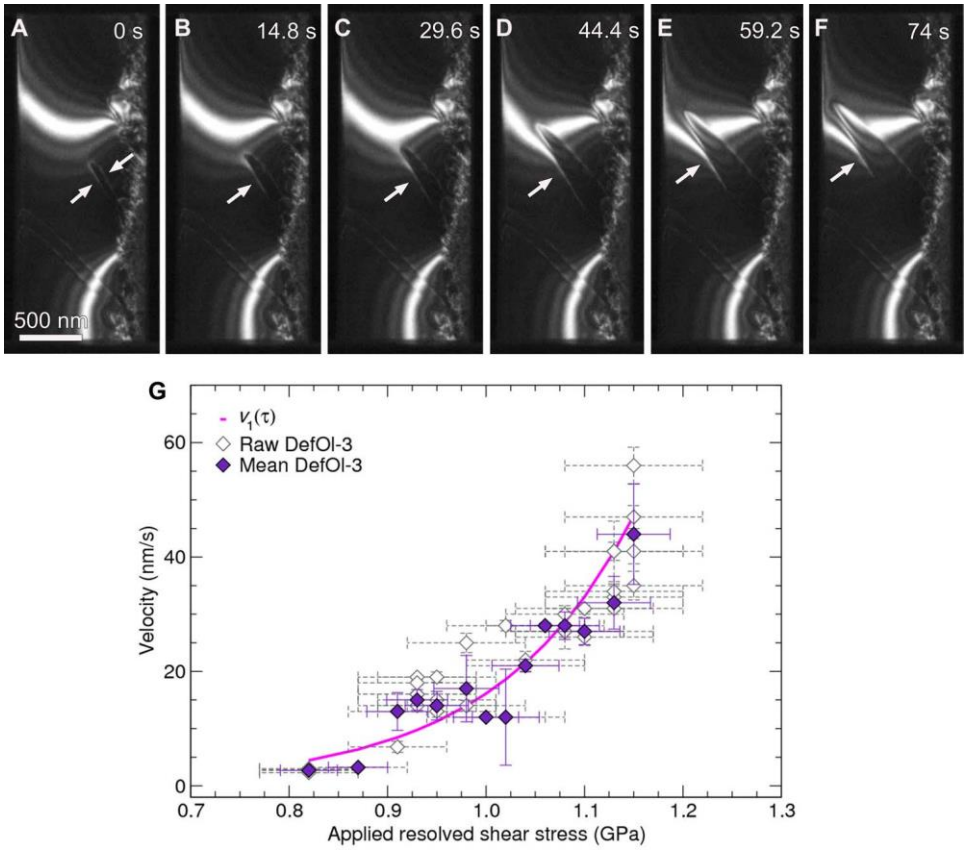

Figure 4.1.3. The sequence **A** to **F** illustrates successive steps of a dislocations gliding across the sample under an applied resolved shear stress of 0.89 GPa. **G** summarises the results giving the stress dependence of the velocity of [001] screw dislocations in (011)

4.1.2. [100] dislocations in forsterite

Contrary to [001] dislocations, the core of the [100] screw dislocation exhibits a clear tendency for spreading in (010). At ambient pressure, the spreading is so large that the [100] dislocation dissociates into a set of two collinear partials dislocations (Fig. 4.1.4). Such a dissociated state is consistent with the experimental evidence of [100](010) slip system in olivine at high temperature (*e.g.* Durham *et al.* 1977). However, as initially proposed by Durinck and co-workers (2005, 2007), based on the evolution of the γ-surface energies as a function of pressure, this [100] dislocation core is strongly sensitive to pressure. Taking advantage of the atomic scale modelling, we showed that the dissociation of [100] dislocations in (010) is associated with a dilatation state of the dislocation core. Therefore, the effect of pressure works against this dilatation state, leading to an intrinsic hardening of the glide properties of [100](010).

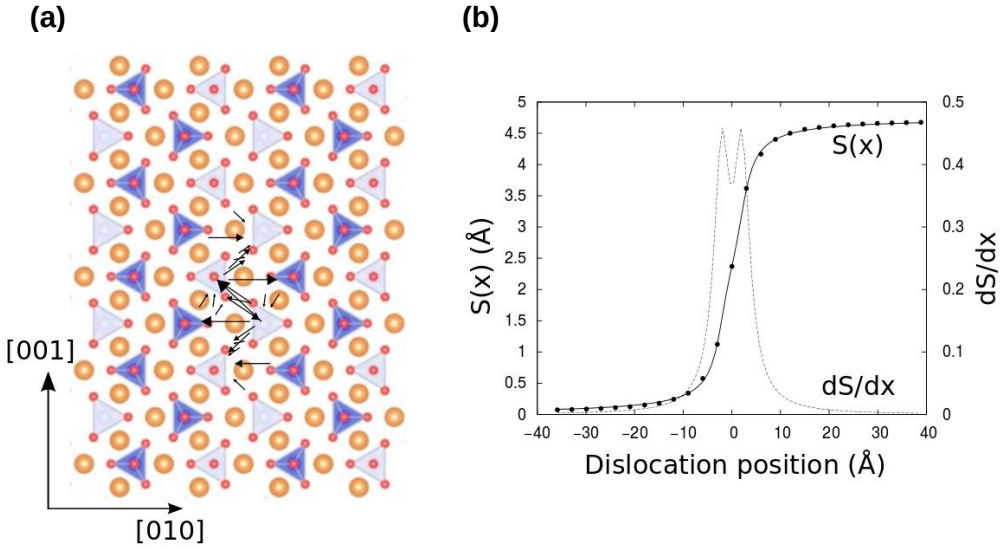

Figure. 4.1.4. [100] dislocation core structure in forsterite at ambient pressure. **(a)** Differential displacement maps of the screw core. The large density of arrows in the vicinity of (010) plane highlights the planar core configuration. **(b)** The corresponding disregistry function computed from the atomic displacement recorded after energy minimisation of the stable dislocation core configuration. The occurrence of two peaks in the density of Burgers vector reveals the collinear planar dissociation

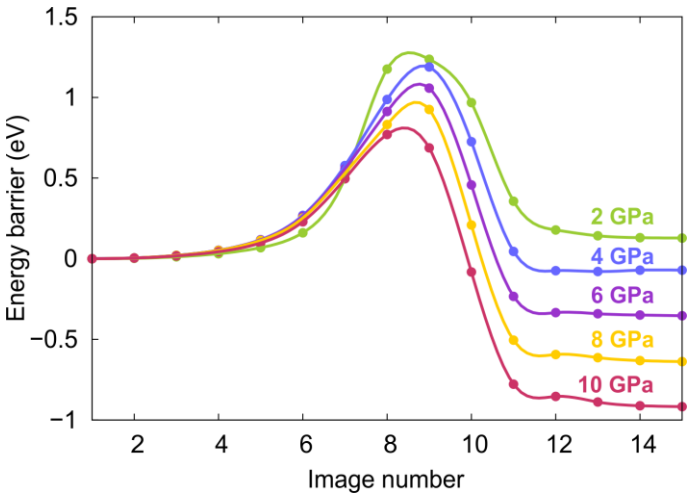

Figure 4.1.5. NEB calculations of the energy barrier associated with the cross slipping of [100] screw dislocation from an initial configuration in (010) (image 1) to a final state in {021} (image 15). One may note that above 4 GPa of hydrostatic pressure the core configuration spread in {021} corresponds to the stable core configuration which glides in {011}

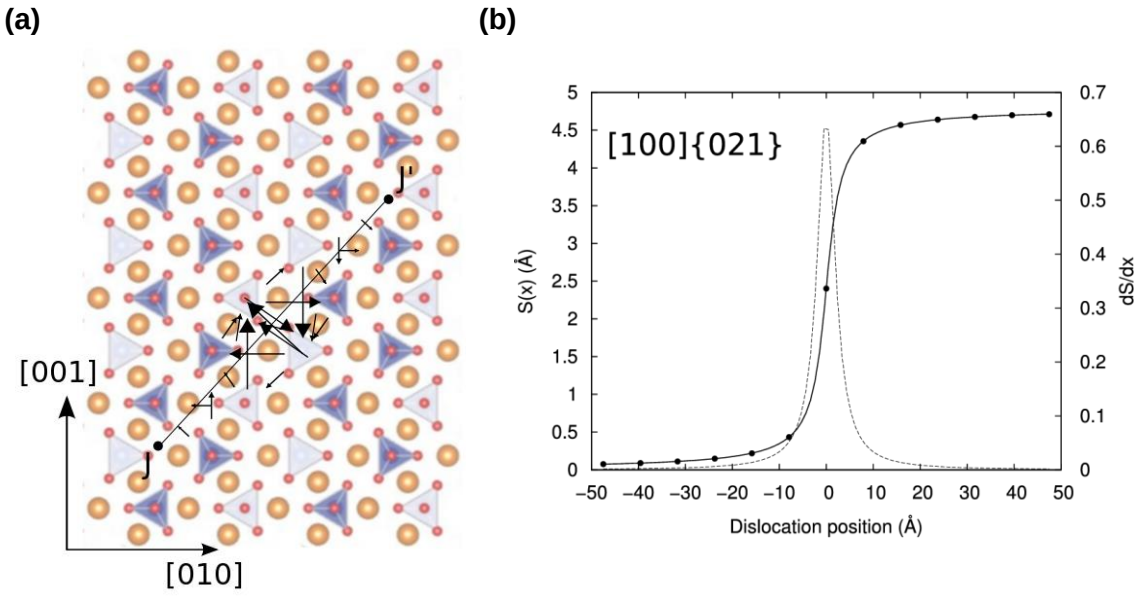

Figure. 4.1.6. [100]{021} dislocation core structure in forsterite. **(a)** Differential displacement maps of the screw core. The large density of arrows in {021} plane highlights the core spreading in this plane . **(b)** The corresponding disregistry function computed from the atomic displacements along {021} produced by the screw dislocation

Indeed, as the pressure is increased up to 10 GPa, we find that the Peierls stress of [100](010) dislocation increases from 3 GPa to a few tens of GPa. In the meantime, the ability for [100] dislocation to cross slip in a different plane is enhanced by the increase of hydrostatic pressure. As shown in Figure 4.1.5, we performed NEB calculations to compute the cross slip energy barrier between (010) and {021} planes. As expected, the pressure hardening of [100](010) is very prominent and it even leads to a change of primary slip plane of [100] dislocations. We find that above the confining pressure of 4 GPa, the core spreading changes to {021}. This dislocation core is illustrated in Figure 4.1.6 and corresponds to the last dislocation core image in Figure 4.1.5. The high pressure [100] screw dislocations glide preferentially in {011} plane (*i.e.* not in the plane where the core tends to spread), following a complex path that involves a combination of displacements in {001} and {021}, leading to the primary slip system [100]{011}.

References

A. Couret & D. Caillard (1989) Philos. Mag. A 59: 783
W.B. Durham *et al.* (1977) J. Geophys. Res. 82: 5755
J. Durinck *et al.* (2005) Phys. Chem. Minerals 32: 646
J. Durinck *et al.* (2007) Eur. J. Mineral. 19: 631
H. Idrissi *et al.* (2016) Sci. Adv. 2: e1501671
G.D. Price & S.C. Parker (1987) Miner. Mag. 51: 157

4.2. Wadsleyite and ringwoodite

For the high-pressure polymorphs of olivine, namely Mg_2SiO_4 wadsleyite and ringwoodite, the dislocations and slip systems properties have been modelled using the semi-continuum Peierls–Nabarro–Galerkin (PNG) method, a generalization of the Peierls–Nabarro (PN) model (section 3.1.2). Generalized stacking fault energies were computed at pressures corresponding to the transition zone conditions using either *ab initio* methods or empirical potentials. Once a dislocation core structure is determined, the Peierls potential is calculated by summing the misfit and elastic strain energy between the pairs of crystal plains, normal to the glide plane, by moving the dislocation structure rigidly through the crystal. Lastly, the thermally-activated glide mobility resulting from nucleation and propagation of kink-pairs was computed based on the elastic interaction (EI) model (*e.g.* Koizumi *et al.* 1993, 1994) . It is worth noticing that modeling kink pairs nucleation for dissociated dislocation cores, like in ringwoodite and wadsleyite, required some additional mathematical development for the EI model. The extra developments of the EI method have been validated with respect to the mechanical properties of $SrTiO_3$ perovskite (Ritterbex *et al.* 2018).

4.2.1. Dislocation glide in wadsleyite

Modeling dislocation glide and lattice friction in Mg_2SiO_4 wadsleyite have been carried out for two potentially important slip system of the structure: ½⟨111⟩{101} and [100](010) (Thurel & Cordier 2003). Following an earlier work of Metsue *et al.* (2010), the core structure of dislocation have been derived from the corresponding generalized stacking fault energies calculated using classical molecular statics approach at confining pressure of 15 GPa. For the two investigated slip systems, the dislocation cores are found to be dissociated.

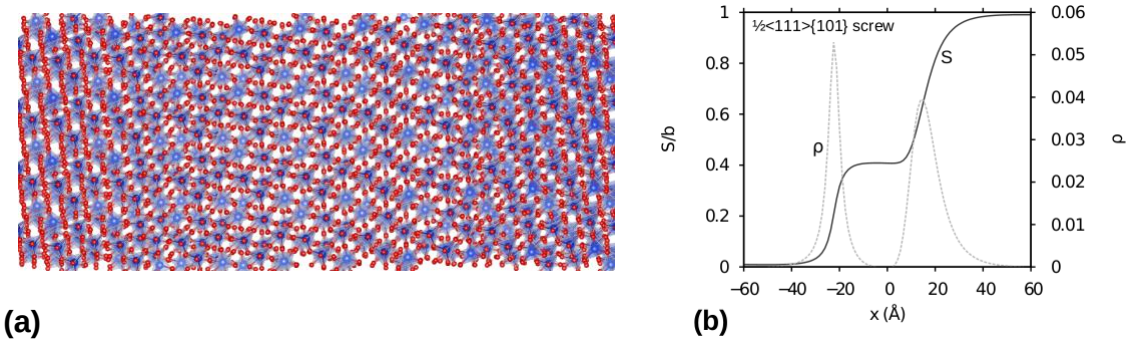

Figure 4.2.1. **(a)** ½⟨111⟩{101} screw dislocation core structure viewed in {101} plane and **(b)** the associated disregistry function computed across {101}

The dissociation scheme for ½⟨111⟩{101} is interesting as the dislocation splits according to the following reaction $^1/_5\langle 111\rangle + {}^3/_{10}\langle 111\rangle$ with a fairly large stacking fault region of 36 Å width (Fig. 4.2.1). Such a significant core extension is in a good agreement with the weak-beam dark-field TEM observations of partial dislocations for the ½⟨111⟩{101} slip system in wadsleyite (Thurel & Cordier 2003).

By computing the Peierls potentials that dislocations have to overcome in order to glide, we show that the lattice friction is always larger for the screw characters. The calculated Peierls stresses are 3.5 GPa and 4.8 GPa for ½⟨111⟩{101} and [100](010), respectively. To

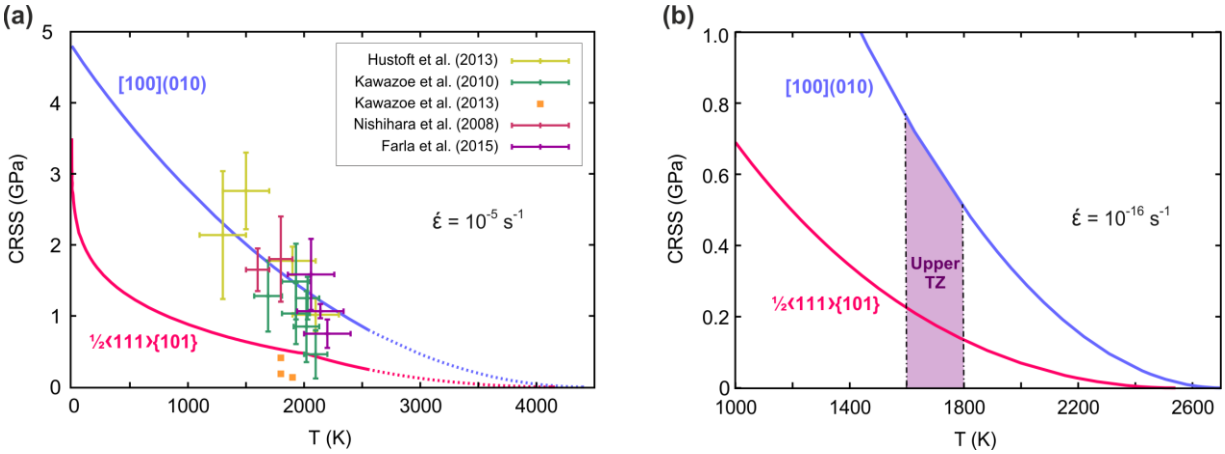

Figure 4.2.2. CRSS computed in wadsleyite for the two different strain rates: **(a)** 10^{-5} s^{-1} for laboratory conditions and **(b)** 10^{-16} s^{-1} as a strain rate in transition zone (TZ)

compare our results with the mechanical data available from high *P-T* experiments (Fig. 4.2.2a), we calculated the critical resolved shear stress over a broad range of temperatures for a typical laboratory strain rate of 10^{-5} s^{-1}. The good quantitative agreement between the strengths measured experimentally and computed numerically suggests that intracrystalline plasticity of wadsleyite under laboratory conditions is mainly governed by the mobility of the rate controlling slip systems.

Moreover, our methodology allows calculating the evolution of CRSS as a function of temperature for typical mantle strain rates (with no extrapolation). From the CRSS plot (Fig. 4.2.2b), one can see that the plastic deformation of wadsleyite under mantle conditions still occurs in a regime where the critical stress is temperature dependent implying that plastic deformation of this phase in the transition zone is controlled by the average mobility of the rate governing screw dislocations.

4.2.2. Dislocation glide in ringwoodite

For ringwoodite, all calculations have been performed at 20 GPa. In particular, γ-surfaces calculations were performed using *ab initio* methods that allow to accurately address the effect of pressure on the atomic bonding. The computed γ-surface energy landscapes for {001}, {110} and {111} are depicted in Figure 4.2.3.

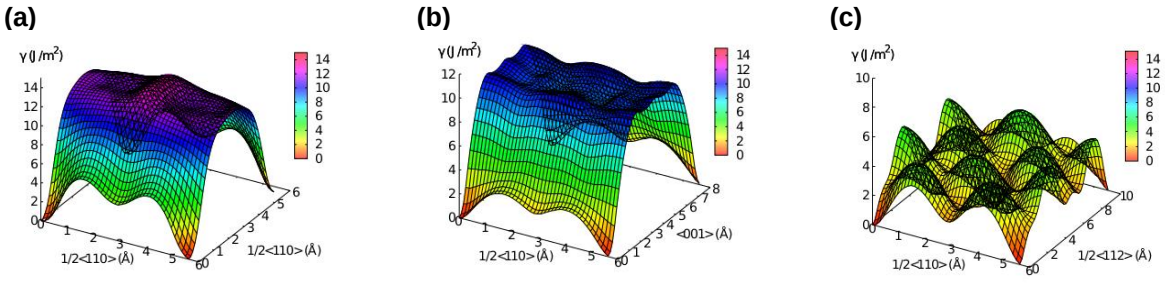

Figure 4.2.3. γ-surfaces computed for **(a)** {001}, **(b)** {110} and **(c)** {111} planes in Mg_2SiO_4 ringwoodite

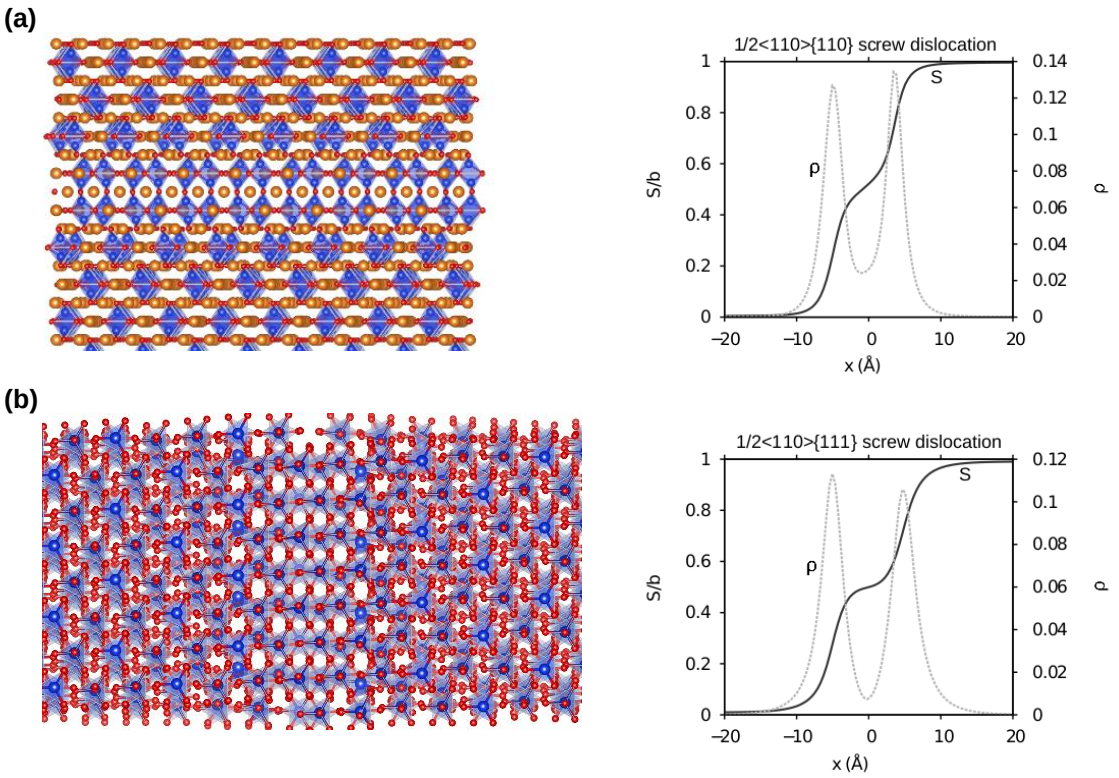

Figure 4.2.4. **(a)** ½⟨110⟩{110} and **(b)** ½⟨110⟩{111} screw dislocation core structures in ringwoodite and the associated disregistry functions. Both slip systems involve dissociated dislocation cores

Regardless of the slip planes, the lowest energy paths are always found along the ⟨110⟩ direction, with a clear metastable configuration at ¼⟨110⟩. Energy landscapes in {110} and {111} along ⟨110⟩ are found to be comparable, therefore, we have modelled dislocations for the two following slip systems ½⟨110⟩{110} and ½⟨110⟩{111}. In both slip planes, the dislocation is dissociated into a set of two collinear partial dislocations. The computed Peierls stresses are systematically close to 10 GPa (*i.e.* $\sigma_P/\mu \sim 10^{-2}$) reflecting the high lattice friction of this minerals.

As in wadsleyite, the mobility of ½⟨110⟩ screw dislocation gliding in {110} and {111} slip planes accounts for most of the plastic strain produced during deformation, hence, we focus on the evolution of the critical resolved shear stress for this screw components. For the typical laboratory strain rate conditions (Fig. 4.2.5a), we demonstrate that our model matches the experimental strength found for ringwoodite with flow stresses evolving from 5 GPa at 300 K down to a few GPa at 1700 K. However, the strain rate sensitivity of glide mechanism in ringwoodite lowers the intrinsic strength of ringwoodite below a few hundreds of MPa in condition of mantle transition zone deformation strain rate as shown in Figure 4.2.5b.

For the two Mg_2SiO_4 polymorphs, the relatively high values (around a few hundreds of MPa) of the critical shear stress that account for the pure single slip dislocation glide suggest that other mechanisms may control the deformation of these two minerals in the Earth's transition zone. In fact, the transition zone is characterized by several phase transformations, which may give a rise to transformation plasticity, sometimes referred as transformational superplasticity. Such phase transformations, often associated with a grain size reduction, or water related weakening processes, may enhance diffusion mechanisms and activate climb-controlled diffusion-based intracrystalline deformation.

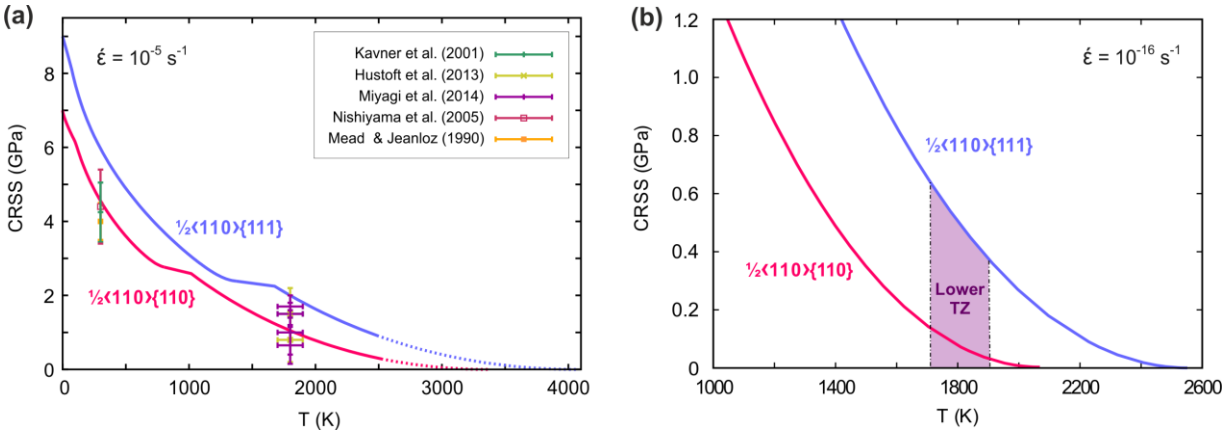

Figure 4.2.5. CRSS computed for ½⟨110⟩ dislocations in ringwoodite as a function of temperature for the two different strain rates: **(a)** 10^{-5} s^{-1} for laboratory conditions and **(b)** 10^{-16} s^{-1} as a strain rate expected in the transition zone (TZ)

References

R. Farla *et al.* (2015) Phys. Chem. Miner. 42: 541
J. Hustoft *et al.* (2013) Earth Planet. Sci. Lett. 361: 7
A. Kavner et al. (2001) Geophys. Res. Lett. 28: 2691
T. Kawazoe *et al.* (2010) J. Geophys. Res. 115: B08208.
T. Kawazoe *et al.* (2013) Phys. Earth Planet. Int. 216: 91
H. Koizumi *et al.* (1993) Acta Metall Mater. 41: 3483
H. Koizumi *et al.* (1994) Philos. Mag. 69: 805
C. Meade & R. Jeanloz (1990) Nature 348: 533
A. Metsue *et al.* (2010) Acta Mater. 58: 1467
L. Miyagi *et al.* (2014) Phys. Earth Planet. Int. 228: 244
Y. Nishihara *et al.* (2008) Phys. Earth Planet. Int. 170: 156
N. Nishiyama *et al.* (2005) Geophys. Res. Lett. 32: L04307
E. Thurel & P. Cordier (2003) Phys. Chem. Miner. 30: 256
S. Ritterbex *et al.* (2018) Philos. Mag. 98: 1397
S. Ritterbex *et al.* (2016) Am. Mineral. 101: 2085
S. Ritterbex *et al.* (2015) Phys. Earth Planet. Int. 248: 20

4.3. Bridgmanite

Bridgmanite $(Mg,Al)(Si,Fe,Al)O_3$ with the perovskite structure is the most abundant phase of Earth's lower mantle (700 - 2900 km). As such, the identification and characterization of elementary mechanisms associated with its plastic flow is of paramount importance, ultimately including dislocations, vacancies, grain boundaries, and the effects of foreign elements (Fe, Al).

To reduce the compositional complexity of this phase, we performed our simulations on the pure magnesium silicate end-member of bridgmanite, *i.e.* $MgSiO_3$ with the perovskite structure. This composition is well described by rigid-ion models, such as the one proposed by Oganov *et al.* (2000), or the one by Alfredsson *et al.* (2005), in the whole range of pressures 26-140 GPa, relevant for the lower mantle conditions.

4.3.1. Dislocation cores and lattice friction

In a first approach, we relied on results obtained in analogue materials, such as $SrTiO_3$ or $KNbO_3$. In those perovskites, the easiest slip system is of the type ⟨110⟩{110}, and these dislocations allow for a significant plastic flow event at low temperature (Brunner *et al.* 2001, Sigle *et al.* 2006, Hirel *et al.* 2012, Hirel *et al.* 2015, Ritterbex *et al.* 2018). By analogy, we proceeded with the study of the equivalent slip systems in bridgmanite.

Because of its orthorhombic lattice, bridgmanite is indexed differently than cubic perovskites. As a result, the easiest slip systems are indexed [100](010) and [010](100) (see Fig. 2.2.4).

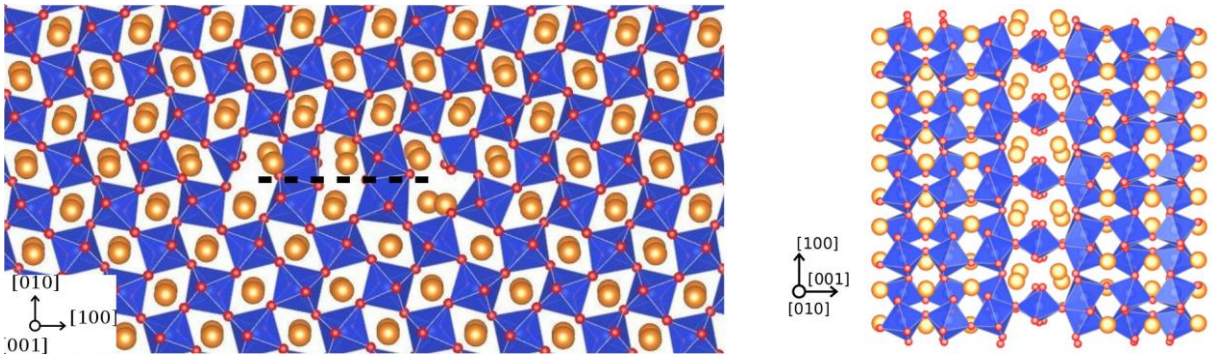

Figure 4.3.1. Atomic structure of the [100](010) dislocation with a pure edge (left) and pure screw (right) character. The dashed line shows the extent of the stacking fault. In both cases the dislocation core is very narrow

The atomic structure of the [100](010) dislocation in $MgSiO_3$ bridgmanite computed at 30 GPa is shown in Fig. 4.3.1. This dislocation has a very narrow core structure, and does not spread much in its glide plane. The modeling of [010](100) dislocations yield similar results. When increasing the pressure up to 130 GPa, these dislocations keep their core structure. These narrow core structures are strikingly different from what is observed in $SrTiO_3$ perovskite, where such dislocations dissociate with a very wide spreading in their glide plane. The elastic theory of dislocation predicts that the narrower the dislocation, the more difficult its motion. The observation of very compact cores in $MgSiO_3$ is a first hint that glide may be more difficult in this material than in other known perovskites.

The lattice friction opposed to the motion of [100] and [010] dislocations was evaluated using two methods. The first method consists in applying a shear strain to the simulation

cell, and monitor the stress necessary for the dislocation to move (see section 3.1.4). In the second method, we used the nudged elastic band (NEB) approach (section 3.1.5) to quantify the Peierls energy barrier associated with the motion of the dislocation from one equilibrium motion to the next, in the absence of any applied deviatoric stress. Then, the Peierls stress was determined from the maximum slope of this energy barrier. Both methods yielded very similar results.

The Peierls stresses obtained for the [100](010) and [010](100) slip systems are reported in Fig. 4.3.2. As expected, dislocations of edge characters move under lower applied stress than their screw counterparts, meaning that glide is limited by the mobility of screw segments. As pressure increases, the Peierls stress for screw dislocations go from 5 GPa at the pressure of 30 GPa, up to 15-18 GPa under the pressure of 140 GPa.

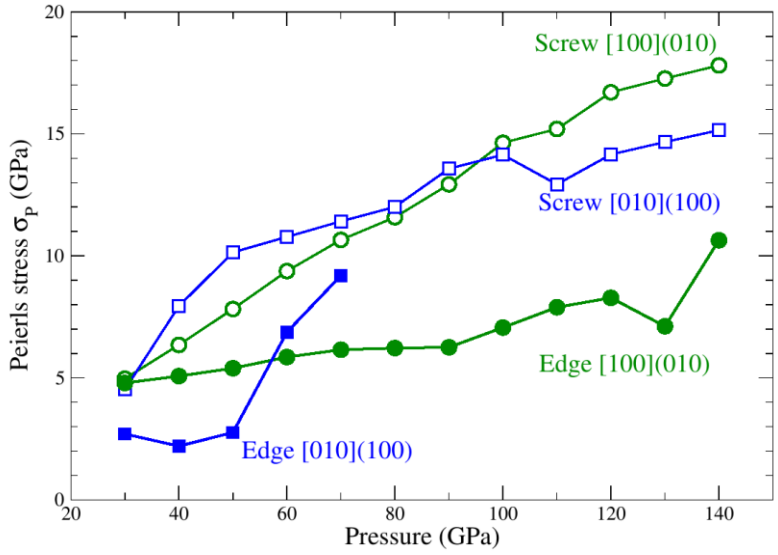

Figure 4.3.2. Evolution of the Peierls stress σ_p with pressure for the motion of [100](010) (in green) and [010](100) (in blue) dislocations. Results for edge characters are represented with filled symbols, those for screw characters with open symbols

The [010](100) edge dislocations exhibit an interesting non-conventional behaviour. This system shares similar features with the [100](010) edge dislocation at low pressure, while a major change of the core structure occurs at *ca.* 80 GPa: the new core spreads in its climb plane (for more details about dislocation climb in bridgmanite, see section 5.2.1). This new core structure is sessile, *i.e.* unable to move by glide, hence no value for the Peierls stress can be reported above this pressure.

4.3.2. Thermally activated dislocation glide

While the Peierls stress is an indicator of the lattice friction, its value corresponds to a theoretical situation where the dislocation moves rigidly and without the assistance of thermal vibrations. At higher temperatures, dislocations are expected to move by different mechanisms (*e.g.* by the formation of kink pairs along the dislocation line), which are thermally activated.

Therefore, in order to evaluate the flow stress associated with dislocation motion as a function of temperature, we developed a model describing the motion of dislocations via the formation of kink-pairs (Kraych *et al.* 2016). As a first step, the formation enthalpy of individual kinks was computed for various applied shear stresses, at the pressures 30 and 60 GPa, for both the [100](010) and [010](100) screw dislocations. Then, these enthalpies were used as input parameters for a model based on the Orowan equation for

dislocation motion. Ultimately, this model predicts the critical flow stress as function of temperature, assuming a given strain rate and dislocation density.

The outcome of this model for bridgmanite at 60 GPa is represented on the right side of Figure 4.3.3. A strain rate 10^{-16} s^{-1}, typical of the Earth's lower mantle, was used, and the dislocation density was set to 10^{8} m^{-2}. For both slip systems, the critical shear stress remains extremely high, greater than 1 GPa, even at the very high temperatures of the lower mantle (1500 - 2500 K). These values are to be compared with stress levels expected in the mantle, of the order of a few 10 MPa.

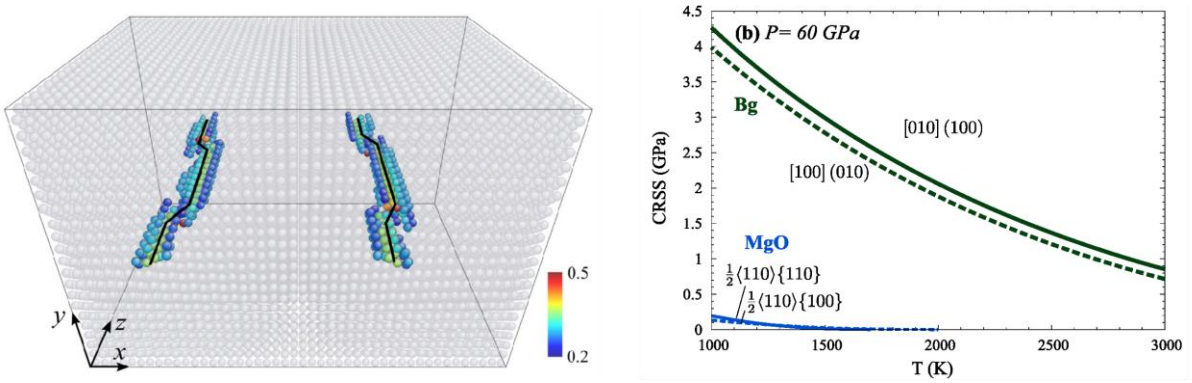

Figure 4.3.3. Left: simulation box used to investigate the formation of kink pairs along dislocation lines in $MgSiO_3$ bridgmanite. Dislocation lines are overlined with thick black lines. Right: the temperature dependence of the flow stress predicted by our model, using a strain rate 10^{-16} s^{-1} and a dislocation density 10^{8} m^{-2}. The results for the two slip systems of bridgmanite (Bg, dark green lines) are compared to those of periclase MgO (blue line)

In summary, dislocations in bridgmanite are characterized by very narrow core structures and very high lattice friction, the latter increasing greatly with pressure. As a result, dislocation glide is extremely difficult, and can be ruled out as a dominant mechanism to explain creep in the extreme conditions of the lower mantle. Other mechanisms, involving vacancy diffusion and dislocation climb, have to be considered. These aspects will be further discussed in section 5.2.

References

M. Alfredsson *et al.* (2005) Phys. Chem. Miner. 31: 671
D. Brunner *et al.* (2001) J. Am. Ceram. Soc. 84: 1161
P. Hirel *et al.* (2012) Acta Mater. 60: 329
P. Hirel *et al.* (2015) Phys. Rev. B 92: 214101
A. Kraych *et al.* (2016) Earth Plan. Science Lett. 452: 60
A. Oganov *et al.* (2000) Phys. Earth and Plan. Int. 122: 277
S. Ritterbex *et al.* (2018) Philos. Mag. 98: 1397
W. Sigle *et al.* (2006) Philos. Mag. 86: 4809

4.4. Post-perovskite

Based on the full atomistic modeling approach, we investigated the structures of [100], [001] and ½⟨110⟩ dislocation cores in $MgSiO_3$ post-perovskite (ppv) at 120 GPa, similarly to the approach used for $MgSiO_4$ olivine (section 4.1) and $MgSiO_3$ bridgmanite (section 4.3). Dislocation cores in $MgSiO_3$ ppv were modelled using the Buckingham form of the pairwise potential originally derived by Oganov *et al.* (2000) for $MgSiO_3$ bridgmanite. This potential was demonstrated to be transferable also for modeling defects in the high-pressure ppv phase (for more details, see Goryaeva *et al.* 2015). The ppv structure is characterized by a very short [100] lattice repeat of 2.5 Å (section 2.2.5), which allowed us modeling [100] screw dislocation cores relying both on the pairwise potential and *ab initio* approaches (DFT within GGA approximation). Atomic scale calculations of {110} deformation twinning were also performed based on the DFT theory.

4.4.1. Dislocation cores and lattice friction

Burgers vector [100]

Screw dislocations with [100] Burgers vector exhibit compact planar cores centred between two neighbouring Mg atoms and spread in the (011) or (0$\bar{1}$1) plane, dependently on location of the dislocation line along [001] (Fig. 4.4.1c). The dislocation core spreading is characterized by a half-width ζ of ~1.9 Å and limited by the Si-layers (Fig. 4.4.1a,b). In the (010) plane, the stable core configurations (I) and (II) are distant by a'=½[001] (Fig. 4.4.1c). This distance describes periodicity of the Peierls potential (Fig. 3.1.10) in this plane.

All the [100] edge dislocations lying on (010), (011) and (001) planes are found to have compact symmetric cores with a half width ζ close to 2b ~5 Å. The atomic structure of [100](001) edge dislocation core is illustrated in Figure 4.4.2.

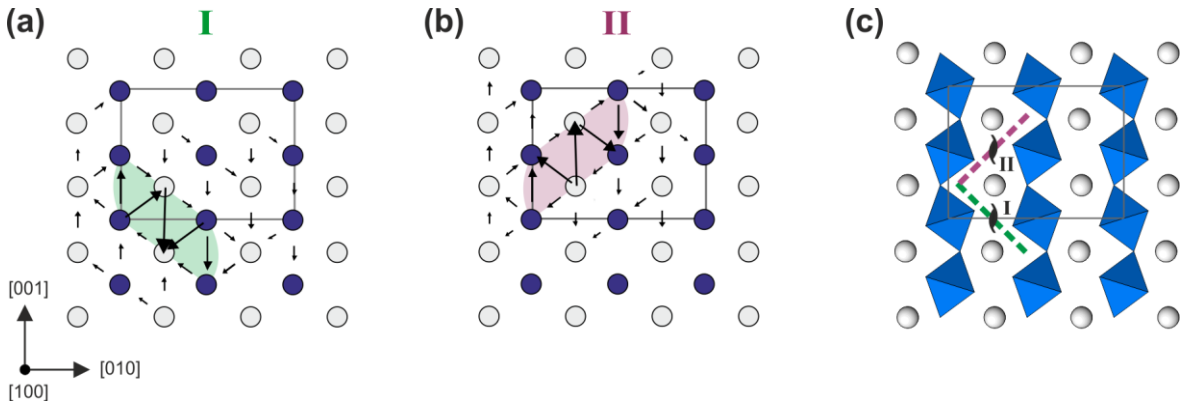

Figure 4.4.1. (a, b) DD maps of [100] screw dislocations viewed along the Burgers vector direction. The anion sublattice is left out. Si atoms are shown with blue balls, Mg atoms – with grey balls; the unit cell – with red rectangle. The arrows between atoms correspond to the [100] component of the relative displacement of the neighbouring atoms produced by the dislocation. The length of the arrows is proportional to the magnitude of these components. **(c)** Location of the dislocation lines (I) and (II) and the corresponding core spreading in the crystal structure

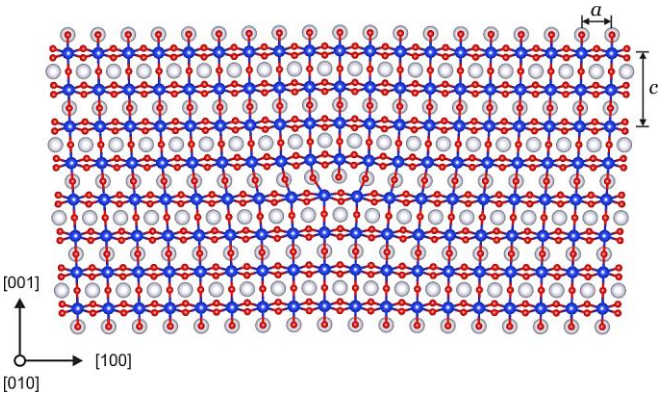

Figure 4.4.2. Atomic structure of the relaxed [100](001) edge dislocation core in $MgSiO_3$ ppv. Si atoms are shown with blue balls, Mg – with white, and O – with red. Unit cell parameters *a* and *c* are indicated with arrows

Lattice friction opposed to the glide of [100] dislocations is found to be highly anisotropic. Mobility of [100] edge dislocations is generally much higher than that of screw dislocations (more than an order of magnitude of difference in the Peierls stress), regardless of the glide plane (Table 4.4.1). Therefore, screw dislocations will account for most of the plastic strain produced during deformation. At the same time, glide of [100] screw dislocations through the post-perovskite structure is characterized by significantly different Peierls stress while moving in (010) within MgO layer or across the rigid SiO_2 layers. According to the results of the performed atomic scale modeling, lattice friction opposed to the glide of [100] screw dislocations in (010) is one order of magnitude lower than that in (001). This behaviour clearly results from the anisotropic crystal chemistry due to the difference in the Mg-O and Si-O bond strength.

Burgers vector [001]

Atomistic modeling of [001] screw and edge dislocations indicates their dissociation in the (010) plane into two symmetric partials separated by a stacking fault.

In case of the screw dislocations (Figs. 4.4.3; 4.4.4), distance *R* between the two partials is 10.8 Å, which is close to 4*a* unit cell parameters. The [001](010) edge dislocation cores are found to be much more spread than the screw ones (the distance *R* is 41.6 Å, which is close to 7*c* unit cell parameters).

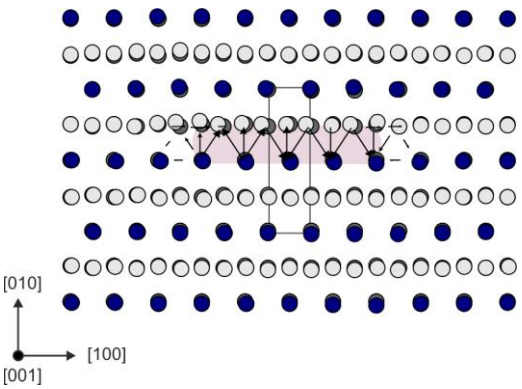

Figure 4.4.3. DD-map of [001] screw dislocation core. The anion sublattice is left out; Si atoms are shown with blue balls; Mg atoms – with light grey balls. Atomic positions in a perfect crystal are displayed in dark grey. The lengths of arrows are proportional to the magnitude of atomic displacements along [001]

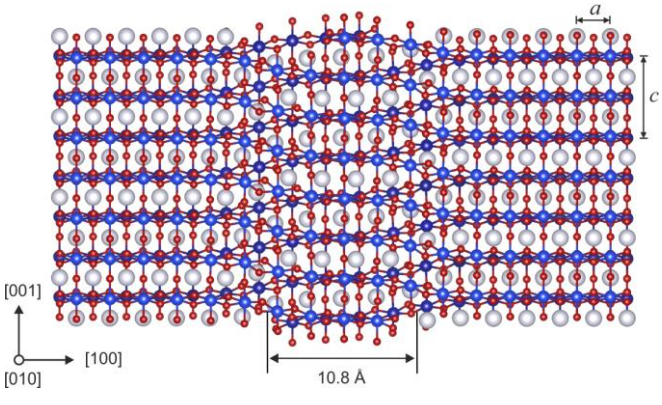

Figure. 4.4.4. Atomic structure of the stable [001] screw dislocation core viewed in the (010) plane (which is highlighted with colour in Fig. 4.4.3). Si atoms are shown with blue balls, Mg – with white, and O – with red. The distance *R* between the two partials and the unit cell parameters *a* and *c* are indicated with arrows

Being dissociated in the (010) plane, [001] dislocations can glide in this plane only. In contrast to the [100] dislocations, the difference in Peierls stress between screw and edge [001] dislocations is not so big (Table 4.4.1). Lattice friction opposed to the glide of [001] screw dislocations is 3 GPa, while that of edge dislocations is 33% lower (Table 4.4.1). Therefore, plastic deformation within the [001](010) slip system will be governed by the screw dislocations.

Burgers vector ½[110]

Atomistic calculations of screw and edge dislocations with ½[110] Burgers vector indicate their strong tendency to spread in the $(0\bar{1}1)$ plane. Indeed, regardless of the dislocation character, a full ½[110] Burgers vector spontaneously dissociates in {110} into two partial dislocations bounding a stacking fault with the typical perovskite-like octahedral interconnections by corners (Fig. 4.4.5b). The burgers vector density $\rho(x)$ indicates that the two partial dislocations are asymmetric with b_p = ⅙[110] and ⅓[110] and the stacking fault width reaches the order of a few nanometres (Fig. 4.4.5a). Under applied stress, screw and edge dislocations exhibit very similar behaviour. Thus, for an edge dislocation core (Fig. 4.4.5) we find that a shear stress in the range of 2.5 - 2.8 GPa triggers the expansion or the closure of the stacking fault, but this process is due to the sole displacement of the ⅙[110] partial dislocation. The onset of motion of the ⅙[110] partial is fairly insensitive to the initial stacking fault width or the investigated atomic system size. The ⅓[110] partial dislocation never glides as a partial dislocation. The full dislocation first recombines into the compact ½[110] Burgers vector dislocation core (requiring an applied stress of 6.5 GPa for the 57 Å core depicted in Figure 4.4.5) before it can actually further glide at an applied stress of 19 GPa.

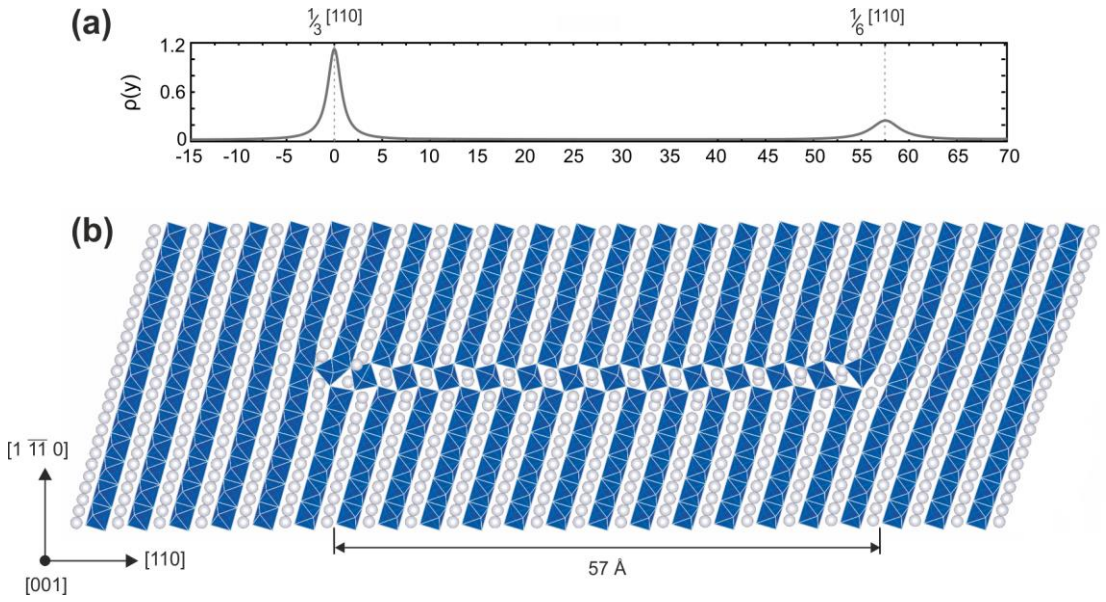

Figure 4.4.5. ½[110](110) edge dislocation core in $MgSiO_3$ ppv. **(a)** Burgers vector density computed from the differential displacement of atoms in the dislocation core region. **(b)** Atomic structure of the edge dislocation core with a perovskite-like stacking fault bounded by two partial dislocations of ⅙[110] and ⅓[110] Burgers vectors

Thus, it appears that for the ½⟨110⟩{110} slip system, the only dislocation that is mobile is the ⅙[110] partial, which expands a stacking fault in its wake. Activation of partial dislocation is a deformation mechanism, known to occur in some materials like Si (Castaing *et al.* 1981) and SiC (Pirouz & Yang 1993), but that may also lead to another mechanism: mechanical twinning, which is described in the next section.

References

J. Castaing *et al.* (1981) Phil. Mag. A 44:1407
A. Goryaeva *et al.* (2015) Phys. Chem. Miner. 42: 781
A. Oganov *et al.* (2000) Phys. Earth. Planet. Inter. 122: 277
J. Perdew & Y. Wang (1992) Phys. Rev. B 45: 13244
P. Pirouz & J. Yang (1993) Ultramicroscopy 51: 189

4.4.2. ⟨110⟩{110} deformation twinning

Dislocation glide and deformation twinning are complementary mechanisms that contribute to plastic deformation. Therefore the occurrence of the highly mobile ⅙[110] partial dislocation in $MgSiO_3$ ppv (see the previous section) raises the possibility of a mechanical twinning mechanism associated with the ½⟨110⟩{110} slip system in this material. Indeed, similar {110} twin domains have been detected in deformed $CaIrO_3$ ppv samples (Niwa *et al.* 2012).

Following the procedure described in the section 3.6.1 (Fig. 3.1.18), we computed the twinning energy landscape (Fig. 4.4.6), corresponding to the twin formation mechanism with b_p = ⅙[110] twinning dislocation in $MgSiO_3$ and $CaIrO_3$ ppv phases. This energy, also called generalized planar fault energy (GPFE), describes the cost per unit area required to form a N-layer twin by shearing N consecutive atomic layers along the [110] direction in the $(0\bar{1}1)$ plane. The GPFE first involves the γ_{us} barrier (Fig. 4.4.6) against a one-layer partial fault becoming a one-layer full fault (Fig. 4.4.7). This barrier is followed by the one-layer intrinsic stacking fault energy γ_{isf}. Nucleation of the second, third and

Table 4.4.1. Anisotropic lattice friction in $MgSiO_3$ post-perovskite

Slip system	Peierls stress σ_p, GPa	
	Screw	Edge
[100](010)	**1.0 // 2.3***	<0.1
[100](011)	>10.4	~0.12
[100](001)	17.5	~0.1
[001](010)	**3.0**	2.0
½⟨100⟩{110}	0.7	**2.8**
½⟨100⟩{110}^{twin}		**0.88***

** DFT calculations*

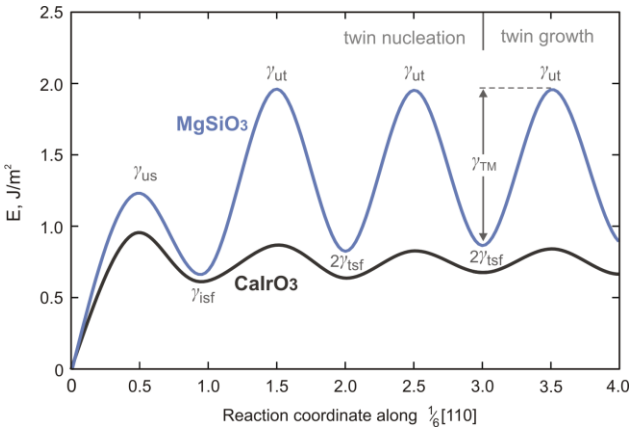

Figure 4.4.6. GPFE landscape for ½[110](110) deformation twinning in $MgSiO_3$ and $CaIrO_3$ post-perovskites characterized by b_p = ⅙[110]

subsequent ⅙[110] dislocations creates the two-, three- and further *N*-layer stacking faults (Figs. 4.4.7 c,d). The energy difference between γ_{ut} and $2\gamma_{tsf}$ (Fig. 4.4.6) defines the so-called twin migration energy γ_{TM}. For the investigated ½⟨110⟩{110} twinning system in $MgSiO_3$ and $CaIrO_3$, the convergence in γ_{TM} energy is reached after nucleation of the third twinning partial dislocation, thus resulting in total shear displacement by a full ½[110] lattice repeat. Hence, further nucleation and propagation of successive ⅙[110] dislocations enable twin growth on the developed three-layer twin nucleus. The geometry of ½⟨110⟩{110} deformation twinning in post-perovskites can be described as the rotation of the parent lattice along the [001] axis by 34.5° in $MgSiO_3$ (Fig. 4.4.7 d) and by 31.1° in $CaIrO_3$.

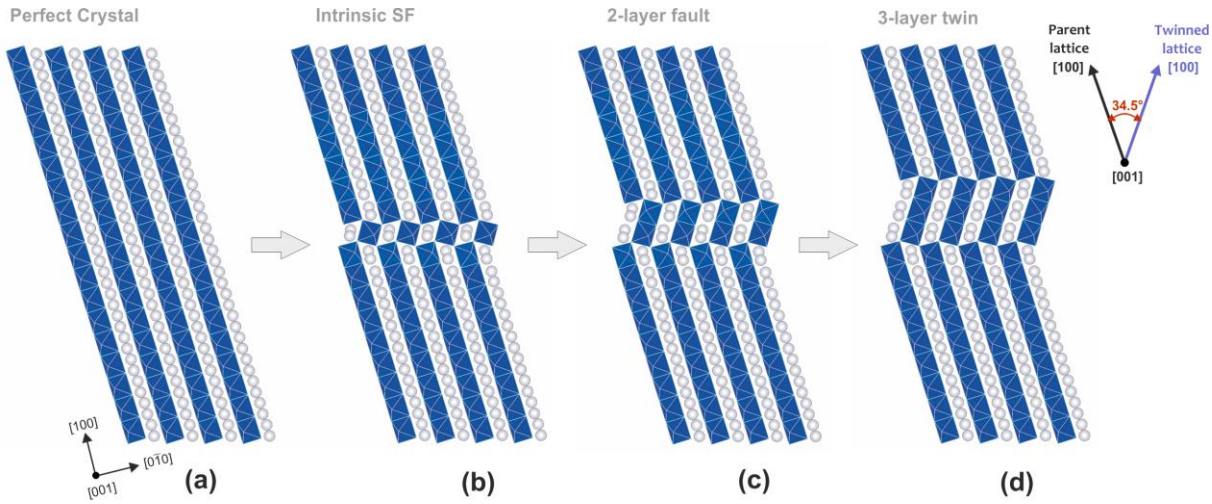

Figure 4.4.7. ½⟨110⟩{110} deformation twinning in $MgSiO_3$ ppv. Starting from the perfect lattice **(a)** viewed along [001], panels **(b)**, **(c)** and **(d)** show the lattice with one-, two-, and three-layer faults after the shearing of successive ⅙[110] twinning dislocations. The four atomic structures correspond to the minimum energy configurations in the GPFE landscape depicted in Fig. 4.4.6.

Relying on the GPFE landscape (Fig. 4.4.6) that contributes to the twin boundary energy E_{GPFE} (Eq. 3.1.10), one can further compute the total energy of a twin lamella E_{tot} (Eq. 3.1.10) as the function of the spacing d between the twinning dislocations (Fig. 3.1.17). The critical twin nucleation stress τ^{cr} can be further defined while minimizing E_{tot} (Eq. 3.1.10) with respect to the distance d: $\partial E_{tot}/\partial d = 0$. Using $N = 3$ derived from the GPFE calculations (Fig. 4.4.6), we found τ^{cr} values of ~880 MPa (Table 4.4.1) and ~620 MPa for the ½⟨110⟩{110} twinning system in $MgSiO_3$ and $CaIrO_3$ ppv. More details about mechanical twinning in the post-perovskite phases can be found in Carrez *et al.* (2017)

References

P. Carrez *et al.* (2017) Sci Reports 7: 17640
K. Niwa *et al.* (2012) Phys. Earth Planet. Inter. 194-195: 10

4.4.3. Thermally activated dislocation glide

At finite temperature, the actual motion of dislocations occurs through nucleation and propagation of kink-pairs. The key parameter describing the efficiency of the dislocation glide at finite temperature is the critical kink-pair formation enthalpy ΔH_{2k}. In $MgSiO_3$ ppv, evolution of the latter with applied stress was computed based on the line-tension (LT) model for the [100](010) screw dislocations, relying both on the pairwise potential modeling and on DFT calculations. For the [001](010) screw dislocations, the $\Delta H_{2k}^{\sigma=0}$ value was estimated based on the observed dislocation core characteristics inferred from the pairwise potential modeling. For the ½⟨110⟩{110} system, we consider the critical twin nucleation stress τ^{cr} as temperature independent.

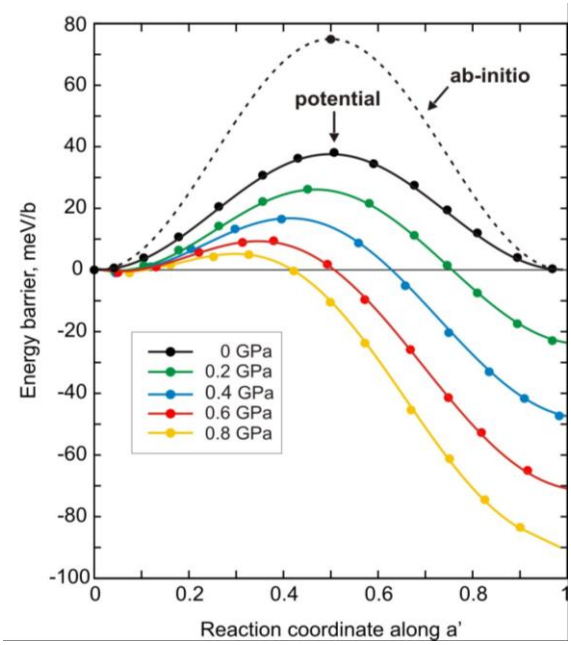

Figure 4.4.8. Peierls barrier V_P (black line) calculated for [100](010) with the pairwise potential (solid line) and DFT (dashed line). Evolution of the energy barrier with applied stress $\Delta H_P = V_P - \sigma_a b a'$, deduced from the nudged elastic band method, is provided in colour

LT model for kink-pairs on [100](010)

Within the LT formulation (Guyot & Dorn 1967; Caillard & Martin 2003), a screw dislocation line can be represented as a 1D function $y(x)$, which describes its position y in the glide plane at each x coordinate along the dislocation line. Then, the dislocation line enthalpy H_{LT} can be estimated according to the following expression:

$$H_{LT}(y(x),\sigma_a) = \int dx \left[V_P\big(y(x)\big) - \sigma_a b y(x) + \frac{\Gamma}{2}\left(\frac{dy}{dx}\right)^2 \right], \qquad (4.4.1)$$

where V_P is the Peierls barrier; $\sigma_a b y(x)$ is the work of applied stress; Γ is the line tension that characterizes the stiffness of the dislocation line. The $V_P\big(y(x)\big) - \sigma_a b y(x)$ term corresponds to the so-called «substrate enthalpy» H_P in the 1D-Frenkel-Kontorova model (Frenkel & Kontorova 1938; Joós & Duesbery 1997). The enthalpy H_P can be computed at the atomic scale using the NEB method as described in the section 3.1.5. Figure 4.4.8 illustrates the computed ΔH_P curves for the [100](010) system in $MgSiO_3$ ppv.

To link the LT model with atomic-scale simulations of Γ, we follow the work of Dezerald *et al.* (2015) and discretize the integral in Eq. (4.4.1) into n segments $\{Y_n\}$ of length b:

$$H_{LT}(\{Y_n\},\sigma_a) = b\sum_n \left[V_P(\{Y_n\}) - \sigma_a b Y_n + \frac{\Gamma}{2b^2}(Y_{n+1} - Y_n)^2 \right] \qquad (4.4.2)$$

where the sum over n accounts for the periodic boundary condition along the dislocation line.

The line tension Γ of [100] dislocations in $MgSiO_3$ ppv was derived from the energy cost associated with a dislocation bow-out (consistent with the first stage of kink-pair formation). The details of this calculations can be found in Goryaeva *et al.* (2016). For the

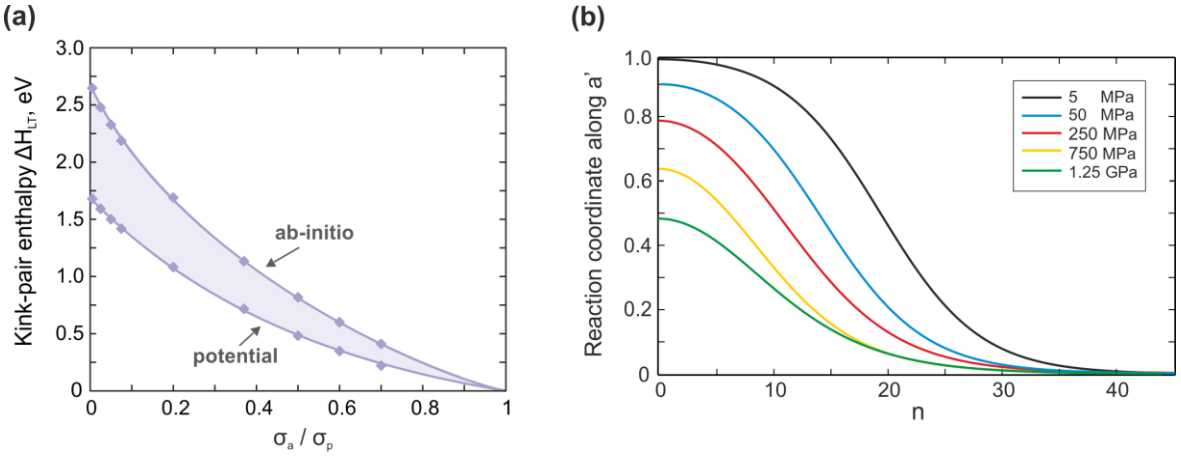

Figure 4.4.9. **(a)** Kink-pair formation enthalpy H_{LT} and its evolution with applied stress computed with the data acquired from DFT and pairwise potential simulations. **(b)** Kink shape computed based on the data acquired from DFT simulations. Along horizontal axis, n corresponds to the number of Burgers vectors b = 2.474 Å

investigated slip system, we found Γ = 9.2 eV/Å based on DFT simulations (vs Γ = 7.1 eV/Å based on the empirical potential by Oganov *et al.* 2000).

Enthalpy and equilibrium shape of the kink-pairs. Once line tension Γ is computed and the Peierls barrier V_P is known, the equilibrium kink-pair shape at a given stress and the corresponding critical kink-pair enthalpy H_{LT} can be calculated using Eq. (4.4.1). To solve the equation, we rely on a trial function $y(x)$ that describes the equilibrium shape of a symmetric kink-pair: $y(x) = \frac{1}{2}a'\left[tahn\big(a(x+m)\big) - tahn(a(x-m))\right]$, where, a' is the periodicity of the Peierls potential and α and m are variable parameters.

The saddle point on the $H_{LT}(\alpha,m)$ energy landscape ultimately defines both the enthalpy H_{LT} (Fig. 4.4.9a) and the equilibrium kink-pair configuration $y(x)$ (Fig. 4.4.9b). The kink-pair enthalpy H_{LT} (Fig. 4.4.9a) is maximum under zero stress, with a value of 2.69 eV, corresponding to twice the energy of a single kink H_k, and it vanishes when the applied stress is equal to the Peierls stress σ_p. Evolution of the enthalpy ΔH_{LT} with applied stress can be described using the following expression: $\Delta H_{LT}(\sigma_a) = 2H_k(1-(\sigma_a/\sigma_P)^p)^q$. As shown on Fig. 4.4.9b, the equilibrium kink-pair configurations in ppv are characterized by extremely large widths in the range of 35-40b (~100 Å) resulting from the very low Peierls barrier V_P (Fig. 4.4.8).

Evolution of CRSS with temperature

As it was previously demonstrated (*e.g.* sections 4.2-3), kink-pair enthalpy evolution as a function of stress (Fig. 4.4.9a) can be used to infer the evolution of the critical shear stress as a function of temperature:

$$\sigma = \sigma_P\left(1-(T/T_a)^{1/q}\right)^{1/p} \qquad (4.4.3)$$

In the equation (4.4.3), coefficients p and q describe the evolution of the kink-pair enthalpy (Fig. 4.1.9*a*). Temperature T_a, often called «athermal temperature» (Fig. 1.1.9), corresponds to the critical temperature at which lattice friction vanishes. Generally, kink-pair energy $2H_k$ scales with T_a according to $2H_k = CkT_a$, where k is the Boltzmann constant; C is a function of a strain rate $\dot{\varepsilon}$, of the dislocation density ρ, and of the kink geometry.

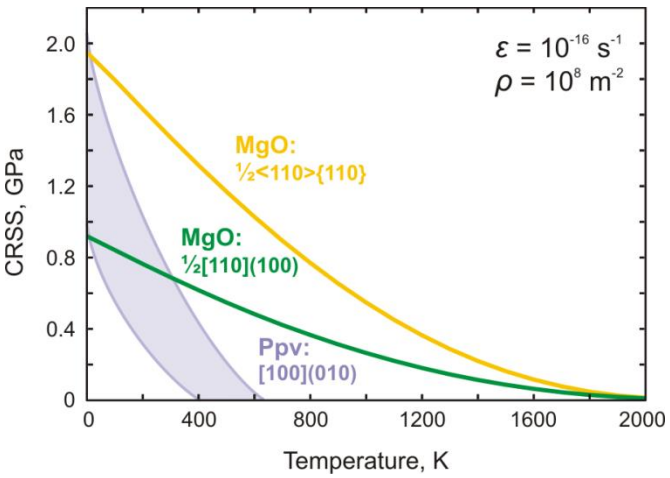

Figure 4.4.10. Evolution of CRSS with temperature for [100](010) system in $MgSiO_3$ ppv at 120 GPa, compared with the easy slip systems in MgO at 100 GPa (Cordier *et al.* 2012). Strain rate $\dot{\varepsilon}$ and dislocation density ρ correspond to the lower mantle conditions

Relying on the computed $2H_k$ = 2.69 eV, p = 0.73 and q = 1.31 for the [100](010) dislocations, one can find that, at the lower mantle conditions with the strain rates $\dot{\varepsilon}$ in the order of 10^{-16} s^{-1} and dislocation density ρ = 10^8 m^{-2}, lattice friction vanishes at the critical temperature T_a=600 K (Fig. 4.4.10). These T_a temperatures are far below the temperature of 3700 – 4400 K (Boehler 2000; Alfè *et al.* 2002) expected in the lowermost mantle, therefore [100] dislocation glide at D'' conditions can be expected to occur *in the athermal regime* (Fig.1.1.9). Considering experimental conditions, *i.e.* strain rates $\dot{\varepsilon}$ ~10^{-5} s^{-1} and dislocation density ρ = 10^{12} m^{-2}, we find that for the [100](010) system in $MgSiO_3$ ppv lattice friction vanishes when the temperature is raised above 1100 K (as an upper bound defined based on DFT calculations).

In case of dissociated [001](010) screw dislocation cores with much more complex geometry (Fig. 4.4.4), we did not determine the full curve describing the evolution of the kink-pair formation enthalpy with applied stress, but only estimated the maximum $2H_{2k}$ = 8.3 eV values describing the energy of the two isolated kink-pairs nucleated simultaneously on the two partials without changing the stacking fault width (for more details, see Goryaeva *et al.* 2017), relying on the elastic interaction model by Koizumi *et al.* (1993). We assume that the kink-pair enthalpy $2H_{2k}$ scales linearly with kT (Kubin 2013). Then, once $2H_{2k}(\sigma=0)$ is defined, the athermal temperature T_a relevant for glide of dissociated [001](010) dislocations can be estimated as $T_a = \frac{2H_{2k}}{kC}$.

Employing the dislocation density ρ = 10^8 m^{-2} and the strain rate $\dot{\varepsilon}$ = 10^{-16}, typical for lower mantle conditions, provides the athermal temperature T_a = 1950 K. These results suggest that [001](010) dislocation glide at the D'' conditions in $MgSiO_3$ post-perovskite would rather occur *in the athermal regime* (Fig. 1.1.9), as well as for the [100](010) system.

References

D. Alfè *et al.* (2002) Earth Planet. Sci. Lett. 195: 91
R. Boehler (2000) Rev. Geophys. 38: 221
D. Caillard & J. Martin (2003) Thermally activated mechanisms in crystal plasticity. Pergamon, pp. 452
P. Cordier *et al.* (2012) Nature 481: 177
L. Dezerald *et al.* (2015) Phys. Rev. B 91: 094105
J. Frenkel & T. Kontorova (1938) Phys. Z. Sowj 13: 1
A. Goryaeva *et al.* (2016) Sci Reports 6: 34771
A. Goryaeva *et al.* (2017) Phys. Chem. Miner. 44: 521
P. Guyot & J Dorn (1967) Canad. J. Phys. 45: 983
B. Joós & M. Duesbery (1997) Phys. Rev. B 55: 11161
H. Koizumi *et al.* (1993) Acta Metall. Mater. 41: 3483
L. Kubin (2013) Dislocations, mesoscale simulations and plastic flow. University Press, Oxford

4.5. Dissemination

The RheoMan project was intended to develop multiscale numerical methods to describe the plasticity of mantle phases. However, this approach is rather general and commonly applied to other crystalline solids. Here we describe four studies which were conducted in parallel with RheoMan and which benefited from the expertise and techniques developed during the project.

4.5.1. Cementite

The results reported in this section are related to the PhD project of Nils Garvik.

Cementite Fe_3C is the main strengthening phase of steels. During forming, for instance by cold working of deep drawing, pearlitic steels undergo extreme deformations which subject cementite lamellae to extreme conditions where they can no longer be considered as non-deformable. However, very few studies had addressed the issue of defects and plasticity in cementite.

We have investigated the theoretical strength of cementite that describes its structural stability as a function of strain (Garvik *et al.* 2013). Calculations were performed by spin polarized DFT using GGA with PAW. When described within the *Pnma* space group, unit cell of Fe_3C has lattice parameters are a = 5.09Å , b = 6.75Å and c = 4.52Å and contains twelve iron and four carbon atoms. The ideal strength of cementite was studied by applying increasing strains to a unit cell. Tensile experiments were performed along [100], [010] and [001]. The maximum tensile strength is reached for 16% and 23% along [100] and [010] with ideal stresses of 22 GPa and 20 GPa, respectively (Fig. 4.5.1). Pulling cementite along [001] leads to the highest ideal stress (32 GPa) reached for the largest elongation (24%).

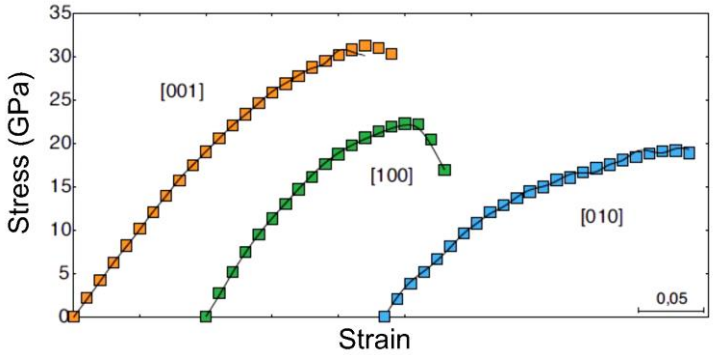

Figure 4.5.1. Stress-strain curve corresponding to uniaxial tensile tests with homogeneous strain until mechanical instability

Shear tests can be divided into two groups revealing the strong anisotropic behaviour of the structure. The first group corresponds to the [100](010), [010](100), [001](100) and [100](001) systems where the maximum shear stress is reached at relatively low strains (below 22%). For the second group, that contains [010](001) and [001](010), the structure can be sheared up to 40% before reaching instabilities. This remarkable behaviour can be explained by the fact that the local environment of interstitial C atoms changes with increasing strain. For [010](001), new Fe-C bonds (up to 7) form above *ca.* 20 % of the total bonding which allows the structure to oppose further resistance until the break above 36% strain.

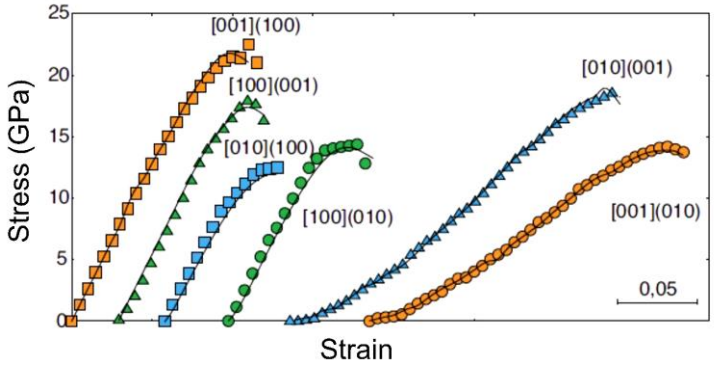

Figure 4.5.2. Stress-strain curves corresponding to shear tests with homogeneous strain until mechanical instability

We used the PNG model (see section 3.1.2) to investigate the core structures of [100], [010] and [001] dislocations in Fe_3C cementite. According to the performed calculations (Garvik *et al.* 2015), [100] screw dislocations spread and dissociate in (010) plane. This result has been confirmed by transmission electron microscopy (Fig. 5.5.3).

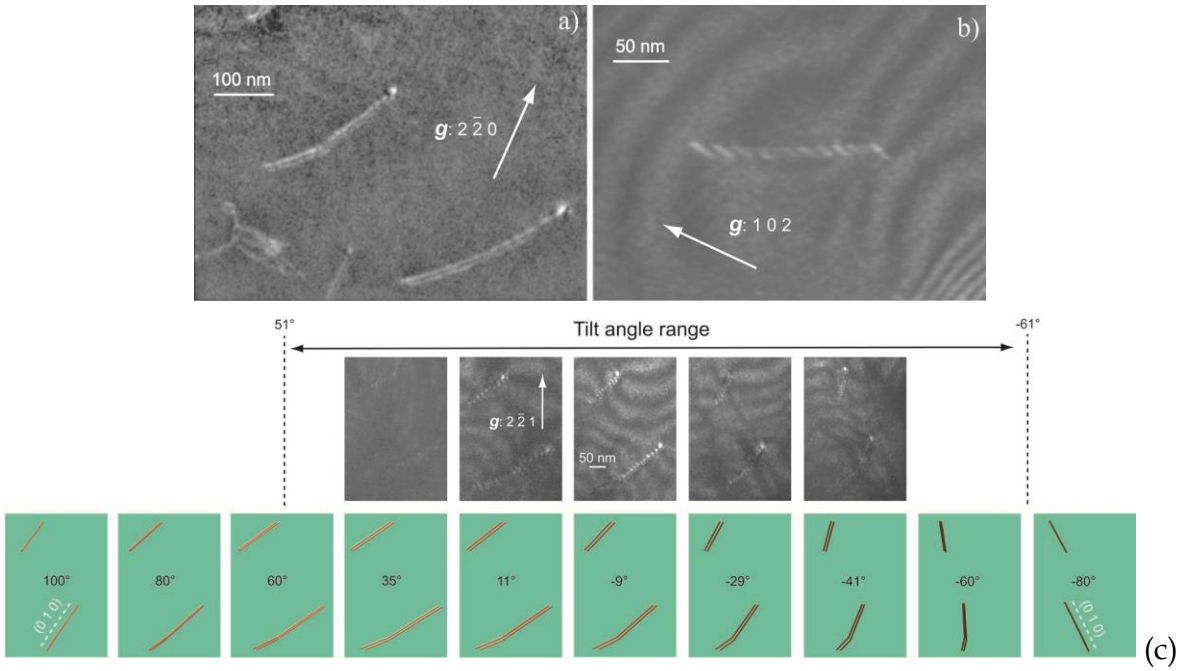

Figure 4.5.3. [100] dislocations in cementite. Weak-beam dark-field images show the two partial dislocations **(a)** and the stacking fault **(b)**; electron tomography **(c)** demonstrates that [100] dislocations are dissociated in (010)

For [001] dislocations, three possible slip planes were considered and screw dislocations are found to spread in (100). The core structure is made of two strongly correlated partial dislocations separated by 10 Å. Such a core geometry is consistent with the TEM observations (Fig. 4.5.4) which evidenced «perfect» [001] dislocations gliding in (100).

For [010] screw dislocations, we found a spread in (001) with a dissociation involving a small edge component. Contrary to the previous cases, this prediction could not be verified since no [010] dislocations has been observed at the TEM.

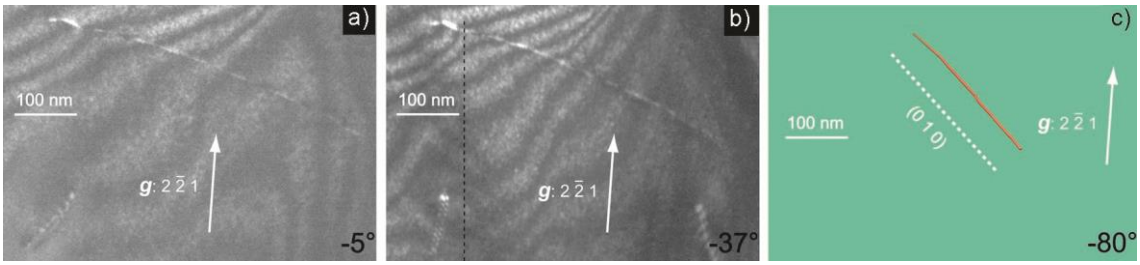

Figure 4.5.4. [001] dislocations in cementite. Weak-beam dark-field images show the dislocations at tilt angles -5° **(a)**, -37° **(b)** and the reconstructed volume corresponding to a tilt angle of -80° **(c)** which indicates the trace of the glide plane: (010)

In overall, only three slip systems have been identified in Fe_3C cementite which involve only two slip planes:

- [100](010)
- [010](001)
- [001](010)

Given the presence of edge components in [010] dislocation cores, we could not model their thermal activation. Concerning the two other slip directions, [100] glide appears to be easier than [001]. The results of our calculations (Fig. 4.5.5) demonstrate that dislocation glide in cementite is clearly more difficult that in (pure iron), notwithstanding the multiplicity of slip systems in this phase.

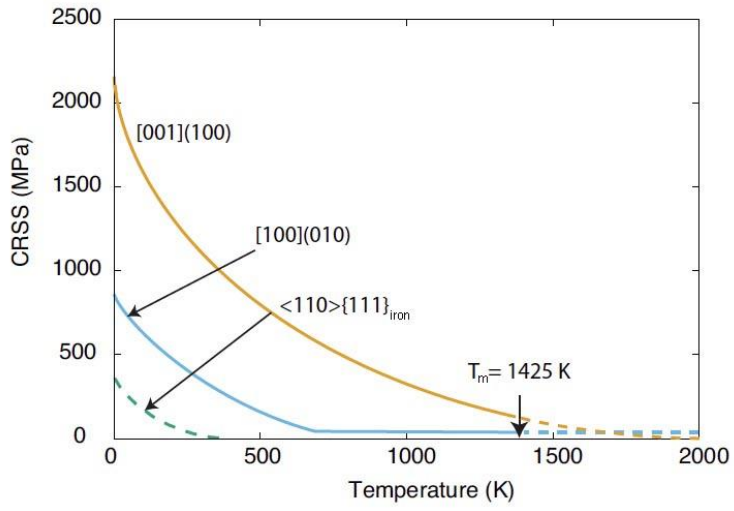

Figure 4.5.5. CRSS of the [100](010) and [001](100) systems in cementite as a function of temperature. Our results are compared with those of ⟨110⟩{111} in ferrite from Naamane *et al.* (2010). T_m is the melting temperature of cementite

References

N. Garvik *et al.* (2013) Mater. Sci. Eng. A 572: 25
N. Garvik *et al.* (2015) Scripta Mater. 99: 61
S. Naamane *et al.* (2010) Int. J. Plasticity 26: 84
A. Mussi *et al.* (2016) Phil. Mag. 17: 1773

4.5.2. MAX phases

The work presented in this section was performed in collaboration with A. Guitton, A. Joulain, L. Thilly and C. Tromas, Institut Pprime, Poitiers.

MAX phases represent a class of hexagonal materials with carbon or nitrogen. The general formula of the ternary carbides or nitrides is $M_{n+1}AX_n$. (n = 1 to 3), where M is a transition metal, A belongs to group IIIA to VIA, and X is either carbon or nitrogen. MAX phases exhibit a combination of metals and ceramics properties which suggest promising technological applications. MAX phases are made up of different layers with $M_{n+1}X_n$ layers interleaved with metallic w layers. Moreover MAX phases have high lattice anisotropy. Little is known yet about the elementary deformation mechanisms of these phases. Microstructural observations on deformed samples suggest the prominence of dislocation activity in the basal plane.

We investigated the core structure and the Peierls stress of $\frac{1}{3}\langle 2\bar{1}\bar{1}0\rangle$ dislocations in Ti_2AlN MAX phase, based on the PNG (section 3.1.2), coupled with first principles calculations of GSF (section 3.1.1).

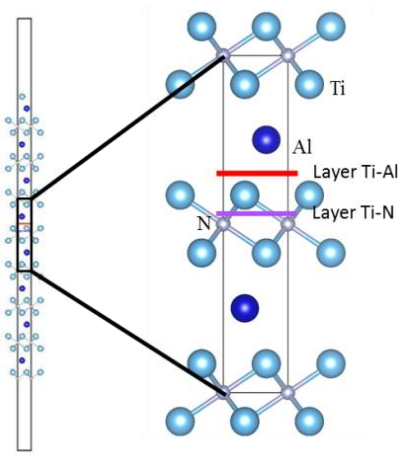

Figure 4.5.6. Supercell of Ti_2AlN structure used for the γ-surface calculations (Gouriet *et al.* 2015). The red (purple) line is the trace of (0001) between Al (N) and Ti layer. The highlighted rectangle corresponds to the unit cell

γ-surfaces in basal plane

Two different cutting levels (Fig. 4.5.6) are calculated in the basal plane and shown in Figure 4.5.7. For a quantitative comparison of the ability of shearing the two levels, the γ-lines along $[\bar{2}110]$ and $[0\bar{1}10]$ are shown in Figure 4.5.8. First, the γ-surface calculation results show that shearing is much easier within the Al-Ti layer. Secondly, a stable stacking fault γ_s is observed at $\frac{1}{3}\langle 1\bar{1}00\rangle$. As a consequence, we expect $\frac{1}{3}[\bar{2}110]$ dislocations to be dissociated with the dissociation path shown on Figure 4.5.7.

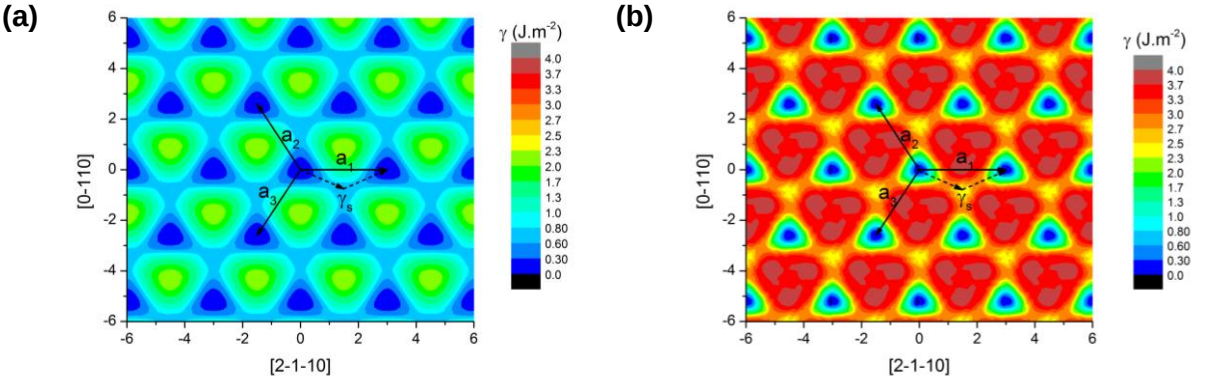

Figure 4.5.7. γ-surfaces (in J/m²) in (0001) with shear **(a)** between Ti and Al atoms and **(b)** between Ti and N atoms. The hexagonal base (a_1, a_2, a_3) is represented, γ_s is the stable stacking fault with **(a)** γ_s=0.72 J/m² and **(b)** γ_s=2.06 J/m². The dashed arrows represent the dissociation path of the dislocation with the a_1 Burgers vector.

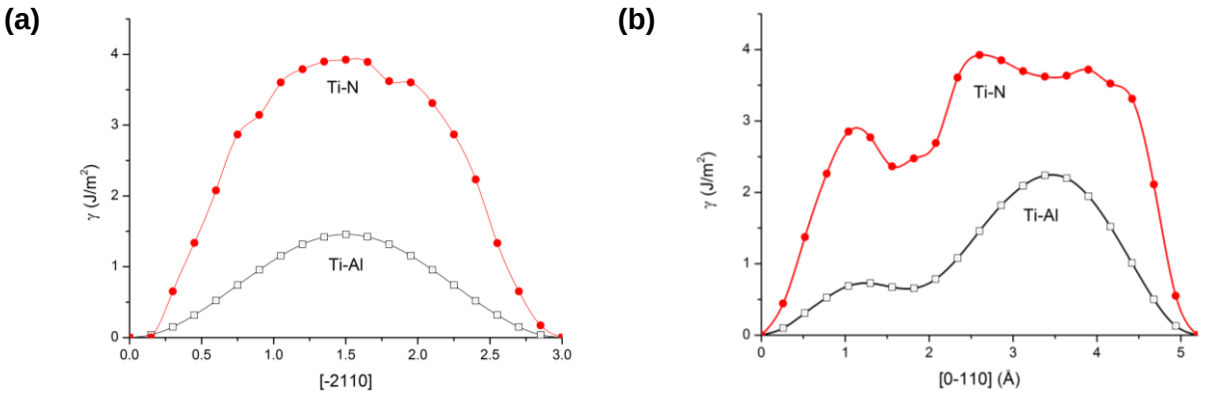

Figure 4.5.8 (a) γ-line along $[\bar{2}110]$ in (0001). **(b)** γ-line along $[0\bar{1}10]$ in (0001). The black line and open square symbol corresponds to the (Ti-Al) layer, and the red line and circle symbol to the (Ti-N) layer

Dislocation core structures

The γ-surface in (0001) with a shear between Ti and Al atoms (Fig. 4.5.7a) and the elasticity tensor are introduced in the PNG model to calculate the dislocation core structures of several dislocation characters. Each character is defined by the angle φ between the dislocation line direction and the $\frac{1}{3}\langle\bar{2}110\rangle$ Burgers vector: 0° (screw), 30°, 60° or 90° (edge).

All the dislocation cores are dissociated into two symmetrical partials, with the dissociation scheme $\frac{1}{3}\langle\bar{2}110\rangle \rightarrow \frac{1}{3}\langle\bar{1}100\rangle + \frac{1}{3}\langle\bar{1}010\rangle$, and separated by a distance Δ below 7 Å (see table 4.5.1). This separation distance increases with the angle between the Burgers vector and the dislocation line. Table 4.5.1 summarises the essential geometric characteristics of the dislocation cores of different characters, including half-widths of each partial ξ_i, the separation distances Δ (calculated value) and Δ_{th} (equilibrium distance according to anisotropic elasticity considering a staking fault energy of 0.72 J/m²) between partials and a' - the periodicity of the misfit energy density.

Finally, we find the Peierls stress σ_p for all the four dislocation core configurations below 1 GPa. However, the 30° and 60° characters are about 50% harder than the screw and edge ones. But experimentally, any of the four characters has been observed with one predominance (Guitton *et al.* 2012).

Table 4.5.1. dislocation core parameters that control the spreading in (0001) plane

Dislocation character	ξ_1, Å	ξ_2, Å	Δ, Å	Δ_{th}, Å	σ_p, MPa	a', Å
0°	1.8	1.9	5.26	3.22	611	$\frac{a_1\sqrt{3}}{2}$
30°	2.2	2.1	6.09	4.91	830	a_1
60°	1.7	1.9	6.58	6.28	957	$\frac{a_1\sqrt{3}}{2}$
90°	1.9	1.8	6.68	5.97	680	a_1

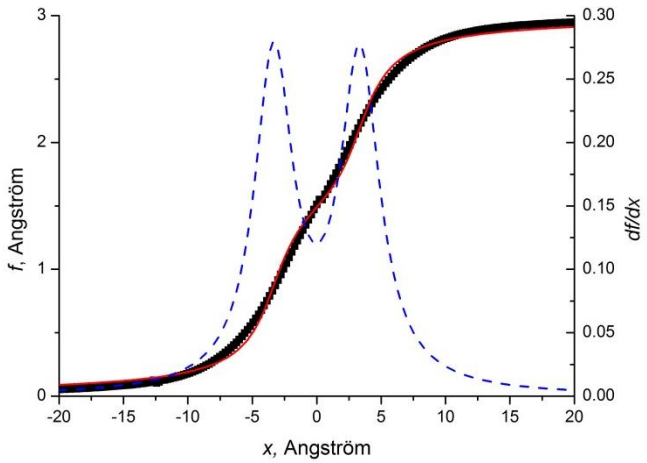

Figure 4.5.9. Core structure of edge dislocations. Disregistry function $f(x)$ and associated Burgers vector density $\rho=df(x)/dx$ (dotted line) are plotted in (0001) plane

References

M.W. Barsoum (2000) Progr Solid State Chem. 28: 201
M.W. Barsoum & T. E.l.-Raghy (2001) Amer. Sci 89: 334
A. Guitton *et al.* (2012) Philos. Mag. 92: 4536

4.5.3. Ice X

The work described in this section is a result of the short-term collaboration with B. Journaux, R. Caracas and I. Daniel, ENS Lyon.

H_2O is very abundant in the solar system and more generally in the galaxy. Some massive ice-rich planets are considered to be in between rocky terrestrial planets and gaseous giant ones. Depending on their distance to the star and properties of their atmospheres, some of them may form a surface water ocean. They are called «Ocean-Planets». Those planets would be composed of a large icy mantle essentially formed of high pressure polymorphs of ice VII and X. The transition toward high-pressure ice would occur below a thick ocean, about 100 km thick. Indeed, the phase diagram of ice (Fig. 4.5.10) is very rich with many polymorphs stable at high pressure. Here we investigate the plasticity of ice X, the ionic polymorph of H_2O ice, stable at pressures in the 100–400 GPa range. The structure of ice X (Fig. 4.5.12) can be seen as an intergrowth between a bcc arrangement of an oxygen sublattice and a fcc arrangement of a hydrogen sublattice, shifted by ¼ along each of the three directions of the primitive cubic unit cell. The resulting space group is *Pn*3*m*.

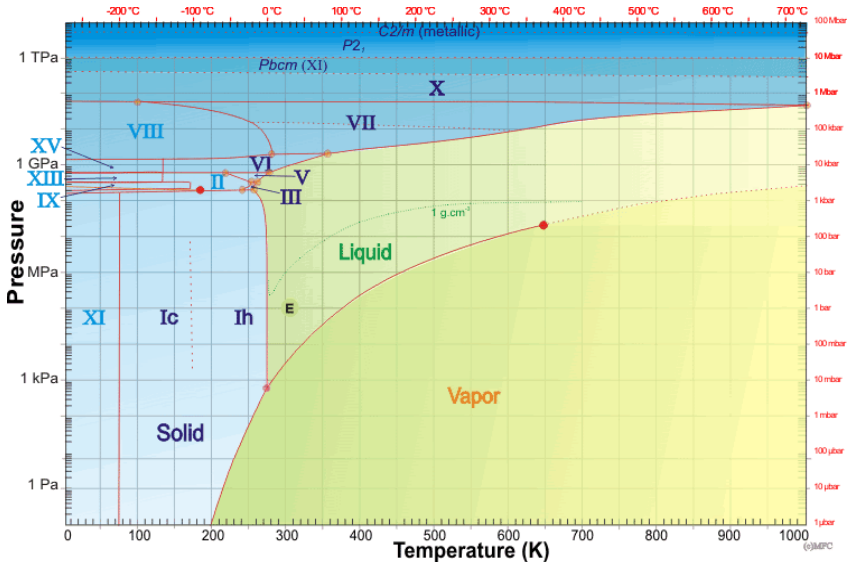

Figure 4.5.10 (a) Phase diagram of H_2O, modified after http://www.lsbu.ac.uk/water/phase.html

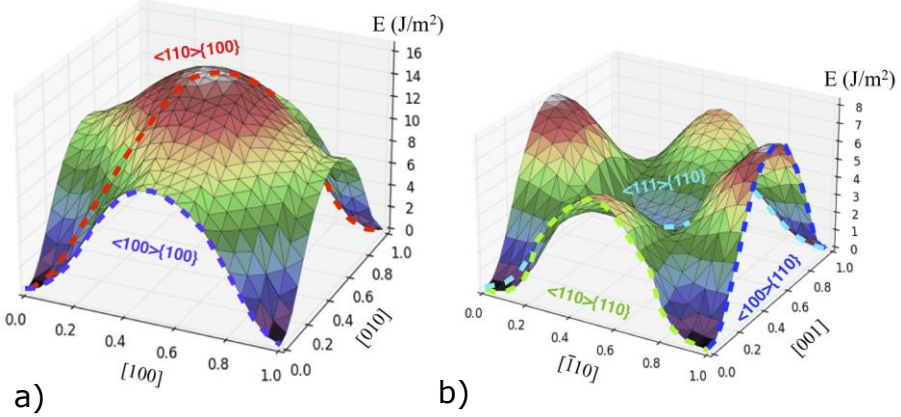

Figure 4.5.11. γ-surfaces at 250 GPa in {100} **(a)** and {110} **(b)** showing the easiest shear paths suggesting the major slip systems

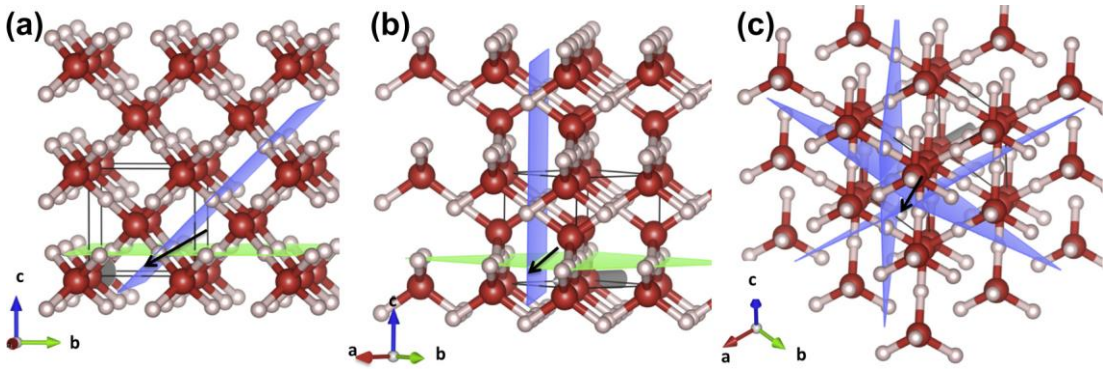

Figure 4.5.12. Slip systems in ice X. **(a)**, **(b)** and **(c)** correspond to the three shear directions: ⟨100⟩, ⟨110⟩, and ⟨111⟩, with the major glide planes coloured: {100} in green, and {110} in blue

In order to apply the Peierls-Nabarro model, the γ-surfaces are calculated at pressures between 100 and 350 GPa. The easiest shear paths are shown in Figure 4.5.11.

The PN analysis shows that the ⟨100⟩{100}, ⟨100⟩{110}, ⟨110⟩{110} slip systems correspond to dislocations with a non-dissociated core structure. On the contrary, dislocations from the ⟨111⟩{110} slip system exhibit two partial dislocations separated by a narrow stacking fault.

The plasticity of ice X is dominated by dislocation glide in the {110} planes at all pressures. At 100–150 GPa the ⟨110⟩{110} is the easiest slip system with dislocation glide being controlled by screw characters; at 250 GPa ⟨100⟩{110} controlled by the motion of edge dislocations becomes easier, while ⟨110⟩{110} becomes one of the hardest ones. At 350 GPa the easiest slip system is ⟨100⟩{110} although it is only slightly easier than ⟨111⟩{110}.

For large ocean exoplanets, where the 250 GPa isobar lays inside the solid ice mantle, our results suggest a possible change in rheology, with different regimes between the shallow and deep parts. Our modeling suggests that the shallower parts would be dominated by a strong plastic anisotropy and a relatively low elastic anisotropy. The deeper parts would have a very strong elastic anisotropy, associated with a relative low plastic anisotropy.

References

B. Journaux *et al.* (2014) Phys. Earth Planet. Sci. 236:10

4.5.4. Phase A

Phase A ($Mg_7Si_2O_8(OH)_6$) is a dense hydrous magnesium silicate (DHMS) phase which forms mainly by destabilization of Mg-phyllosilicates in hydrated lithologies, between 200 and 350 km depths in cold hydrous parts of the subducting slabs. Because of its chemical composition, phase A is potentially the major water carrier at these depths and is viewed as a key phase for water transfer from the serpentine stability field down to the transition zone in cold environments (*e.g.* Poli & Schmidt 1997).

Mussi *et al* (2012) proposed a first study of the deformation mechanisms of phase A over a 400-700°C temperature range at 11 GPa, using transmission electron microscopy (TEM) on samples recovered after stress relaxation experiments. Here, we studied dislocation core structure of ⅓[$2\bar{1}\bar{1}0$] and [$01\bar{1}0$] Burgers vectors using a numerical approach based on the Peierls-Nabarro-Galerkin (PNG) model and generalized stacking faults (γ-surface) calculations. The DFT calculations were performed within GGA approximation and PAW method.

Core structures of $\frac{1}{3}[2\bar{1}\bar{1}0]$ and $[01\bar{1}0]$ screw dislocations

In a hexagonal structure, ⅓[$2\bar{1}\bar{1}0$] and [$01\bar{1}0$] dislocations can potentially glide in the basal plane (0001), in ($01\bar{1}0$) and in ($2\bar{1}\bar{1}0$) prismatic planes or in pyramidal planes. The γ-surfaces corresponding to these planes are shown in Figure 4.5.13. Dislocation core structures are then calculated with the PNG model using, as an input, γ-surfaces and the elasticity tensor.

The screw dislocations are found to spread widely in the basal plane only. The core spreading leads to dissociation into several partials with a core width of 10 Å (1.5×*a*, Figure 4.5.14a) for ⅓[$2\bar{1}\bar{1}0$] and 35 Å (5×*a*, Figure 4.5.14b) for [$01\bar{1}0$].

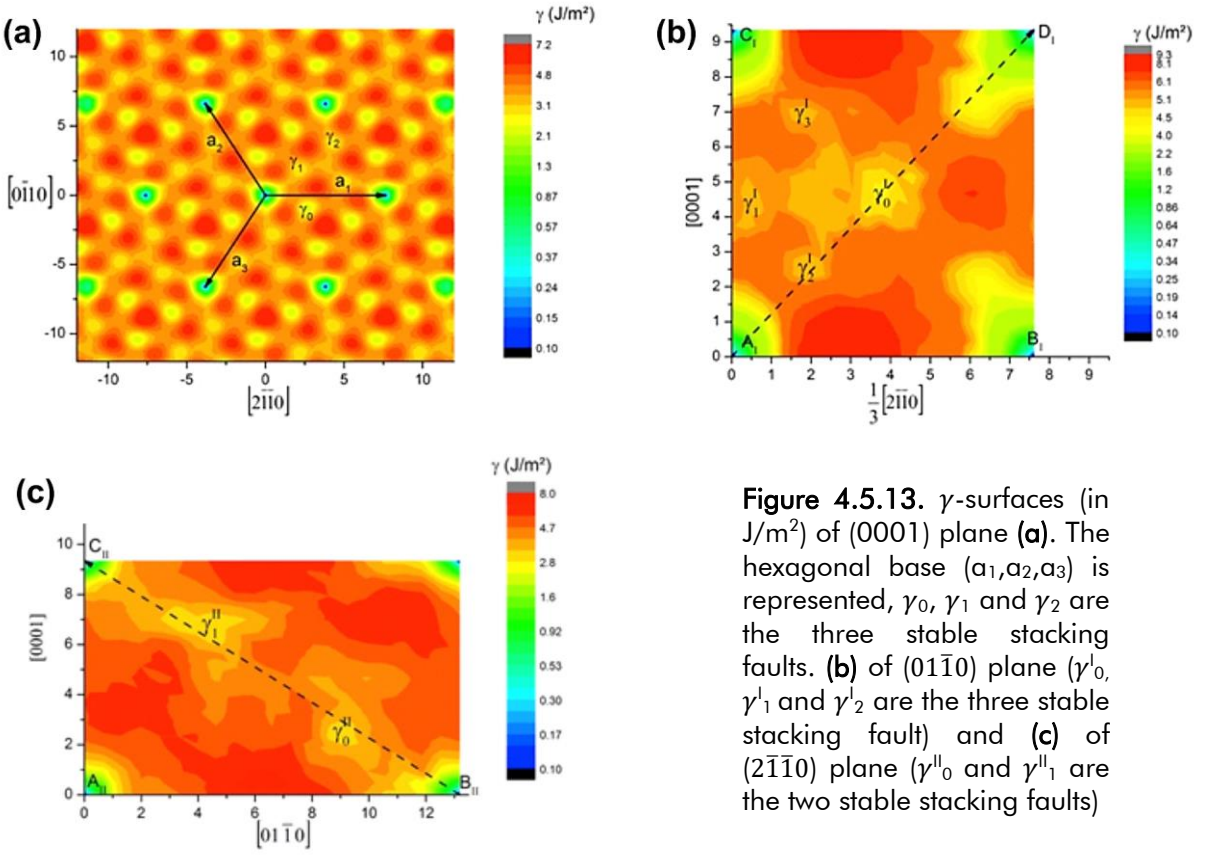

Figure 4.5.13. γ-surfaces (in J/m^2) of (0001) plane **(a)**. The hexagonal base (a_1,a_2,a_3) is represented, γ_0, γ_1 and γ_2 are the three stable stacking faults. **(b)** of ($01\bar{1}0$) plane (γ^I_0, γ^I_1 and γ^I_2 are the three stable stacking fault) and **(c)** of ($2\bar{1}\bar{1}0$) plane (γ^{II}_0 and γ^{II}_1 are the two stable stacking faults)

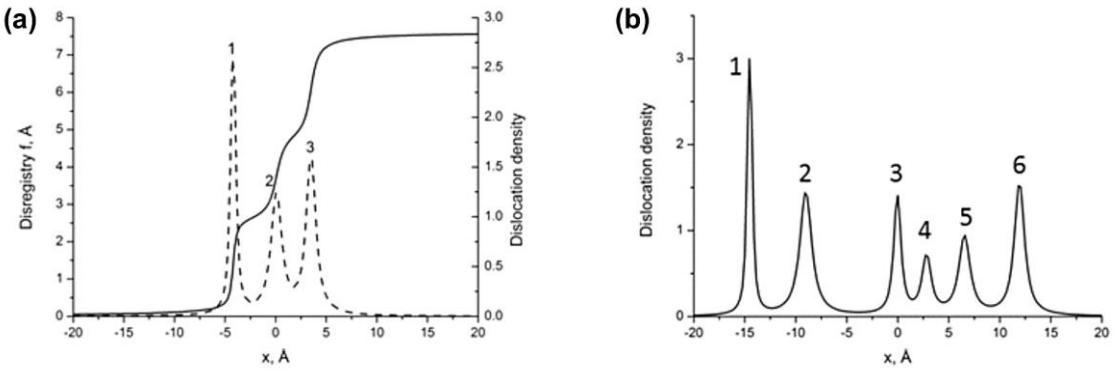

Figure 4.5.14. (a) Core structure of ⅓$[2\bar{1}\bar{1}0]$ screw dislocation. Disregistry function *f(x)* and associated Burgers vector density $\rho=df(x)/dx$ (dotted line) are plotted in (0001) plane. The number *i* corresponds to the i^{th} partial. 1 and 3 correspond to $\frac{1}{21}[5\bar{4}\bar{1}0]$and 2 to $\frac{1}{21}[41\bar{5}0]$. **(b)** Core structure of $[01\bar{1}0]$ screw dislocation. Associated Burgers vector density $\rho=df(x)/dx$ is plotted in (0001) plane. The number *i* corresponds to the i^{th} partial. 1, 2 and 6 correspond to $\frac{1}{21}[\bar{1}5\bar{4}0]$, 3 to $\frac{1}{21}[41\bar{5}0]$, 4 to $\frac{1}{21}[\bar{2}3\bar{1}0]$ and 5 to $\frac{1}{21}[12\bar{3}0]$

Finally, we compute the Peierls stresses, by shearing the nodal mesh. Dislocations with the $\frac{1}{3}[2\bar{1}\bar{1}0]$ Burgers vector have the smallest Peierls stress of 0.81 GPa, while those with $[01\bar{1}0]$ Burgers vector have larger, albeit still relatively low, values for the Peierls stress of 1.5 GPa.

Our results compare well with TEM observations by Mussi *et al.* (2012) who report significant dislocation activity in the basal plane. From the computations, glide in the basal plane is easy (large dissociation of dislocations resulting in a low lattice friction) compared to glide in prismatic planes. However the dislocations with ⅓$[2\bar{1}\bar{1}0]$ Burgers vectors observed in the basal plane by Mussi *et al.* (2012) appear as perfect ones. The equilibrium distances we compute between each partial of both ⅓$[2\bar{1}\bar{1}0]$ and $[01\bar{1}0]$ dislocations are indeed lower than 13 Å (Figs. 4.5.14, 4.5.15), meaning these individual partial dislocations cannot be resolved by TEM (best resolution in weak-beam dark-field is of the order of a few nanometers). Finally Mussi *et al.* (2012) observed in the basal plane a typical partial ⅓$[01\bar{1}0]$. Our calculations indeed suggest a dissociation of $[01\bar{1}0]$ dislocations which involve this component ⅓$[01\bar{1}0]$.

References

K. Gouriet *et al.* (2015) Phys. Earth Planet. Int., 248:1
A. Mussi, P. Cordier & D.J. Frost (2012) Eur. J. Mineralogy 24: 429
S. Poli & M.W. Schmidt (1997) Tectonophys. 273: 169

Chapter 5

Modeling Creep

5.1. Creep in olivine

5.1.1. The message from microstructures: on the role of climb and recovery

This section of the book outlines the study of olivine deformation microstructure at temperatures ranging from the uppermost lithospheric mantle to the lithosphere/asthenosphere boundary. Most observations reported here have been performed on specimens deformed by Sylvie Demouchy (Geosciences Montpellier) during a long-term collaboration.

Geometry of slip

Commonly, TEM observations of dislocation microstructures in olivine deformed at relatively low temperature (*i.e.* below 1200 K) describe screw dislocations which exhibit high lattice friction (Fig. 5.1.1) and thus appear as straight segments. Such a microstructure challenges the use of electron tomography (described in the section 3.3.1) for glide plane characterization since TEM thin foils often exhibit dislocations segments with only one direction (such as the yellow segments in Fig. 5.1.1c). In that case, we take advantage of the presence of any additional dislocation segments to determine the glide plane, even if edge-on position that we are looking for to identify the plane is beyond the tilt range allowed by the sample holder. The most important results of slip planes definition in olivine at low temperature conditions are summarized in Table 5.1.1.

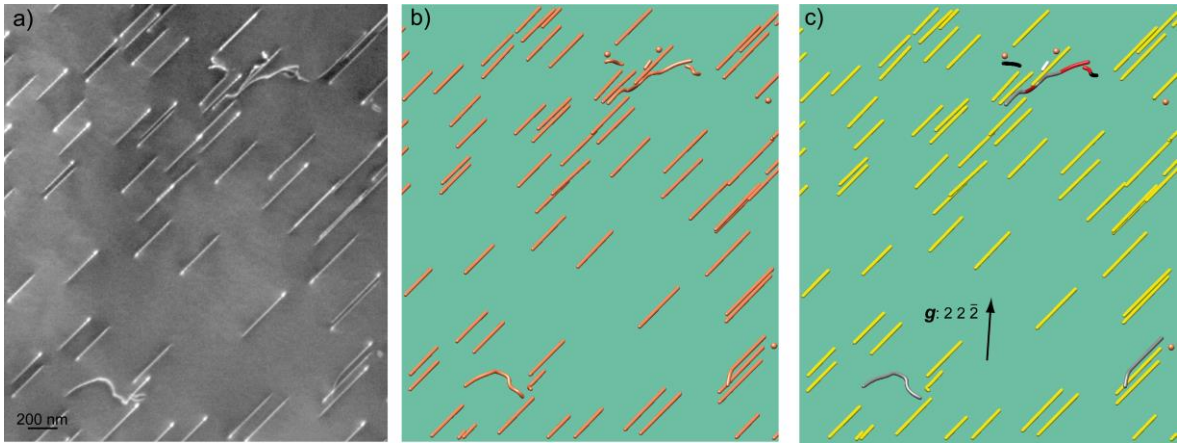

Figure 5.1.1. **(a)** Typical processed TEM WBDF micrograph of dislocations in olivine deformed at 800°C and its tomography reconstructions **(b, c)** obtained with g: **22$\bar{2}$**. The specimen contains very few non-screw dislocation segments, that can be seen in the corresponding indexed tomography reconstruction, where dislocations which could not be indexed alone due to their straight-line configurations appear in yellow in **(c)**

Table 5.1.1. Slip planes observed in the olivine samples deformed at low temperature

	[001] dislocations	[100] dislocations
Slip planes	{110} (100) {1n0} - *n*=2, 3, 4 (010) - very few	(010) {041} {011} {021} (001)

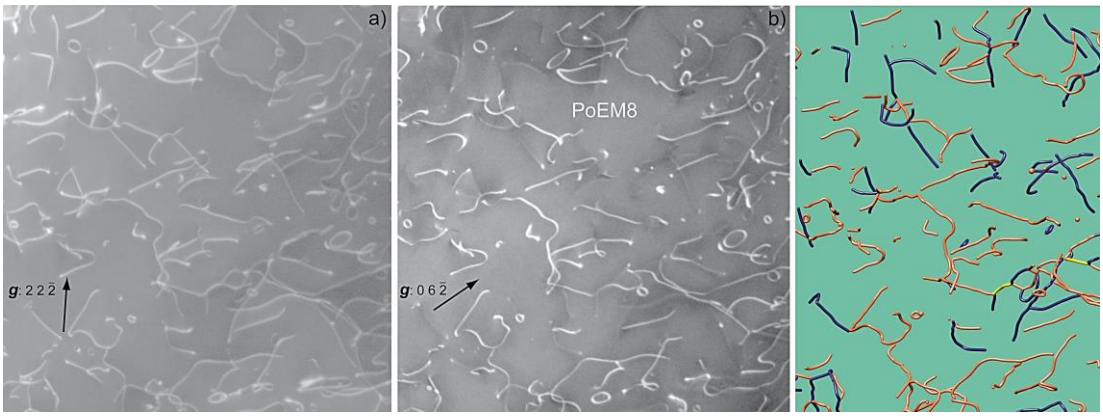

Figure 5.1.2. Typical processed TEM WBDF micrograph of dislocations in olivine deformed at 1090°C and obtained **(a)** with g: $22\bar{2}$ (where [100] and [001] dislocations are in contrast) and **(b)** with g: $06\bar{2}$ (only [001] dislocations are in contrast). **(c)** The corresponding 3D reconstruction ([100], [001] and $[10\bar{1}]$ dislocations are shown in blue, orange and yellow colours, respectively). PoEM8 is the name of the sample

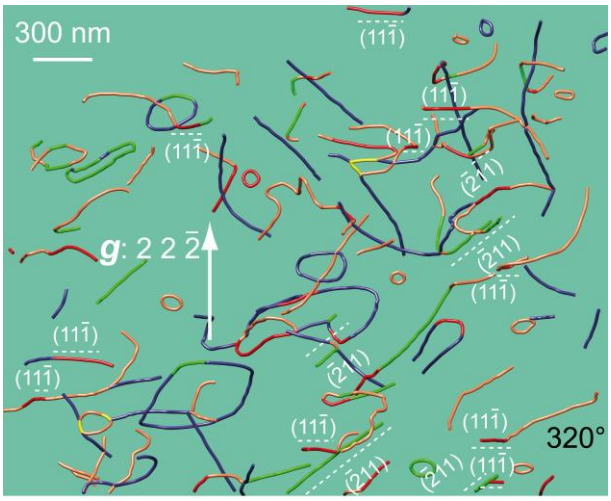

Figure 5.1.3. Olivine single crystal deformed at 1090°C. Dislocation segments lying on the {111} planes are coloured in red and the dislocation segments lying on {211} are coloured in green

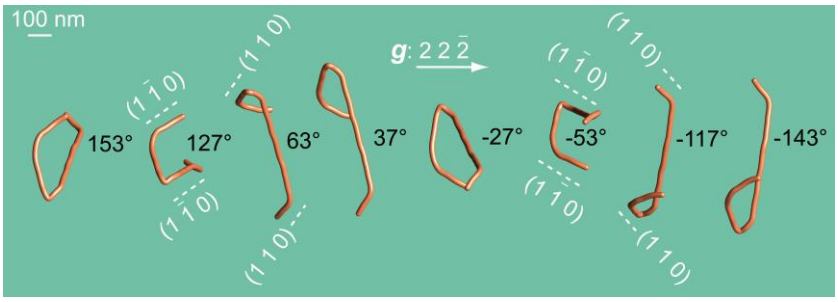

Figure 5.1.4. Double cross-slip mechanism: reconstructed volume of a [100] dislocation obtained with g = $22\bar{2}$, the (110) planes are edge-on for the −117° and 63° tilt angles and the $(1\bar{1}0)$ planes are edge-on for the −53° and 127° tilt angles

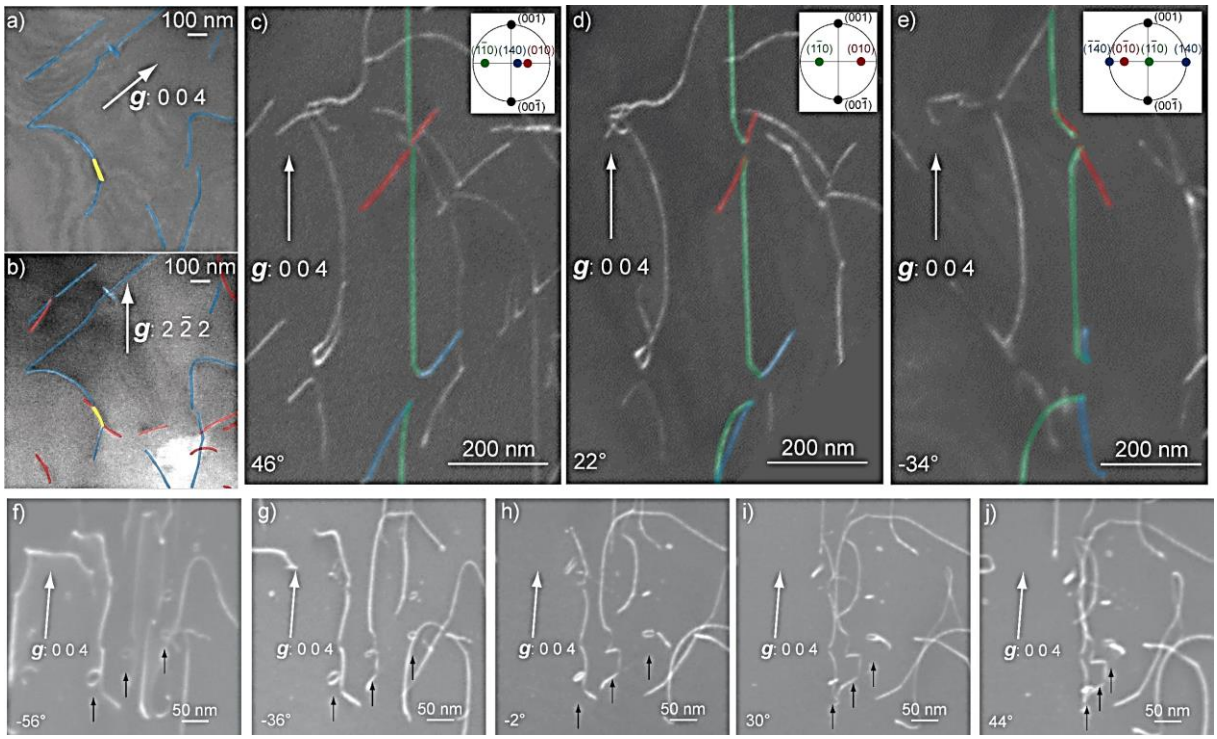

Figure 5.1.5. Dislocations interactions in olivine polycrystal deformed at 900°C: **(a)** [001] dislocations (shown in blue) and [101] junction (shown in yellow) are in contrast with g: 004. **(b)** [100] dislocations (coloured in red), [100] and [101] dislocations are all in contrast with g: 22$\bar{2}$. **(c)** [001] dislocations coloured in green, blue and red are gliding in (1$\bar{1}$0), (140) and (010) respectively, with the (1$\bar{1}$0) glide plane nearly edge on with a tilt angle of 46°. **(d)** All the three glide planes are tilted with a tilt angle of 22°. **(e)** The (140) glide plane is practically edge on and the (1$\bar{1}$0) glide plane is perpendicular to the electron beam with a tilt angle of -34°. Two collinear interactions are clearly shown in **(c)**, **(d)** and **(e)**. **(f-j)** Three loops with projected angles of **(f)** -56°; **(g)** -36°; **(h)** -2°; **(i)** 30°; and **(j)** 44°. The dislocation loop located in the middle of the micrograph is actually a sessile dislocation segment resulting from a collinear interaction between a sessile dislocation loop and a gliding dislocation

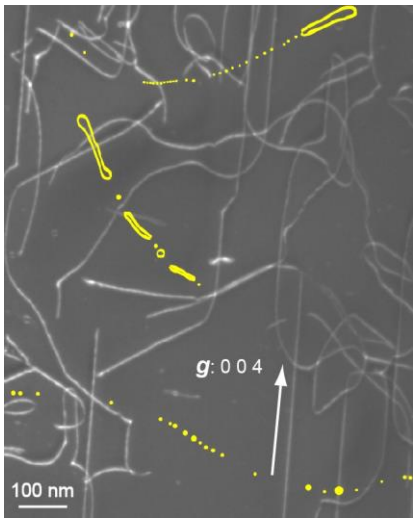

Figure 5.1.6. Olivine crystal deformed at 850°C (WBDF micrograph with g: 004), where three dislocation dipoles (highlighted in yellow) annihilate by climb

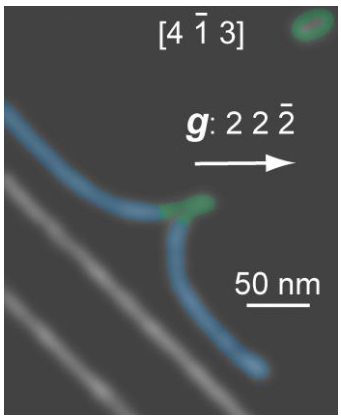

Figure 5.1.7. Collinear annihilation resulting from the interaction between a gliding dislocation (in blue) and a loop (in green)

Since most observations have been carried out on specimens deformed at low temperature, most information (from statistical point of view) have been gained on [001] dislocations.

At higher temperatures, the activity of [100] dislocations becomes more important (Fig. 5.1.2). One also finds an evidence of dislocations which escape the glide planes. Figure 5.1.3 illustrates several occurrences of dislocations in climb configurations in the {111} and {211} planes. In these specimens we also found planes which correspond neither to glide nor to climb. We interpret these structures as the result of double cross slip (Fig. 5.1.4).

Dislocation interactions

The detailed analysis of the geometry of dislocation lines by electron tomography has shed some new light on the mechanisms of dislocation interaction in olivine. Three varieties of dislocation interactions have been evidenced in olivine. Above 1000° C, both [100] and [001] slip are activated in olivine. This raises the question about the interaction between these two dislocation types. We indeed have detected some ⟨101⟩ (Figs. 5.1.5 a-b). It is not possible to withdraw information about the strength of this interaction but considering their rare occurrence and the fact that this junction involves dislocations with perpendicular Burgers vectors, we do not expect them to contribute much to forest hardening. More importantly, elastic interactions between non-screw segments of dislocations lead to the formation of dipoles which shrink due to dislocation climb (Figs. 5.1.6 and 5.1.12). The resulting small sessile dislocation loops (less than 10 nm in diameter) interact with gliding dislocations of the same type but with opposite Burgers vectors through collinear annihilations (Figs. 5.1.5 f-j and 5.1.7). This interaction mechanism has been recently shown to be a major component of strain hardening in fcc metals, it seems to play an important role in olivine as well. Thus, in Figure 5.1.5 c-e, one can see a [001] dislocation gliding in $(1\bar{1}0)$ (in green) which crosses two dislocations with opposite Burgers vectors which glide in (010) and (140) (in red and blue respectively) at the crossing point, the interaction leads to an annihilation (a segment is missing on the micrographs). The points where the dislocations segments meet have a limited mobility and this «junction» is very difficult to destroy. This mechanism is likely to contribute strongly to strain hardening. Additionally, double cross-slip mechanisms (Fig. 5.1.4) produce larger 3D sessile dislocation loops (from 10 nm to several hundreds of nm in diameter) which also form collinear annihilations with gliding dislocations. All those interaction mechanisms lead to the lower effective mobility of dislocations.

Recovery

Many observations of dislocation interactions were shown to result from the collinear annihilation with dislocation loops (Fig. 5.1.7). Trying to identify the origin of those loops, we found that some of them were organised in strings resulting from the shrinkage of dislocation dipoles by climb (Fig. 5.1.6). This remarkable microstructure is thus an indication of the activation of recovery processes.

References

S. Demouchy *et al.* (2013) Phys. Earth Planet. Inter. 220: 37
A. Mussi *et al.* (2017) Philos. Mag. 97: 3172
A. Mussi *et al.* (2015a) Philos. Mag. 95: 335
A. Mussi *et al.* (2015b) Eur. J. Miner. 27: 707

5.1.2. Dislocation dynamics modeling of creep in olivine

High-temperature creep

In this part, we present the results of dislocation creep modeling in olivine at high Temperature conditions (above *ca.* 1400 K), similar to that of the experiments. In this regime, intragranular plastic deformation results mostly from the motion of [100] dislocations involving thermally activated glide and climb. Glide and climb mechanisms are characterized by different kinetics of the dislocation motion, independent from each other. Dislocation glide is a conservative motion controlled, at a given temperature, by stress (Fig.1.1.9); while climb is mostly controlled by the flux of vacancies exchanged between the dislocation and the bulk (Fig. 1.1.10). The dislocation velocity laws represent fundamental parameters both for glide and climb processes. In olivine, glide is always several orders of magnitude faster than climb (Fig. 5.1.8) regardless of the temperature conditions. This is the usual framework describing dislocation creep in agreement with the conventional models of Weertman (1955, 1957).

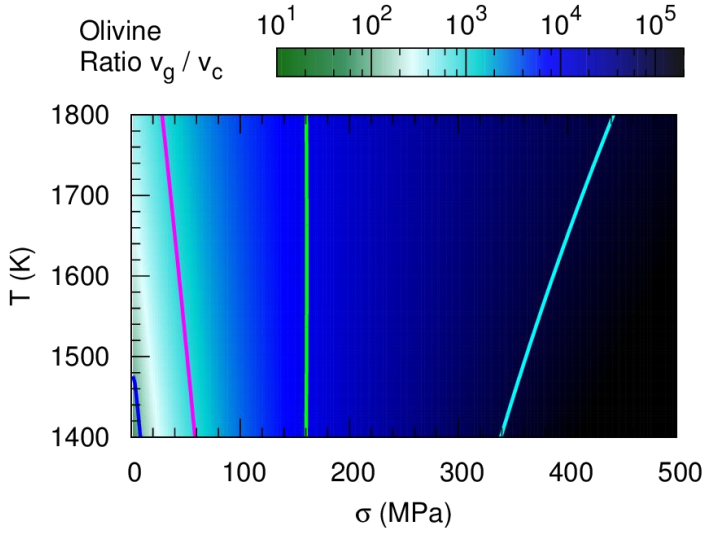

Figure 5.1.8. Comparison between the glide velocity (v_g) and the climb velocity (v_c) of dislocations in olivine at ambient pressure

By employing 2.5-D dislocation dynamics simulations (for more details about this technique, see section 3.2.1.) we can describe the interplay between glide and climb to shed some light on the microstructural processes occurring during creep. First of all, we can model the creep behaviour in the absence of climb. Under applied stress, the dislocations start to move by glide until positions where they are stopped by elastic (or local) interaction from other dislocations. Very rapidly, this leads to a configuration which is not able to further evolve (unless the applied stress would be increased to release some dislocations, as illustrated in Figure 5.1.9a. Once the climb is activated, the situation becomes completely different. In this case, steady state deformation conditions are reached and plastic strain is continuously produced with elapsed time. The climb mechanism, in fact, allows dislocations to annihilate and the microstructure to move from a «quasi-equilibrium configuration» to another one, providing continually new mobile dislocations. However, the prominent strain producing mechanism remains glide as shown in Figure 5.1.9b. Dislocation motion by climb produces only a marginal fraction of the plastic strain (in agreement with the strong velocity contrast between the two mechanisms, see Fig. 5.1.8). Activation of climb is, however, crucial for constraining the plastic strain rate. At the steady-state the plastic strain ε increases linearly with time and the dislocation density ρ oscillates around a constant value (Fig. 5.1.10b). Both the strain rate and the steady state dislocation density depend on the creep stress (Fig. 5.1.10).

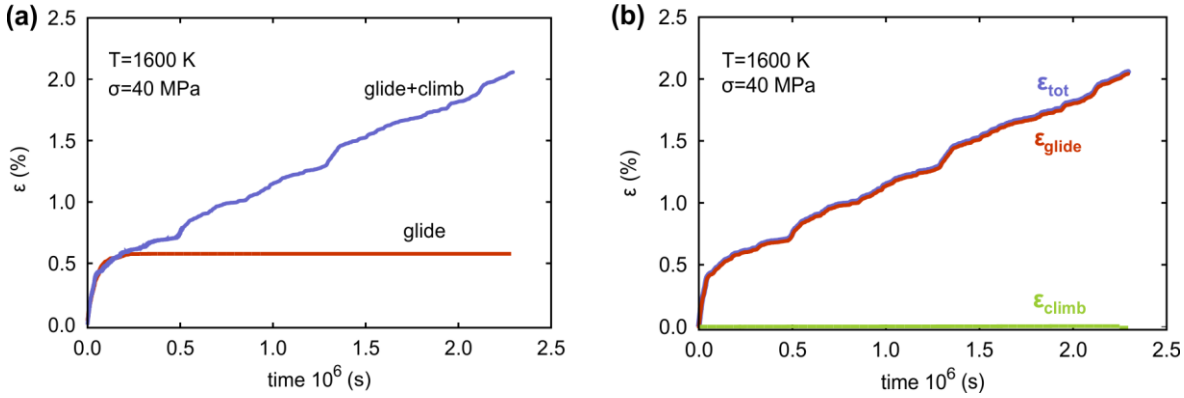

Figure 5.1.9. Modelling creep in olivine at high temperature. **(a)** Creep curves describing the evolution of strain as a function of time. The red curve corresponds to the case where only glide is allowed. In blue, both glide and climb are activated. **(b)** Comparison of the effective contributions of glide (in red) and climb (green) to the total strain (in blue) for the case where both deformation mechanisms operate

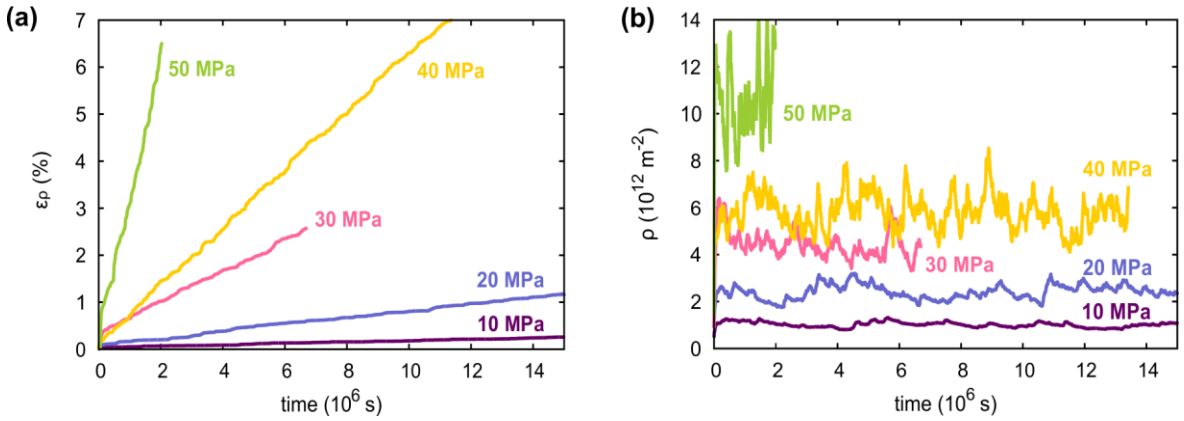

Figure 5.1.10. **(a)** Creep curves of the total plastic strain rate as a function of time, computed for five values of applied stress at T=1600K. **(b)** Corresponding evolution of dislocation density *vs* time

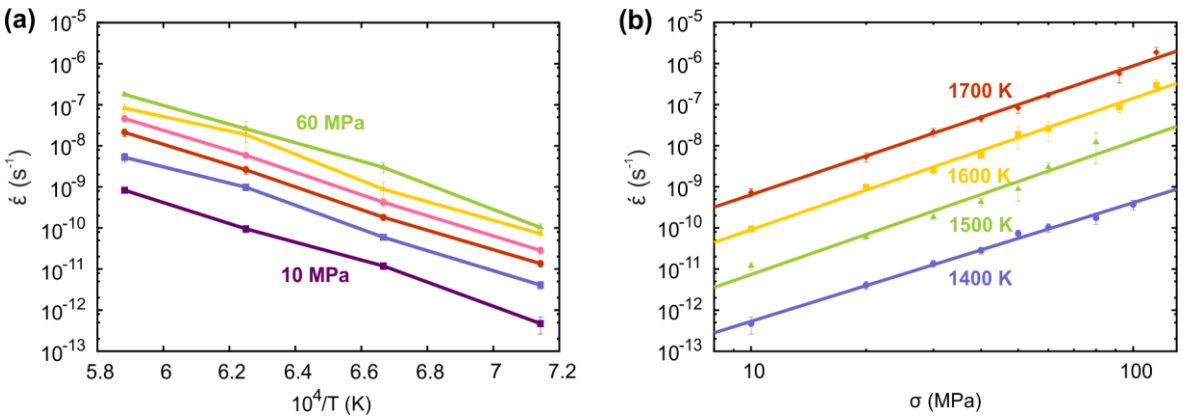

Figure 5.1.11. Strain rate $\dot{\varepsilon}$ from the DD calculations as a function **(a)** of reciprocal temperature and **(b)** of applied stress

The creep simulations have been carried out in the temperature and stress range of 1400-1700 K and 10 - 120 MPa. The resulting strain rates are then extracted and analysed as a function of stress and reciprocal temperature, *i.e.* as experimental ones would be, to determine the stress sensitivity and activation energy. Figure 5.1.11 shows that all data can be well described by a power law characterized by a constant stress exponent close to 3 and an activation enthalpy barrier of 5.1 eV (490 kJ/mol).

Then creep of olivine at high temperature is captured by dislocation dynamics and can be described by a power law of the type:

$$\dot{\varepsilon}_{HT} \sim \sigma^3 \, exp\left(-\frac{5.1}{k_B T}\right) \tag{5.1.1}$$

Extending to low temperatures

In the laboratory, when olivine is deformed at low/moderate temperatures (1000 - 1200 K), its behavior is completely different. Olivine is stronger, instabilities develop and steady state is not reached (Demouchy *et al.* 2013). TEM investigations show numerous entanglements (see an illustration on Fig. 5.1.12) which are interpreted as a source of this hardening. However, surprisingly, even at temperatures as low as 1000 K, one finds an evidence for some recovery mechanisms (Fig. 5.1.12c). These observations lead us to make the hypothesis that the observed hardening as well as the absence of steady-state could be a consequence of the high laboratory strain rates which would not let enough time for recovery mechanisms to operate.

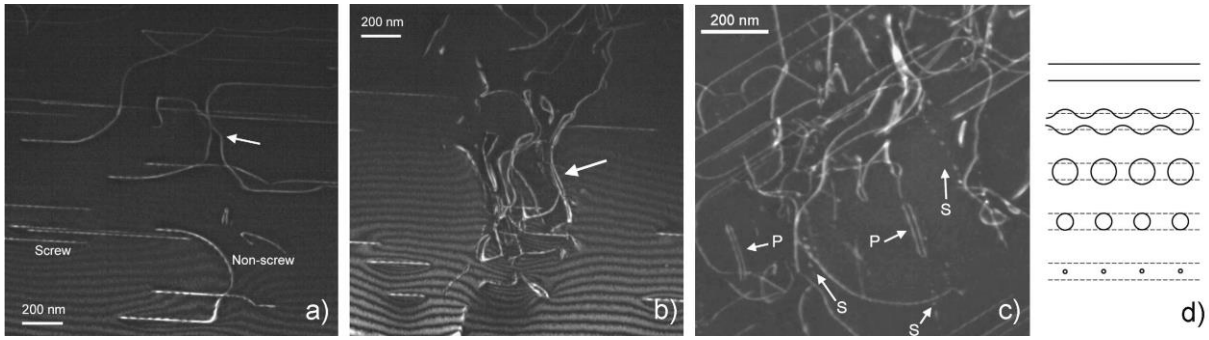

Figure 5.1.12. Olivine crystal deformed at 900°C: **(a)** onset of interaction between two non screw segments leading to **(b)** further entanglements. Within those entanglements, one can find evidence of recovery, even at 850°C as in **(c)**. Following the mechanism depicted in **(d)**, dipoles pinch (P) and breakdown in strings (S) of sessile loops which shrink and disappear by diffusion

By using the dislocation dynamics (DD) model, we checked this hypothesis and investigated dislocation creep in olivine at low to moderate temperatures, relevant for the lithospheric mantle. Taking into account the temperature range involved, the DD simulations were run with [001] dislocations. Similarly to high temperature creep, the interplay between glide and climb leads to steady state deformation conditions, even to temperatures as low as 800°C. Obviously, since the creep rate is controlled by diffusion which becomes extremely slow, the strain rates reach values which eventually become unrealistic. These experiments demonstrate however that there is no abrupt change to be expected in the rheology of olivine as temperature decreases. Under a given stress, the creep rate can reach a steady state, but the process slows down. Maintaining a constant

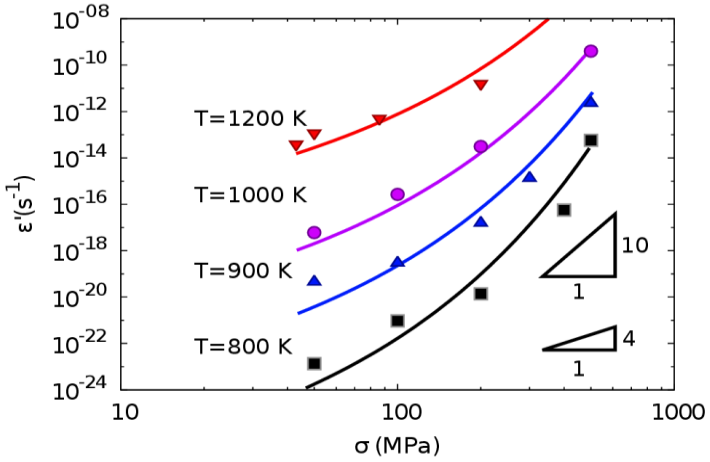

Figure 5.1.13. Calculated 2.5-D DD strain-rate values $\dot{\varepsilon}$ as a function of the applied creep stress σ. Solid lines show the fit obtained using Equation (5.1.2)

creep rate would require stress to be further raised. However, the lower the temperature, the larger is the stress increase needed. This behaviour is well illustrated in Figure 5.1.13 where the curvature of the curves becomes more prominent as temperature decreases. In this temperature range, the rheology of olivine cannot be described by a power law as already pointed out in experiments.

This so-called «power law breakdown» phenomenon has been known for a long time. In 1979, while describing the hardness data, Evans and Goetze proposed to introduce a functional form of the free energy of activation of slip :

$$\Delta G(\sigma) = \Delta G_0 \left[1 - \left(\frac{\sigma}{\sigma_P}\right)^p\right]^q \tag{5.1.2}$$

where ΔG_0, σ_P, p and q are constants. This leads to the so-called exponential law which is used since then to describe the rheology of olivine at low temperature. Using this formalism, we propose the following rheological law which corresponds to the fit of the 2.5-D DD data presented in Figure 5.1.13:

$$\dot{\varepsilon} = 5.068 \times 10^7 \, exp\left[-\frac{5.4}{k_B T}\left(1 - \left(\frac{\sigma(\mathrm{MPa})}{3460}\right)^{0.5988}\right)^{1.1506}\right] \tag{5.1.3}$$

On the power law breakdown

The power law breakdown is commonly described in the literature as the transition between two different creep regimes, possibly involving distinct deformation mechanisms. We have shown above that the same kind of creep simulations based on 2.5-D DD can be described either with a power law or an exponential law. Here, we should point out that our studies were conducted for different dislocations ([100] dislocations at high temperature and [001] dislocations at low temperature) and within distinct temperature ranges. To shed more light on this transition we have further performed a set of calculations where similar elementary deformation mechanisms were introduced (coefficient of diffusion, glide mobility law, …) and the with stress and temperature conditions that vary in wide intervals: 800 K - 1700 K and 50 MPa - 500 MPa. The results are displayed in Figure 5.1.14, which demonstrates that there is no real physical boundary between the power law and the exponential law regimes. Instead, one goes smoothly from one regime to another. Also, contrary to a common belief, we find that the transition is not triggered by temperature, but by stress exclusively.

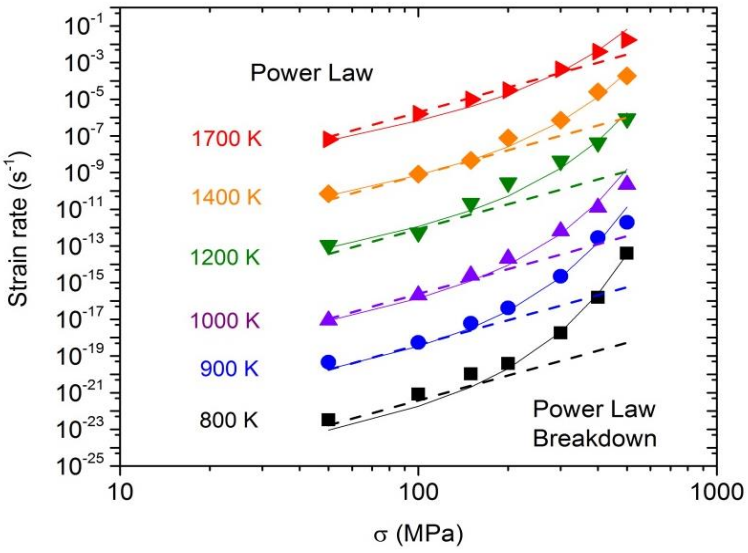

Figure 5.1.14. DD strain-rate values as a function of the applied creep stress σ, for different temperatures T. The dashed lines represent the fit by a power law and the solid lines represent the fit by an exponential law

Indeed, provided that the stress remains below *ca.* 200 MPa, all data can be well described by a power law (dashed straight lines on the figure).

$$\dot{\varepsilon}_{DD,PL} \sim \sigma^{4.5} exp\left(\frac{-4.6}{k_B T}\right) \tag{5.1.4}$$

Above this threshold of 200 MPa, a curvature appears on all the curves of Figure 5.1.14. Deviation from the linear plot (corresponding to the power law) is smaller at high temperature, but it can be detected even at 1700 K. The curvature is very strong for the lowest temperature considered (800 - 900 K). The analysis of internal variables of the simulation reveals no characteristic differences between the two regimes, suggesting that only *one* regime should be considered. The creep behaviour can be described by one law or another depending on the range of parameters considered. However, we show that the exponential law can describe well the creep properties of olivine in the whole stress-temperature ranges:

$$\dot{\varepsilon}_{DD,EL} = 1.7 \times 10^{16} \left(\frac{\sigma}{\mu}\right)^{2.95} exp\left(\frac{-4.77}{k_B T}\left(1 - \left(\frac{\sigma(MPa)}{\tilde{\sigma}}\right)^{1.52}\right)^{2}\right) \tag{5.1.5}$$

where $\tilde{\sigma}$ is a parameter called the mechanical resistance which is equal to 2 GPa in Figure 5.1.14.

References

F. Boioli *et al.* (2015) Phys. Rev. B 92: 014115
F. Boioli *et al.* (2015) Earth Planet. Sci. Lett. 432: 232
S. Demouchy *et al.* (2013) Phys. Earth Planet. Inter. 220: 37
B. Evans & C. Goetze (1979) J. Geophys. Res. 84: 5505
J.R. Weertman (1957) J. Appl. Phys. 28: 362
J.R. Weertman (1955) J. Appl. Phys. 26: 1213

5.2. Pure climb (Nabarro) creep

5.2.1. Climb dissociation in bridgmanite

One of the most striking results presented in section 4.3. is that dislocation glide is severely inhibited in the most abundant silicate minerals of the mantle. Bridgmanite constitutes an extreme case, with Peierls stresses of several GPa that makes dislocation glide in this phase difficult in laboratory conditions, and almost impossible at the extremely low strain rates of the Earth's lower mantle.

Since bridgmanite is deformed at very high temperatures (1500 - 2500 K) in the lower mantle, we decided to go beyond static calculations and to investigate explicitly the effect of temperature on the atomic structure of edge dislocations in bridgmanite. Starting from the [100](010) edge dislocation already described before (and reported again in Figure 5.2.1a), we performed high-temperature molecular dynamics simulations (for technical details, see Hirel *et al.* 2016a).

The configuration of lowest total energy is reported in Figure 5.2.1b. On can see that the dislocation is not spread in its glide plane anymore. Due to the thermal vibrations, it evolved into a different core structure, where the anti-phase boundary (APB) is spread in the (100) climb plane. Hence, we refer to this core as the climb-dissociated dislocation core.

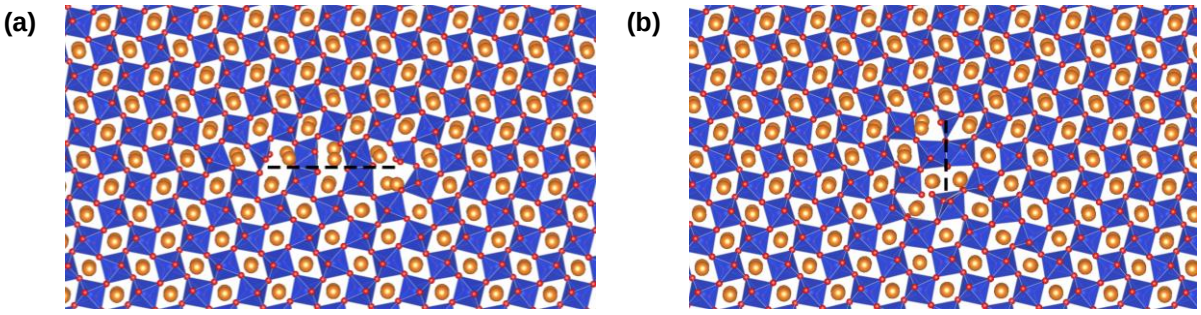

Figure 5.2.1. Atomic configurations of the [100](010) edge dislocation in bridgmanite. Anti-phase boundaries (APB) are overlaid with a dashed line, showing the plane where the dislocation is spread. **(a)** The glide-dissociated core, which is spread and can glide in the (010) plane. **(b)** The climb-dissociated core obtained after high-temperature molecular dynamics and relaxation. This core spreads in the (100) climb plane, and it is sessile, *i.e.* unable to move by glide

In order to characterize this mechanism, we proceeded with the calculation of the energy barrier to transform one core into the other, by means of nudged elastic band (NEB) calculations (section 3.1.5). These calculations revealed that the dislocation overcomes two energy barriers, of 0.013 eV/Å and 0.042 eV/Å respectively. These energy barriers correspond to the separation of SiO_6 octahedra in the initial (010) glide plane, and their bonding in the (100) plane. The energy cost of this mechanism is very small, indicating that it may occur even at moderate temperatures (for more details, see Hirel *et al.* 2016a).

Another surprising result from these simulations is that the energy of the climb-dissociated core is lower by about 0.74 eV/Å than the energy of the initial glide-dissociated core. This is counter-intuitive, because when one introduces an edge dislocation into the system, it spontaneously relaxes into the glide-dissociated core shown in Figure 5.2.1a. There are two reasons for that. First, dislocations are introduced using the displacements of an edge dislocation from the elasticity theory, which assume a «cutting plane»: by construction the dislocation is already dissociated in its glide plane. The sec-

ond reason is that minimization algorithms such as conjugate-gradients only converge towards the closest local minimum of energy, and are completely unable to find the absolute minimum of energy. On the contrary, we demonstrate that climb dissociation occurs by the crossing of energy barriers, which conjugate-gradients cannot cross, but that can be crossed in a molecular dynamics simulation.

Similarly to what was done for the glide-dissociated dislocation, we submitted the climb-dissociated dislocation to shear strain. The dislocation was unable to move up to more than 20 GPa of shear strain, and then critical failure occurred (crystal planes separated in the simulation, which is not realistic). We conclude that the climb-dissociated dislocation is completely sessile, *i.e.* unable to glide. This is consistent with the fact that the APB is spread in the (100) plane, which is normal to the (010) glide plane.

These results reach conclusions beyond the fact that dislocation glide is just *difficult*. Since one character of the dislocations becomes sessile, the whole slip system becomes inhibited at high temperature. The glide of ⟨**100**⟩ dislocations is not just difficult, it becomes simply impossible in the conditions of the Earth's lower mantle.

Moreover, this study points to the limits of static calculations (Peierls-Nabarro modeling or molecular statics calculations). While such calculations can provide accurate results for dislocation glide (like the Peierls stress and energy), they have two drawbacks: first, they rely on a given mechanism (dislocation glide for instance); and second, they do not account for the effects of temperature explicitly (static calculations are commonly referred to as «0 K calculations»). Temperature is introduced only in analytical models, often through the transition state theory. Consequently, any non-trivial effect of temperature (like a change in the atomic core structure) is completely ignored by static models.

5.2.2. Climb as a deformation mechanism

If some dislocations become sessile at high temperature and low strain rate, the only mechanism left for them to move is climb, which occurs when a dislocation absorbs or emits point defects and moves out of its glide plane (Fig. 1.1.10). In the case of bridgmanite, the most abundant and mobile point defects at high temperature are vacancies.

We have investigated the interactions between a [100](010) edge dislocation and individual vacancies in bridgmanite, at the pressure of 30 GPa. Starting from the relaxed configuration, a single atom was removed to create a vacancy, followed by relaxation of the system. The interaction enthalpy is defined as the difference in enthalpy between the systems with and without the vacancy, reduced by the formation enthalpy of a vacancy in the bulk, defect-free material. Performing such a calculation for each possible site provided us with interaction maps for individual magnesium, silicon, and oxygen vacancies.

These interaction maps are summarized in Figure 5.2.2. The interaction enthalpy is reported with a color code, from red (repulsive interaction) to blue (attractive interaction). These interaction maps reveal that the dislocation forms an attractive well for magnesium and silicon vacancies, and is repulsive to oxygen vacancies. Furthermore, the interaction is almost isotropic, *i.e.* it depends only on the dislocation-vacancy radial distance, and not on the fact that the vacancy is above or below the (010) glide plane. These results cannot be explained by considering only elastic effects: indeed, the theory of elasticity predicts that vacancy energy depends whether it is located above or below the glide plane, as evidenced in metals. Here, the peculiar behavior comes from the fact that bridgmanite is an ionic material; hence the Coulomb interaction must be accounted for.

While the electric charge of vacancies is known (it is opposite to the charge of the ion removed), the one of the dislocation was unknown. While vacancies can be approximated as point charges, the dislocation must be approximated as a linear charge distribution. To estimate the electric charge of the dislocation, we developed an atomic-to-continuum approach, inspired by the Ewald summation method. All ions were replaced by a gaussian distribution of charges projected in the plane normal to the dislocation line, and the width of the gaussians was chosen so that their sum resulted in a vanishing electric charge where there was only bulk, defect-free material. Only at defect sites, the sum of gaussians results in non-vanishing electric charge. Then, the resulting electric charge distribution was integrated around the defect, thus yielding its electric charge. At first, we tested this approach with vacancies, and confirmed that it yielded the charge that was expected for this vacancy. Then, when applied to the [100](010) dislocation, we obtained a linear charge of $\boldsymbol{\lambda} \approx 9.17\ 10^{-11}$ C/m, thus confirming that the dislocation carries a positive electric charge.

Further, we developed a model describing the dislocation-vacancy interaction, including both elastic and electrostatic (Coulomb) effects, and fitted this model to the enthalpies obtained from atomistic simulations (Hirel *et al.* 2016b). The fitting parameters are the linear charge $\boldsymbol{\lambda}$ of the dislocation, and the charge q of the vacancy. After the fitting procedure, we obtained a good agreement of the model with simulation data, as shown by the dashed curves in Figures 5.2.2 b, d, and f. Moreover, the fitting procedure yielded a value $\boldsymbol{\lambda} \approx 10^{-10}$ C/m for the charge of the dislocation, close to the one obtained with the previous method.

Then, after removing a magnesium or silicon ion from the dislocation core, we verified that the dislocation then became negatively charged, and attractive to oxygen vacancies.

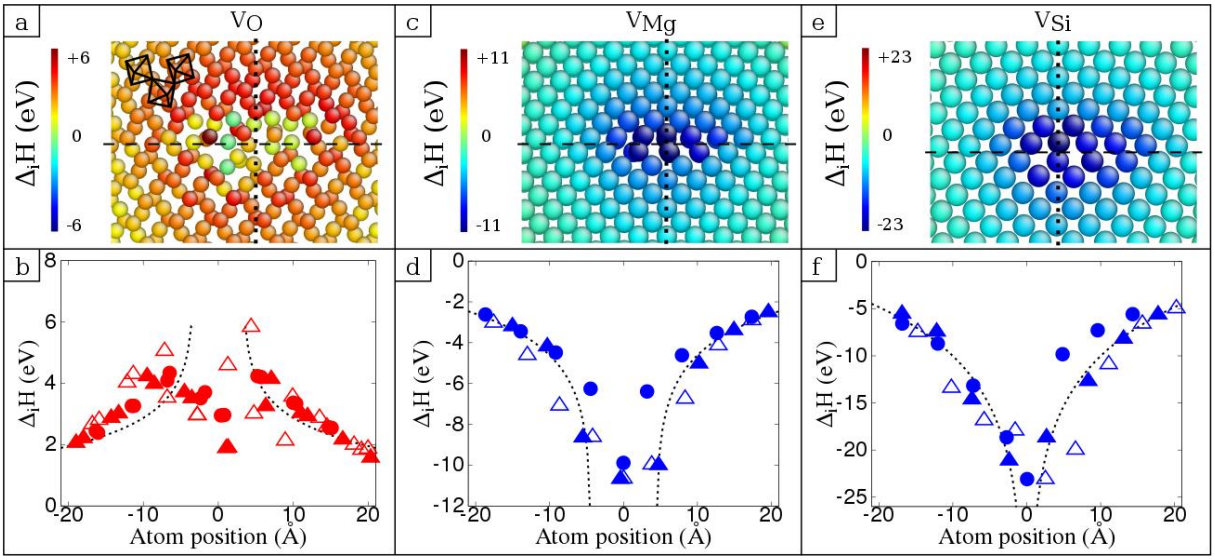

Figure 5.2.2. Interaction enthalpy maps of the [100](010) edge dislocation in bridgmanite with **(a, b)** oxygen vacancies; **(c, d)** magnesium vacancies; **(e, f)** silicon vacancies. Top figures: for each chemical species, only the sites of that species are represented, other atoms are hidden. Yellow to green colors correspond to positive interaction enthalpy (repulsive), shades of blue to negative ones (attractive). Green color corresponds to vanishing interaction enthalpy (*i.e.* the vacancy has the same energy as in the bulk material). Bottom figures: profile of the interaction enthalpies in the (010) plane. Dashed lines are a fit of a model accounting for the Coulomb interaction

This suggests that, as the dislocation climbs, the absorption of vacancies change its electric charge, and makes it attractive to vacancies with an opposite charge. Thus, the dislocation attracts alternatively cation vacancies, then oxygen vacancies, then cation vacancies again, and so on. The details of this mechanism, and the role of jogs in the absorption of vacancies, remain unclear, and should be investigated in future studies.

5.2.3. Pure climb (Nabarro) creep in bridgmanite

Since dislocation glide in bridgmanite is strongly inhibited in the whole pressure range and strain rates of the lower mantle, the standard dislocation (Weertman) creep cannot be considered as an effective deformation mechanism for bridgmanite in the mantle. Alternatively, we propose that dislocations (which are already, for some of them, in climb configuration, see Figure 5.2.1) can move by climb and produce strain along the creep model proposed by Nabarro in 1967 (see section 1.3.1). This model predicts a constitutive equation of the type:

$$\dot{\varepsilon} = \frac{1}{\pi \, ln\left(\frac{4\mu}{\pi\sigma}\right)} \frac{D^{sd}\mu b}{k_B T} \left(\frac{\sigma}{\mu}\right)^3 \tag{5.2.1}$$

where D^{sd} is the self–diffusion coefficient as discussed above, b is the Burgers vector, σ is the applied, deviatoric stress and μ is the shear modulus. Here, it is important to highlight that this equation is based on physics and that it does not depend on adjusted parameters. Hence it is valid for stress and strain-rate conditions of the mantle without any extrapolation.

Alternatively, we have assessed the possibility of bridgmanite to deform by pure climb creep by using dislocation dynamics (Boioli *et al.* 2017). Figure 5.2.3 illustrates the numerical model designed to investigate pure climb creep in bridgmanite. The minimum configuration requires two sets of dislocations with perpendicular Burgers vectors to act as sources and sinks for point defects. Here, contrary to what was presented above for olivine (section 5.1.2), no glide is allowed. Dislocations can only climb at a rate controlled by diffusion. In Boioli *et al.* (2017) we demonstrate that with this configuration, a steady state establishes by exchange of point defects between the two sets of dislocations. In these calculations, the dislocation density was imposed and maintained fixed. Two dislocations densities 10^8 and 10^{12} m^{-2} were considered.

In Figure 5.2.4, we compare the results of the DD simulations of Boioli *et al.* (2017) with the equation of Nabarro (1967). Contrary to Boioli *et al.* (2017) Nabarro's model accounts for steady state conditions by allowing the microstructure to adjust its equilibrium dislocation density with respect to the applied stress. Consequently, the strain rate depends on stress to the power of three. Indeed, in pure climb creep, the dislocation network is established under the balancing influences of dipole annihilation and multiplication from the operation of Bardeen–Herring sources. To compare the results of Boioli *et al.* (2017) with the Nabarro model, one needs to determine which stress corresponds to a given dislocation density. For that purpose, we used the Taylor equation:

$$\rho = \left(\frac{\sigma}{\alpha b \mu}\right)^2 \tag{5.2.2}$$

where α is the adimensional Taylor coefficient (set to unity here), b is the Burgers vector and μ is the shear modulus. The estimated values are b = 4.65 Å and μ = 167 GPa. From

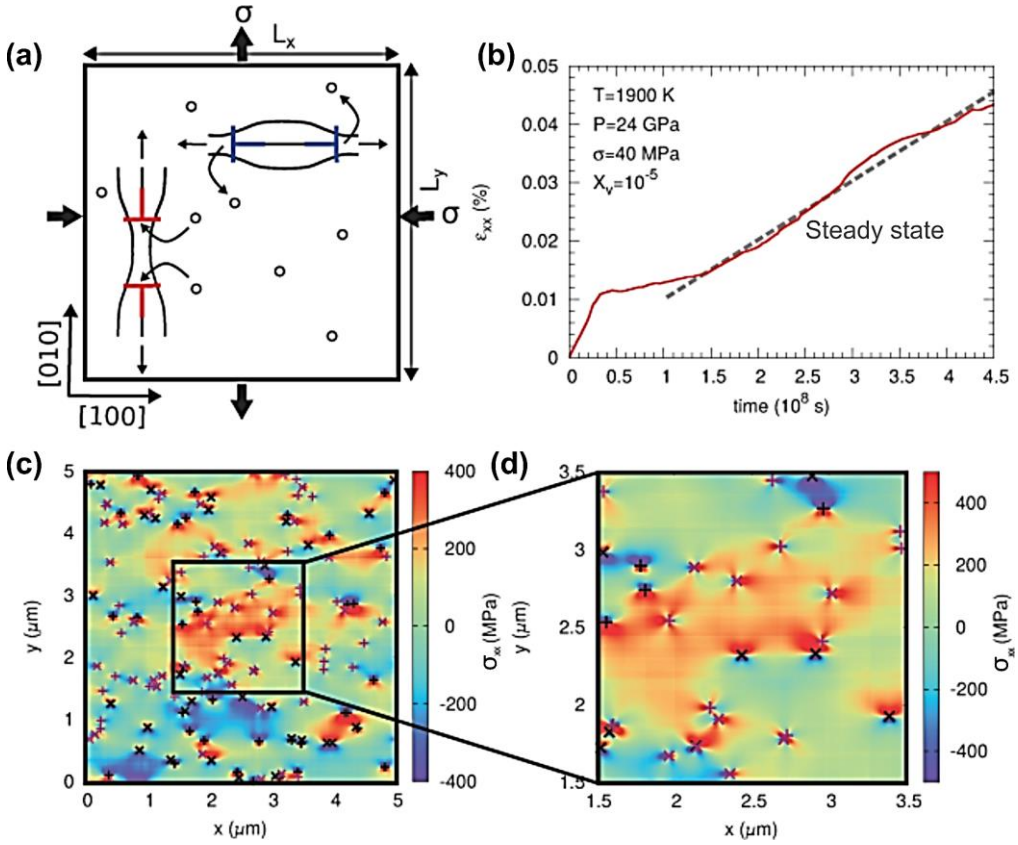

Figure 5.2.3. **(a)** Sketch of a 2D simulation box; **(b)** DD stress-strain curve obtained by applying a creep stress s of 40 MPa at $T = 1900$ K and $P = 24$ GPa. In this case, the initial dislocation density is 10^{12}m^{-2} ; **(c)** Dislocation microstructure and σ_{xx} stress field extracted from the creep simulation at $\varepsilon_{xx} = 0.045\%$. **(d)** Detail of the dislocation microstructure shown in **(c)**

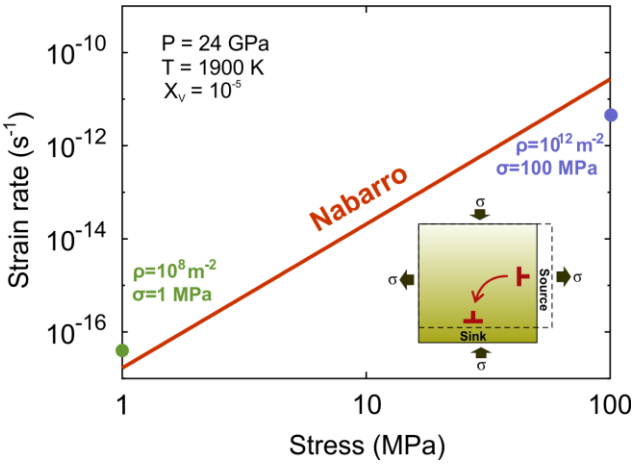

Figure 5.2.4. Comparison of the data from pure climb numerical modeling obtained with DD (circles) with the analytical Nabarro model (red line). The *P-T* conditions as well as the vacancy concentration X_v, are the same for the current model and the numerical simulations results The exact values are provided in the key of the figure

Equation (5.2.2) one finds that that dislocation densities of 10^8 and 10^{12} m^{-2} considered by Boioli *et al.* (2017) correspond to stresses of 1 and 100 MPa respectively. These two values are (Fig. 5.2.4) are in very good agreement with the analytical model (Eq. 5.2.1).

Thus, we can use the Nabarro equation (5.2.1) to model flow properties of bridgmanite under the lower mantle conditions (with no need to extrapolate on the strain rates). However, one faces here another major challenge. Pure climb creep is ultimately controlled by diffusion of some point defects and data on diffusion in bridgmanite are still

very scarce. A careful review of available data (presented in Reali *et al.* 2018) shows that there are two major limitations. First of all, experiments are limited by the extreme *P-T* conditions of the lower mantle down to the CMB. Moreover, diffusion appears to be very slow in bridgmanite and it is difficult to produce diffusion profiles which extend far enough to be reliably measured. From the numerical side, the kinetics of migration of defects can be accurately calculated, but the determination of the actual diffusion coefficient requires knowledge of vacancy concentrations which depend on chemistry, redox state, *etc*. Indeed, the major lesson from computation is that diffusion has to be extrinsic since intrinsic equilibrium concentrations of point defects under mantle *P-T* conditions are far too low (see Fig. 5.2.5a). Taking all these uncertainties into account, we can however produce constraints on the flow of bridgmanite as a function of depth across the whole lower mantle (Fig. 5.2.5b).

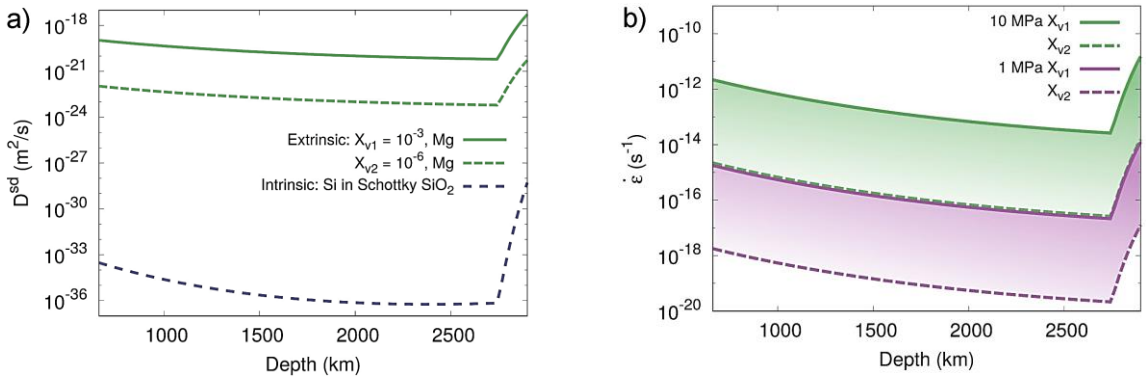

Figure 5.2.5. (a) Diffusion coefficients D^{sd} along the geotherm. The values for intrinsic diffusion obtained from the Si Schottky vacancy formation enthalpy are shown in black. The extrinsic values are given for Mg obtained with two vacancies concentrations $X_{v1} = 10^{-3}$ and $X_{v2} = 10^{-6}$. **(b)** Strain rates of bridgmanite along the geotherm calculated with the pure climb (Nabarro) creep model for stresses of 10 and 1 MPa and vacancy concentrations of 10^{-3} and 10^{-6}

A few messages can be drawn from the Figure 5.2.5b. First of all, the strain rates produced by this model (which has not been adjusted on any *ad hoc* parameter) are in good agreement with those expected in the lower mantle. The sole effect of temperature and pressure across the lower mantle (along the geotherm of Stacey & Davies 2004) yields to a monotonous decrease of the strain rate of less than two *log* units. This variation is much smaller than what can be induced by stress variations (since the rheology of bridgmanite is expected to be nonlinear with $n = 3$) and most importantly by changes in point defect chemistry which may be linked to chemical heterogeneities.

References

F. Boioli *et al.* (2017) Sci. Adv. 3: e1601958
P. Hirel *et al.* (2016a) Scripta Mater. 120: 67
P. Hirel *et al.* (2016b) Acta Mater. 106: 313
F.R.N. Nabarro (1967) Philos. Mag. A 16: 231
R. Reali *et al.* (2018) submitted
F. Stacey & P. Davis (2004) Phys. Earth Planet. Int. 142: 137

Chapter 6

Grain Boundaries

6.1. Modeling disclinations

This work results from a strong collaboration with Claude Fressengeas and Vincent Taupin in Metz

6.1.1. Disclinations as a structural component of grain boundaries

The experimental observation of disclinations in grain boundaries in olivine reported by us in the 06 March 2014 issue of *Nature* (see section 6.3.2 below) has renewed interest in these defects with a particular focus on their potential role in the structure and dynamics of grain boundaries. We have carried out a detailed theoretical study of grain boundaries following the development of the so-called «discrete-to-continuum» crossover method (section 3.2.2 and Fig. 3.2.3). With this technique, one can obtain the relevant kinematic and defect density fields from the knowledge of discrete atomic displacements.

Our approach has been first applied to a Σ37 (610)/[100] symmetrical tilt boundary (Figs. 6.1.1, 6.1.2) with misorientation of 18.9° in copper (Sun *et al.* 2016a). With a misorientation value slightly greater than 15°, one could expect such a boundary to be constructed

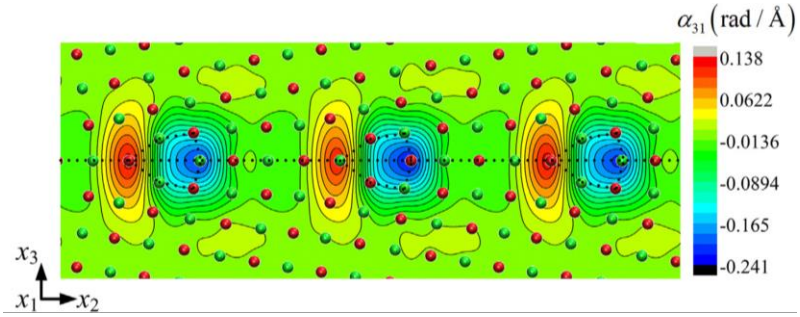

Figure 6.1.1. Copper: (610)/[001] tilt boundary of misorientation 18.9°. Edge dislocation density components α_{31} on top of the relaxed atomic structure. The component α_{31} renders dislocation lines of edge character aligned along the axis x_1 and with their Burgers vectors along the axis x_3

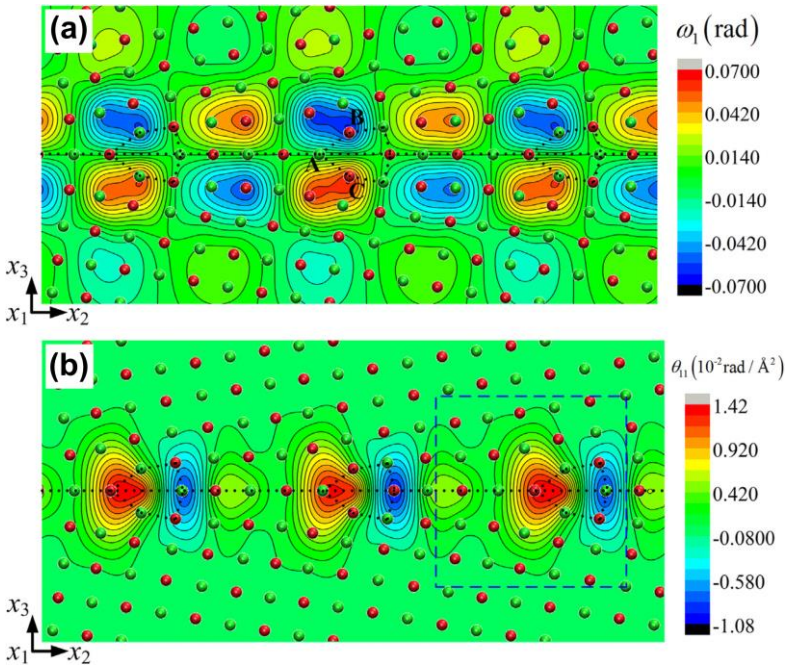

Figure 6.1.2. Copper: (610)/[001] tilt boundary of misorientation 18.9°. **(a)** Tilt rotation field ω_1; **(b)** wedge disclination density field θ_{11}

by geometrically necessary dislocations exclusively. Indeed, we observe a dislocation density field within the boundary which is consistent with its tilt character.

Besides dislocations, one observes discontinuities in the tilt rotation field ω_1 which indicate the presence of disclinations within the boundary (Fig. 6.1.2). Moreover one also observes that the boundary contains local shear strain discontinuities (Fig. 6.1.3). This situation goes beyond the cases originally described by Volterra where discontinuities were considered only on the elastic displacement field (leading to a dislocation density tensor) and to the elastic rotation field (leading to a dislocation density tensor). The strain fields remained continuous in those cases. In the more general case where the elastic distortion tensor exhibits discontinuities, the concept of disclinations must be generalized. In 2012, Acharya and Fressengeas defined a third-order elastic second distortion tensor **G**:

$$\mathbf{G} = \mathbf{grad}\,\mathbf{U} \tag{6.1.1}$$

If discontinuities of the elastic distortion are present, the tensor **G** contains an additional incompatible part whose curl yields the third-order generalized-disclination density tensor:

$$\boldsymbol{\pi} = \mathbf{curl}\,\mathbf{G} \tag{6.1.2}$$

Figure 6.1.3a shows the discontinuities of the shear strain field E_{23} that translates into a non-vanishing generalized-disclination field whose component π_{321} is displayed in Figure 6.1.3b.

This study reveals an unexpected complexity of grain boundaries. Despite its apparent simplicity (simple chemistry, symmetrical tilt boundary, low misorientation), a simple description in term of edge dislocations fails to describe all aspects of the Σ37 (610)/[100] tilt boundary. Indeed, our analysis shows the presence of standard wedge disclination dipoles, but in addition to that, unexpected features are evidenced, such as the presence of localized shear distortion discontinuities and second-order incompatibility associated with the presence of generalized-disclination dipoles in the structural units.

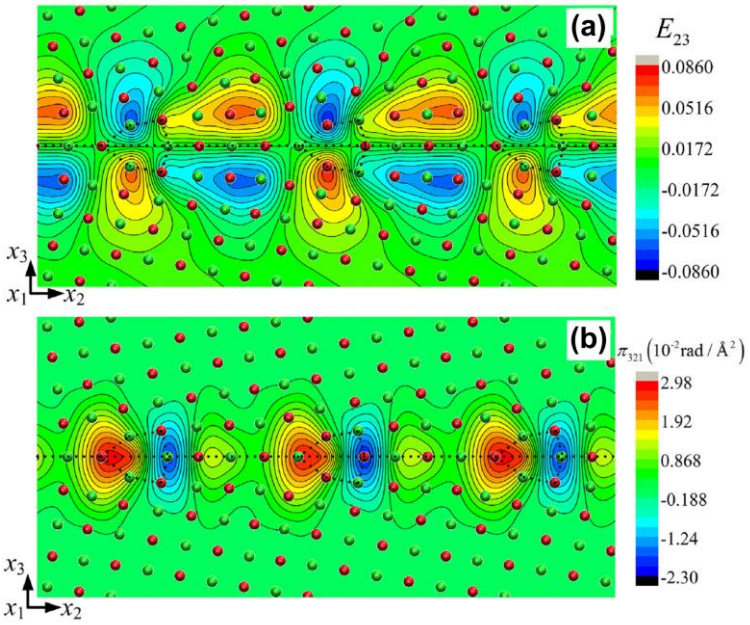

Figure 6.1.3. Copper: (610)/[001] tilt boundary of misorientation 18.9°. **(a)** In-plane Green-Lagrange shear strain E_{23}; **(b)** corresponding generalized-disclination component π_{321}

6.1.2. Disclination dynamics and shear-induced grain boundary migration

One of the main expectations in developing a disclination-based theory of grain boundaries is not only to provide a more accurate description of boundaries, but also of their dynamics (Acharya 2001, Taupin *et al.* 2014). Applying elastic shear strains generates couple stresses in the defective areas (similarly to the Peach-Koehler forces to dislocations) which set disclinations (and hence the boundary) into motion (Fig. 6.1.4). Disclination motion implies motion of the associated dislocation density which in turn produces plastic shear. The grain boundary migration is thus accompanied by plastic shear.

These results suggest that an appropriate, continuous description involving displacement and crystal defect density fields that are smooth over a length scale of interatomic spacing can be adequate for the purpose of describing the structure but also the dynamics of boundaries.

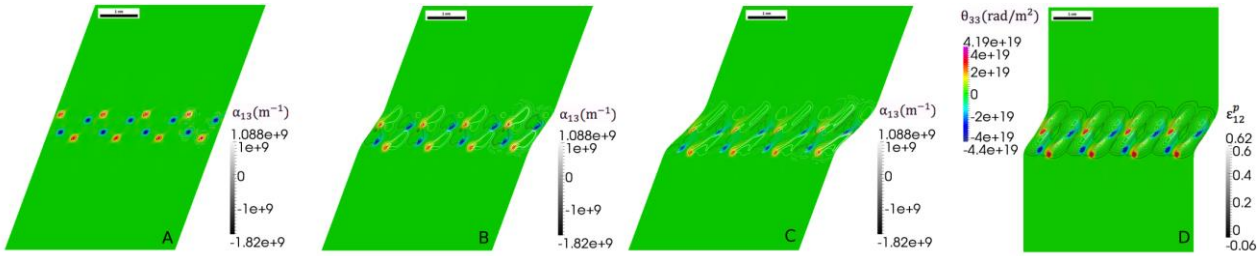

Figure 6.1.4. Shear-coupled boundary migration of a grain boundary made of a distribution of disclination quadrupoles. Images **(A)** to **(C)** show the downward migration of the disclinations when a positive shear strain is applied. Black and white contours show the edge dislocation density. **(D)** depicts the unloaded bicrystal revealing shear-coupled migration

6.1.3. Disclinations, disconnections and shear-induced grain boundary migration

Some recent *in situ* transmission electron microscopy studies (Rajabzadeh *et al.* 2014) have suggested that, under stress, grain boundary migration occurs via the motion of elementary steps. The moving steps possess a dislocation content and thus are generally termed *disconnections* (Hirth & Pond 1996). To clarify the nature of those defects, we have used our discrete-to-continuum crossover method (Fig. 3.2.3) to build the relevant kinematic and defect density fields of a Σ17 (410) tilt boundary in a copper bicrystal involving ledges on the basis of discrete atomic displacements (Combe *et al.* 2016). The ledges appear to be characterized by discontinuities of the elastic rotation and dilatation fields, which are reflected by non-vanishing generalized disclination density fields (Fig. 6.1.5).

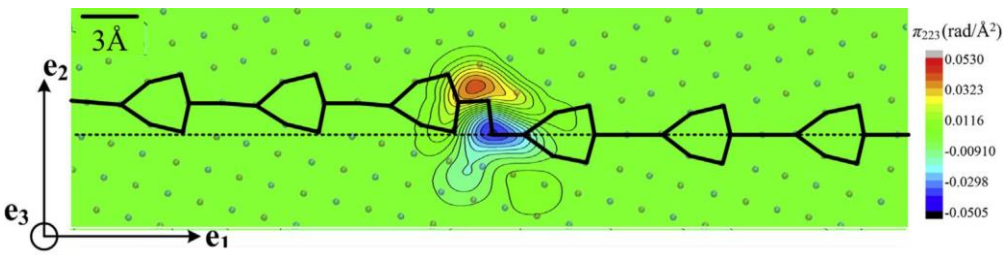

Figure 6.1.5. Copper: g-disclination π_{223} field on top of a ⟨100⟩ ledge in a tilt boundary Σ17(410)/[001]

The elastic properties of so-called disconnections, their response to an applied stress and their interactions with other crystal defects may therefore be interpreted by using the elastostatic equations of the mechanical theory of dislocation and *g*-disclination fields (Acharya & Fressengeas 2012). The present analysis opens avenues for the incorporation of grain boundary dynamics in coarse-grained models of plasticity.

References

A. Acharya (2001) J. Mech. Phys. Solids 49: 761
A. Acharya & C. Fressengeas (2012) Int. J. Frac. 174: 87
N. Combe *et al.* (2016) Phys. Rev. B 93: 024109
J. Hirth & R. Pond (1996) Acta Mater. 44: 4749
A. Rajabzadeh *et al.* (2014) Acta Mater. 77: 223
V. Taupin *et al.* (2014) Int. J. Plast. 53: 179
X-Y. Sun *et al.* (2016a) Int. J. Plast. 77: 75

6.2. Grain boundaries and disclinations in MgO

Recent experimental works (*e.g.* Cordier *et al.* 2014) highlight that grain boundaries could play a major role in the deformation of olivine. Given the high temperatures involved, it seems natural to expect that they also play a role in the deformation of other abundant minerals of the lower mantle – (Mg,Fe,Al)(Si,Fe,Al)O_3 bridgmanite and (Mg,Fe)O ferropericlase. In this section we focus on symmetric tilt grain boundaries (STGBs) in MgO.

6.2.1. Atomic description

Constructing planar defects such as grain boundaries in ionic crystals commonly rises the problem of charge compensation. The rocksalt lattice of MgO contains charge-neutral rows along certain crystallographic directions, like ⟨**100**⟩ or ⟨**111**⟩. This ensures that, when cutting a crystal along any plane containing such a direction, the remaining part of the crystal is charge-neutral, which simplifies the construction of grain boundaries. We investigated symmetric tilt grain boundaries (STGBs) in MgO at the atomic scale using the procedure described in section 3.1.7.

The first results of these calculations is the grain boundary formation energy, plotted in Figure. 6.2.1 as a function of the misorientation angle (varying from $\alpha = 0$ up to $\alpha = 90°$). At the beginning, for $\alpha = 0°$ up to $\alpha = 20°$, the formation energy increases smoothly. Observation of the atomic structure shows that these low-angle grain boundaries are formed of individual dislocations with a Burgers vector $b = [010]$, equally spaced and separated by perfect crystal, as shown at the top left of Figure 6.2.2. These results are consistent with the Read-Shockley model of low-angle grain boundaries, which energies are also represented as a dashed curve in Figure 6.2.1.

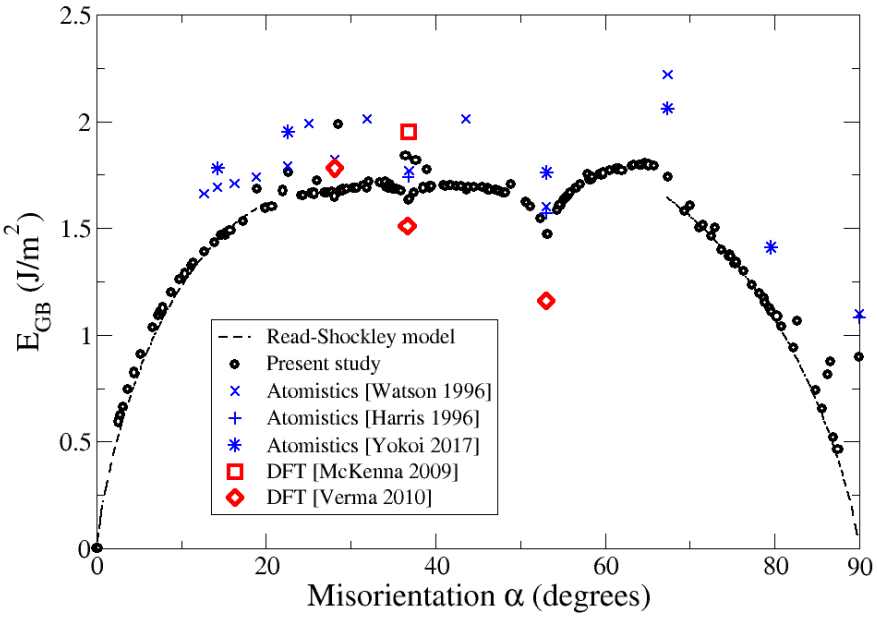

Fig. 6.2.1. Energy of {hk0}[001] symmetric tilt grain boundaries in MgO, as a function of the misorientation between the two grains. Black circles represent our results from atomistic simulations. Our results are compared with previous atomistic simulations (shown in blue), with *ab-initio* calculations (shown in red), and with the Read-Shockley model (dashed lines, using [010] dislocations for $0° < \alpha < 20°$, and ½[110] dislocations for $67.4° < \alpha < 90°$)

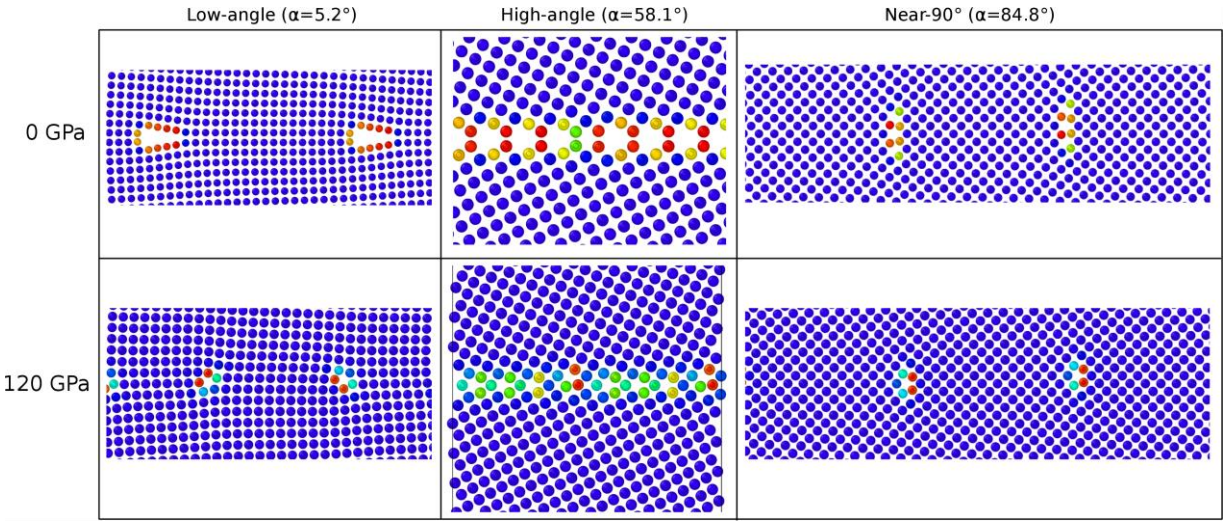

Figure 6.2.2. Atomic structure of some grain boundaries at ambient pressure (0 GPa, top figures), and at 120 GPa (bottom figures). Low-angle grain boundaries are characterized by an array of individual dislocations, with [010] Burgers vector for $\alpha<20°$ (left figures), and ½[110] Burgers vector for $67.4<\alpha<90°$ (right figures). In between, high-angle grain boundaries ($20°<\alpha<67.4°$) are characterized by periodic structural units, in the form of hollow cages at ambient pressure (middle top figure), which become much more compact at high pressure (middle bottom figure). The color code highlights local strain concentration in the system

6.2.2. Effect of pressure

All grain boundaries previously constructed at ambient pressure (P = 0 Pa) were brought to high pressures. Four pressures relevant to the Earth's lower mantle were considered: 30 GPa (close to the transition zone), 60 GPa, 90 GPa, and 120 GPa (close to the core-mantle boundary). In addition to the formation enthalpy, the excess volume was computed and monitored as pressure increased. The excess volume represents the expansion of the crystal that is due to the grain boundary.

The enthalpy of the grain boundary formation increases drastically with pressure (Fig. 6.2.3). While it plateaued around 1.7 J/m² at ambient pressure, it increases to almost 3 J/m² at 30 GPa, and saturates around 5 J/m² at 120 GPa.

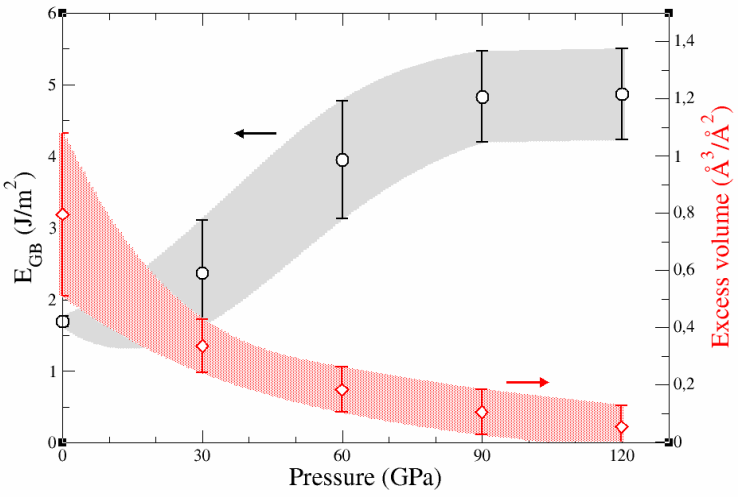

Figure 6.2.3. Evolution of the mean grain boundary formation enthalpy (shown in black and grey), and of the formation excess volume (shown in red) with pressure

Now, the most spectacular change lies in the atomic structures of the grain boundary. With increasing pressure, the hollow cages that existed at ambient pressure are replaced by more compact structural units, as illustrated in Figure 6.2.2.

All grains adopt a new compact configuration at 30 GPa. Then, some of them keep this configuration up to 120 GPa, while others change their configuration again as the pressure increases. Because of this, the increase in energy is not linear with pressure, and depends on the grain boundary that is considered. Nonetheless, the increase in energy can be averaged over the pressure range studied, as reported in Figure 6.2.3. The overall evolution with pressure is interpolated, and represented as a grey area. This overview shows that formation enthalpies increase with pressure, up to about 90 GPa where they seem to saturate.

The compaction of grain boundaries can be quantified by the excess volume, which is the ratio of the volume of the cell containing a grain boundary and a defect-free cell, divided by the area of the boundary. This quantity is maximum at ambient pressure, because in the absence of any applied force, atoms tend to maintain their equilibrium distance with their neighbors, which results in the hollow structural units described before. Excess volumes reach about 0.8 ± 0.2 Å. This situation changes dramatically as pressure increases: atoms are then forced closer to one another, and they have to find ways to achieve greater compaction to minimize their energy. This results in a large drop of excess volume to a value of 0.35 ± 0.1 Å at 30 GPa, as reported in Figure 6.2.3. As pressure increases, excess volumes decrease further, reaching a very low value of *ca.* 0.1 Å at 120 GPa.

6.2.3. Continuous fields and disclinations

Figure 6.2.4 illustrates the atomic structure of (310)/[001] symmetric tilt boundary in MgO with misorientation of 36.8°. Similarly to copper, one finds that the tilt boundary cannot be described with dislocations only and that disclinations and *g*-disclinations (since discontinuities were found on components of the distortion tensor) must be introduced to fully describe the boundary. Compared to monoatomic copper, MgO has an anionic and a cationic sublattice. Our atomistic-to-continuum crossover method (Fig. 3.2.3) provided identical results for these sublattices (Fig. 6.2.5) indicating that they are fully equivalent from the displacement point of view. The fields can thus be calculated by measuring displacements from any atomic species in this structure (Sun *et al.* 2017).
The evolution of the disclination content in a (310)/[001] grain boundary with pressure has been studied up to 150 GPa (Sun *et al.* 2016b). The results presented in Figure 6.2.6 correspond to the asymmetric boundary which, at high pressure, appears to be more stable than the symmetric one. The strong effect of pressure on the structure of grain boundaries also strongly influences the structural content of defects.

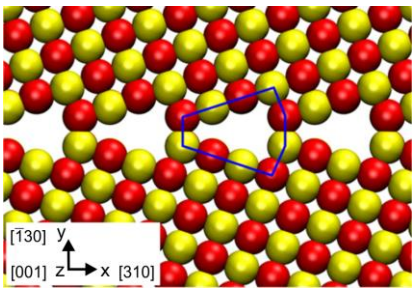

Figure 6.2.4. Atomic structure of a symmetric (310)/[001] grain boundary in MgO. Mg atoms are shown in yellow, O - in red

Up to 50 GPa (Fig. 6.2.6 a-b), the disclination dipoles are arranged in a zigzag manner, similar to that in rotation fields. At 100 GPa and above (Fig. 6.2.6 c-d) their structure is very different. Disclination dipoles are arranged along a straight line parallel to the boundary plane. We anticipate that such changes have potential impact on the mobility of boundaries

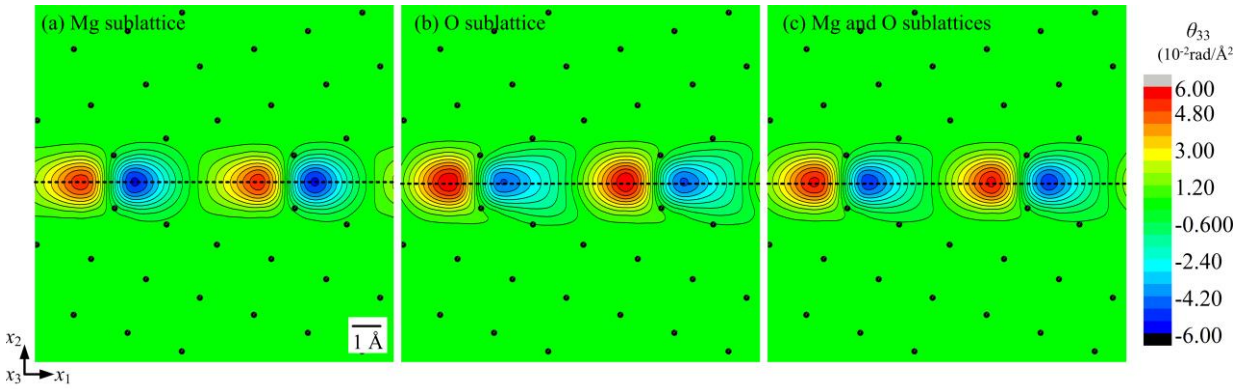

Figure 6.2.5. Disclination density fields of a symmetric (310)/[001] grain boundary in MgO calculated for different sub-lattices

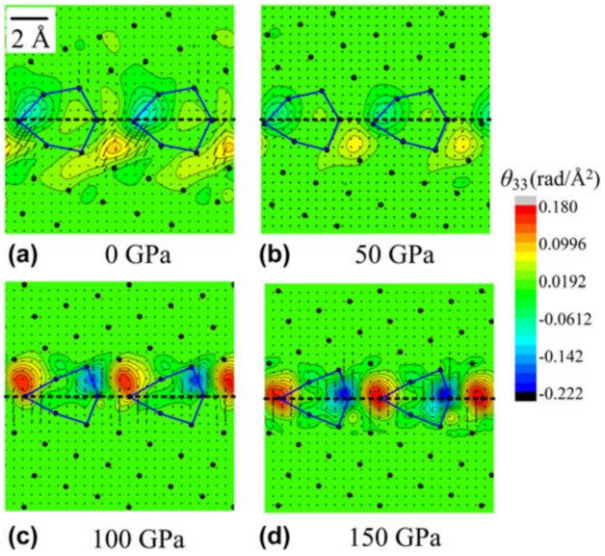

Figure 6.2.6. Disclination density field for a asymmetric (310)/[001] grain boundary in MgO computed at pressures of **(a)** 0 GPa, **(b)** 50 GPa, **(c)** 100 GPa, and **(d)** 150 GPa. The local Burgers vectors are shown with arrows

under stress, which consequently could affect the contribution of grain boundaries to the plasticity of polycrystalline aggregates. To quantify these effects further calculations should be performed.

References

P. Cordier *et al.* (2014) Nature 507: 51
D. Harris *et al.* (1996) Phil. Mag. 74: 407
K. McKenna & A. Shluger (2009) Phys. Rev. B 79: 224116
X.-Y. Sun *et al.* (2016b) J. Mater. Res. 31: 3108
X.-Y. Sun *et al.* (2017) Eur. J. Miner. 29: 155
A. Verma & B. Karki (2010) Amer. Miner. 95: 1035
G. Watson *et al.* (1996) J. Chem. Soc. Faraday Trans. 92: 433
T. Yokoi & M. Yoshiya (2017) Physica B Cond Matter 532: 2

6.3. Grain boundaries and disclinations in olivine

6.3.1. Continuous description of a grain boundary in forsterite

Here we consider a high-angle 60.8° symmetric (011)/[100] tilt boundary in forsterite for which a model at the atomic scale had been calculated (Adjaoud *et al.* 2012). In a silicate olivine, the rendering of a smooth continuous description from atomic positions needs to face the complexity of crystal chemistry. We have applied our technique independently to the three sub-lattices: O, Si and Mg. Figure 6.3.1 illustrates the computed rotation fields.

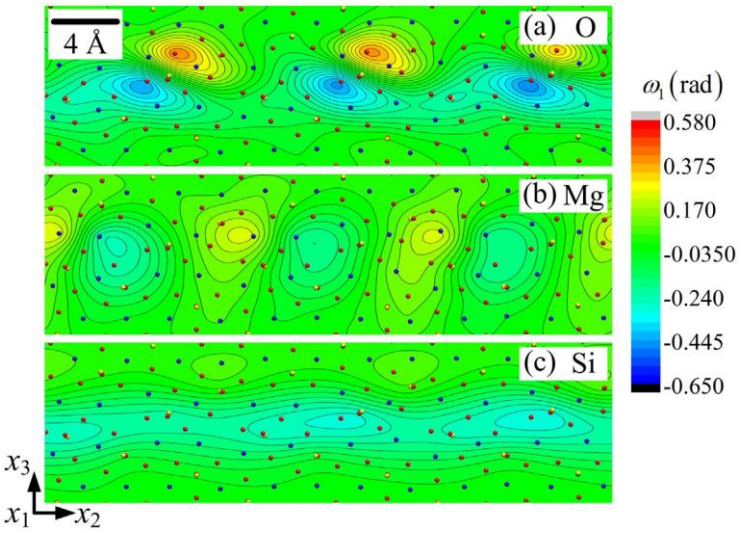

Figure 6.3.1. Forsterite: 60.8° symmetric (011)/[100] tilt boundary. Rotation fields $\boldsymbol{\omega_1}$ for the **(a)** oxygen, **(b)** magnesium and **(c)** silicon sub-lattices

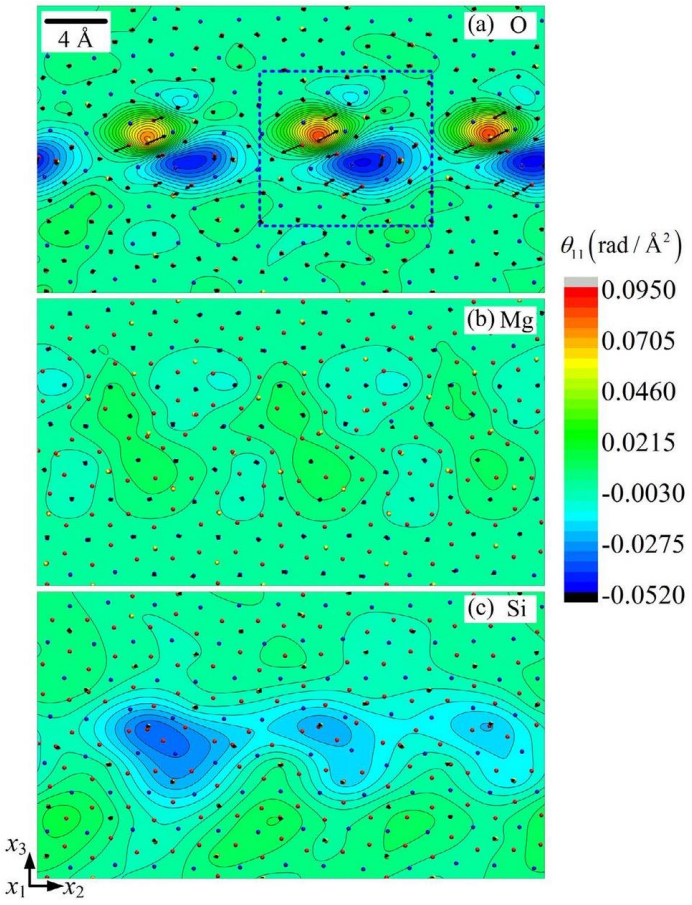

Figure 6.3.2. Forsterite: 60.8° symmetric (011)/[100] tilt boundary. Dislocation density fields $\boldsymbol{\theta_{11}}$ (shown in colour) and Burgers vector fields (shown with arrows) for **(a)** oxygen, **(b)** magnesium and **(c)** silicon sub-lattices

From the point of view of the deformations, the grain boundary represents a layer about 5 Å thick with a clear periodicity of features (essentially dipolar for O and Mg) along the boundary. The presence of discontinuities on the rotation field is clearly visible with dipoles where rotation abruptly changes sign. Without surprise, this gives rise to a marked distribution of disclination dipoles along the boundary (Fig. 6.3.2).

The structure of forsterite can be considered as orthorhombically distorted hcp array of oxygen anions, where one half of the available octahedral interstitial sites are occupied by Mg cations and one-eighth of the tetrahedral sites by Si cations (see section 2.2.1 for more details about olivine structure). Since the densely packed oxygen sub-lattice represents the skeleton of the structure, it carries most of the incompatible strain and curvature fields associated with the dislocation and disclination fields. Because of the strong covalent Si-O bonding, the Si sub-lattices also carries a significant contribution whereas the contribution of the Mg sub-lattice is close to zero.

6.3.2. Observation of disclinations in olivine by EBSD

One of the reasons which have slowed down the recognition of the importance of disclinations in materials science is the lack of observations since disclinations cannot be imaged by standard microstructural investigation techniques like TEM. The development of EBSD and associated post-treatment techniques developed in Metz by B. Beausir and C. Fressengeas has however opened new avenues in the characterization of disclinations. With EBSD (data acquisition presented here have been performed in Montpellier), one has access with a high spatial and angular resolution to the local orientations of crystals.

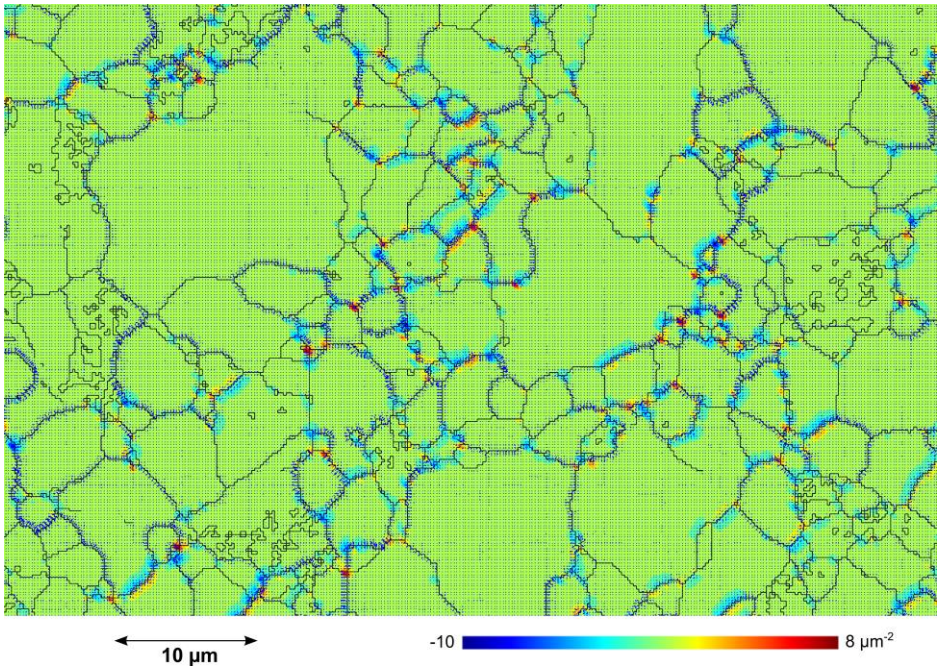

Figure 6.3.3. Density of wedge disclinations θ_{33} (in rad/μm^2) in a sintered olivine sample. The experiment was published in Cordier *et al.* (2014)

From the orientation differences $\Delta\theta_i$ between neighbouring points separated by Δx_j the elastic curvature tensor κ_{ij}^e (with only six accessible components) can be captured:

$$\kappa_{ij}^e = \frac{\partial \theta_i}{\partial x_j} \approx \frac{\Delta \theta_i}{\Delta x_j} \tag{6.3.1}$$

The Nye dislocation α and disclination density θ tensors can be deduced from the knowledge of κ_{ij}^e :

$$\begin{aligned} \alpha_{ij} &= \delta_{ik}\kappa_{mm}^e - \kappa_{ki}^e \\ \theta_{ij} &= e_{jkl}\kappa_{il,k}^e \end{aligned} \tag{6.3.2}$$

Using this technique, disclination dipoles could be observed in all investigated olivine samples (natural, experimentally deformed and not deformed). It must be pointed out that both numerical and experimental approaches are scale-dependent and by nature they do not capture the same aspects.

Disclinations do exist. We can now detect them. It took about 40 years between the proposition of *distorsions* by V. Volterra and the first observations of dislocations in transmission electron microscopy. Sixty more years have been necessary before disclinations could be imaged in crystalline solids. This concept is really a new-born in a field, the mechanics of grain boundary, which is also in its infancy. We need more observations to assess the importance and effective contribution of disclinations to the dynamics of grain boundaries. How many years before we can see disclinations moving as we could, for the first time, with dislocations in olivine during this project ?

6.3.3. Grain boundary migration in forsterite

Here we present some preliminary results showing the evidence for grain boundary migration in forsterite. Figure 6.3.4a shows an orientation map in a deformed forsterite aggregate where three grains containing subgrain boundaries can be seen. The subgrain boundary labelled «1» and the grain boundary «3» exhibit curvy shapes which deviate

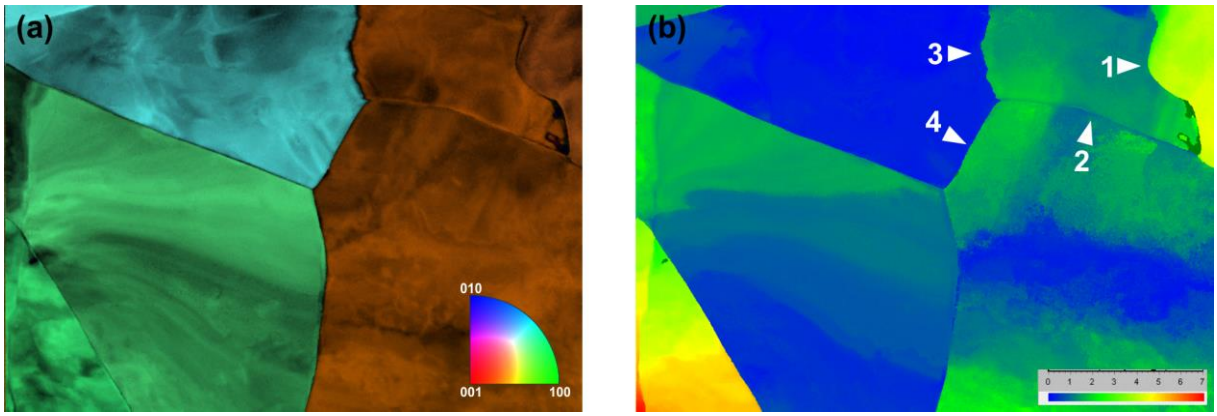

Figure 6.3.4. Forsterite aggregate deformed at 110°C, 3.5 GPa, 25% (C. Bollinger). **(a)** Inverse pole figure corresponding to the direction perpendicular to the plane of view. Colour code indexed in the *Pnma* space group is inserted. **(b)** GROD (Mis2Mean see section 3.3.2) map corresponding to **(a)**

From the equilibrium straight configurations. Such curvatures can be interpreted as an indication of mobility by grain boundary migration. This is however usually difficult to demonstrate in *post-mortem* specimens. The main driving force for grain boundary migration is the strain energy stored in the grains resulting from dislocations introduced during plastic deformation. Here we show that the GROD map provides a visualization of the intragranular misorientations which constitutes a good proxy for the stored strain energy. We see that in good agreement with the theoretical description, the highest strained area is associated with the centre of curvature of the subgrain «1». The same conclusion is more difficult to draw with the grain boundary «3» given the smallest wavelength of the waviness of the boundary. However, there is a clear gradient of strain, hence driving force across this boundary. Interestingly, grain boundaries «3» and «4» which are only slightly different (different misorientation due to the subgrain «2» and slightly different planes) exhibit different aspects. Only «3» suggest being mobile while «4» seems to be more «at equilibrium». This may reflect a strong orientation dependence of grain boundaries mobility, an important aspect to take into account in the mechanics of grain boundaries.

References

O. Adjaoud *et al.* (2012) Phys. Chem. Miner. 39: 749
P. Cordier *et al.* (2014) Nature 507: 51

Chapter 7

Implications

Implications

The RheoMan project represents a sustained effort to design a new approach of the rheology of the mantle based on the physics of deformation of minerals. In this chapter we summarise and discuss some important geophysical implications that can be derived from the rheological properties of the abundant mantle minerals described in previous chapters.

7.1. Olivine in the lithospheric mantle: weaker than previously thought?

The rheology of the lithospheric mantle plays an important role in plate tectonics. Continental plates deform, but the question how. From the mineral physics point of view, this issue is addressed through the rheology of olivine. Most deformation experiments on this phase have been performed at high temperature. The empirical flow laws determined at high temperature and laboratory strain rates in the order of $\dot{\varepsilon} = 10^{-5}$ s^{-1} must be extrapolated to *ca.* 873 K and $\dot{\varepsilon} = 10^{-14}$ s^{-1} to infer the behaviour of the lithospheric mantle and this leads to stresses of about 1 GPa which suggest that it may deform by brittle failure. This possibility is however challenged by the low occurrence of mantle earthquakes in continental domains. Several experimental programs have been devoted to the low-temperature plasticity of olivine. The results are scattered but the vast majority of them point to quite high stress levels (Fig. 7.1.1).

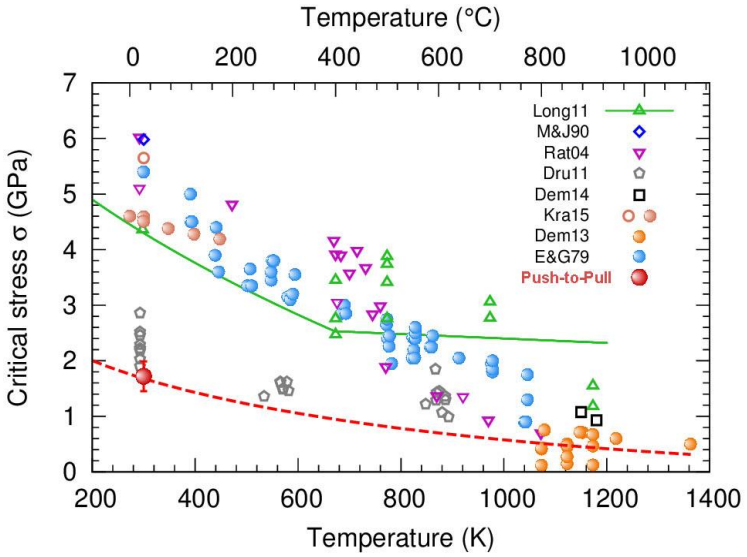

Figure 7.1.1. Critical stress for plastic flow of olivine as a function of temperature. The red dots describe our work based on the DD calculations informed by the dislocation velocity measurements of the Push-to-Pull experiments (see sections 3.3.3 and 4.1.1). The reported Push-to-pull results are from Idrissi *et al.* (2016). Orange dots are from Demouchy *et al.* (2013). Our proposition (red dashed line) is close to the results from Druiventak *et al.* (2011). For the other references on the experimental data, please refer to the reference list in the end of this section. The figure was published in Idrissi *et al.* (2016)

There are however good reasons to question the relevance of these results. A recent study has proposed that some measurements might be biased by a «size effect» (Kumamoto *et al.* 2017). We consider that these tests driven under high stresses are strongly strain-hardened. The process is illustrated in Figure 5.1.12 which describes the onset of dislocations entanglements that create obstacles to further glide. Due to the low tempera-

ture, recovery mechanisms are too slow to operate. Moreover dislocation mobility is low and dislocations continuously produced accumulate and reach high densities. Most experiments presented in Figure 7.1.1 thus characterize the rheology of strongly hardened olivine which might poorly describe how olivine is creeping in the lithospheric mantle. As recognized by Kumamoto *et al.* (2017) we suggest that our mixed approach (Idrissi *et al.* 2016) involving micromechanical tests and DD numerical modelling may be a better approach to describe flow of olivine in nature. Figure 7.1.1 illustrates our proposition of what the lower bound of olivine rheology might be at low temperature (dashed red line). This curve links our data obtained at room temperature in the push-to-pull (sections 3.3.3 and 4.1.1) and the recent accurate mechanical data of Demouchy *et al.* (2013) obtained in the Paterson apparatus (orange symbols). From this curve, one can infer the rheology of olivine at the temperatures of the lithospheric mantle. Complementary to the experiments, several numerical creep tests have been conducted by Boioli *et al.* (2015). The main results of these calculations are presented in section 5.1.2 and summarized here in Figure 7.1.2 in comparison with geodynamical data for lithospheric plates.

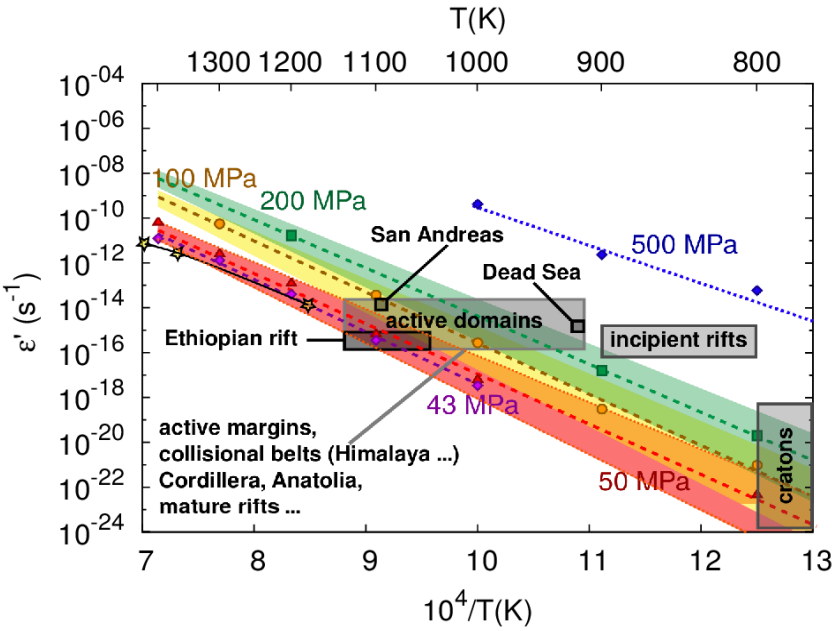

Figure 7.1.2. Calculated 2.5-D DD strain-rate values $\dot{\varepsilon}$ as a function of the reciprocal temperature. Colors indicate calculations for different stresses. The creep strain-rates obtained by using the Si self-diffusion coefficient measured in anhydrous forsterite (Fei *et al.* 2012) are shown by full symbols and dashed lines (D_0 =2.51 × 10 $^{-7}$ m^2/s and H_{Si}^{sd} = 4.25 eV = 410 kJ/mol). The upper and the lower limits of the colored bands represent the 2.5-D DD results obtained by considering the Si self-diffusion coefficient values of: D_0 = 1.68·10^{-7} m^2/s and H_{Si}^{sd} = 3.71 eV = 358 kJ/mol (Costa & Chakraborty 2008) and D_0 = 6.31·10^{-5} m^2/s; H_{Si}^{sd} = 5.48 eV = 529 kJ/mol (Dohmen *et al.* 2002), for anhydrous and hydrous olivine, respectively. Squares delimitate strain-rate – temperature conditions inferred for lithospheric plates in different geodynamic situations. The figure is taken from Boioli *et al.* (2015)

In this figure, the coloured bands represent the uncertainty on the diffusion data introduced in the model depending either hydrous or anhydrous conditions are considered. The boxes describe orders of magnitude for some natural processes where strain-rates are constrained by GPS data and temperatures are estimated at the Moho. Our results suggest that, except in incipient rifts, most of the deformation observed can be produced

by stress levels <200 MPa, which is consistent with the stresses related to convection processes.

References

F. Boioli *et al.* (2015) Earth Planet. Sci. Lett. 432: 232
F. Boioli *et al.* (2017) Sci. Adv. 3: e1601958
B. Buffett (2007) Geophys. Res. Lett 34: L17302
F. Costa & S. Chakraborty (2008) Earth Planet. Sci. Lett. 166: 11
S. Demouchy *et al.* (2013) Phys. Earth Planet. Int. 220: 37
S. Demouchy *et al.* (2014) Tectonophysics 623: 123
R. Dohmen *et al.* (2002) Geophys. Res. Lett. 29: 26
A. Druiventak *et al.* (2011) Earth Planet. Sci. Lett. 311: 199
B. Evans *et al.* (1979) J. Geophys. Res 84: 5505
H. Fei *et al.* (2012) Earth Planet. Sci. Lett. 345: 95
H. Idrissi *et al.* (2016) Sci. Adv. 2: e1501671
H. Long *et al.* (2011) Earth Planet.Sci. Lett. 186: 23
C. Meade & R. Jeanloz (1990) Nature 348: 533
K. Kranjc *et al.* (2015) Geophys. Res. Lett. 43: 176
K.M. Kumamoto *et al.* (2017) Sci. Adv. 3: e1701338
P. Raterron *et al.* (2004) Phys. Earth Planet. Int. 145: 149

7.2. Climb in the deep mantle

One of the most important results of the project with profound implications on our understanding of mantle rheology is that in silicates, lattice friction drastically increases with pressure. This fact is observed already in the high-pressure polymorphs of olivine present in the mantle transition zone: wadsleyite and ringwoodite. Similarly to olivine (Fig. 5.1.8) we provide here the ratios between the glide and the climb velocities in the minerals of the transition zone (Fig. 7.2.1).

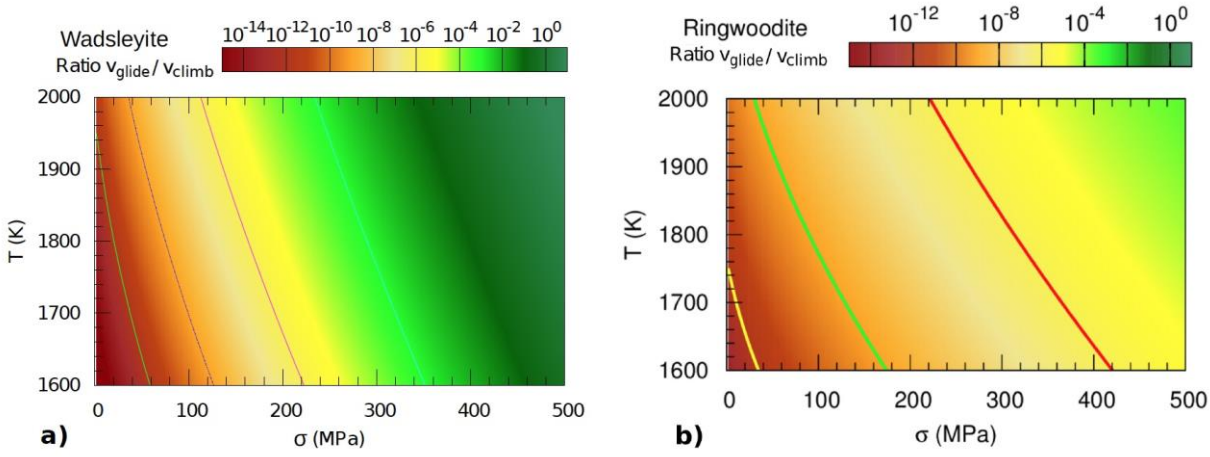

Figure 7.2.1. Ratio of the glide vs climb velocities as a function of the applied stress σ and temperature T for: **(a)** the easiest ½⟨111⟩{101} slip system in wadsleyite at 15 GPa; **(b)** the easiest ½⟨110⟩{110} slip system in ringwoodite at 20 GPa

In Figure 7.2.1, one can see that the standard hypothesis for Weertman creep, where strain is produced by faster gliding dislocations can only be achieved at high stresses and strain-rates (here the calculations are equally valid for laboratory conditions, *i.e.* high stresses and strain-rates, and for the mantle conditions, *i.e.* low stresses and strain-rates, with no extrapolations). At mantle strain-rates corresponding to stresses of a few tens of MPa at the most, Figure 7.2.1 shows that dislocations in both ringwoodite and wadsleyite are immobile in glide compared to their climb mobility. This phases must then deform by pure (Nabarro) climb creep (Fig. 1.1.12b) under the mantle conditions. This is a very important message which illustrates the unique contribution of our approach since these results could not be derived from experiments. The transition zone is, however, a complex region of the mantle where phase transformations occur. This induces grain size reduction at the transformation and possibly transformation plasticity. However, for grain sizes larger than *ca.* 0.5 mm, pure climb creep should be more efficient than diffusion creep (Fig. 1.1.12a).

Pure climb creep is ultimately constrained by diffusion. Figure 7.2.2 gathers the available experimental data for diffusion in wadsleyite and ringwoodite. In this plot, we also report the diffusion coefficients for majorite garnet which is the other major component in the transition zone. It is striking that all the data are very comparable and all the values fall in the same range. In this study, no specific calculations have been made for majorite. However, garnets are silicates which exhibit rather high lattice friction and we can still speculate that dislocation glide in majorite in the transition zone should be at least as difficult as in wadsleyite and ringwoodite. Hence we predict a transition zone to be rather homogeneous from the rheological point of view with no transition at 520 km depth and little viscosity contrast between the major phases.

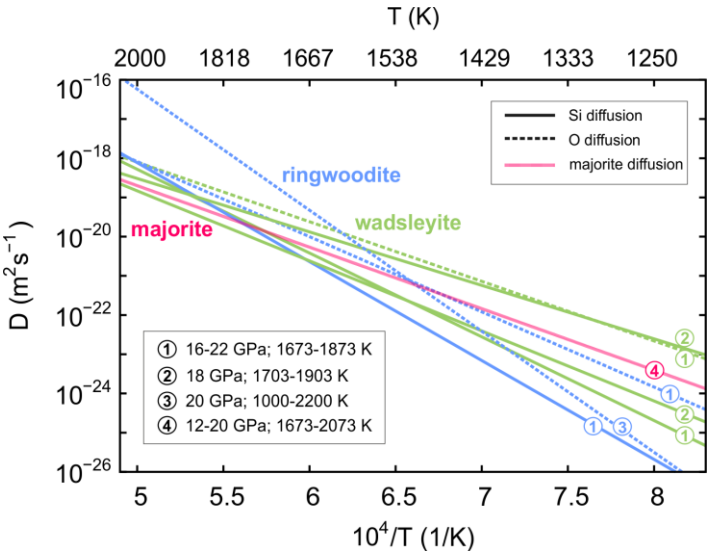

Figure 7.2.2. Arrhenius plot showing the self-diffusion coefficients for Si, and $Mg_4Si_4O_{12}$ majorite in wadsleyite, ringwoodite and majorite-pyrope diffusion couple. The curves marked with numbers correspond to (1) Shimojuku *et al.* (2009); (2) Shimojuku *et al.* (2004), (2010); (3) Zhang *et al.* (2011); (4) van Mierlo *et al.* (2013)

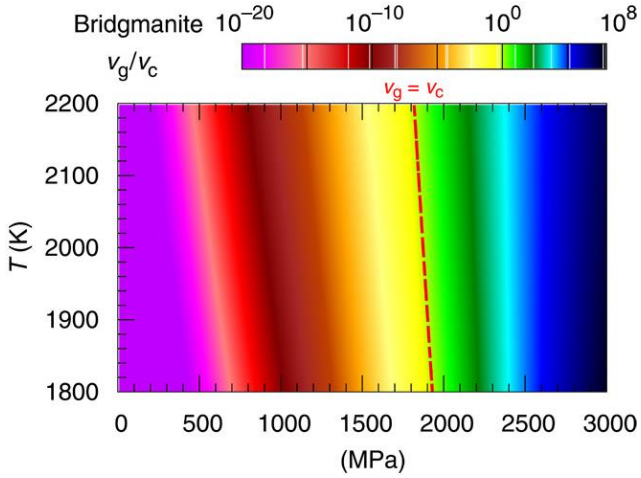

Figure 7.2.3. Comparison between the glide velocity (v_g) and the climb velocity (v_c) of dislocations in $MgSiO_3$ bridgmanite at 30 GPa

Given its importance, bridgmanite is the phase which has received a lot of attention during this project. This phase is particularly resistant to dislocation glide (Figs. 4.3.2 and 4.3.3). To assess its behaviour during creep, we compare the glide and the climb velocities (Fig. 7.2.3), similarly to what was described above for the lower pressure phases.

From the Figure 7.2.3 one can clearly see that dislocation glide can only be activated under laboratory conditions with very high stresses. This is very consistent with the recent results from Girard *et al.* (2016) who succeeded in performing the first deformation experiments of bridgmanite in the *P-T* conditions of the uppermost lower mantle. Even in that case, Nzogang *et al.* (2018) have shown that very little dislocation activity could be demonstrated unambiguously and that strain was produced by amorphous lamellae. On the opposite side, low stresses conditions of the mantle correspond to a completely different regime where dislocation motion can only occur by climb. Thus, similarly wadsleyite and ringwoodite, bridgmanite represents a particular case where mantle rheology cannot be extrapolated from laboratory experiments.

Based on our calculations, we suggest that bridgmanite in the lower mantle deforms by pure climb creep, also called Nabarro creep (Fig. 1.1.12b). This conclusion has a strong impact on our understanding of the mantle convection. So far, it was believed that either diffusion creep or dislocation creep (Weertman creep) was to be considered. Since the lower mantle does not show strong evidence for seismic anisotropy, it was very com-

monly assumed that diffusion creep, which does not lead to CPO development, is the dominant deformation mechanism in the lower mantle. However, diffusion is slow in bridgmanite which introduces some severe constraints on the ability of diffusion creep to yield mantle strain-rates. This has been evaluated in details in a recent study of Glišović *et al.* (2015) who showed that, even when considering relatively fast diffusion data from Ammann *et al.* (2010), the grain size in the mantle is bound to millimetre size and grain size becomes the controlling parameter of mantle convection. More generally, this hypothesis raises strong issues for the capability of large planetary bodies to undergo convection since the tendency to inhibit dislocation glide and vacancy diffusion seems to be fundamental.

Pure climb creep introduces an additional variable in the system: the dislocation density which controls the mean diffusion path between sources and sinks of vacancies. This is a much more versatile parameter than grain size, which is more likely to adjust with mechanical conditions. Indeed, this is the origin of the stress exponent $n = 3$ in Nabarro creep equation which describes how the internal microstructure adjusts to the applied stress (Equations 1.1.14 and 5.2.1).

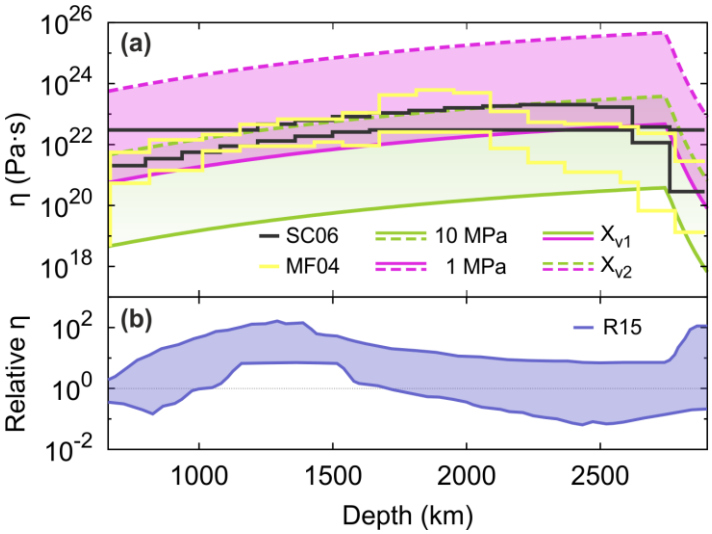

Figure 7.2.4. Viscosity of bridgmanite along the geotherm for stresses of 1 and 10 MPa and vacancy concentrations $X_{v1}=10^{-3}$ and $X_{v2}=10^{-6}$. Comparison is provided with the data of Mitrovica & Forte (2004), Steinberger & Calderwood (2006) and Rudolph *et al.* (2015)

The viscosity profile predicted from pure climb creep is displayed in Figure 7.2.4 in green and pink colours. It is impossible to make a full prediction on the bridgmanite viscosity as it depends on parameters which are poorly know (the vacancy concentration is likely extrinsic, *i.e.* constrained by the chemical composition, even at the impurity level in bridgmanite, the redox conditions, *etc*…), but one can still provide some constraints. We consider the possibility that vacancy concentrations vary between 10^{-3} and 10^{-6}. Since rheology of bridgmanite is expected to be non-linear, we also show the effect of varying stress between 1 and 10 MPa. The evolution of viscosity that we predict mimics very well the one proposed by Mitrovica & Forte (2004), shown in yellow, and, to some extent, the data of Steinberger & Calderwood (2006), shown in black. These models predict a viscosity decrease which cannot be explained if stress and vacancy concentrations are kept fixed, but the amplitude of their viscosity data is perfectly consistent within the parameter variations that we consider. More recently, elaborating on consistent reports of slab stagnation below the 670 km discontinuity, Rudolph *et al.* (2015) have proposed the existence of a viscosity hill between 1000 and 1500 km. They don't provide the absolute values of the viscosity that could be compared with ours, but the amplitude of the vis-

cosity variations that they find (shown in blue in Fig. 7.2.4) fits well to our predicted range.

Pure climb creep is in excellent agreement with the absence of CPO evidence in the lower mantle since climb does not induce any lattice rotation. This mechanism is also able to account for some key observations on mantle plumes morphology. Mantle plumes have been considered quite elusive, but recent tomographic models present compelling evidence for structures with diameters from 800 to 1000 km (French & Romanowicz 2015). This at odds with the usual view of thermal plumes as they develop in Newtonian fluids with a big mushroom head over a narrower stem (Fig. 7.2.5a). However, the laboratory experiments (Davaille *et al.* 2013) have shown that thick plumes can develop in a complex fluid which exhibits a yield stress (Fig. 7.2.5b).

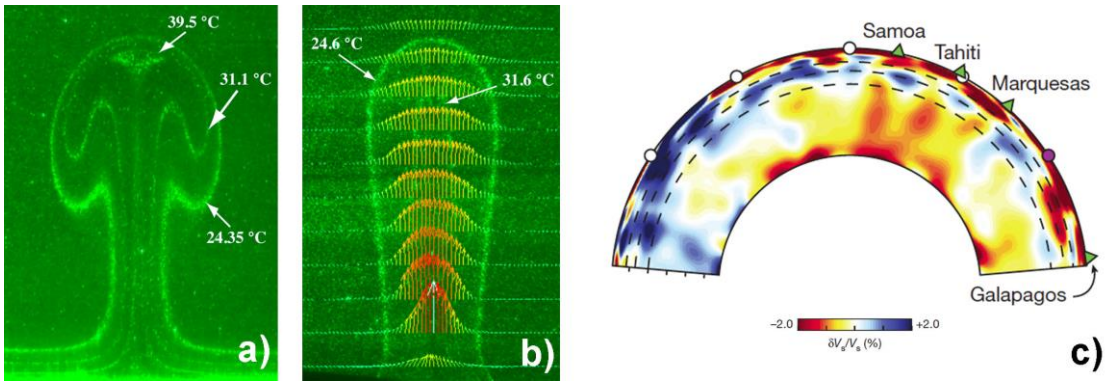

Figure 7.2.5. **(a)** Thermal plume in a Newtonian fluid and **(b)** in in a yield stress fluid (Davaille *et al.* (2018). **(c)** Mantle depth cross-section of shear-velocity variations in model SEMUCB-WM1 in the vicinity of Samoa, Tahiti and the Marquesas hot spots (from French & Romanowicz 2015).

This kind of rheology is compatible with the pure climb creep (and not with the Nabarro-Herring diffusion creep) since the yield stress depends on the defects microstructure and more specifically on the dislocation density. Scaling relationships suggest that yield stress values between 1 and 10 MPa (hence, the dislocation densities between 10^8 and 10^{10} m^{-2} in accord with the Equation 5.2.2 and Figure 5.2.4) would allow a development of plumes with diameter ranging from 600 to 1000 km, as considered previously.

References

M.W. Ammann *et al.* (2010) Nature 475: 462
A. Davaille *et al.* (2013) J. Non-Newtonian Fluid Mech. 193: 144
A. Davaille *et al.* (2018) Geophys. Res. Lett. 45: 1349
S.W. French & B. Romanowicz (2015) Nature 525: 95
P. Glišović *et al.* (2015) Geophys. Res. Lett. 42: 6278
J. Girard *et al.* (2016) Science 351: 144
J. Mitrovica & A.M. Forte (2004) Earth Planet. Sc. Lett. 225: 177
B. Nzogang *et al.* (2018) Geochem. Geophys. Geosyst. 19: 582
M. L. Rudolph *et al.* (2015) Science 350: 1349
A. Shimojuku *et al.* (2004) Geophys. Res. Lett. 31: 13606
A. Shimojuku *et al.* (2009) Earth Planet. Sc. Lett. 284: 103
A. Shimojuku *et al.* (2010) Phys. Earth Planet. Int. 183: 175
B. Steinberger & A.R. Calderwood (2006) Geophys. J. Int. 167: 1461
W.L. van Mierlo *et al.* (2013) Nature Geosciences 6: 400
B. Zhang *et al.* (2011) Solid State Ionics 186: 20

7.3. Easy flow at the core-mantle boundary

7.3.1. Post-perovskite: weak silicate at the bottom of the mantle

Lattice friction in the lowermost lower mantle

Post-perovskite (ppv) exhibits a very peculiar layered crystal structure (Fig. 2.2.5) which has strong implications on the anisotropic plasticity of this high-pressure phase (see section 4.4). In contrast to the other silicate minerals described in the previous sections, ppv is characterized by a remarkably low lattice friction opposed to the dislocation glide within MgO layers. To highlight the importance of this difference, it's worth comparing the behaviour of $MgSiO_3$ ppv with that of $MgSiO_3$ bridgmanite. The atomic-scale study of bridgmanite indicates that pressure has a strong effect on the lattice friction and the latter has been shown to increase significantly over the pressure range of the lower mantle. Figure 7.3.1 compares the Peierls stress of the easiest screw dislocations in bridgmanite with that in the ppv. The change in crystal structure results in a drastic drop of lattice friction. Thus, from completely different perspective, our calculations support the suggestion of Ammann *et al.* (2010), based on the study of anisotropic diffusion in $MgSiO_3$: the transition of bridgmanite to ppv is very likely responsible for the weak D'' layer in regions dominated by the ppv phase.

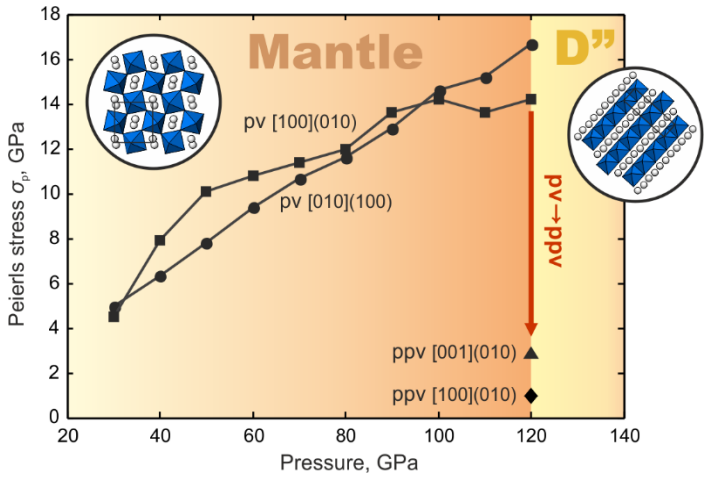

Figure 7.3.1. Lattice friction opposed to the easiest dislocation glide in $MgSiO_3$ bridgmanite and in the ppv phases in the lower mantle pressure range

CPO development in ppv and its implications on seismic anisotropy in the D" layer

In $MgSiO_3$ ppv, easy dislocation glide in (010) parallel to the structural layering suggests low strengths for mantle flow by dislocation creep in the D" domains with high volume fractions of ppv. In contrast, since similar models for bridgmanite predict extremely high lattice friction, bridgmanite should deform by pure climb (see the previous section and Boioli *et al.* 2017). The corollary of these models is that ppv-rich domains in D" should develop strong CPO, leading to a marked anisotropy of physical properties, whereas bridgmanite-rich ones should have much lower anisotropies, dominated by the CPO of ferropericlase.

From the VPSC modeling (Tommasi *et al.* 2018), one can see that simple shear results in development of a monoclinic CPO in ppv, which progressively rotates into parallelism with the dominant [100](010) slip system and the macroscopic shear (Fig. 7.3.2). The [010] axis displays the strongest concentration, which tends, for shear strains greater than 2, to align normal to the shear plane.

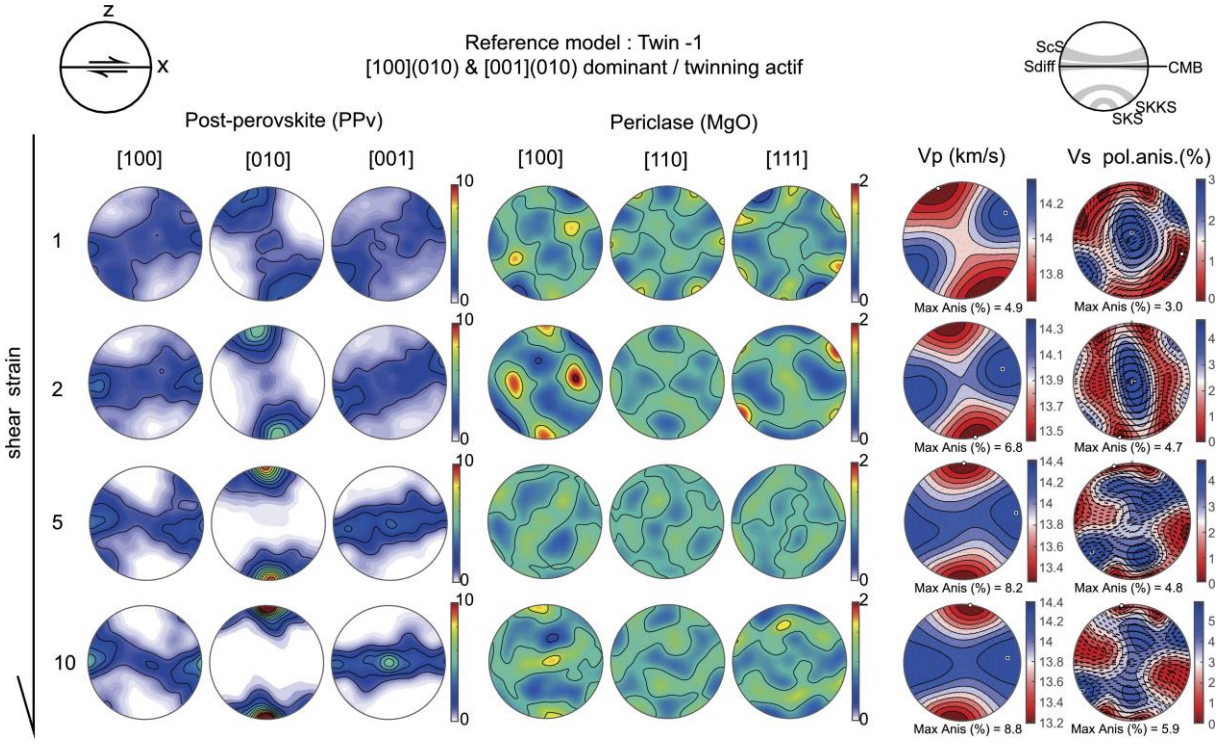

Figure 7.3.2. Evolution of CPOs in $MgSiO_3$ ppv and MgO periclase and of the seismic anisotropy (70% ppv + 30% MgO) with increasing shear strain. Lower hemisphere stereographic projections, contours at 1 multiple of uniform distribution (m.u.d) for ppv and 0.2 m.u.d for MgO. Horizontal X axis are parallel to the shear direction, vertical Z axis are normal to the shear plane. Insert on top right shows the directions sampled by different S-waves traveling in D" if the shear plane is parallel to the CMB. The calculations are performed by A. Tommasi based on the stress values from Table 4.4.1.

Activation of the {110} deformation twinning in ppv results in rotation of the twinned fractions that produces dispersion of [100] and of [010] on the XZ plane with development of weak secondary maxima at *ca.* 35° to the shear direction. Suppression of twinning in the ppv leads to faster intensification of the ppv CPO with increasing strain and, hence, to higher maximum seismic anisotropies at a given finite strain.

Due to similar viscoplastic strengths of MgO and ppv, that are expected to coexist in the cold regions of the D", strain tends to be evenly partitioned between the two phases. However, the high number of available slip systems results in weaker CPO in MgO with respect to that in the ppv (Fig. 7.3.2).

Our results cannot explain the deformation textures observed in high-pressure silicate ppv during DAC experiments. The CPO developed after compression in DAC might result from pre-texturing of ppv due to viscoplastic deformation of the precursor phases and inheritance upon phase transition, as proposed to explain the (100) and (102) textures (Miyagi *et al.* 2010) in ppv; or due to the high differential stresses that occur in the experiments and may allow the activation of slip systems with high CRSS, such as [100](001). The latter behaviour has been observed during cold compression of wadsleyite (Thurel & Cordier 2003). Despite significant differences in bond strengths and elastic properties between $MgSiO_3$ and $CaIrO_3$ ppv, CPOs predicted in our study are in excellent agreement with those observed in experimental deformation of the low pressure $CaIrO_3$ ppv in both compression and simple shear (Yamazaki *et al.* 2006; Miyagi *et al.* 2008; Niwa *et al.* 2012).

Development seismic anisotropy in D" resulting from CPO development in ppv and MgO have been analysed by A. Tommasi (Tommasi *et al.* 2018). This study suggests that fast S-waves are polarized mainly parallel to the flow direction. For shear parallel to the CMB, at low shear strain, the inclination of ScS, Sdiff, and SKKS fast polarizations and delay times vary depending on the propagation direction. At moderate and high shear strains, all S-waves are polarized sub-horizontally. Downwelling flow produces Sdiff, ScS, and SKKS fast polarization directions and birefringence that vary gradually as a function of the back-azimuth from nearly parallel to up to 70° to CMB and from null to ~5%. Change in the flow to shear parallel to the CMB results in dispersion of the CPO, weakening of the anisotropy, and strong azimuthal variation of the S-wave splitting up to 250 km from the corner. Transition from horizontal shear to upwelling also produces weakening of the CPO and complex seismic anisotropy patterns, with dominantly inclined fast ScS and SKKS polarizations, over most of the upwelling path. Models with twinning in ppv explain most observations of seismic anisotropy in D", but heterogeneity of the flow at scales < 1000 km is needed to comply with the dominant evidence for low apparent birefringence (<2%) in D".

Low viscosity and attenuation of seismic waves

Dislocations in $MgSiO_3$ ppv can easily glide within the (010) Mg-layers where chemical bonding is much weaker than that in Si-layers. The relative ease of slip between the silicate ppv and MgO (Fig. 4.4.10) suggests that, due to the structural layering, the high pressure $MgSiO_3$ phase could be as ductile as MgO.

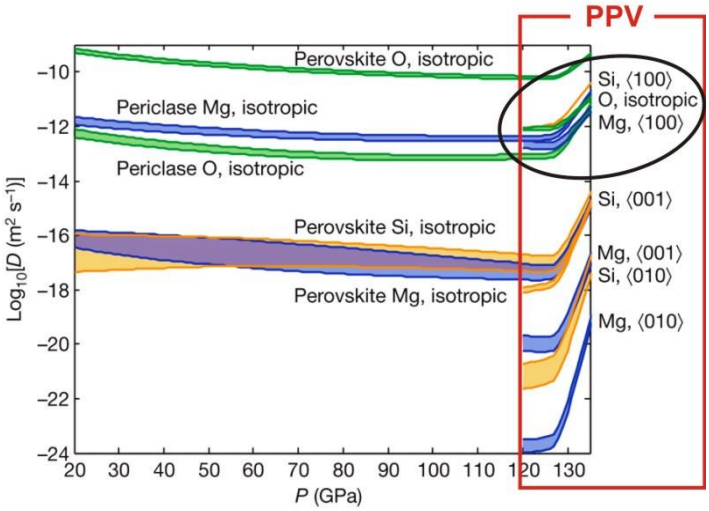

Figure 7.3.3. Vacancy diffusion coefficients along a geotherm in MgO periclase, $MgSiO_3$ perovskite (bridgmanite) and $MgSiO_3$ ppv inferred from the *ab-initio* calculations by Ammann *et al.* (2010)

Under the lower mantle conditions, dislocations in these two phases are expected to glide in the athermal regime (Fig. 1.1.9), *i.e.* without lattice friction opposed to their motion in the glide plane. In absence of intrinsic resistance of the lattice, dislocation creep is controlled by interaction of dislocations and by its rate of recovery which is ultimately controlled by diffusion (see Chapter 5). Diffusion is $MgSiO_3$ ppv is known to be highly anisotropic (Amman *et al.* 2010). The fastest diffusion in this phase occurs along the shortest [100] direction (Fig. 7.3.3) and interestingly, the corresponding diffusion coefficient is very close to that in MgO. Again here, one can see the proximity between MgO periclase and the MgO sublattice in $MgSiO_3$ ppv. Taking into account that both MgO and ppv deform in the athermal regime and have similar characteristics of the (fast) diffusion, one can expect that these phases exhibit comparable creep properties and, hence,

viscosities. Contribution of more difficult deformation mechanisms normal to structural layering (either involving dislocations or slowest diffusion) may however affect the strength of polycrystalline ppv aggregates (which is difficult to evaluate quantitatively at this point). Thus, ppv may be somewhat stronger than coexisting periclase. At this stage we can only highlight the fact of surprising resemblance between the two phases.

A strong implication of a low viscosity layer at the CMB is the enhancement of heat transfer from the core across the CMB, as was earlier indicated by Buffett (2007) and more recently investigated numerically (*e.g.* Nakagawa & Tackley 2011).

Another important implication of the presence of ppv in D″ concerns *attenuation of seismic waves*. So far, most studies that were trying to link seismic attenuation with mineral physics have been driven by the example of olivine. However, olivine exhibits high lattice friction; thus, dislocations are prescribed to stay in their Peierls valleys, and dislocation damping can only result in a limited contribution from kink migration. For this reason, the most important source of attenuation in olivine has been linked to diffusionally assisted grain boundary sliding. The situation is very different for the ppv which deforms in the athermal regime at temperatures of the D″ layer, *i.e.* its dislocations moving freely without lattice friction.

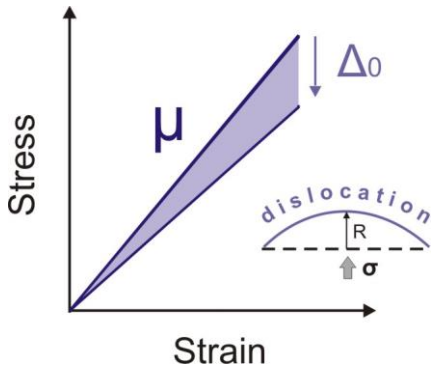

Figure 7.3.4. When a dislocation bows out under stress, it sweeps an area of the crystal corresponding to a small plastic strain which leads to an apparent decrease of the modulus (here the shear modulus μ)

A seismic (body-) wave corresponds to strains in the range of 10^{-8}-10^{-6}, with periods in the range of 1-10 s. These values correspond to stresses of a fraction of a MPa at most, applied at a strain rate of 10^{-6} s^{-1} or lower. Under these conditions, the athermal temperature T_a will be greater than in Figure 4.4.10, but still lower than 1400 K (the value corresponding to a strain-rate of 10^{-5} s^{-1}, constraining the dislocation density at 10^8 m^{-2}).

Under an applied stress σ_a and without lattice friction, a dislocation segment of length l will bow out with a curvature $R = \frac{1}{2}\frac{\mu b}{\sigma_a}$ (μ is the shear modulus). This bowing gives rise to a reduction of the effective shear modulus, called the *modulus defect* or *relaxation strength*: $\frac{\Delta\mu}{\mu} = \Delta_0 = \frac{1}{6}\rho l^2$, where ρ is the dislocation density. Assuming that l scales with $\frac{1}{\sqrt{\rho}}$, one can conclude that Δ_0 could be as high as 15% (as an upper bound). Consequently, a shear wave travelling through the post-perovskite containing dislocations could encounter a maximum velocity reduction $\frac{\Delta V_S}{V_S}$ approximately 7% compared to the ideal structure. In this regime, dislocation damping can be described using the vibrating string model which assumes that under an applied alternating stress, a dislocation characterized by a line tension can execute forced vibrations like a vibrating string. An alternating stress, such as the one associated with a seismic wave, will result in damping and energy dissipation. This model has two important consequences. At sufficiently high frequency, there exists a peak in $\tan\phi$ versus w with a resonance at w_0 such that $w_0^2 = \frac{12\Gamma}{m_l l^2}$. The fre-

quency w_0 is a function of Γ, the line tension of the dislocation and of m_l, the effective mass per unit length of the dislocation line. This effective mass m_l can be computed by summing the squared displacements dq_i of all atoms i in a simulation cell in which a dislocation has moved from one Peierls valley to the next one, *i.e.*, by $dQ=a'$, using the following expression:

$$m_l = \sum_i M_i \left(\frac{dq_i}{dQ}\right)^2 \tag{7.3.1}$$

where M_i corresponds to the mass of atom i; the effective mass of the dislocation thus incorporates the kinetic energy of surrounding atoms as if they were to respond adiabatically to dislocation motion. Computed from different cell sizes to account for finite size effects, we find (in units of atomic mass per unit length) $m_l \sim 9.7\ u/\text{Å}$, which results in $w_0 \sim 3.3 \cdot 10^4\ s^{-1}$. This frequency is higher than that of seismic waves, but it could allow experimental verification in the laboratory. At lower frequencies corresponding to seismic waves, the internal friction is proportional to ρl^4 and to the frequency w.

Our proposition of post-perovskite being highly attenuating is consistent with the report of higher attenuation in the D" by Anderson & Hart (1978) and Lawrence & Wysession (2006). However, attenuation in the D" layer is still not well constrained; this issue deserves more attention in the future to verify our prediction.

7.3.2 Magnesiowüstite: when iron matters

The main feature which emerged from recent studies of the CMB is the presence of the so-called LLSVPs (see section 2.1) which are accompanied by small-scale structures, the ULVZs in localized regions. Many ULVZs are thought to be compositionally distinct and relatively dense (Li *et al.* 2017). Early interpretations of the ULVZs involved a partial melt origin. However, iron enrichment of solid phases can simultaneously increase density and reduce compressional and shear velocity. Recent experimental results on sound velocities of a solid iron-enriched (Mg,Fe)O (referred hereafter as magnesiowüstite) at CMB pressures have led to suggest that the presence of a small fraction of magnesiowüstite can explain many of the properties of the ULVZs (Bower *et al.* 2011, Wicks *et al.* 2017). We have thus investigated the creep properties of magnesiowüstite in the *P-T* conditions of the CMB. The main difficulty is to assess the diffusion coefficients which control creep in the relevant thermodynamics conditions. In (Mg, Fe)O, the presence of aliovalent cations leads to the formation of cation vacancies to preserve charge balance which in turn limits the formation of oxygen vacancies. Oxygen self-diffusion coefficients are at least 2 to 3 orders of magnitude smaller than those of magnesium at any investigated temperature and hence, oxygen self-diffusion D_{Ox} is considered as the rate-limiting mechanism for dislocation climb. To estimate oxygen self-diffusion in the CMB, we rely on the standard scaling involving the homologous temperature:

$$D_{ox} = D_0\, exp\left(\frac{gT_m}{T}\right) \tag{7.3.2}$$

where T_m is the melting temperature and D_0 and g are empirical constants. This relation can also account for the effect of pressure through its influence on melting, and of the composition since incorporation of iron significantly decreases the melting temperature (Fig. 7.3.5a). The homologous temperature scaling with respect to intrinsic diffusion on

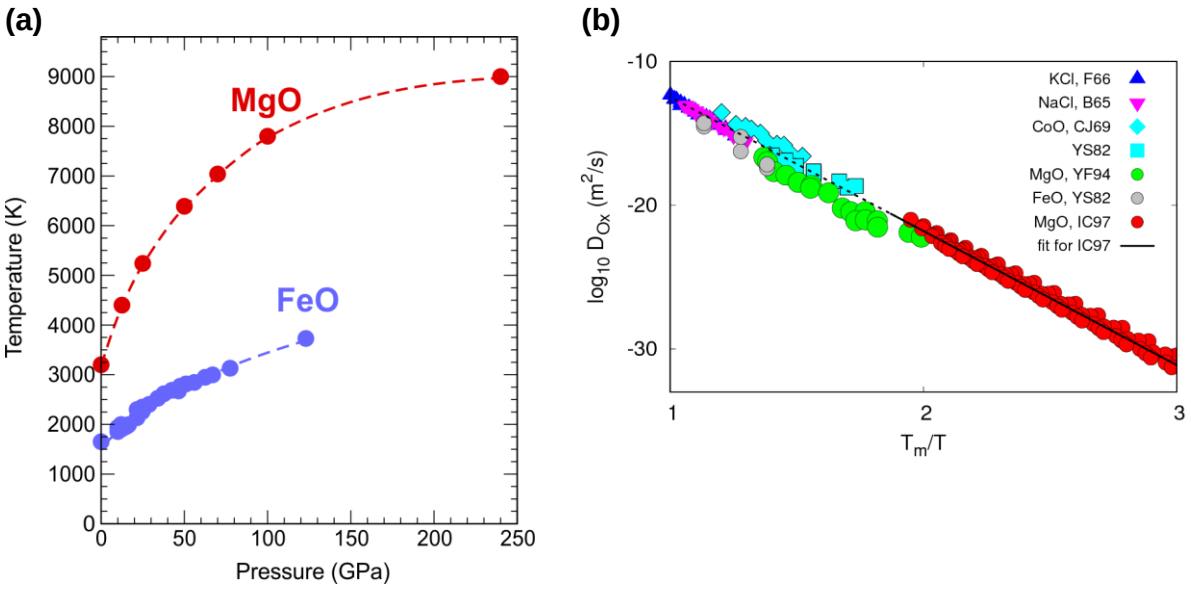

Figure 7.3.5. **(a)** Influence of pressure on the melting curves of MgO and FeO. **(b)** Oxygen self-diffusion coefficients D_{Ox} as a function of the homologous temperature for different oxides and halides. The high pressure, high temperature numerical data on MgO obtained by Ita & Cohen (1997) (red dots) are fit using the homologous temperature relation described in Eq. 7.3.2 (black line). Excellent agreement is shown with other intrinsic, oxygen self-diffusion experimental data of oxides and halides: Fuller (1966), Barr *et al.* (1965), Chen & Jackson (1969), Yamaguchi & Someno (1982), Yang & Flynn (1994)

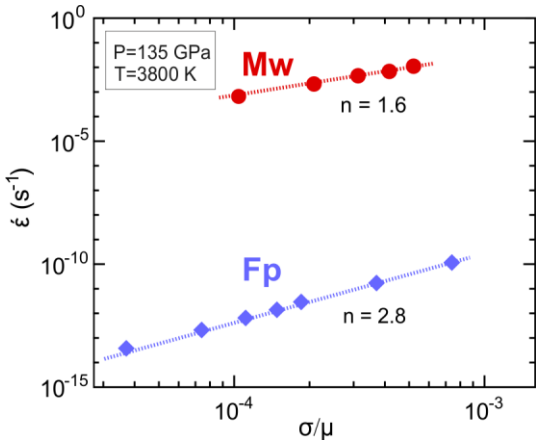

Figure 7.3.6. Creep strain rates as a function of stress (normalized by the shear modulus) of $(Mg_{0.16}Fe_{0.84})O$ magnesiowüstite (Mw) at 135 GPa and 3800 K. Comparison is provided with $(Mg_{0.80}Fe_{0.20})O$ ferropericlase (Fp)

the anion sublattice gives indeed excellent results in ionic compounds with the rock-salt structure which can be seen in Figure 7.3.5b.

From these estimations, we have carried out DD calculations corresponding to dislocation (Weertman) creep in iron-rich magnesiowustite $(Mg_{0.16}Fe_{0.84})O$ at 135 GPa and 3800 K. To better illustrate the influence of iron, the same calculations have been performed for ferropericlase with a Mg-content typically expected in the lower mantle: $(Mg_{0.80}Fe_{0.20})O$.

The results are shown in Figure 7.3.6. Both phases exhibit creep rates which obey a power law. The faster diffusion in magnesiowüstite (compared to ferropericlase) results in a very strong increase in the creep rate about ten orders of magnitude. It is also interesting

to note that it affects the dynamics of creep since the stress exponent is as low as 1.6 in magnesiowüstite, compared to 2.8 under the same conditions for $(Mg_{0.80}Fe_{0.20})O$ ferropericlase. Under these conditions, $(Mg_{0.16}Fe_{0.84})O$ magnesiowüstite exhibits a very low viscosity of the order of 10^{10} Pa·s. Of course, magnesiowustite is not the only phase present, nor it is the most abundant. However, if the ULVZ were to be significantly enriched of this phase, or if some segregation could occur, very spectacular behaviour could be expected.

References

M. Ammann *et al.* (2010) Nature 465: 462
D.L. Anderson & R.S. Hart (1978) J. Geophys. Res. 83: 5869
L.W. Barr *et al.* (1965) J. Appl. Phys. 36: 624
F. Boioli *et al.* (2017) Sci. Adv. 3: e1601958
D.J. Bower *et al.* (2011) Earth Planet. Sci. Lett. 241: 962
B. Buffett (2007) Geophys. Res. Lett 34: L17302
W.K. Chen & R.A. Jackson (1969) J. Phys. Chem. Solids 30: 1309
R.G. Fuller (1966) Phys. Rev. B 142: 524
J.F. Lawrence & M.E. Wysession (2006) Earth Planet. Sci. Lett. 303: 193
M. Li *et al.* (2017) Nature Comm. 8: 177
L. Miyagi *et al.* (2008) Earth Planet. Sci. Lett. 268: 515
L. Miyagi *et al.* (2010) Science 329: 1639
T. Nakagawa & P. Tackley (2011) Geophys. Res. Lett 38: 1
K. Niwa *et al.* (2012) Phys. Earth. Planet. Inter. 194 :10
E. Thurel & P. Cordier (2003) Phys Chem Miner 30: 256
A. Tommasi *et al.* (2018) Earth Planet. Sci. Lett. 492: 35
J.K. Wicks *et al.* (2017) Geophys. Res. Lett 44: 1
S. Yamaguchi & M. Someno (1982) Trans. Jap. Inst. Metals. 23: 259
D. Yamazaki *et al.* (2006) Earth Planet. Sci. Lett. 252: 372
M.H. Yang & C.P. Flynn (1994) Phys. Rev. Lett. 73: 1809

Conclusion

Conclusion

A project is the point where a need, a scientific question, meets with an idea, a conviction. Here we were motivated by the conviction that standard approaches aimed to address the rheology of minerals were facing some ultimate limits as long as they would rely on empirical laws for which extrapolation to natural conditions raise obvious concerns. Our standpoint was that our theoretical concepts on the physics of deformation as well as our computational capabilities were reaching a point allowing the rheology of mantle phases to be addressed by the approach developed in materials science and called multiscale numerical modelling. This conviction has been proved to be valid, at least in some cases. At the end of this project, we have obtained the first fully-numerical models of the dislocation based plasticity in most major mantle phases. These models are not adjusted on empirical or experimental parameters. The two major goals have been reached for the first time. First, the effect of pressure is described from the fundamental effect that this thermodynamic parameter has on the electronic structure and bonding, and not through a conventional phenomenological parameter (the activation volume), as it was done previously. Secondly, since we describe the kinetics of elementary thermally activated mechanisms, our constitutive equations are valid equally under the stresses and strain-rates of experiments and of nature without the need of performing extrapolations. This unique capability has immediately yielded new and important results.

First to be mentioned is the paramount role of pressure on plasticity. This effect was anticipated given the well-known effect of pressure on elasticity. Our work has however allowed to quantify it and most importantly to reveal some unexpected specific behaviours. The general trend is simple, our calculations have demonstrated in all phases a strong effect of pressure which stiffens the bonds and thus increases lattice friction. During the course of our project, very significant progress have been made in performing deformation experiments at high-P, high-T in large volume presses, including in the conditions of the uppermost lower mantle. This has provided a very useful benchmark for our models and has shown that for wadsleyite, ringwoodite and bridgmanite, our predictions were reproducing very well the experimental data.

In bridgmanite, a very strong effect of pressure was evidenced on the core of [010] dislocations which become sessile and, thus, immobile in glide in the deep mantle. We found also some very unexpected results for the post-perovskite. Marking a strong break with the tendency built by pressure from transition zone pressures to the bottom of the lower mantle, we found that [100] dislocations in post-perovskite could glide very easily within the Mg-layers of this structure. We also demonstrated that mechanical twinning could be an additional deformation mechanism in this structure.

To get these results, we have conducted a systematic study on dislocation glide in the high-pressure silicate phases of the mantle. We have developed an original strategy which involves as a first step identifying the most efficient dislocations (as far as glide is concerned as a strain-producing mechanism) and slip systems in minerals where this fundamental information was not available. Our strategy was to model the core of screw dislocations looking for the plane where they would tend to spread. This usually gives a good indication on the easiest slip planes where further calculations can be done on edge dislocations. Some exceptions were found however in post-perovskite and olivine where some dislocations do not glide preferentially in the planes where their cores spread. Having determined the easiest dislocations and slip systems from the dislocation cores and lattice friction, we modeled the thermal activation of glide based on the kink-pair formalism. As a result of this work, we have now, for most important phases of the mantle (namely wadsleyite, ringwoodite, ferropericlase, bridgmanite and post-perovskite),

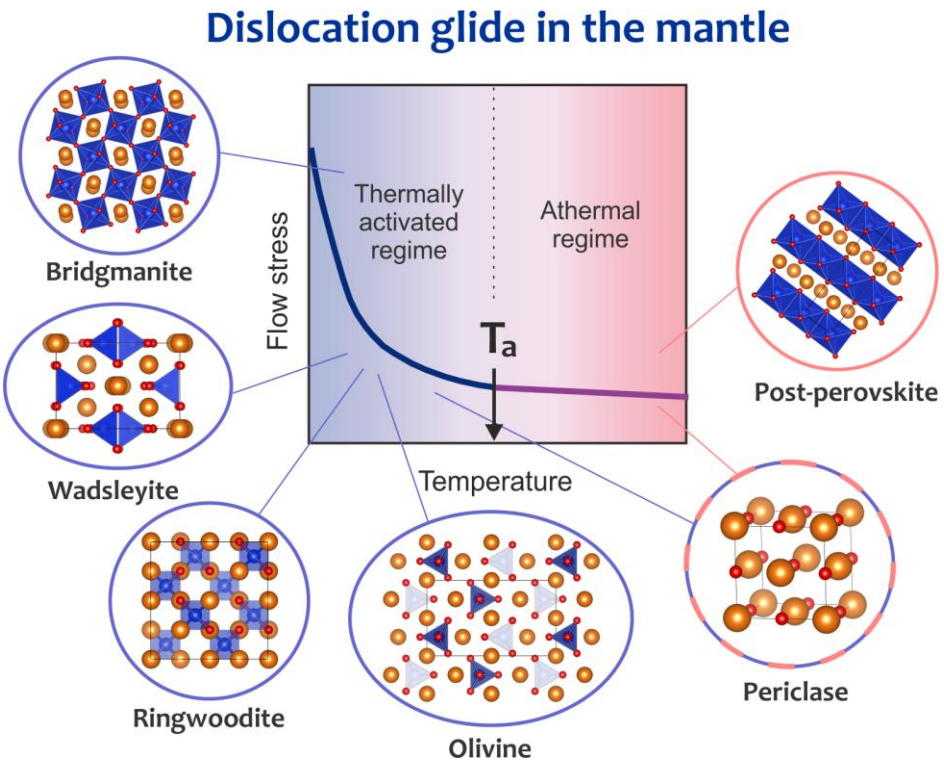

the knowledge of the most important slip systems (*i.e.* the most efficient strain-producing mechanisms) and of the velocity laws of those dislocations at relevant pressures and as a function of temperature and stress, including those corresponding to natural strain-rates, with no extrapolation. Altogether, these results represent one of the most comprehensive set of information about dislocation glide including core structure, lattice friction and thermal activation ever gathered for mantle minerals (see a summary in the figure above).

Another major output of the project, not fully anticipated at its onset, is the ability to model creep as a result of glide and climb of dislocations. The approach is still simple and calls for further developments in the future, but we are already able at this stage, using 2.5-D dislocation dynamics, to describe the collective behaviour of dislocations as a response of glide and climb. These calculations have been first applied and benchmarked on olivine and further on periclase. They have clarified and expanded our understanding on creep and on the respective role of glide and climb. We propose, as a tool to evaluate the response of minerals to creep, to plot maps of the ratio between the glide and the climb velocities as a function of stress and temperature. These maps are extremely useful since they show that in some cases (bridgmanite, but also wadsleyite and ringwoodite), the mechanisms activated at high stress in the laboratory differ from those expected at mantle strain rates. This allowed us to propose a completely new vision for the elementary mechanisms responsible for the rheology of the mantle (see a summary in the figure below). A major result of the project is that, in the lower mantle, creep in bridgmanite occurs by pure climb of dislocations which otherwise would be immobile at such low stresses. We are convinced that this mechanism which has been overlooked so far, represents a major mechanism for the convection of planetary interiors. A major goal of the coming years will be to test this mechanism against observables, but so far pure climb creep in bridgmanite:

- produces strain rates which are compatible with those expected in the mantle (given our best estimates of diffusion in this phase)

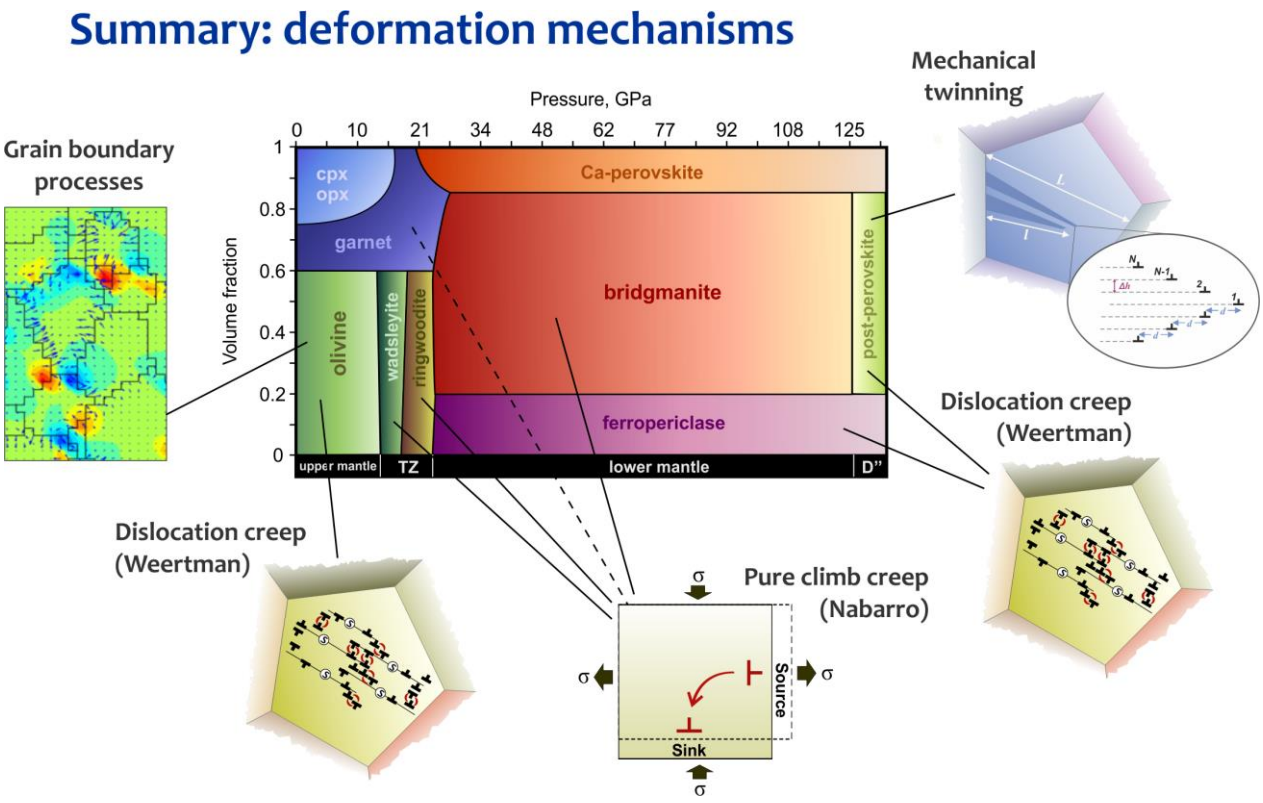

- is compatible with the absence of strong seismic anisotropy in the lower mantle
- accounts for the yield stress that is needed to accounts for the morphology of (fat) plumes

But not all phases follow this trend and some phases still flow along the standard dislocation creep proposed by Weertman: ferropericlase and for some component post-perovskite. We have even found that enrichment in iron in magnesiowustite could lead to a very ductile behaviour in the ULVZ. The figure above gives a sketch of the main deformation mechanisms identified during this project for mantle phases.

Besides the initial targets present in the proposal, new, unexpected, research directions have emerged. Among those, the work done on grain boundary processes is one of the most important. In the last years there were a growing body of compelling evidence suggesting that grain boundary processes play a key role on the deformation of olivine. This might also concern other phases. Disclinations are crystal defects proposed theoretically from the origins of the theory of defects, but they have been completely overlooked in solids. We have shown them to be a fundamental component of grain boundaries with some observations made on olivine where the role of grain boundaries in plasticity is prominent. From the theoretical point of view, we have developed an original crossover method to derive smooth continuous fields from atomistic calculations. This has allowed to gain a lot of understanding in the structure of grain boundaries with potential applications in coarse-graining. Surprisingly, such efforts to cross-link atomic scale models and continuum field descriptions have been rarely developed. We believe that this represents an important output of the project which could find applications in many other fields. A major question which arises after our work is related to the dynamic behaviour of grain boundaries and how their mobilities contribute to plastic deformation of aggregates.

Another important effort performed during this project was to build new interfaces with experimental approaches. Electron microscopy is an obvious interface between theory and experiments since it gives access to dislocation microstructures. However, more quantitative approaches are needed. During the project, we have developed the electron tomography of dislocations in mineralogy. Applied to olivine, this has led to a significant leap in our understanding of elementary deformation mechanisms. We have also shown that well-designed experiments taking advantage of current possibilities of nanomechanical testing could open the field of *in situ* deformation of silicates, but also and more importantly give access to fundamental parameters directly comparable or complementary to those obtained by numerical modeling.

Besides all the results gathered during the course of this project, we think that it has demonstrated that a new approach of the rheology of minerals and rocks is possible, more linked to the understanding of elementary mechanisms. This is probably an important part of the legacy of the RheoMan project. This approach requires obviously some simplifications and the constant search for the most relevant degrees of approximation. It has however the unique capability to integrate with a great confidence the influence of parameters very challenging, if not impossible, to account for like pressure or strain-rate. The multiscale numerical modeling approach simply did not exist in mineral physics before this project and a significant effort was required. However, the contribution of experiments must not be overlooked and the next challenge will be to design a more complete approach where numerical modeling and innovative experiments will complement.

RheoMan Team

(alphabetic order)

Francesca Boioli

Post-doc (March 2013 - August 2015)
After her PhD in the university of Milano Bicocca (Italy) in Nanostructures and Nanotechnology entitled: «Dislocation modelling in SiGe nanostructures». Francesca joined the RheoMan team in March 2013 to develop dislocation creep modeling by 2.5D dislocation dynamics including climb mechanism. She has studied the influence of climb on creep in olivine and the role of pure climb creep in bridgmanite.

Philippe Carrez

Professor of Physics
Philippe Carrez is in charge of the numerical modelling of dislocations in mineral phases. His research interests include the atomic structure of dislocation cores, dislocation mobility and dislocation interactions at the mesoscale. Together with Patrick Cordier, he has lead development of a multi-scale model of plasticity for mantle minerals in pressure and temperature conditions relevant of the Earth interiors.

Patrick Cordier

Professor of Physics, leader of the RheoMan Project
Trained as a materials scientist, Patrick Cordier worked mostly in the field of mineral physics. His research interests are related to the mechanical properties of solids with a special focus on dislocation theory. Specialist of TEM he has pioneered the application of Large Angle Convergent Beam Electron diffraction to defect characterization in minerals and now Scanning Precession Electron Diffraction and orientation mapping in the TEM. In 2015, Patrick Cordier received the Grand Prix Kuhlmann of the Société des Sciences, de l'Agriculture et des Arts de Lille (SSAAL) and in 2016 he received the Dana Medal of the Mineralogical Society of America of which he is a Fellow (since 2008).

Alexandra Goryaeva

PhD student (September 2013-December 2016)
Trained as crystallographer at Lomonosov Moscow State University (Russian Federation), Alexandra joined the group to study plasticity in $MgSiO_3$ post-perovskite. Her PhD thesis entitled «Modeling Defects and plasticity in $MgSiO_3$ post-perovskite at the atomic scale» was awarded the prize Haüy-Lacroix 2017 from the French Society of Mineralogy and Crystallography (SFMC)

Karine Gouriet

Assistant professor
Karine Gouriet is a lecturer in Physics. Her main responsibility in RheoMan project is to investigate dislocations core's structures using the Peierls Nabarro model and plasticity at the mesoscopic scale based on dislocation dynamics.

Pierre Hirel

Assistant professor

Pierre Hirel joined the RheoMan team as a post-doc in November 2012 to study elementary climb mechanisms in $MgSiO_3$ perovskite at the atomic scale. Since 2016, Pierre is assistant professor at the University of Lille, teaching physics. Pierre also develops and distributes Atomsk, the swiss-army knife of atomistic simulation. Before joining the RheoMan project, he has hold a post-doc position in Karlsruhe Institut fur Technologie/ Fraunhofer-IWM Freiburg, Germany. There he studied planar and linear defects in functional perovskite materials such as $SrTiO_3$ and $BaTiO_3$.

Antoine Kraych

PhD student (September 2012 – June 2016)

Trained as a physicists at the university of Lille, Antoine has prepared his Master in Physics (within the field of Materials Science) in our group before starting his PhD project. Antoine has defended his PhD entitled «Modélisation à l'échelle atomique du rôle des dislocations dans la déformation de la bridgmanite» on June 2016.

Srinivasan Mahendran

PhD student (January 2015 – July 2018)

After completion of his Master in Computational Materials Science at the TU Bergakademie Freiberg, Germany, Srinivasan joined the team to prepare his PhD on the atomic-scale modeling of dislocation properties in olivine (forsterite) Mg_2SiO_4.

Alexandre Mussi

Assistant professor

Alexandre Mussi is lecturer in Physics and a specialist in transmission electron microscopy. He has characterized dislocations and slip systems in several beam-sensitive minerals deformed under mantle and subduction zone conditions. He joined the RheoMan project in January 2014 to develop electron tomography of dislocations in the TEM to study the plastic deformation mechanisms in olivine in relationship with numerical modeling.

Billy Nzogang

PhD student (from October 2015)

Physicist trained at the university of Yaoundé (Cameroon), Billy came to France to prepare his Master within a joined program with the university of Orléans. His Master project was devoted to the influence of texture on the infrared response of semi-transparent materials. Billy joined the RheoMan team to prepare his PhD aiming to develop new methods using transmission electron microscopy and to characterize dislocations and plasticity in minerals in connection with numerical models. *His PhD grant has been financially supported by the University of Lille.*

Riccardo Reali

PhD student (October 2014 – September 2018)
Riccardo is a geologist specialized in experimental mineralogy mainly on lower mantle phases, especially diamond and ferro-periclase. At the University of Padova (Italy) he has developed skills in single crystal X-ray diffraction crystallography and studied the structure of ferro-periclase in diamond-related inclusions in order to obtain the pressure of formation of the diamond-inclusion pair. He joined the RheoMan team in October 2014 to start his PhD on the modeling of creep in (Mg, Fe)O in the lower mantle using dislocation dynamics.

Sebastian Ritterbex

PhD student (January 2013 – June 2016)
Sebastian Ritterbex joined the RheoMan team in 2013, after finishing his Master studies in Geophysics at the University of Utrecht, the Netherlands (Thesis Title: «The significance of grain size dependent composite solid-state flow in upper mantle dynamics»). He has defended his PhD entitled «Modelling the plasticity of wadsleyite and ringwoodite : on the motion of dislocations in the Earth's transition zone» on June 2016.

Simon Thilliez

Undergraduate student (September 2017- January 2018)
Student at the IUT A of Lille, at the Physical Measurement department, Simon is specialized in materials science and follows the class «Materials and physical/chemical analyses of products». His research project deals with the study of plastic deformation of ringwoodite and wadsleyite in the transition zone conditions, studying orientation maps obtained with a transmission electron microscope.

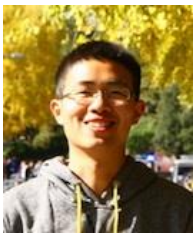

Xiao-Yu Sun

Post-doc (October 2014 - October 2017)
Xiao-Yu Sun has defended his PhD at the Tsinghua University (China) in Mechanics. It was entitled: «Surface/Interface effects on mechanical properties of nanomaterials». He is generally interested in theoretical analyses and computer simulations on discovering the fundamental molecular mechanisms of nanomaterials. Xiao-Yu joined the RheoMan team to model disclinations making a crossover between atomistic and continuous fields modeling.

Acknowledgments

This work has been made possible by the funding from European Research Council under the Seventh Framework Programme (FP7), ERC grant N°290424 – RheoMan.

During those six years, we have welcomed many visitors from all over the world: Jonathan Amodeo (MATEIS, INSA Lyon, France), Nathalie Bolfan-Casanova (LMV, Clermont-Ferrand, France) Caroline Bollinger (BGI, Bayreuth, Germany), Hélène Couvy (Washington University in Saint Louis, USA), Anne Davaille (FAST Orsay, France), Huw Davies (Cardiff University, UK), Steve Fitzgerald (University of Oxford, UK), Jennifer M. Jackson (California Institute of Technology, Pasadena, USA), Patrick Ganster (Ecole des Mines de Saint Etienne, France), Sébastien Groh (TU Bergakademie Freiberg, Germany), Laurent Jolivet (Université d'Orléans, France), Baptiste Journaux (ENS Lyon, France), Matous Mrovec (ICAMS, Bochum, Allemagne), Eiji Ohtani (Tohoku University, Sendai, Japan), Jeffrey S. Pigott (CWRU, Cleveland, USA), Laurent Pizzagalli (Institut P', Poitiers, France), Louisette Priester (Université Paris 11, Orsay, France), Neil Ribe (FAST Orsay, France), Yannick Ricard (ENS Lyon, France), Antoine Rozel (ETH Zurich, Switzerland), Rouzbeh Shahsavari (Rice University, Houston, USA), Döme Tanguy (Institut Lumière Matière, Lyon, France), Jeannot Trampert (Utrecht University, The Netherlands), James A. van Orman (CWRU, Cleveland, USA), not forgetting Antoine Adant and Arthur Dekeriel.

Prof. Jeannot Trampert (Utrecht University, the Netherlands) visiting RheoMan team.
Lille, June 2015

We have fruitfully collaborated with several people and research groups. We can not list them all. It is our pleasure to acknowledge here some outstanding relationships that we had during this project with Hans-Peter Bunge (LMU, Muenchen, Germany), Sylvie Demouchy (Géosciences Montpellier, France), Benoit Devincre (LEM, Châtillon, France), Claude Fressengeas (LEM3, Metz, France), Hosni Idrissi (EMAT, Anvers, Belgium), Ladislas Kubin (LEM, Châtillon, France), David Mainprice (Géosciences Montpellier, France), Vincent Taupin (LEM3, Metz, France) and Andrea Tommasi (Géosciences Montpellier, France).

Besides the scientific team, many people have contributed to the project. Catherine Dupas played a key role in the preparation of the project, which, from the side of the host institution has been accompanied and managed by Martine Lecoutre, Muriel Vernay, Danièle Duveau, Célia Deléglide and Safae Ennadir.

Finally, we thank all those people who, at a stage or another, have supported this project.

List of publications produced during the project

-2018-

(45) B. Nzogang, S. Thilliez, A. Mussi, T. Kawazoe, N. Miyajima, J. Bouquerel, P. Cordier (2018) Application of Scanning Precession Electron Diffraction in the Transmission Electron Microscope to the characterization of deformation in wadsleyite and ringwoodite. Minerals **8**: 153 Open access

(44) A. Tommasi, A.M. Goryaeva, Ph. Carrez, P. Cordier, D. Mainprice (2018) Deformation, crystal preferred orientations, and seismic anisotropy in the Earth's D" layer. Earth Planet. Sci Lett. **492**: 35-46 Open access

(43) X.-Y. Sun, C. Fressengeas, V. Taupin, P. Cordier, N. Combe (2018) Disconnections, dislocations and generalized disclinations in grain boundary ledges. Int. J. Plasticity **104**: 134-146 Open access

(42) B. Nzogang, J. Bouquerel, P. Cordier, A. Mussi, J. Girard, S.-I. Karato (2018) Characterization of bridgmanite and ferropericlase aggregates deformed at HP-HT by Scanning Precession Electron Diffraction. Geochem. Geophys. Geosys. **19**: 582-594 Open access

(41) S. Ritterbex, P. Hirel, Ph. Carrez (2018) On low temperature glide of dissociated ⟨110⟩ dislocations in strontium titanate. Philos. Mag. **98**: 1397-1411 Open access

(40) A. Davaille, Ph. Carrez, P. Cordier (2018) Fat plumes may reflect the complex rheology of the lower mantle. Geophys. Res. Lett. **45**: 1349-1354 Open access

-2017-

(39) Ph. Carrez, A.M. Goryaeva, P. Cordier (2017) Prediction of mechanical twinning in magnesium silicate post-perovskite. Sci. Reports **7**: 17640 Open access

(38) Ph. Carrez, and P. Cordier (2017) Plastic deformation of materials under pressure. MRS Bulletin **42**: 714-717

(37) A. Mussi, P. Cordier, S. Demouchy, B. Hue (2017) Hardening mechanisms in olivine single crystal deformed at 1090°C: an electron tomography study. Philos. Mag. **97**: 3172-3185 Open access

(36) A.M. Goryaeva, Ph. Carrez, P. Cordier (2017) Modeling defects and plasticity in $MgSiO_3$ post-perovskite: Part 3 – screw and edge [001] dislocations. Phys. Chem. Miner. **44**: 521-533 Open access
Erratum to this article: doi.org/10.1007/s00269-017-0891-4

(35) X-Y. Sun, P. Cordier, V. Taupin, C. Fressengeas, B. Karki (2017) Continuous description of grain boundaries using crystal defect fields: the example of a 310/[001] tilt boundary in MgO. Eur. J. Miner. **29**: 155-165 Open access

(34) S. Mahendran, Ph. Carrez, S. Groh, P. Cordier (2017) Dislocation modelling in Mg_2SiO_4 forsterite: an atomic-scale study based on the THB1 potential. Model. Simul. Mater. Sci. Eng. **25**: 054002 **Highlights of MSMSE 2017** Open access

(33) S. Jahn, and X.-Y. Sun (2017) Atomic-scale modelling of crystal defects, self-diffusion and deformation processes. In "Mineral reaction kinetics: Microstructures, textures, chemical and isotopic signatures". Ed. W. Heinrich, R. Abart. EMU Notes in Mineralogy **16**(8): 215-253

(32) F. Boioli, Ph. Carrez, P. Cordier, B. Devincre, K. Gouriet, P. Hirel, A. Kraych, S. Ritterbex (2017) Pure climb creep mechanism drives flow in the Earth's lower mantle. Science Advances **3**: e1601958 Open access

(31) R. Reali, F. Boioli, K. Gouriet, Ph. Carrez, B. Devincre, P. Cordier (2017) Modeling plasticity of MgO by 2.5D dislocation dynamics simulations. Mater. Sci. Eng. A **690**: 52-61 Open access

-2016-

(30) X.-Y. Sun, V. Taupin, P. Cordier, C. Fressengeas, B. Karki (2016) Influence of pressure on dislocation, disclination and g-disclination structures of a 310/[001] tilt boundary in MgO. J. Mater. Res. **31**: 3108-3114 **Invited feature paper** Open access

(29) S. Ritterbex, Ph. Carrez, P. Cordier (2016) Modeling dislocation glide and lattice friction in Mg_2SiO_4 wadsleyite in conditions of the Earth's transition zone. Amer. Miner. **101**: 2085-2094 **Editors Selection of American Mineralogist, September 2016** Open access

(28) A.M. Goryaeva, Ph. Carrez, P. Cordier (2016) Low viscosity and high attenuation in $MgSiO_3$ post-perovskite inferred from atomic-scale calculations. Sci Reports **6**: 34771 Open access

(27) A. Kraych, Ph. Carrez, P. Cordier (2016) On dislocation glide in $MgSiO_3$ bridgmanite. Earth Planet. Sci. Lett. **452**: 60-68 Open access

(26) X.-Y. Sun, P. Cordier, V. Taupin, C. Fressengeas, S. Jahn (2016) Continuous description of a grain boundary in forsterite from atomic scale simulations: the role of disclinations. Philos. Mag. **96**: 1757-1772 Open access

(25) P. Hirel, Ph. Carrez, P. Cordier (2016) From glissile to sessile: effect of temperature on ⟨110⟩ dislocations in perovskite materials. Scripta Mater. **120**: 67-70 Open access

(24) H. Idrissi, C. Bollinger, F. Boioli, D. Schryvers, P. Cordier (2016) Low-temperature plasticity of olivine revisited with in situ TEM nanomechanical testing. Science Advances **2**: e1501671 Open access

(23) P. Hirel, P. Carrez, E. Clouet, P. Cordier (2016) The electric charge and climb of edge dislocations in perovskite oxides: the case of high-pressure $MgSiO_3$ bridgmanite. Acta Mater. **106**: 313-321 Open access

(22) A. Kraych, Ph. Carrez, P. Hirel, E. Clouet, P. Cordier (2016) Peierls potential and kink-pair mechanism in high-pressure $MgSiO_3$ perovskite: an atomic scale study. Phys. Rev. B **93**: 014103 Open access

(21) X.-Y. Sun, V. Taupin, C. Fressengeas, P. Cordier (2016) Continuous description of the atomic structure of grain boundaries using dislocation and generalized-disclination density fields. Int. J. Plasticity **77**: 75-89 Open access

(20) A. Mussi, P. Cordier, S. Ghosh, N. Garvik, B. C. Nzogang, Ph. Carrez, S. Garruchet (2016) Transmission electron microscopy of dislocations in cementite deformed at high pressure and high temperature. Philos. Mag. **96**: 1773-1789 Open access

(19) S. Merkel, and P. Cordier (2016) Deformation of core and mantle materials in "Deep Earth: Physics and Chemistry of the Lower Mantle and Core" Eds: H. Terasaki, R. Fischer. AGU Monograph, Wiley, pp. 89-100

-2015-

(18) A. Mussi, M. Nafi, S. Demouchy, P. Cordier (2015) On the deformation mechanism of olivine single crystals at lithospheric temperatures: an electron tomography study. Eur. J. Miner. **27**: 707 Open access

(17) F. Boioli, A. Tommasi, P. Cordier, S. Demouchy, A. Mussi (2015) Steady state and low stresses in the lithospheric mantle inferred from dislocation modeling of creep in olivine. Earth Planet. Sci. Lett. **432**: 232-242 Open access

(16) S. Ritterbex, Ph. Carrez, K. Gouriet, P. Cordier (2015) Modeling dislocation glide in Mg_2SiO_4 ringwoodite: Towards rheology under transition zone conditions. Phys. Earth Planet. Inter. **248**: 20-29 Open access

(15) K. Gouriet, N. Hilairet, E. Amiguet, N. Bolfan-Casanova, Y. Wang, B. Reynard, P. Cordier (2015) Plasticity of the dense hydrous magnesium silicate Phase A at subduction zones conditions. Phys. Earth Planet. Inter. **248**: 1-11 Open access

(14) K. Gouriet, Ph. Carrez, P. Cordier, A. Guitton, A. Joulain, L. Thilly, C. Tromas (2015) Dislocation modelling in Ti_2AlN MAX Phase based on the Peierls-Nabarro model. Philos. Mag. **95**: 2539-2552

(13) F. Boioli, Ph. Carrez, P. Cordier, B. Devincre, M. Marquille (2015) Modeling the creep properties of olivine by 2.5-D dislocation dynamics simulations. Phys. Rev. B **92**: 014115 Open access

(12) A.M. Goryaeva, Ph. Carrez, P. Cordier (2015) Modeling defects and plasticity in $MgSiO_3$ post-perovskite: 1- Generalized stacking faults. Phys. Chem. Miner. **42**: 781–792 Open access

(11) A.M. Goryaeva, Ph. Carrez, P. Cordier (2015) Modeling defects and plasticity in $MgSiO_3$ post-perovskite: 2- screw and edge [100] dislocations. Phys. Chem. Miner. **42**: 793–803 Open access

(10) Ph. Carrez, J. Godet, P. Cordier (2015) Atomistic simulations of ½⟨110⟩ screw dislocation core in magnesium oxide. Comp. Mater. Sci. **103**: 250-255 Open access

(9) P. Cordier (2015) News & Views - Strength under pressure. Nature Geoscience **8**: 255-256

(8) J. Amodeo, B. Schuberth, H–P. Bunge, Ph. Carrez, P. Cordier (2015) On the role of thermal heterogeneities on the rheology of MgO under conditions of the Earth's lower mantle. Phys. Earth Planet. Inter. **242**: 1-8 Open access

(7) A. Mussi, P. Cordier, S. Demouchy (2015) Characterization of dislocation interactions in olivine using electron tomography. Phil. Mag. **95**: 335-345

-2014-

(6) A. Mussi, P. Cordier, S. Demouchy, C. Vanmansart (2014) Characterization of the glide planes of the [001] screw dislocations in olivine using electron tomography. Phys. Chem. Miner. **41**: 537-545 Open access

(5) B. Journaux, R. Caracas, Ph. Carrez, K. Gouriet, P. Cordier, I. Daniel (2014) Elasticity and dislocations in ice X under pressure. Phys. Earth Planet. Inter. **236**: 10-15

(4) P. Hirel, A. Kraych, Ph. Carrez, P. Cordier (2014) Atomic core structure and mobility of [100](010) and [010](100) dislocations in $MgSiO_3$ perovskite. Acta Mater. **79**: 117-125 Open access

(3) P. Cordier, S. Demouchy, B. Beausir, V. Taupin, F. Barou, C. Fressengeas (2014) Disclinations provide the missing mechanism for deforming olivine-rich rocks in the mantle. Nature **507**: 51-56

(2) J. Amodeo, B. Devincre, Ph. Carrez and P. Cordier (2014) Dislocation reactions, plastic anisotropy and forest strengthening in MgO at high temperature. Mech. Mater. **71**: 62-73

(1) K. Gouriet, Ph. Carrez, P. Cordier (2014) Modelling [100] and [010] screw dislocations in $MgSiO_3$ perovskite based on the Peierls-Nabarro-Galerkin model. Model. Simul. Mater. Sci. Eng. **22**: 025020 Open access

List of publications related to the project

(7) P. Hirel (2015) Atomsk: a tool for converting and manipulating atomic data files. Comp. Phys. Comm. **197**: 212-219

(6) P. Hirel, A. F. Mark, M. Castillo-Rodriguez, W. Sigle, M. Mrovec, C. Elsässer (2015) Theoretical and experimental study of the core structure and mobility of dislocations and their influence on the ferroelectric polarization in perovskite $KNbO_3$. Phys. Rev. B **92**: 214101

(5) N. Garvik, Ph. Carrez, P. Cordier (2015) Numerical modeling of the core structure of [100] dislocations in Fe_3C cementite. Scripta Mater. **99**: 61-64

(4) N. Garvik, Ph. Carrez, P. Cordier (2013) First-principles study of the ideal strength of Fe_3C cementite. Mater. Sci. Eng. A **572**: 25-29

(3) J. Amodeo, Ph. Carrez, P. Cordier (2012) Modeling the effect of pressure on the critical shear stress of MgO single crystals. Philos. Mag. **92**: 1523-1541

(2) P. Cordier, J. Amodeo, Ph. Carrez (2012) Modelling the rheology of MgO under Earth's mantle pressure, temperature and strain-rates. Nature **481**: 177-180

(1) J. Amodeo, Ph. Carrez, B. Devincre, P. Cordier (2011) Multiscale modelling of MgO plasticity. Acta Mater. **59**: 2291-2301

List of abbreviations

bcc	Body-Centered Cubic (lattice, structure)
CCD	Charge Coupled Device (image sensor, camera)
CMB	Core-Mantle Boundary
CPO	Crystal Preferred Orientation
DAC	Diamond Anvil Cell
DD	Dislocation Dynamics
D-DIA	Deformation DIA (cubic-anvil apparatus)
DD-map	Differential Displacement Map
DFT	Density Functional Theory
EBSD	Electron Backscatter Diffraction
EI	Elastic Interaction (model)
EoS	Equation of State
fcc	Face-Centered Cubic (lattice, structure)
FEG	Field Emission Gun
FIB	Focused Ion Beam
GB	Grain Boundary
GGA	Generalized Gradient Approximation
GOS	Grain Orientation Spread
GPSF	Generalized Planar Fault Energy
GROS	Grain Reference Orientation Deviation
GSF	Generalized Stacking Fault
HATA	High Angular Triple Axis
hcp	Hexagonal Close Packed (structure)
HRTEM	High Resolution TEM
ISF	Intrinsic Stacking Fault
ISS	Ideal Shear Stress
KAM	Kernel Average Misorientation
KK	Kink-Kink interaction (model)
LGA	Local Density Approximation
LHDAC	Laser-Heated Diamond Anvil Cell
LLSVP	Large Low Shear-Wave Velocity Province
LT	Line Tension (model)
MD	Molecular Dynamics
MEMS	Micro-Electro-Mechanical-System
MEP	Minimum Energy Path
MORB	Mid-Ocean Ridge Basalt
NEB	Nudged Elastic Band (method)
Opx	Orthopyroxene
PAW	Projector Augmented Wave (method)
PN	Peierls-Nabarro (model)
PNG	Peierls-Nabarro-Galerkin (model)
PPv	Post-Perovskite
PREM	Preliminary Reference Earth Model
PTP	Push-to-Pull
Pv	Perovskite
SEM	Scanning Electron Microscopy
SF	Stacking Fault
STEM	Scanning Transmission Electron Microscopy
STGB	Symmetric Tilt Grain Boundary
TEM	Transmission Electron Microscopy
TZ	Transition Zone
ULVZ	Ultralow Velocity Zone
VBF	Virtual Bright Field
VPSC	Viscoplastic Self-Consistent (model)
WBP	Weighted Back Projection (technique)
XRD	X-Ray Diffraction